LEARNING BASED MULTIPLE INPUT MULTIPLE OUTPUT RADAR IMAGING

by
KUDRET AKÇAPINAR

Submitted to the Graduate School of Engineering and Natural Sciences
in partial fulfilment of
the requirements for the degree of Doctor of Philosophy

Sabancı University
March 2024

KUDRET AKÇAPINAR 2024 ©

All Rights Reserved

ABSTRACT

LEARNING BASED MULTIPLE INPUT MULTIPLE OUTPUT RADAR IMAGING

KUDRET AKÇAPINAR

Electronics Engineering Ph.D. Dissertation, March 2024

Dissertation Supervisor: Prof. Özgür Gürbüz

Dissertation Co-Supervisor: Dr. Naime Özben Önhon

Keywords: MIMO radar, FMCW, neural networks, deep-learning, inverse problems, PnP ADMM, radar range profile reconstruction, radar imaging, radar image reconstruction, angle of arrival estimation, radar measurement models

Multiple Input Multiple Output (MIMO) radars, with their unique antenna configuration, offer superior angular resolution by forming a "virtual array" with fewer antennas compared to phased-array radars. Through digital beamforming techniques, MIMO radars can generate 3D radar images of their surroundings without the need for mechanical rotation. Reconstructing an unknown field such as range/azimuth profile or full radar reflectivity image from radar returns, which are both noisy and band-limited, presents a challenging and ill-posed inverse problem. Conventional reconstruction methods typically involve inversion of the measurements through a fully known mathematical measurement model that mimics the underlying physics of measurements. However, conventional approaches often rely on a measurement model and model-based inversion techniques may not fully leverage the prior knowledge of the unknown field being reconstructed when such information is known. To incorporate prior information of the radar data into the reconstruction process, regularizers can be employed to promote specific spatial patterns within the radar data. Nevertheless, these regularizers often fall short in

effectively capturing the intricate spatial patterns within the field data being reconstructed, or they may not readily allow for analytical minimization of the cost function. Recently, the Alternating Direction Method of Multipliers (ADMM) framework has emerged as a means to provide a way of decoupling the model inversion from the regularization of the priors, enabling the incorporation of any desired regularizer into the inversion process in a plug-and-play (PnP) fashion. In this thesis, we implement the ADMM framework to address the radar range profile and image reconstruction problems where we propose to employ deep learning networks as a regularization method for enhancing the quality of the inversion process which usually suffers from the ill-posed nature of the problem. We demonstrate the efficacy of deep learning networks as a regularization method within the ADMM framework via our simulation results for the inverse problems in MIMO radar context. We assess the performance of the ADMM framework employing CNN and U-Net architectures as a regularizer for radar range profile and radar image reconstruction problems, respectively. We conduct a comparative analysis against alternative methods under different measurement scenarios. Notably, among the methods under investigation, ADMM with deep learning networks used as a regularizer stands out as the most successful method for both radar range profile and image reconstruction problems in terms of reconstruction error. Furthermore, we study the problem of target angle estimation in MIMO radars, proposing the use of artificial neural networks for this purpose. Through comprehensive experiments, we show the potential of our proposed method across a range of measurement scenarios, verifying its effectiveness especially in the presence of measurement model uncertainties.

ÖZET

ÖĞRENME TABANLI ÇOK GİRİŞLİ ÇOK ÇIKIŞLI RADAR GÖRÜNTÜLEME

KUDRET AKÇAPINAR

Elektronik Mühendisliği Doktora Tezi, Mart 2024

Tez Danışmanı: Prof. Dr. Özgür Gürbüz

Tez Eş-Danışmanı: Dr. Naime Özben Önhon

Anahtar Kelimeler: MIMO radar, FMCW, yapay sinir ağları, derin öğrenme, ters problemler, PnP ADMM, radar menzil profili, radar görüntüleme, radar görüntüleme, geliş açısı tahmini, radar ölçüm modelleri

MIMO radarlar, özel anten konfigurasyonlari sayesinde, faz dizili radarların aksine çok daha az anten kullanarak "yapay dizi" oluşturup üstün açısal çözünürlük sağlar. Sayısal hüzme oluşturma teknikleri vasıtası ile, MIMO radarlar çevrelerinin 3B radar görüntüsünü mekanik olarak döndürmeye gerek kalmadan oluşturmaya imkan tanırlar. Hem gürültülü hem de bant sınırlı olan radar ölçümlerinden menzil/azimut profili veya radar yansıtıcılığı görüntüsü gibi bir radar bilinmeyenin geri çatımı, zor ve kötü tanımlı bir ters problemi sunar. Geleneksel geri çatma yöntemleri genellikle, altta yatan ölçüm fiziğini taklit eden tamamen bilinen bir matematiksel ölçüm modeli aracılığıyla ölçümlerin ters çevrilmesine dayanır. Ancak, geleneksel yaklaşımlar çoğunlukla ölçüm modellerine dayanır ve model tabanlı geri çatma teknikleri, geri çatımı yapılan radar bilinmeyeni hakkında her hangi bir önsel bilgi mevcut dahi olsa, bu önsel bilgileri tam olarak kullanmayabilir. Geri çatımı yapılan radar bilinmeyeni hakkındaki önsel bilgilerin geri çatım adımlarına dahil etmek için, radar bilinmeyeni içindeki belirli mekansal düzenlilikleri teşvik etmek amacıyla düzenleyiciler kullanılabilir. Bununla birlikte, bu düzenleyiciler

genellikle geri çatımı yapılan radar bilinmeyeni içindeki karmaşık mekansal korelasyonları etkili bir şekilde yakalamada yetersiz kalabilir veya maliyet fonksiyonunun analitik minimizasyonuna kolayca izin vermeyeblir. Son zamanlarda, Alternatif Yönlendirme Çarpanları Yöntemi (ADMM), ölçüm verisini düzenleyici fonksiyondan ayırmayı mümkün kılarak, istenen herhangi bir düzenleyiciyi geri çatma sürecine tak-çalıştır (PnP) şeklinde dahil etmeyi mümkün kılmaktadır. Bu tezde, ADMM methodu ile menzil profil ve radar görüntüsü geri çatma problemlerini ele almak üzere uyguluyoruz ve geri çatma kalitesini artırmak için düzenleme yöntemi olarak derin öğrenme ağlarını kullanmayı öneriyoruz. MIMO radar bağlamında ters problemler için simülasyon sonuçlarımız üzerinden ADMM yöntemi içinde bir düzenleme yöntemi olarak derin öğrenme ağlarının etkinliğini gösteriyoruz. Radar menzil profil ve radar görüntü geri çatma problemleri için düzenleyici olarak CNN ve U-Net mimarilerini kullanan ADMM yönteminin performansını farklı ölçüm senaryoları altında alternatif yöntemler ile karşılaştırmalı bir analizle değerlendiriyoruz. İncelenen yöntemler arasında, hem radar menzil profili hem de görüntü geri çatma problemleri konusunda geri çatma performansı olarak en başarılı yöntem olarak ADMM, derin öğrenme ağlarının düzenleyici fonksiyon olarak kullanılması durumunda öne çıkmaktadır. Ek olarak, MIMO radarlarda hedef açı tahmini problemi üzerine çalışıp ve problem özelinde yapay sinir ağlarının kullanımı öneriyoruz. Kapsamlı deneyler üzerinden, çeşitli ölçüm senaryolarında, önerilen tekniğin tahmin doğruluğunu gösteriyoruz. Simulasyon sonuçları ile önerilen yöntemin özellikle de ölçüm modelinde belirsizlikler olduğu durumlarda etkinliğini gösteriyoruz.

ACKNOWLEDGEMENTS

I am deeply grateful to my advisor, Prof. Özgür Gürbüz, for her unlimited support throughout my doctoral journey. From the very beginning to the end, she has provided invaluable technical assistance and mentorship during challenging times. Navigating through the long and arduous path of a PhD can be challenging, but her encouragement and belief in my abilities never stopped. Without her guidance and support, this thesis would not have been possible.

I extend my heartfelt thanks to my thesis co-advisor Dr. Naime Özben Önhon for her technical guidance and contribution to my study. Her profound knowledge and background significantly contributed the outcome of my thesis.

I am indebted to Prof. Müjdat Çetin for his exceptional guidance and profound insights in the areas of inverse problems and SAR imaging. His visionary outlook and technical expertise have been instrumental in shaping my doctoral study and guiding me in the right direction. Our discussions have been enlightening, and his contribution to my intellectual growth is immeasurable. I am truly grateful for his support and mentorship.

I extend my sincere appreciation to Prof. Özgür Erçetin for agreeing to be a part of my thesis committee and providing valuable feedback during my progress meetings.

I also wish to express my gratitude to thesis jury members Assoc. Prof. Ahmet Onat and Assoc. Prof. Erchan Aptoula for accepting being in my thesis committee and providing their valuable inputs to improve my thesis.

I would like to acknowledge Dr. Süleyman Baykut, my former department head at BILGEM, TUBITAK, for his support, assistance and all the technical discussions about radars that we have had.

Special thanks to my friends Mehdi Abad, Ahmet Ersel Tuncer and Fatih Yeşil for their uplifting discussions and motivation.

I am deeply grateful to my parents, Ali Akçapınar, Çevri Akçapınar, Yaşar Kalcıoğlu, Hamiye Kalcıoğlu, my sister Özge Acar, and my brothers Bekir Acar and Sedat

Tolga Kalcıoğlu, for their unconditional love, unwavering support, and encouragement. Their support has been a source of strength throughout my PhD journey.

I am grateful to my nephews Yusuf and Deniz for bringing joy into my life and being a source of happiness during the challenging times of my PhD.

Last but certainly not least, I extend my heartfelt gratitude to my beloved wife, Binnaz, for her unwavering support, motivation, and endless patience. She is the invisible hero behind this thesis dissertation. Her support has been the cornerstone of my success, and I am deeply thankful for everything she has done for me.



Canım aileme...

Contents

Contents **xi**

List of Tables **xv**

List of Figures **xvi**

1 INTRODUCTION **1**

1.1 MIMO Radars 1

1.2 Contributions 5

1.3 Organization 7

2 MIMO RADAR ARRAY PROCESSING **9**

2.1 Array Antennas 9

2.2 MIMO Radar Simulation 14

3 RADAR INVERSE PROBLEMS AND ADMM FRAMEWORK **17**

3.1 Problem Definition 18

3.2 Approaches to Inverse Problems 20

3.3 Least-squares Solution and Ties to SVD 22

3.3.1 Least-squares Solution from Optimization Perspective 22

3.3.2 Least-squares Solution from Linear Algebraic Perspective . . 23
3.4 Probabilistic Approach 25
3.5 Regularized Inversion 29
3.5.1 Alternating Direction Method of Multipliers (ADMM) . . . 29

4 ARTIFICIAL NEURAL NETWORK BASED RADAR TARGET ANGLE ESTIMATION 33

4.1 Introduction 34
4.2 System Model and Signal Processing 36
4.2.1 Range Processing 38
4.2.2 Angular Processing 43
4.3 ANN Based DoA Estimation 48
4.3.1 MIMO Simulation & Training Data Generation 51
4.3.2 Proposed Neural Network Architecture & Training 54
4.4 Numerical Results 56
4.4.1 Computational Analysis 62
4.4.2 Extension to 2D DoA 63
4.5 Conclusions 65

5 PnP-ADMM BASED RADAR RANGE PROFILE RECONSTRUCTION USING DEEP PRIORS 66

5.1 Related Work 67
5.2 Observation Model for Side-Looking Radars 72
5.2.1 Signal Processing 74
5.2.2 Radar Measurement Model 80

5.3 Complex-valued Range Profile Formation with Magnitude and Phase Regularization 81
5.3.1 Problem Formulation 81
5.3.2 Investigation on Phase Regularization 82
5.3.3 PnP-ADMM Based Range Profile Formation 85
5.3.3.1 Optimization of Data Fidelity for Magnitudes . . . 86
5.3.3.2 Optimization of Data Fidelity for Phases 87
5.3.3.3 Prior Updates Using Convolutional Neural Networks 87
5.3.3.4 PNP ADMM Framework with Complete Solution . 94
5.4 Complex-valued Range Profile Formation with Magnitude Regularization Only 98
5.4.1 ADMM Formulation 98
5.4.2 Simulation Results 100
5.5 Real-valued Range Profile Formation 103
5.6 Conclusions 110

6 RADAR IMAGING WITH DEEP LEARNING 115

6.1 Related Work 115
6.2 Surface Imaging with Side-Looking MIMO Radar with Post-processing Learning 118
6.2.1 Derivation of Observation/Forward Model 120
6.2.2 Sampling over Fourier Space 123
6.2.3 Learning Post-processing 125
6.2.4 Numerical Results 130
6.3 Near-field MIMO Radar Imaging Using Plug and Play Denoisers . . 138

6.3.1 Plug-and-Play Radar Image Formation 142
6.3.2 Numerical Results 146
6.4 Conclusion 148

7 CONCLUSIONS **154**

Bibliography **156**

List of Tables

2.1 Parameters for single target simulation 14

2.2 Cartesian coordinates of the targets 16

4.1 Radar parameters used in the MIMO radar simulations. 51

4.2 The average computation times of DoA methods, calculated with 1500 runs of each method. 63

5.1 Training parameters for CNN 102

5.2 Performance comparison of different methods 103

6.1 Measurement conditions for considered superresolution and denoising problems 130

List of Figures

1.1 Representation of formation of the virtual array in MIMO radars . 4

1.2 Array beam patterns of a uniform linear array with 8 elements and a MIMO radar with 2 Tx and 4 Rx antennas 4

2.1 2D planar antenna array geometry. 10

2.2 ULAs used for MIMO radar simulations 12

2.3 Array pattern of an example linear MIMO radar 13

2.4 FMCW signal used in the simulations and its spectrogram. 15

2.5 Radar scene in Cartesian and polar representation 15

2.6 Range and azimuth profiles 16

2.7 Radar scene in Cartesian and polar representation 16

3.1 Representation of forward and inverse problems 18

3.2 Forward and inverse problems in imaging. 20

4.1 Simplified model of a MIMO radar system 37

4.2 Transmitted and received chirp signals 39

4.3 MIMO radar transmit and receive antenna array configuration . . . 43

4.4 Array factor calculation for a MIMO radar 46

4.5 Left: Radar data acquired by an 8×8 MIMO radar system showing three targets. Middle: Radar data post range FFT processing, revealing the targets' range information. Right: Radar data post angle FFT processing, unveiling the targets' angular information. . 49

4.6 Normalized angle measurements of a point target with an RCS of 40 db located 400m away from the array center at each virtual MIMO element in complex IQ plane with respect to changing target azimuth angle. Numbers next to each plot represent the corresponding virtual array index. With 6 transmit and 10 receive antenna, we form a virtual array with 60 elements. 50

4.7 Linear up-chirp FMCW signal considered in our simulations 51

4.8 An illustrative MIMO measurements for a single target 53

4.9 Artificial neural network used for the regression of the AoA. The numbers below the each layer represent the number of neurons in each layer 54

4.10 Mean square error plots during the progression of the training (100 epochs) of the six different networks trained at six different RCS levels. MSE performance is plotted for train, test and validation data sets with a circle mark indicating the best validation performance during the training 55

4.11 Data processing steps of the proposed method: 1) Range extraction through FFT along the fast-time axis 2) Target detection 3) DoA estimation with the trained neural network. 56

4.12 Regression performances of 6 different networks trained at different target RCS level. Each data points show true azimuth angle of the network prediction. Correlation coefficient for each regression is also given on the top of the figures. Equation for the best line fit is provided in the y axis of the each plot. $y = x$ line is also plotted to provide goodness of the each fit 59

4.13 Histogram plots of the 6 different networks trained at 6 different target RCS. Error bars for the train, validation and test set are colored in blue, green and red, respectively. Zero error level is also indicated with vertical red line. Each histogram uses 30 bins. 60

4.14 Performance comparison of the proposed technique with other existing DoA methods 61

4.15 Simulation results for the randomly distributed target experiment . 62

4.16 Neural network architecture used for 2D DoA estimation 63

4.17 Training and test results of the network for 2D DoA estimation . . 64

5.1 Decision tree for the proposed algorithms' use cases with their respective sections in the manuscript. 70

5.2 Simplified representation of a side-looking radar observation model . 72

5.3 RF block diagram for bi-static FMCW radar in its simplest form . . 74

5.4 FMCW waveform 76

5.5 Magnitude & phase map of a Gotcha SAR image of a scene 83

5.6 Correlation matrices for the range and azimuth bins obtained from a SAR radar image 84

5.7 Network architecture 88

5.8 Layer by layer description of network 88

5.9 An example set of synthetically created radar scenes and representative monostatic measurements taken around a radar scene at several observation angles. 89

5.10 A representative set of radar range profiles is obtained by applying the Radon transform to synthetic radar scenes at various observation angles 90

5.11 Training loss and RMSE during training of magnitude and phase networks with training data set with $\sigma = \sigma_0$ 92

5.12 An arbitrary sample input-output pairs to magnitude and phase CNNs. 92

5.13 CNN response to a given noisy radar range profile reconstructed by FFT 93

5.14 A block diagram representation of alternating optimization steps of PnP ADMM framework: Forward model is inverted for magnitude and phase and any appropriate denoiser can be chosen in a Plug-And-Play manner 95

5.15 ADMM progression on arbitrary range profile 96

5.16 Performance comparison of conventional (FFT based) and proposed range profile reconstruction technique under different data availability and noise power conditions on two test profiles 97

5.17 A block diagram representation of alternating optimization steps of ADMM 99

5.18 Implemented CNN architecture. 100

5.19 A sample set of input/output pairs of range profiles used during training. Range profiles in blue are obtained with a single pulse, while range profiles in red are obtained by integrating successive 64 pulses non-coherently 101

5.20 Loss during training of the network 102

5.21 Performance comparison of conventional (FFT based) and ADMM based based range profile reconstructions with different PnP denoisers. Denoised range profiles with 64-pulse non-coherent integration are shown in blue and range profiles reconstructed from a single pulse with different techniques are shown in red. a) Conventional reconstruction (FFT based) b) ADMM based reconstruction with Total Variation (TV) denoiser c) ADMM based reconstruction with Recursive Filter (RF) denoiser d) ADMM based reconstruction with CNN denoiser 103

5.22 Convolutional neural network architecture 104

5.23 Network architecture with the detailed layer information. Total number of learnables is 124.8k. 105

5.24 A block diagram representation of alternating optimization steps of ADMM. 106

5.25 A sample set of range profiles used in the simulations. (Horizontal axis is the range axis and vertical axis is the radar reflectivity magnitude) 107

5.26 Loss during training of the network 108

5.27 Comparison of various range profile reconstruction approaches on an example range profile data in terms of MSE performance under different noise - Reconstruction at three different measurement noise values (full-bandwidth) 112

5.28 Comparison of various range profile reconstruction approaches on an example range profile data in terms of MSE performance under different bandwidth conditions - Reconstruction at three measurement bandwidth values (no measurement noise present) 113

5.29 MSE performance comparison of different reconstruction methods under different bandwidth availability and measurement noise conditions 114

6.1 Simplified imaging geometry 119

6.2 Projection of imagery setup onto 2D horizontal plane. 120

6.3 Fourier space observations with different antenna settings. 124

6.4 Training and testing stages of the proposed reconstruction method with post-processing learning 126

6.5 Architecture of the implemented U-Net with the connections 127

6.6 Detailed layers of the implemented U-Net architecture with the layer types and respective number of parameters used 128

6.7 Deep network designer GUI of Deep Learning Toolbox in Matlab. . 129

6.8 Denoising problem - Performance of conventional FFT based reconstruction and post-processing with U-Net 133

6.9 Denoising problem - Performance of conventional FFT based reconstruction and post-processing with U-Net 134

6.10 Superresolution problem - Performance of conventional FFT based reconstruction and post-processing with U-Net 135

6.11 Superresolution problem - Performance of conventional FFT based reconstruction and post-processing with U-Net 136

6.12 Superresolution problem - Performance of conventional FFT based reconstruction and post-processing with U-Net 137

6.13 Performance comparison of conventional (FFT based) and proposed range profile reconstruction technique under different measurement data availability and measurement noise conditions 138

6.14 Representative imaging setup 139

6.15 MIMO radar antenna configuration 140

6.16 A block diagram representation of alternating optimization steps of ADMM: Forward model is inverted to solve the subproblem in (6.27a) and any appropriate denoiser can be chosen in a Plug-And-Play manner to solve for subproblem in (6.27b) 144

6.17 Flow chart describing the ADMM iterations for model/data and priors update. Model/data update is executed by computing the solution in (6.27b), and priors update is accomplished through a denoising U-Net. 145

6.18 MIMO radar antenna configuration 147

6.19 Measurement to unknowns ratio: 25% ($\frac{M}{N} = 25\%$) 149

6.20 Measurement to unknowns ratio: 50% ($\frac{M}{N} = 50\%$) 150

6.21 Measurement to unknowns ratio: 75% ($\frac{M}{N} = 75\%$) 151

6.22 Measurement to unknowns ratio: 100% ($\frac{M}{N} = 100\%$) 152

6.23 Average PNSR and SSIM comparison of different reconstruction methods 153

List of Abbreviations

ADMM	Alternating Direction Method of Multipliers
CS	Compressive Sensing
CNN	Convolutional Neural Network
DL	Deep Learning
FFT	Fast Fourier Transform
MIMO	Multiple Input Multiple Output
MSE	Mean Squared Error
PSNR	Peak Signal-to-Noise Ratio
pdf	Probability Density Function
PnP	Plug-and-Play
RF	Recursive Filter
RCS	Radar Cross Section
SSIM	Structural Similarity Index Measure
TV	Total Variation

Chapter 1

INTRODUCTION

In this chapter, we first provide a brief overview of MIMO radars and their various types. Following this introduction, we explain three distinct problems associated with MIMO radars, which serve as the primary focus of this dissertation. We then outline our proposed data-driven approaches to address these problems, highlighting our rationale for favoring data-driven methods over traditional model-based radar reconstruction techniques. Finally, we present the contributions made by this dissertation and outline its organizational structure.

1.1 MIMO Radars

Radar, short for "Radio Detection and Ranging" are used in a variety of sensing applications [1–3]. Radars operate by transmitting electromagnetic waves. When these waves encounter a reflective object, they are reflected back to the radar. Receiver antennas then capture these reflected waves, which are subsequently processed to extract various information about the object. The extracted information varies depending on the application. For surveillance radar, for example, this typically includes positional data about detected objects.

As an emerging radar type, active phased array radars have garnered significant interest, as discussed in the survey [4]. These radar systems were developed to

eliminate the necessity for mechanical rotation in large antennas. Leveraging digital beam-forming capabilities, phased array radars enable precise beam steering toward desired directions, concentrating energy into narrower beams. They achieve this by transmitting coherent pulses with linearly shifted phase to direct the beam.

On the other hand, another radar system introduced in the 1990s, known as Synthetic Impulse and Aperture Radar (SIAR) [5], showcased an innovative approach. Unlike phased array radar that transmits coherent pulses, each element within the SIAR array transmits orthogonal waveforms, ensuring that the amalgamation of transmitted signals can be effectively separated at the receiving end. In terms of cooperative mechanisms, SIAR bears similarity to Multiple Input Multiple Output (MIMO) systems in wireless communications. As a result, the radar community has adopted this nomenclature to categorize radar systems involving cooperating transmitters [6–8].

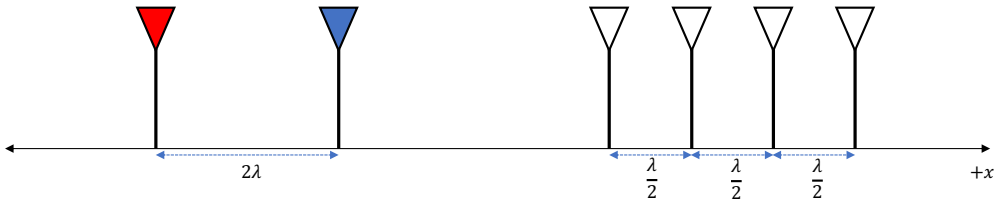
In [9], MIMO radar is defined as a radar system capable of transmitting multiple orthogonal waveforms and jointly processing radar returns across multiple receivers. Unlike conventional phased array radars that concentrate radiation energy, MIMO radars evenly distribute energy throughout space. This leads to processing gain losses compared to phased array radars, where energy is focused into a narrower beam. In MIMO operation each transmit antenna emits orthogonal waveforms that are collected by multiple receiving antennas simultaneously. Due to the orthogonality of these signals, receivers are able to disentangle the transmitted signals from various transmitters. MIMO radars fall into two main categories: Co-located MIMO and widely separated MIMO.

In widely separated MIMO radars, transmitter and receiver antennas span across a vast area, enjoying the spatial properties of radar targets. Radar targets present a complex scattering environment, resulting in a significant dependency of Radar Cross Section (RCS) on the aspect angle. This dependency can lead to RCS fluctuations of up to 5-20 dB [9]. A comprehensive explanation on how to make use of the RCS fluctuation through spatial diversity is detailed in [10]. The distinct advantage of widely distributed MIMO radars lies in these substantial variations

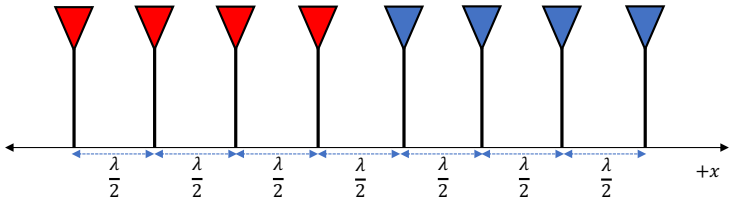
in radar returns with respect to the aspect angle. This phenomenon bears a resemblance to fading wireless channels. Thus, a strong correlation exists between the MIMO concept in wireless communications and radar systems. In wireless communications, the time-varying nature of the channel induces fluctuations in received power, termed as fading. Drawing an analogy, the channel in wireless communications aligns with the radar target. Similar to the improved decoding performance achieved by combining uncorrelated channels in MIMO communications, pairing MIMO radar transmitters/receivers with diverse look angles enhances target detection performance. Diversity stands as a critical element in both systems. The fundamental distinction lies in the means of achieving diversity: uncorrelated wireless channels in MIMO communications versus diverse look angles in MIMO radar.

Contrary to widely separated MIMO radars, co-located MIMO radars do not capitalize on the spatial diversity of targets. This limitation arises from the close proximity of antennas. As a result of the array elements' tight configuration, each element perceives targets at nearly identical angles, leading to a lack of look angle diversity and consequently, no RCS diversity is achieved. Nonetheless, smart configurations of MIMO antennas enable the creation of what is known as virtual arrays, surpassing the physical size of the array through the principle of *digital beam-forming*. This technique enhances angular resolution, offering higher cross-range resolution, particularly in imaging applications. To illustrate this, we consider a simple example of a linear MIMO array featuring 2 transmitters and 4 receivers, as shownn in Figure 1.1a.

Here, the colored antennas represent the transmit antennas. Note that the transmit antennas are spaced apart by 2λ, which equals the number of receive antennas times half the wavelength. In this configuration, there are total of 8 distinct Tx-Rx pairs, despite having only 6 physical elements. Consequently, it is as if we have a full array of 8 elements with a separation of $\lambda/2$. This virtual expansion arises from the linear phase shifts between different Tx-Rx pairs. The formed virtual array is depicted in Figure 1.1b. The position of the the virtual array elements is determined by the convolution of the position of each transmit and receive element. Figure 1.2 displays the array beam patterns of transmit and receiver arrays,

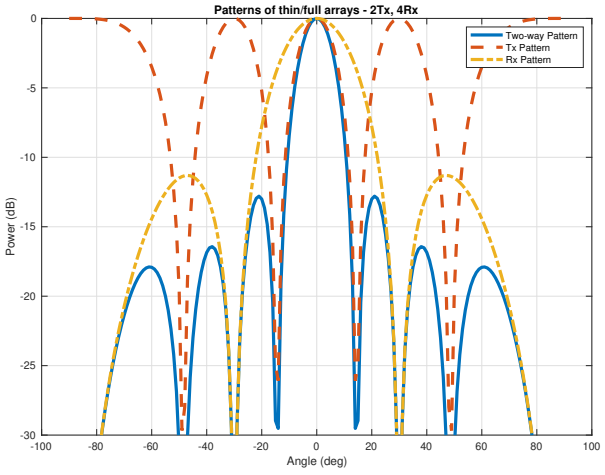


(A) Linear MIMO radar with 4 Rx element and 2 Tx elements

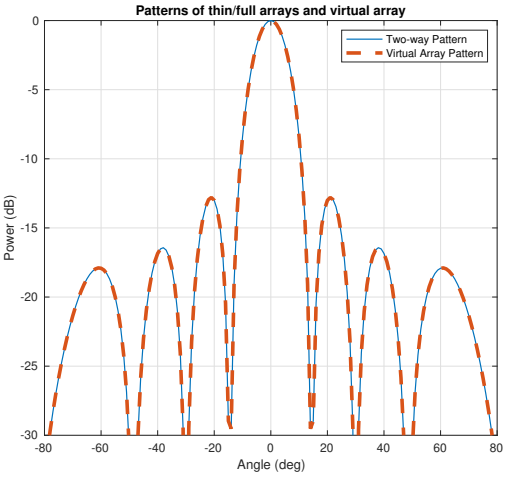


(B) Virtual array with 8 elements

FIGURE 1.1: Representation of formation of the virtual array in MIMO radars



(A) Array patterns of Tx and Rx arrays and overall array pattern



(B) Array patterns of 2×4 MIMO and 1×8 ULA

FIGURE 1.2: Array beam patterns of a uniform linear array with 8 elements and a MIMO radar with 2 Tx and 4 Rx antennas

alongside the linear array of 8 elements uniformly distributed with half-wavelength separation. As it is clear from the beam patterns of each, both arrays exhibit identical array patterns, consequently offering the same angular resolution. Despite the MIMO system having a total of 6 antennas, it performs equivalently to an 8-element uniform linear array. This characteristic stands as the most promising feature of MIMO radar, enabling achieving uniform array-level angular resolution with fewer antennas.

Due to their advantages, MIMO radars have seen widespread adoption across

various domains, including target detection, tracking, parameter identification, imaging, and more. Many of these applications pose challenges in the form of inverse problems, where the goal is to estimate physical quantities from limited and noisy radar measurements.

Traditionally, these inverse problems are tackled by directly inverting radar measurements using a mathematical model that mimics the underlying physics. However, the effectiveness of such methods is often limited by factors such as measurement bandwidth and noise. Furthermore, they typically do not incorporate any prior knowledge about the physical quantities being estimated, although such information can be used to facilitate the inversion process.

With the evolution of machine learning algorithms, data-driven approaches have begun leveraging inverse problems. Notably, the inverse problems encountered in radar applications represent an ideal domain for the application of machine learning in radar technology. These problems may involve estimating radar range/angle profiles, determining radar target parameters, or creating radar reflectivity map of a radar scene for instance. Motivated by the open research areas where MIMO radar inverse problems can be leveraged by the use of machine learning techniques we study the following three distinct inverse problems of MIMO radars by utilizing machine learning techniques:

1. Angle of radar target estimation problem
2. Radar range profile reconstruction problem
3. 2D radar image reconstruction problem

1.2 Contributions

The contributions of this thesis per studied topic can be listed as follows:

Angle of radar target estimation problem

- A data-driven approach to the problem of angle estimation of radar targets using MIMO radar is proposed. Instead of relying on a measurement model sensitive to the array geometry and calibration of the RF components, the measurement model is directly learned from training/calibration data.
- We propose an artificial neural network-based calibration technique for the estimation of target angle using a single snapshot angle measurements. The proposed solution is capable of maintaining angular estimation performance, even in the presence of inaccuracies in the measurement model.
- We investigate the performance of the proposed approach under different SNR conditions and model uncertainty in comparison with the existing methods through the extensive end-to-end Frequency Modulated Continuous Wave (FMCW) MIMO radar simulations performed in the physical layer.

Radar range profile reconstruction problem

- We explore the inverse problem of radar range profile reconstruction from band-limited noisy radar measurements for real and complex valued radar range profile by utilizing Plug-and-Play (PnP) Alternating Direction of Method (ADMM) framework.
- For the complex-valued range profile, we propose two solutions with magnitude regularization only and magnitude and phase regularization combined depending on the significance of the spatial phase patterns of the radar range profile being reconstructed.
- We provide a clear formulation of radar range profile reconstruction problem for a side-looking FMCW radar setup with both continuous and discrete Fourier-based observation models for a side-looking radar, which relates the radar range profile to radar measurements.

- We directly use the raw radar measurement data and propose a solution for a PnP ADMM-based reconstruction for a given raw radar data. To our knowledge, this study represents the first direct application of PnP ADMM directly to raw radar phase history data.
- We implement various convolutional neural networks and train them using diverse datasets, aiming to learn the intricate spatial patterns within both the magnitude and phase components of the radar range profile data.

2D radar image reconstruction problem

- We investigate two distinct MIMO radar imaging scenarios and derive their mathematical measurement models.
- We propose two different deep-learning methodologies for the studied image reconstruction problems. Firstly, we employ a U-Net architecture to enhance the final quality of the reconstructed radar image through post-processing. Secondly, we utilize a PnP-ADMM framework, where we iteratively optimize data and priors in alternating steps. Notably, this study marks the pioneering use of the PnP ADMM framework for 2D near-field radar imaging using a MIMO radar.
- Different than previous works, which required separate networks trained for different SNR levels, we show the practical applicability of utilizing a single network trained on mixed SNR data through various simulations scenarios.

1.3 Organization

We allocate dedicated chapters for each of the aforementioned MIMO radar problems. Each chapter includes an introductory overview of the specific problem and a review of the existing literature pertinent to that particular problem. The remaining structure of the thesis is outlined as follows:

In Chapter 2, we provide a concise overview of MIMO radars, accompanied by analytical derivations for the beam patterns of uniform antenna arrays. Additionally, we present the results of MIMO radar simulations, considering scenarios involving single and multiple targets. We present the inverse radar problems in Chapter 3 and explain the solutions from both linear algebraic and Bayesian perspective. We formulate the ADMM steps for the studied discrete linear inverse problems. Chapter 4 delves into our artificial neural network based approach for target angle estimation based using MIMO radar measurements. We explore the potential of ANN methodologies in enhancing target angle estimation accuracy. The PnP ADMM framework for radar range profile reconstruction is introduced in Chapter 5, offering powerful computational framework for addressing range profile reconstruction problems in radar systems. In Chapter 6, we focus on two distinct imaging scenarios employing MIMO radars. Here, we illustrate the formation of 2D radar images utilizing the PnP ADMM framework and least-squares solution post-processed by a trained U-Net architecture. Finally, Chapter 7 presents our conclusions, summarizing the key findings and contributions of this dissertation.

Chapter 2

MIMO RADAR ARRAY PROCESSING

MIMO radars typically comprise Tx and Rx antenna arrays arranged in a specific configuration. The most prevalent setup is uniform arrays, with antenna elements evenly spaced. These arrays can be linear or planar, depending on the application. In this chapter, we derive mathematical formulations for the array radiation patterns of uniform planar antenna arrays. Utilizing these expressions, we calculate the array pattern for an example case featuring a 4×8 MIMO radar. In the final section, we perform radar environment simulations using a MIMO radar, examining both single and multiple target scenarios.

2.1 Array Antennas

We consider a 2D Uniform Rectangular Array (URA) geometry where antenna elements are placed over the xy plane, as shown in Figure 2.1. Once we have obtained the array pattern functions for a 2D geometry, deriving 1D array patterns from the 2D patterns becomes straightforward. Let us assume that an incident electromagnetic wave impinge on the URA shown in Figure 2.1. Let $\mathbf{k}$ be the

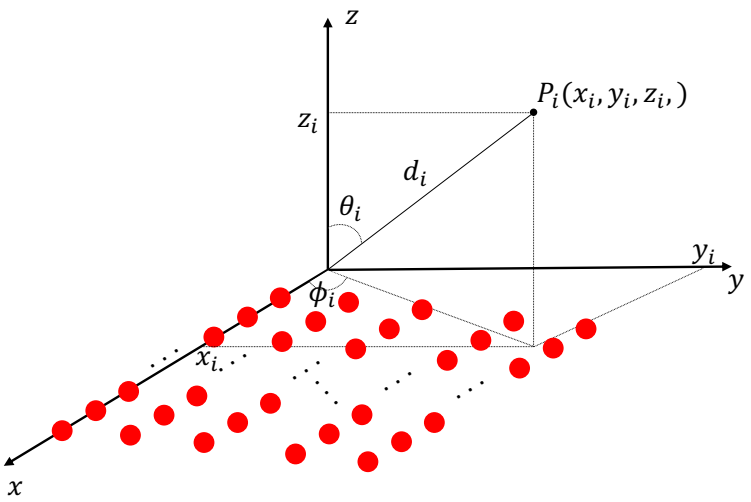


FIGURE 2.1: 2D planar antenna array geometry.

angular wave vector of the incident wave. The wave vector $\mathbf{k}$ represents the angular frequency of the wave, indicating how many radians it traverses per unit of distance. Its magnitude is related to the wavelength λ by the equation:

$$|\mathbf{k}| = \frac{2\pi}{\lambda}.$$

Then, $\mathbf{k}$ can be decomposed into three components in Cartesian coordinate system:

$$\mathbf{k} = \mathbf{k}_x + \mathbf{k}_y + \mathbf{k}_z. \tag{2.1}$$

Similarly $\mathbf{k}$ is represented with the spherical coordinate system's unit vector as follows:

$$\mathbf{k} = \frac{2\pi}{\lambda}(\cos\theta \sin\phi \mathbf{x} + \sin\theta \sin\phi \mathbf{y} + \cos\phi \mathbf{z}) \tag{2.2}$$

We also define vector $\mathbf{r}^n$ to denote the position of the nth antenna element of the array with respect to the center of the array:

$$\mathbf{r}^n = \mathbf{r}_x^n + \mathbf{r}_y^n + \mathbf{r}_z^n. \tag{2.3}$$

Moreover, the digital circuitry within the antenna array introduces gain and phase changes to the received signal by each array element to steer the beam in a specific direction. Denoting the complex gain of each array element as I_n, it can be

represented as a phasor:

$$I_n = A_n e^{j\alpha_n} \tag{2.4}$$

where A_n denotes the gain and α_n denotes the phase shift introduced digitally by the nth element of the array. The array factor as a function of the angle of arrival can then be expressed as the following sum:

$$\begin{aligned} g(\theta, \phi, \lambda) &= \sum_{n=1}^{N} I_n e^{-j\mathbf{k}.\mathbf{r}} \\ &= \sum_{n=1}^{N} I_n e^{-j\frac{2\pi}{\lambda}(\cos\theta \sin\phi r_x^n + \sin\theta \sin\phi r_y^n + \cos\phi r_z^n)} \end{aligned} \tag{2.5}$$

As evident from Eq. (2.5), controlling the beam of the array is achieved by altering the complex gain of each array element. This digital manipulation of complex gain at each antenna element is known as digital beamforming. The overall radiation pattern of an array antenna is the product of the array factor and the individual radiation pattern of each element, given by:

$$G(\theta, \phi, \lambda) = f(\theta, \phi, \lambda) g(\theta, \phi, \lambda) \tag{2.6}$$

where $f(\theta, \phi, \lambda)$ denotes the individual radiation pattern of the elements of the array. Based on $G(\theta, \phi, \lambda)$, one can calculate the directivity of the array as follows:

$$D(\theta, \phi, \lambda) = 4\pi \frac{|G(\theta, \phi, \lambda)|^2}{\int_0^{2\pi} \int_0^{\pi} |G(\theta, \phi, \lambda)|^2 \sin\phi d\phi d\theta} \tag{2.7}$$

For a uniformly sampled planar array with N_x antennas placed along the x-axis and N_y antennas along the y-axis, Eq. (2.5) becomes:

$$g(\theta, \phi, \lambda) = \sum_{n=1}^{N} I_n e^{-j\frac{2\pi}{\lambda}(\cos\theta \sin\phi(n-1)\Delta_x + \sin\theta \sin\phi(n-1)\Delta_y)} \tag{2.8}$$

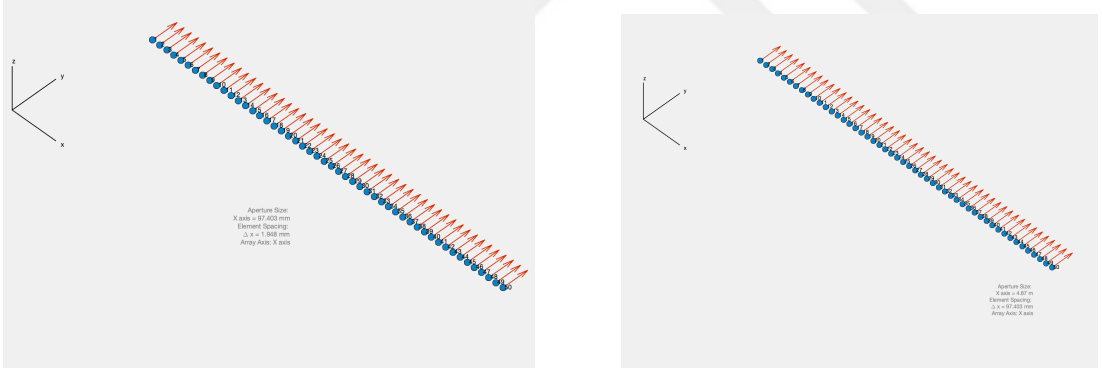
Assuming uniform complex gains at each receiver, i.e., $I_n = 1$ for all $n \in \{1, \ldots, N\}$, we have the following array factor:

$$g(\theta, \phi, \lambda) = \frac{\sin\left(\frac{N_x}{2}\frac{2\pi}{\lambda}\Delta_x \sin\phi\cos\theta\right)}{\sin\left(\frac{\frac{2\pi}{\lambda}\Delta_x \sin\phi\cos\theta}{2}\right)} \cdot \frac{\sin\left(\frac{N_y}{2}\frac{2\pi}{\lambda}\Delta_y \sin\phi\sin\theta\right)}{\sin\left(\frac{\frac{2\pi}{\lambda}\Delta_y \sin\phi\sin\theta}{2}\right)}. \tag{2.9}$$

The array pattern for 1D uniform linear arrays can be readily derived from Eq. (2.9). For example, for a linear array positioned along the x-axis (i.e., $\theta = 0$) with elements evenly distributed at intervals of Δ_x, it simplifies to:

$$g(\theta, \phi, \lambda) = \frac{\sin\left(\frac{N_x}{2}\frac{2\pi}{\lambda}\Delta_x \sin\phi\right)}{\sin\left(\frac{\frac{2\pi}{\lambda}\Delta_x \sin\phi}{2}\right)} \tag{2.10}$$

Note that the expression (2.10) represents the Fourier transform of the complex gains, I_n. This is why its array factor exhibits a sinc-shaped pattern when $I_n = 1$. With these mathematical formulations, we are equipped to calculate the array factor of an N-element antenna array.



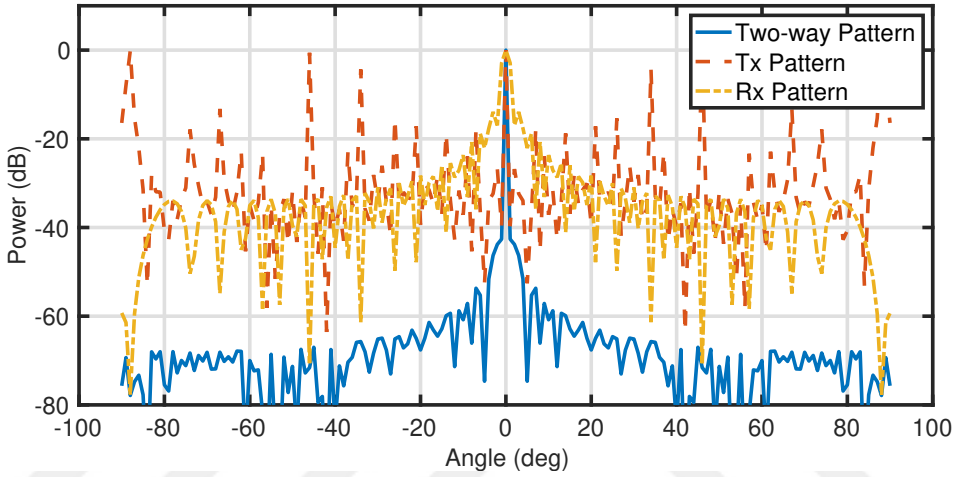
(A) Rx array with 50 antennas (B) Tx array with 50 antennas

FIGURE 2.2: ULAs used for MIMO radar simulations

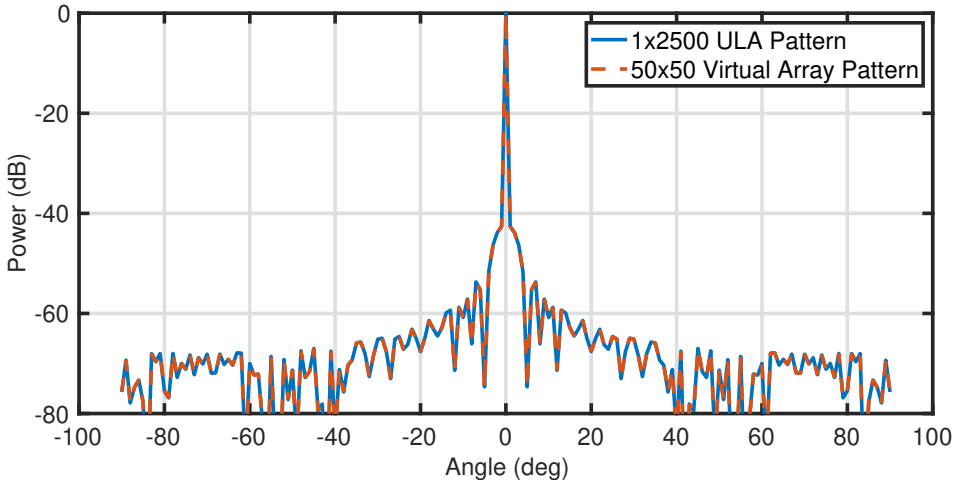
To practice the expressions derived for the ULAs we consider an example MIMO radar with 50 receive antennas and 50 transmit antennas operating at 77 GHz, as depicted in Figures 2.2a and 2.2b, respectively. The receive antennas are spaced by $d_r = \frac{\lambda}{2}$, and the transmit antennas are spaced by $d_t = N_t\frac{\lambda}{2}$.

Array patterns of the receiver, the transmitter, and the overall MIMO radar (combination of Tx and Rx patterns) are computed using Eq. (2.10) and illustrated in

Figure 2.3a. It's noteworthy that the overall resulting array factor for a MIMO radar is given by the product of the individual transmit and receive arrays' antenna patterns. In Figure 2.3b, array patterns of a 50×50 MIMO radar and a 1×2500 array are compared. As evident from the figure, the 50×50 MIMO radar can achieve the same array pattern as the 1×2500 ULA. Hence, in terms of angular resolution, MIMO radars can provide equivalent performance with significantly fewer antenna elements.



(A) Array patterns of Tx and Rx arrays



(B) Array patterns, 50×50 MIMO radar vs 1×2500

FIGURE 2.3: Array pattern of an example linear MIMO radar

2.2 MIMO Radar Simulation

In this section, we perform FMCW MIMO radar simulation. We first focus on radar scenario with single target only, then extend our scenario to multi targets. Details of the radar simulation are summarized in Table 2.1

Parameter	Description	Unit	Value
Chirp Time	Time duration of the chirp signal	μs	10
Range resolution	Resolution in the range direction	m	3
Chirp Bandwidth	Bandwidth of the chirp signal	MHz	150
Sampling frequency	Frequency at which samples are taken	MHz	300
Target RCS	Radar Cross Section of the target	m^2	100
Target Speed	Speed of the target	m/s	0
Target Range	Distance of the target from the radar	m	282.8
Target Azimuth	Azimuth angle of the target	deg	45
Tx Antenna Gain	Gain of the transmitting antenna	dB	20
Rx Antenna Gain	Gain of the receiving antenna	dB	20
Peak power	Peak power of the transmitted signal	mW	200
Receiver noise figure	Noise figure of the receiver	dB	0

TABLE 2.1: Parameters for single target simulation

We use a 50×50 MIMO radar, as shown in Figure 2.2. Linear chirp signals are transmitted from the MIMO radar with the following form depicted in Figure 2.4 with time-domain and spectrogram representation:

The chirp signals are transmitted from the transmitter antennas in a time-division manner. Transmitted signals reflect from the object, and the reflected signals are collected by the receiver antenna. After range and angle processing, as will be discussed in Chapter 4 in detail, a 2D radar image is formed. Figure 2.5a displays the radar image of the scene with a single target positioned at $(x = 200m, y = 200m)$. This image is a polar representation of the radar scene, with rows representing the range and columns representing the azimuth angles. The Cartesian representation is demonstrated in Figure 2.5b. As can be seen from Figure 2.5b, a peak appears at position $(200m, 200m)$, verifying our method of radar scene formation with the respective scales in both range and azimuth dimensions.

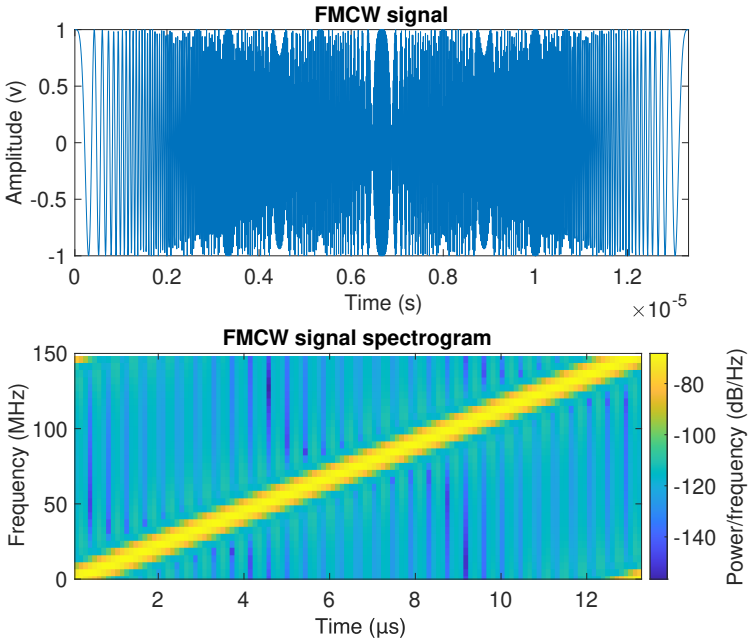
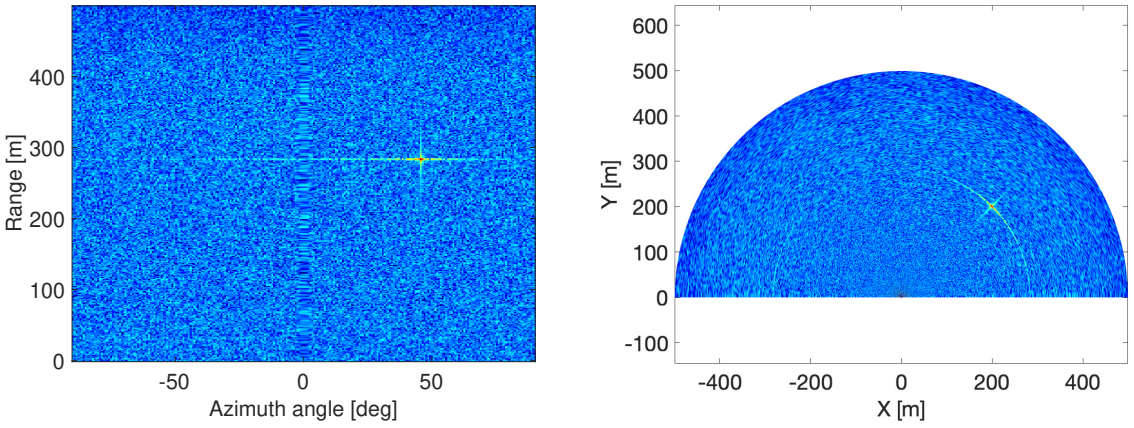


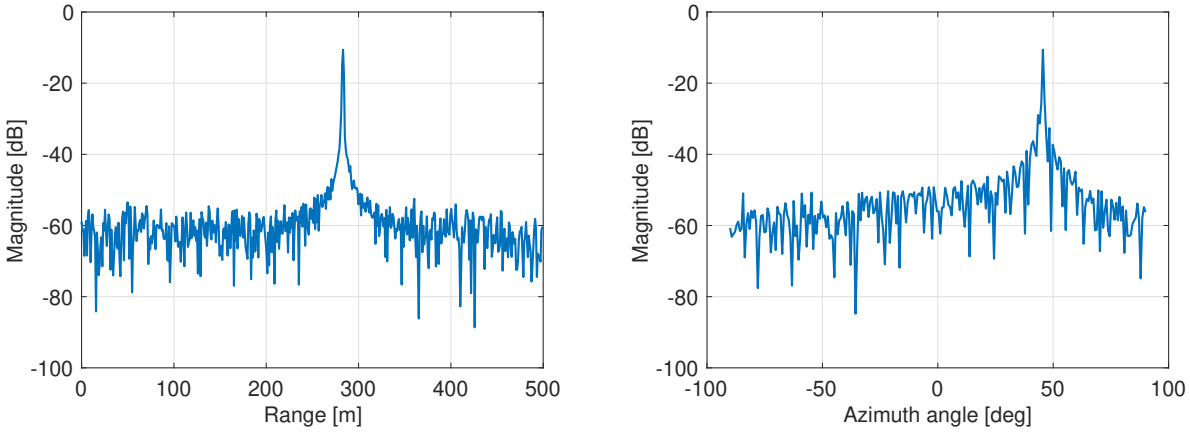
FIGURE 2.4: FMCW signal used in the simulations and its spectrogram.



(A) Polar representation (B) Cartesian representation

FIGURE 2.5: Radar scene in Cartesian and polar representation

Additionally, Figures 2.6a and 2.6b showcase the range and azimuth profiles for the single target. These profiles represent horizontal and vertical slices extracted from Figure 2.5a at the respective rows and columns where the target appears.



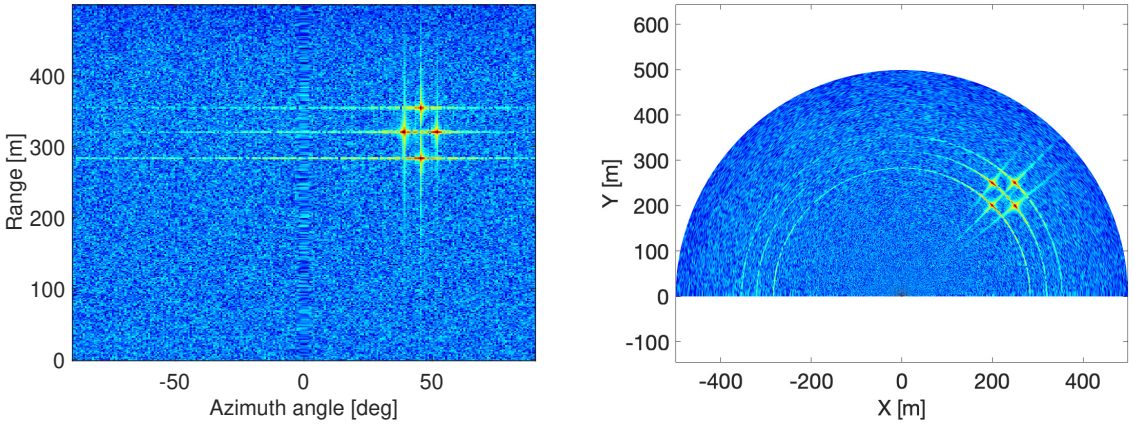
(A) Range profile (B) Azimuth profile

FIGURE 2.6: Range and azimuth profiles

	Target 1	Target 2	Target 3	Target 4
x (m)	200	250	200	250
y (m)	200	200	250	250
z (m)	0	0	0	0

TABLE 2.2: Cartesian coordinates of the targets

We repeat the same scenario, but with 4 targets in order to see the radial and angular resolution capability of the considered MIMO radar. For this purpose we place 4 target in the positions given in Table 2.2. Reconstructed polar and cartesian radar images are shown in Figure 2.7a and 2.7b, respectively.



(A) Polar representation (B) Cartesian representation

FIGURE 2.7: Radar scene in Cartesian and polar representation

Chapter 3

RADAR INVERSE PROBLEMS AND ADMM FRAMEWORK

In many of the engineering applications, we seek to estimate an underlying physical field/quantity through an observation process. These observations, which encompass various aspects of physics such as geometry, sensor configurations, and measurements channels, are encapsulated in a sensing or measurement model. This model mathematically describes the observation process and establishes the relationship between the unknown field and the measurements.

For example, in radar imaging, the unknown field corresponds to the reflectivity distribution of the radar scene, while the observations consist of radar measurements. The observation model accounts for the two-way propagation channel between the radar transmitter and the scene, as well as between the scene and the receiver. This channel incorporates factors such as attenuation, time delays due to propagation in the medium, and phase alterations resulting from the Doppler effect induced by the nonzero radial velocity of either the radar platform or the scatterers.

3.1 Problem Definition

Let us establish a naming convention: we denote the unknown vector field we aim to estimate as $\mathbf{q}$ and the observations as $\mathbf{r}$. $\mathbf{q}$ and $\mathbf{r}$ are related through a measurement model, denoted by $\mathbf{f}(.)$. Transitioning from $\mathbf{q}$ to $\mathbf{r}$ constitutes the forward problem, while the reverse direction represents the inverse problem. Typically, our focus is on estimating the unknown field, aiming to find an estimate for $\mathbf{q}$ given the measurements $\mathbf{r}$ and the observation model $\mathbf{f}(.)$. Figure 3.1 provides a visual representation of both the forward and inverse problems.

When one has complete access to the forward model, they can fully simulate measurements, which constitutes the forward problem. However, solving the inverse problem—going from measurements to the unknown field—is not as straightforward. This is often the case in blind or semi-blind inverse problems, where complete knowledge of the observation model $\mathbf{f}(.)$ may not be available. Even when $\mathbf{f}(.)$ is known, it may not have a straightforward inverse function. Additionally, when measurement noise is introduced, the problem becomes even more challenging. Even if $\mathbf{f}(.)$ is reversible and one can compute its inverse function $\mathbf{f}^{-1}(.)$, small perturbations in data can lead to significant changes in the solution space due to the presence of measurement noise.



(A) Forward problem (B) Inverse problem

FIGURE 3.1: Representation of forward and inverse problems

Any radar reconstruction problem is inherently an inverse problem, where the objective is to estimate an unknown field from radar measurements. The aim is to derive an estimate of the unknown field that minimizes reconstruction errors. These types of problems can be formulated in a discrete manner as follows:

$$\mathbf{r} = \mathbf{f}(\mathbf{q}) + \mathbf{w} \tag{3.1}$$

Here, $\mathbf{r}$ represents the sampled radar measurement vector, and $\mathbf{q}$ denotes the unknown radar field vector we aim to determine. This field may include radar range or azimuth profiles, specific parameters related to radar targets, or even the complete radar scene for which we seek an estimate. The measurement noise $\mathbf{w}$ arises from inherent physical distortions and sensor electronics. The relationship between $\mathbf{r}$ and $\mathbf{q}$ is governed by the forward model $\mathbf{f}(.)$, which encompasses all the physical effects inherent in the measurement process. While the forward model is inherently nonlinear in many cases, under certain assumptions, it can be linearized to simplify mathematical computations. In this dissertation, we primarily focus on linear forward models and establish the requisite mathematical groundwork for their utilization. We operate under the assumption that the forward model is fully known. Within this context of a linear forward model, the problem expressed by Eq. (3.1) can be presented in the following form:

$$\mathbf{r} = \mathbf{T}\mathbf{q} + \mathbf{w} \tag{3.2}$$

Here, $\mathbf{T} \in \mathbb{C}^{M \times N}$ denotes the matrix representing the linear measurement model, where M represents the number of radar measurements, and N denotes the number of unknowns. Consequently, the measurement and parameter vectors have the following sizes: $\mathbf{r} \in \mathbb{C}^{M \times 1}$ and $\mathbf{q} \in \mathbb{C}^{N \times 1}$, respectively. Note also that all the terms in Eq. (3.2) are complex-valued. Viewed as a linear system, Eq. (3.2) establishes a system where $\mathbf{q}$ serves as the input, $\mathbf{r}$ stands as the observed output, and $\mathbf{T}$ represents the system transfer function, fully delineating the relationship between $\mathbf{r}$ and $\mathbf{q}$. The term $\mathbf{w}$ represents the noise disturbance affecting the measurement accuracy.

The inverse problem of determining an estimate for $\mathbf{q}$ from a measurement vector $\mathbf{r}$, utilizing the forward model $\mathbf{T}$ is often intricate. Various scenarios might arise: a unique solution might not exist due to measurement noise, or there could be an infinite number of solutions complying with the model equation. In instances without a unique solution, a least-squares minimization approach can be employed. Conversely, when faced with an infinite set of solutions adhering to the model

equations, regularization becomes necessary to narrow down the solution space.

In this chapter, we offer an insight into the inverse problem encountered during the reconstruction of a radar range/azimuth profile or an entire radar scene. Initially, we outline the problem, categorize the proposed approaches from different viewpoints, providing a concise overview. Next, we delve into the inversion process, exploring geometric and linear algebraic perspectives of the problem. Following this, we assess the problem through a Bayesian lens. Lastly, we present a numerical solution using the Alternating Direction Method of Multipliers (ADMM). While this chapter furnishes a generic ADMM formulation, our subsequent chapters will tailor this framework to address more specific radar signal processing problems detailed in this dissertation.

3.2 Approaches to Inverse Problems

Inverse problems are encountered across various engineering disciplines and are extensively studied, particularly in the field of image processing and computational imaging. Some common examples of inverse problems from these areas include image restoration, deconvolution, pansharpening, concealment, inpainting, deblocking, demosaicking, super-resolution (SR) and compressive sensing (CS). These problems can be categorized under two main groups, as depicted in Figure 3.2: 1) Analytical solutions and 2) Deep learning-based solutions. While the former category has been extensively researched and well-established in literature, the latter, involving deep learning, has gained increasing attention in the last decade.

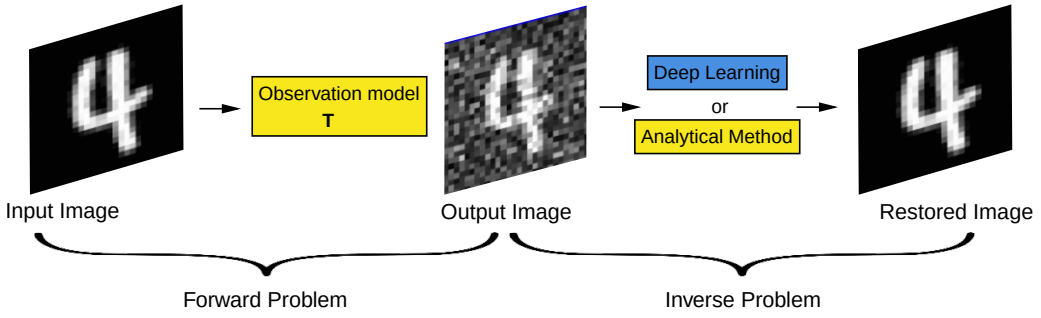


FIGURE 3.2: Forward and inverse problems in imaging.

In analytical approaches, the typical procedure involves several steps. First, the observation process is described, and a mathematical forward model is constructed if fully known. Then, a criterion is established to obtain a solution, and finally, a computational method is employed to find the solution. Analytical models can further be categorized into deterministic and stochastic models.

Deterministic models treat the inverse problem as an optimization task, where the objective is to minimize a predefined criterion, often chosen as the l_2 norm of the error vector, $\|\mathbf{r} - \mathbf{T}\mathbf{q}\|_2^2$. Additionally, prior knowledge can also be incorporated into the optimization problem as a constraint, a technique known as regularization. For instance, if it's known that the the field to be reconstructed is highly sparse, then a sparsity-promoting regularizer can significantly simplify the problem solution by narrowing down the solution space. Regularization helps to explore the solution within a more constrained space. Stochastic approaches, on the other hand, consider the unknown field being estimated and measurements as random quantities, such that the conditional density of $\mathbf{q}$ given $\mathbf{r}$, denoted as $p(\mathbf{q}|\mathbf{r})$, is estimated. However, obtaining a full posterior characterization is often impractical, so the estimation of $\mathbf{q}$ is typically based on a partial characterization of the posterior probability.

Deep learning-based inversion approaches have gained significant popularity in recent years, primarily due to their ability to outperform traditional analytical inversion methods. This surge in popularity is also facilitated by the advancement of computationally powerful Graphical Processing Units (GPUs), which provide ample computational resources. A comprehensive overview of how deep learning can address inverse problems can be found in [11]. Furthermore, in Chapter and 5 and 6, we delve into how deep learning techniques can be leveraged specifically in the domain of radar range profile formation and MIMO radar imaging problems, respectively.

3.3 Least-squares Solution and Ties to SVD

The least-squares estimate solution to the problem (3.2), denoted as $\hat{\mathbf{q}}_{LS}$, minimizes $\|\mathbf{r}-\mathbf{T}\mathbf{q}\|_2^2$ in a least-squares sense. In this section, we embark on deriving the least-squares estimate, initially from an optimization standpoint. Subsequently, we derive the least-squares solution through a linear algebraic perspective utilizing Singular Value Decomposition (SVD). Additionally, we outline the conditions necessary for the existence of the least-squares solution.

3.3.1 Least-squares Solution from Optimization Perspective

Since we are searching for a solution that minimizes the cost function, $\|\mathbf{r}-\mathbf{T}\mathbf{q}\|_2^2$, we first evaluate the optimality conditions of this cost function with its first order derivative with respect to $\mathbf{q}$. Let us first expand the cost function as follows:

$$\begin{aligned}\|\mathbf{r}-\mathbf{T}\mathbf{q}\|_2^2 &= \left\| \begin{array}{ll} r_1-(t_{11}\times q_1+t_{12}\times q_2+ & \ldots \quad +t_{1N}\times q_N) \\ r_2-(t_{21}\times q_1+t_{22}\times q_2+ & \ldots \quad +t_{2N}\times q_N) \\ & \vdots \\ r_M-(t_{M1}\times q_1+t_{M2}\times q_2+ & \ldots \quad +t_{MN}\times q_N) \end{array} \right\|_2^2 \\ &= \sum_{i=1}^{M}\left(r_i-\sum_{j=1}^{N}t_{ij}q_j\right)^2 \end{aligned} \tag{3.3}$$

then we can obtain the first order partial derivative with respect to $\mathbf{q}$ as follows:

$$\frac{\partial\left(\|\mathbf{r}-\mathbf{T}\mathbf{q}\|_2^2\right)}{\partial q_k} = \sum_{i=1}^{M} -2\,t_{ij}\left(r_i-\sum_{j=1}^{N}t_{ij}q_j\right), \quad \forall k\in\{1,2,\ldots,N\} \tag{3.4}$$

Exchanging the inner and outer sums, the first-order optimality condition can be written as follows:

$$\frac{\partial\Big(\ \|\mathbf{r}-\mathbf{T}\mathbf{q}\|_2^2\ \Big)}{\partial q_k} = \sum_{i=1}^{M} -2\,t_{ij}\left(r_i - \sum_{j=1}^{N} t_{ij}q_j\right) = 0, \quad \forall k \in \{1,2,\ldots,N\} \tag{3.5}$$

By grouping the terms, we obtain:

$$\sum_{j=1}^{N}\left(\sum_{i=1}^{M} t_{ik}t_{ij}\right)q_j = \sum_{i=1}^{M} t_{ik}r_i, \quad \forall k \in \{1,2,\ldots,N\} \tag{3.6}$$

Eq. (3.6) denotes a linear system of equations, which are known as "normal equations". In matrix form, it is given by

$$\left(\mathbf{T}^H\mathbf{T}\right)\mathbf{q} = \mathbf{T}^H\mathbf{r} \tag{3.7}$$

where H denotes the Hermitian transpose since $\mathbf{T}$ is complex-valued. By multiplying both sides with the inverse of $\mathbf{T}^H\mathbf{T}$, we obtain the least-squares estimate of $\mathbf{q}$ as follows:

$$\hat{\mathbf{q}}_{LS} = \left(\mathbf{T}^H\mathbf{T}\right)^{-1}\mathbf{T}^H\mathbf{r} \tag{3.8}$$

3.3.2 Least-squares Solution from Linear Algebraic Perspective

Let $\{\mathbf{u}_k\}_{k=1}^m$ and $\{\mathbf{v}_k\}_{k=1}^n$ be the left and right singular vectors, respectively and λ_k be the singular values. By SVD, measurement matrix $\mathbf{T}$ can be expanded as:

$$\mathbf{T} = \sum_{k=1}^{r} \lambda_k \mathbf{u}_k \mathbf{v}_k^T \tag{3.9}$$

and measurement vector can be written as follows:

$$\mathbf{b} = \sum_{k=1}^{m} \mathbf{u}_k(\mathbf{u}_k^T\mathbf{r}) \tag{3.10}$$

since $\{\mathbf{u}_k\}_{k=1}^m$ forms a basis for the measurement space. Then, $\|\mathbf{r}-\mathbf{T}\mathbf{q}\|_2^2$ can be written as follows:

$$\begin{aligned}\|\mathbf{r}-\mathbf{T}\mathbf{q}\|_2^2 &= \left\|\sum_{k=1}^{m}\mathbf{u}_k(\mathbf{u}_k^T\mathbf{r})-\sum_{k=1}^{r}\lambda_k\mathbf{u}_k(\mathbf{v}_k^T\mathbf{q})\right\|^2 \\ &= \left\|\left(\sum_{k=1}^{r}\mathbf{u}_k(\mathbf{u}_k^T\mathbf{r})+\sum_{k=r+1}^{m}\mathbf{u}_k(\mathbf{u}_k^T\mathbf{r})\right)-\sum_{k=1}^{r}\lambda_k\mathbf{u}_k(\mathbf{v}_k^T\mathbf{q})\right\|^2 \\ &= \left\|\left(\sum_{k=1}^{r}\mathbf{u}_k(\mathbf{u}_k^T\mathbf{r})-\sum_{k=1}^{r}\lambda_k\mathbf{u}_k(\mathbf{v}_k^T\mathbf{q})\right)+\sum_{k=r+1}^{m}\mathbf{u}_k(\mathbf{u}_k^T\mathbf{r})\right\|^2\end{aligned} \tag{3.11}$$

By writing the first term in the $\mathbf{u}_k$ to parenthesis, we obtain

$$\begin{aligned}\|\mathbf{r}-\mathbf{T}\mathbf{q}\|_2^2 &= \left\|\sum_{k=1}^{r}\mathbf{u}_k\left(\mathbf{u}_k^T\mathbf{r}-\lambda_k\mathbf{v}_k^T\mathbf{q}\right)+\sum_{k=r+1}^{m}\mathbf{u}_k(\mathbf{u}_k^T\mathbf{r})\right\|^2 \\ &= \sum_{k=1}^{r}\left|\mathbf{u}_k^T\mathbf{r}-\lambda_k\mathbf{v}_k^T\mathbf{q}\right|^2+\sum_{k=r+1}^{m}\left|\mathbf{u}_k^T\mathbf{r}\right|^2\end{aligned} \tag{3.12}$$

where we have used the Pythagorean Theorem in the last step of expression (3.12) as linear combinations of $\{\mathbf{u}_k\}$ is also perpendicular. Note that the second term in the final expression in (3.12) is independent of the choice of $\mathbf{q}$ and the first term can take the minimum value of 0 if and only if

$$\mathbf{v}_k^T\hat{\mathbf{q}} = \frac{\mathbf{u}_k^T\mathbf{r}}{\lambda_k} \quad \text{for} \quad k\in\{1,2,\ldots,r\} \tag{3.13}$$

which leads to the following least-squares solution:

$$\hat{\mathbf{q}}_{LS} = \left(\sum_{k=1}^{n}\frac{1}{\lambda_k}\mathbf{v}_k\mathbf{u}_k^T\right)\mathbf{r} \tag{3.14}$$

Note the equivalence between the least-squares solution given by equations (3.8) and (3.14). The nature of the measurement matrix, $\mathbf{T}$, can lead to three distinct cases for solving problem (3.2):

1. There may be infinitely many solutions, i.e. $rank(T) = M < N$
2. There is a unique solution for every vector $\mathbf{r}$, i.e. $rank(T) = M = N$

3. There may not be a solution due to the noise, i.e. $rank(T) = N < M$

Case 1 occurs when the number of measurements exceeds the size of the vector $\mathbf{q}$. Due to the presence of measurement noise, a solution does not exist, and the least-squares solution needs to be used to minimize the l_2 distance between $\mathbf{r}$ and $\mathbf{Tq}$.

Case 2 represents an idealistic scenario where the measurement matrix is square and invertible. However, such an ideal case rarely exists in practical measurement systems due to inherent noise.

In Case 3, the number of measurements is less than the size of the vector $\mathbf{q}$. Here, the null space of the measurement matrix, $\mathbf{T}$, is not empty, resulting in non-uniqueness of least-squares solutions satisfying the system of equations. Consequently, the least-squares solution with the minimum l_2-norm is chosen among the alternatives. Nevertheless, this method is highly susceptible to perturbations and noise in the measured data.

To overcome these challenges, robust regularization techniques are required. Regularization involves incorporating prior knowledge about $\mathbf{q}$ into the inversion process. Its fundamental goal is to enhance stability and resilience against measurement noise and lack of data by refining the solution based on existing knowledge. Especially when the measurement matrix is ill-conditioned, noise components in the measurement data will be amplified, leading to an unacceptable solution that is far from the true solution.

3.4 Probabilistic Approach

In this section of the dissertation, we delve into the inverse problem of estimating a vector field from noisy radar measurements, exploring it from a probabilistic perspective. Based on Bayes' formula, we then proceed to derive the "Maximum A Posteriori" estimator for the problem described in Eq. (3.2).

In the Bayesian framework, $p_{\mathbf{q}}(\mathbf{q})$ is referred to as the prior density of $\mathbf{q}$ and captures all the knowledge about $\mathbf{q}$. The conditional density $p_{\mathbf{r}|\mathbf{q}}(\mathbf{r}|\mathbf{q})$ on the other hand fully characterizes how $\mathbf{r}$ stores information about $\mathbf{q}$, generally specified by the measurement model, in our case linear operator $\mathbf{T}$.

Let us use $\hat{\mathbf{q}}(\mathbf{r})$ to denote our estimate of $\mathbf{q}$ based on the observation vector $\mathbf{r}$. In the Bayesian approach, we choose the "best" estimator based on a performance metric. For this purpose, we define a cost function $C(\mathbf{x}, \hat{\mathbf{x}})$, which returns the cost of estimating an arbitrary vector $\mathbf{x}$ as $\hat{\mathbf{x}}$. Then the "optimal" estimator is the one that minimizes the mean cost, that is,

$$\hat{\mathbf{q}}(\mathbf{r}) = \underset{\mathbf{q}(.)}{\operatorname{argmin}} E\left[C\left(\mathbf{q}, \hat{\mathbf{q}}(\mathbf{r})\right)\right] \tag{3.15}$$

The expected cost is given by

$$\begin{aligned} E\left[C\left(\mathbf{q}, \hat{\mathbf{q}}(\mathbf{r})\right)\right] &= \int_{-\infty}^{+\infty}\int_{-\infty}^{+\infty} C\left(\mathbf{q}, \hat{\mathbf{q}}(\mathbf{r})\right) p_{\mathbf{q},\mathbf{r}}(\mathbf{q}, \mathbf{r})\, d\mathbf{q}\, d\mathbf{r} \\ &= \int_{-\infty}^{+\infty}\left[\int_{-\infty}^{+\infty} C\left(\mathbf{q}, \hat{\mathbf{q}}(\mathbf{r})\right) p_{\mathbf{q}|\mathbf{r}}(\mathbf{q}|\mathbf{r})\, d\mathbf{q}\right] \underbrace{p_{\mathbf{r}}(\mathbf{r})}_{\geq 0}\, d\mathbf{r} \\ &= \int_{-\infty}^{+\infty} C\left(\mathbf{q}, \hat{\mathbf{q}}(\mathbf{r})\right) p_{\mathbf{q}|\mathbf{r}}(\mathbf{q}|\mathbf{r})\, d\mathbf{q} \end{aligned} \tag{3.16}$$

Let us define the following cost function

$$C(\mathbf{q}, \hat{\mathbf{q}}) = \begin{cases} 1, & \text{if } |\mathbf{q} - \hat{\mathbf{q}}| > \epsilon \\ 0, & \text{otherwise} \end{cases} \tag{3.17}$$

Note that this cost function uniformly penalizes all the estimates irrespective of the magnitude of the estimation error. Plugging this cost function into (3.16) we

obtain the Minimum Uniform Cost (MUC) estimator

$$\begin{aligned}\hat{\mathbf{q}}_{MUC}(\mathbf{r}) = &\quad \underset{\mathbf{q}}{\operatorname{argmin}} \left[1 - \int_{\mathbf{q}-\epsilon}^{\mathbf{q}+\epsilon} p_{\mathbf{q}|\mathbf{r}}\left(\mathbf{q}|\mathbf{r}\right)\ d\mathbf{q}\right] \\ = &\quad \underset{\mathbf{q}}{\operatorname{argmax}} \int_{\mathbf{q}-\epsilon}^{\mathbf{q}+\epsilon} p_{\mathbf{q}|\mathbf{r}}\left(\mathbf{q}|\mathbf{r}\right)\ d\mathbf{q}\end{aligned} \tag{3.18}$$

In the limit as ϵ approaches 0, the minimum uniform cost estimator becomes the "*Maximum A Posteriori*", commonly abbreviated as the MAP estimator. That is,

$$\hat{\mathbf{q}}_{MAP}(\mathbf{r}) = \underset{\mathbf{q}}{\operatorname{argmax}}\, p_{\mathbf{q}|\mathbf{r}}\left(\mathbf{q}|\mathbf{r}\right) = \lim_{\epsilon \to 0} \hat{\mathbf{q}}_{MUC}(\mathbf{r}) \tag{3.19}$$

Assuming that posterior probability is differentiable with respect to $\mathbf{q}$, one can compute the stationary points of the posteir density function. At these stationary points, Jakobian is zero:

$$\frac{\partial p_{\mathbf{q}|\mathbf{r}}\left(\mathbf{q}|\mathbf{r}\right)}{\partial \mathbf{q}} = \mathbf{0} \tag{3.20}$$

For these stationary points to be local maximum points, the Hessian matrix has to have negative definiteness at these points:

$$\frac{\partial^2 p_{\mathbf{q}|\mathbf{r}}\left(\mathbf{q}|\mathbf{r}\right)}{\partial \mathbf{q}^2} < \mathbf{0} \tag{3.21}$$

In situations with multiple local maxima, the posterior needs evaluation at each of these peaks. If the range of $\mathbf{q}$ is finite, i.e., $\mathbf{q}$ is only defined over a certain region, then the posterior density must also be evaluated at the boundaries as well. Typically, determining the maximum of the posterior density involves calculations based on likelihood and priors.

$$p_{\mathbf{r}|\mathbf{q}}\left(\mathbf{r}|\mathbf{q}\right) = \frac{p_{\mathbf{r}|\mathbf{q}}\left(\mathbf{r}|\mathbf{q}\right) p_{\mathbf{q}}\left(\mathbf{q}\right)}{p_{\mathbf{r}}\left(\mathbf{r}\right)} \tag{3.22}$$

The value of $\mathbf{q}$ which maximizes the posterior will also maximize the product of likelihood and prior, since $p_{\mathbf{r}}\left(\mathbf{r}\right) > 0$. Additionally, since common density functions

involve exponential terms, it is preferable to take a logarithm. It is important to note that this does not affect the maximization process, as the logarithm is a monotonically increasing function. Therefore, the MAP estimator is given by:

$$\begin{aligned}\hat{\mathbf{q}}_{\mathrm{MAP}} &= \underset{\mathbf{q}}{\operatorname{argmax}} \left\{ \log\left(p_{\mathbf{q}|\mathbf{r}}\left(\mathbf{q}|\mathbf{r}\right)\right) \right\} \\ &= \underset{\mathbf{q}}{\operatorname{argmax}} \left\{ \log\left(p_{\mathbf{r}|\mathbf{q}}\left(\mathbf{r}|\mathbf{q}\right)\right) + \log\left(p_{\mathbf{q}}\left(\mathbf{q}\right)\right) \right\}\end{aligned} \tag{3.23}$$

Solution of (3.23) is calculated by differentiation with respect to $\mathbf{q}$:

$$\frac{\partial}{\partial \mathbf{q}} \log\left(p_{\mathbf{r}|\mathbf{q}}\left(\mathbf{r}|\mathbf{q}\right)\right) + \frac{\partial}{\partial \mathbf{q}} \log\left(p_{\mathbf{q}}\left(\mathbf{q}\right)\right) = \mathbf{0} \tag{3.24}$$

Solutions satisfying (3.24) and producing negative definite Hessian matrix are the local maxima points. Assuming that measurement noise samples, $\mathbf{w}$ are independent identically distributed complex Gaussian noise with the variance of σ^2, hence, p.d.f of $\mathbf{w}$ is given by

$$p_{\mathbf{w}}\left(\mathbf{w}\right) \propto \exp\left(-\frac{1}{2\sigma^2}\left\|\mathbf{w}\right\|_2^2\right) \tag{3.25}$$

In this case, the likelihood function will be of the following form:

$$p_{\mathbf{r}|\mathbf{q}}\left(\mathbf{r}|\mathbf{q}\right) \propto \exp\left(-\frac{1}{2\sigma^2}\left\|\mathbf{r}-\mathbf{T}\mathbf{q}\right\|_2^2\right) \tag{3.26}$$

Let us define the following p.d.f for $\mathbf{q}$:

$$p_{\mathbf{q}}\left(\mathbf{q}\right) \propto \exp\left(-\mu\Phi\left(\mathbf{q}\right)\right) \tag{3.27}$$

Substituting (3.27) and (3.26) into (3.23), the maximization problem becomes a minimization problem after a sign-change:

$$\begin{aligned}\hat{\mathbf{q}}_{\mathrm{MAP}} &= \underset{\mathbf{q}}{\operatorname{argmin}} \left\{ \frac{1}{2\sigma^2}\left\|\mathbf{r}-\mathbf{T}\mathbf{q}\right\|_2^2 + \mu\Phi\left(\mathbf{q}\right) + const \right\} \\ &= \underset{\mathbf{q}}{\operatorname{argmin}} \left\{ \frac{1}{2\sigma^2}\left\|\mathbf{r}-\mathbf{T}\mathbf{q}\right\|_2^2 + \mu\Phi\left(\mathbf{q}\right) \right\}\end{aligned} \tag{3.28}$$

Note that the constant term in (3.28) comes from the normalizers in $p_{\mathbf{r}|\mathbf{q}}\left(\mathbf{r}|\mathbf{q}\right)$ and $p_{\mathbf{q}}\left(\mathbf{q}\right)$.

3.5 Regularized Inversion

A typical formulation of the regularized inversion is as follows:

$$\hat{\mathbf{q}} = \underset{\mathbf{q}}{\operatorname{argmin}} \left\{ \mathcal{D}(\mathbf{q}) + \lambda \mathcal{R}(\mathbf{q}) \right\} \tag{3.29}$$

with $\mathcal{D}(\mathbf{q})$ denoting data fidelity and $\mathcal{R}(\mathbf{q})$ denoting regularization over $\mathbf{q}$. Data fidelity is usually chosen as least-squares in many applications:

$$\mathcal{D}(\mathbf{q}) \overset{\text{def}}{=} \|\mathbf{r} - \mathbf{T}\mathbf{q}\|_2^2 \tag{3.30}$$

Data fidelity determines the extent to which the measurements, $\mathbf{r}$, should align with the $\mathbf{T}\mathbf{q}$. Conversely, the regularization term dictates how much predefined or desired characteristics of $\mathbf{q}$ should be emphasized during the inversion process. This balance is governed by the choice of the regularization parameter, $\lambda \in \mathrm{R}^+$. It is worth noting that the formulation of the maximum a posteriori problem, as given in Eq. 3.23, is achieved when the likelihood and prior functions are set as: $\mathcal{D}(\mathbf{q}) = -\log\left(p_{\mathbf{q}|\mathbf{r}}\left(\mathbf{q}|\mathbf{r}\right)\right)$ and $\lambda\mathcal{R}(\mathbf{q}) = -\log\left(p_{\mathbf{q}}\left(\mathbf{q}\right)\right)$.

3.5.1 Alternating Direction Method of Multipliers (ADMM)

ADMM has gained significant traction in solving regularized reconstruction problems, such as the one described in Eq. (3.29), particularly within the field of computational imaging. ADMM offers a method to separate the data from the regularizer, allowing for independent computation of each component. To cast the problem into the ADMM framework, we begin by splitting the variable $\mathbf{q}$:

$$\begin{aligned} \left(\hat{\mathbf{q}}, \hat{\mathbf{h}}\right) = \quad & \underset{\mathbf{q},\mathbf{h}\in\mathbb{C}^{N\times 1}}{\operatorname{argmin}} \left\{ \mathcal{D}(\mathbf{q}) + \lambda \mathcal{R}(\mathbf{h}) \right\} \\ \text{s.t.} \quad & \mathbf{q} - \mathbf{h} = 0 \end{aligned} \tag{3.31}$$

The augmented Lagrangian for (3.31) is given by

$$\mathcal{L}_\rho(\mathbf{q},\mathbf{h},\mathbf{y}) = \mathcal{D}(\mathbf{q}) + \lambda\mathcal{R}(\mathbf{h}) + \mathbf{y}^T(\mathbf{q}-\mathbf{h}) + \frac{\rho}{2}\left\|\mathbf{q}-\mathbf{h}\right\|_2^2 \tag{3.32}$$

where $\mathbf{y}$ is Lagrange multiplier and $\rho > 0$ is the penalty parameter. The following problem is equivalent to problem (3.31):

$$\begin{aligned}\left(\hat{\mathbf{q}},\hat{\mathbf{h}}\right) = \quad & \underset{\mathbf{q},\mathbf{h}\in\mathbb{C}^{N\times 1}}{\operatorname{argmin}} \left\{\mathcal{D}(\mathbf{q}) + \lambda\mathcal{R}(\mathbf{h}) + \frac{\rho}{2}\left\|\mathbf{q}-\mathbf{h}\right\|_2^2\right\} \\ \text{s.t.} \quad & \mathbf{q}-\mathbf{h} = 0\end{aligned} \tag{3.33}$$

In this case, ADMM iterations are defined as follows:

$$\mathbf{q}_{k+1} := \underset{\mathbf{q}\in\mathbb{C}^{N\times 1}}{\operatorname{argmin}}\, \mathcal{L}_\rho(\mathbf{q},\mathbf{h}_k,\mathbf{y}_k) \tag{3.34a}$$

$$\mathbf{h}_{k+1} := \underset{\mathbf{h}\in\mathbb{C}^{N\times 1}}{\operatorname{argmin}}\, \mathcal{L}_\rho(\mathbf{q}_{k+1},\mathbf{h},\mathbf{y}_k) \tag{3.34b}$$

$$\mathbf{y}_{k+1} := \mathbf{y}_k + \rho(\mathbf{h}_{k+1}-\mathbf{q}_{k+1}) \tag{3.34c}$$

with k denoting the ADMM iterations. As a more common version, ADMM can be written in a scaled form. Let us define the residual vector $\mathbf{r} = \mathbf{q}-\mathbf{h}$. Then last two terms in augmented Lagrangian in (3.32) is

$$\begin{aligned}\mathbf{y}^T\mathbf{r} + \frac{\rho}{2}\left\|\mathbf{r}\right\|_2^2 = \quad & \mathbf{y}^T\mathbf{r} + \frac{\rho}{2}\left\|\mathbf{r}\right\|_2^2 + \frac{1}{2\rho}\left\|\mathbf{y}\right\|_2^2 - \frac{1}{2\rho}\left\|\mathbf{y}\right\|_2^2 = \left\|\sqrt{\frac{\rho}{2}}\mathbf{r} + \frac{1}{\sqrt{2\rho}}\mathbf{y}\right\|_2^2 - \frac{1}{2\rho}\left\|\mathbf{y}\right\|_2^2 \\ = \quad & \left\|\sqrt{\frac{\rho}{2}}\left(\mathbf{r}+\frac{1}{\rho}\mathbf{y}\right)\right\|_2^2 - \frac{1}{2\rho}\left\|\mathbf{y}\right\|_2^2 = \frac{\rho}{2}\left\|\left(\mathbf{r}+\frac{1}{\rho}\mathbf{y}\right)\right\|_2^2 - \frac{1}{2\rho}\left\|\mathbf{y}\right\|_2^2 \\ = \quad & \frac{\rho}{2}\left\|(\mathbf{r}+\mathbf{u})\right\|_2^2 - \frac{\rho}{2}\left\|\mathbf{u}\right\|_2^2\end{aligned} \tag{3.35}$$

where we have added and subtracted $\frac{1}{2\rho}\left\|\mathbf{y}\right\|_2^2$ and defined $\mathbf{u} = \frac{1}{\rho}\mathbf{y}$ to be scaled dual variable. Our constrained minimization problem then becomes

$$\left(\hat{\mathbf{q}},\hat{\mathbf{h}},\hat{\mathbf{u}}\right) = \underset{\mathbf{q},\mathbf{h},\mathbf{u}\in\mathbb{C}^{N\times 1}}{\operatorname{argmin}} \left\{\mathcal{L}_\rho(\mathbf{q},\mathbf{h},\mathbf{u})\right\} \tag{3.36}$$

where $\mathcal{L}_\rho$ in the scaled-form augmented Lagrangian form is given by

$$\mathcal{L}_\rho(\mathbf{q}, \mathbf{h}, \mathbf{u}) = \mathcal{D}(\mathbf{q}) + \lambda\mathcal{R}(\mathbf{h}) + \frac{\rho}{2}\left\|(\mathbf{q} - \mathbf{h} + \mathbf{u})\right\|_2^2 - \frac{\rho}{2}\left\|\mathbf{u}\right\|_2^2 \tag{3.37}$$

Then, ADMM steps involve the following sub-minimization problems:

$$\mathbf{q}_{k+1} := \underset{\mathbf{q}\in\mathbb{C}^{N\times 1}}{\operatorname{argmin}}\, \mathcal{L}_\rho(\mathbf{q}, \mathbf{h}_k, \mathbf{u}_k) \tag{3.38a}$$

$$\mathbf{h}_{k+1} := \underset{\mathbf{h}\in\mathbb{C}^{N\times 1}}{\operatorname{argmin}}\, \mathcal{L}_\rho(\mathbf{q}_{k+1}, \mathbf{h}, \mathbf{u}_k) \tag{3.38b}$$

$$\mathbf{u}_{k+1} := \mathbf{u}_k + (\mathbf{h}_{k+1} - \mathbf{q}_{k+1}) \tag{3.38c}$$

Here k denotes the iteration index. Thus, the whole optimization procedure to find the minimum of $\mathcal{L}_\rho$ involves iterative steps which alternate between minimization over $\mathbf{q}$ and $\mathbf{h}$, respectively, while updating scaled dual variable. By introducing two extra variables $\tilde{\mathbf{q}} = \mathbf{h} - \mathbf{u}$ and $\tilde{\mathbf{h}} = \mathbf{q} + \mathbf{u}$, ADMM sub-problems can be rewritten as in [12] as follows:

ADMM suboptimization problems

ADMM framework decouples model and prior optimization steps:

Model Optimization

$$\hat{\mathbf{q}}_{k+1} := \underset{\mathbf{q}\in\mathbb{C}^{N\times 1}}{\operatorname{argmin}} \left\{ \mathcal{D}(\mathbf{q}) + \frac{\rho}{2}\left\|\mathbf{q} - \tilde{\mathbf{q}}_k\right\|_2^2 \right\} \tag{3.39}$$

Prior optimization

$$\hat{\mathbf{h}}_{k+1} := \underset{\mathbf{h}\in\mathbb{C}^{N\times 1}}{\operatorname{argmin}} \left\{ \lambda\mathcal{R}(\mathbf{h}) + \frac{\rho}{2}\left\|\tilde{\mathbf{h}}_k - \mathbf{h}\right\|_2^2 \right\} \tag{3.40}$$

Auxiliary variable update

$$\mathbf{u}_{k+1} := \mathbf{u}_k + (\mathbf{h}_{k+1} - \mathbf{q}_{k+1}) \tag{3.41}$$

Here, sub-problem (3.39) corresponds to the data alignment step, which solely relies on the measurements and the forward model. On the other hand, sub-problem

(3.40) is the priors optimization step, dependent only on the prior distribution of the data. Sub-problem (3.39) signifies the inversion of the measurements using the forward model, while sub-problem (3.40) represents a denoising operator applied to $\tilde{\mathbf{h}}_k$. Notably, the data alignment subproblem is decoupled from the prior optimizations in this framework. The flexible modularity of ADMM allows the plug-and-play of different denoisers in an isolated manner, ensuring that the data alignment subproblem remains unaffected.

To provide a clearer illustration of how the solution to subproblem (3.40) acts as a denoiser, let us choose $\mathcal{R}(\mathbf{h}_k)$ to be $\mathcal{R}(\mathbf{h}_k) = -\log\left(p\left(\tilde{\mathbf{h}}_k\right)\right)$. Then, (3.40) serves as the Maximum A Posteriori (MAP) estimator designed to remove additive Gaussian noise with a power of $\sigma^2 = \lambda/\rho$ from the noisy version of $\mathbf{h}$ and acts as a Gaussian denoiser on $\tilde{\mathbf{h}}$, minimizing the residue between the clean and noisy signal using priors $\tilde{\mathbf{h}}_k$. This becomes more evident when σ is substituted into (3.40):

$$\hat{\mathbf{h}}_{k+1} := \quad \underset{\mathbf{h}\in\mathbb{C}^{Nx1}}{\operatorname{argmin}} \left\{ \mathcal{R}(\mathbf{h}) + \frac{1}{2\sigma^2} \left\| \tilde{\mathbf{h}}_k - \mathbf{h} \right\|_2^2 \right\} \tag{3.42}$$

It is also important to note that σ is the only parameter controlling regularization on $\mathbf{h}$, and ρ does not contribute to the final reconstruction. However, ρ plays a role in controlling the weight of the constraint in the augmented Lagrangian form, influencing the convergence of the optimization.

Establishing this chapter as the foundational formulation of the ADMM framework for the subsequent sections, we delve into the practical applications of the ADMM framework in real radar scenarios in Chapter 5, addressing the radar range profile reconstruction problem, and in Chapter 6, focusing on the radar image formation problem. We elaborate on the adjustments made to the ADMM steps outlined above, contingent upon whether $\mathbf{q}$ is real-valued or not in these chapters.

Chapter 4

ARTIFICIAL NEURAL NETWORK BASED RADAR TARGET ANGLE ESTIMATION

In this chapter, an artificial neural network (ANN) based approach is proposed for the estimation of the target angle using Multiple Input Multiple Output (MIMO) radars operating in Frequency Modulated Continuous Wave (FMCW) mode. The proposed technique operates in two stages, the first stage being the formation of the range profile at each MIMO element via Discrete Fourier Transform (DFT) and the second stage being the estimation of the target azimuth angle via an artificial neural network. The range profile formed in the first stage is fed to the second stage as a single snapshot angle measurement. The performance of the proposed technique is apprised with other existing methods under different Signal-to-Noise Ratio (SNR) conditions and measurement model uncertainties. The simulations performed show that the learning capability of the model strongly hinges on SNR conditions and the learning process is ameliorated as SNR in training data increases as anticipated. Under low SNR conditions, the proposed technique performs better than other techniques in terms of Mean Square Error (MSE). We have also shown that our solution remains unaffected by the model uncertainties as it fully relies on the calibration data, while the performance of the model-based angle

estimation techniques dramatically degrades as the uncertainty in the underlying model grows.

4.1 Introduction

Radars have been used in a broad spectrum of sensing applications. These applications may vary from drone detection [13] or runway surveillance to detect the presence of any foreign object debris on a runway [3] to precise surface imaging in industrial areas [14]. Amongst the other radar types, specifically, MIMO radars have recently gained significant momentum due to the angular resolution improvement over the conventional phased array radars. Additionally, MIMO radars provide waveform diversity enabling significant superiority over its phased-array counterpart in terms of improved parameter identifiability [15].

With an array of antennas, it is possible to find the direction of incident signals without the necessity of highly directional antennas being mechanically steered. The direction of arrival (DoA) of signals is achieved by digital beamforming algorithms in antenna arrays. This problem has been extensively studied in the literature of array signal processing. Consequently, several DoA algorithms applicable to the MIMO radar context already exist. The classical approaches are conventional beamformer(Barlett) as described in [16], Estimation of Signal Parameters via Rotational Invariance Technique (ESPRIT) in [17] and Multiple Signal Classification (MUSIC) in [18]. A detailed study on the comparison of these algorithms can be found in [19]. Another class of techniques developed for the solution of DoA problems consists of sparsity-based approaches, which have also been studied in the MIMO radar context as in [20, 21]. The compressive-sensing based approaches provide quite good results, particularly for the cases in which the azimuth spectrum of the arrival signals is known to be sparse as *a priori*. On the other hand, the recent advances in the machine learning frameworks have motivated researchers to seek machine learning-based solutions for the various radar

estimation problems as an alternative to the model-based methods. Moreover, machine learning-based solutions are partially or fully data-driven meaning that they don't count on any prior assumption on the underlying measurement model and consequently are expected to be less affected by the possible array imperfections as compared to their model- based counterparts [22]. Therefore, learning-based parameter estimation in the MIMO radar context has drawn significant attention. For instance, recently a deep-learning framework has been used in [23] where supervised deep neural networks are used to map the received signals to their DoAs in the MIMO communication system context. Similarly, in [24], a fully connected deep learning model is adept to find the number of signal sources in the sensing environment and their respective directions. [25] uses an ensemble of convolution neural networks to estimate the 2D DoA using a circular array antenna. In [26], the authors propose a deep learning-based super-resolution DoA estimator using single snapshot MIMO radar data.

In principle, one can design perfect arrays to perform all kind of array processing algorithms, however, when it comes to practice, the performance of array processing algorithms significantly suffer from practical issues. For example, external environmental factors may cause the antenna positions to deviate from their intended positions, giving rise to the array model uncertainties. The uncertainty in the underlying model leads to performance deterioration of the array signal processing algorithms. That being the case, inaccuracies in the model ought to be removed before a MIMO radar is deployed to benefit from its angular resolution advantages to the utmost.

In this study, we adopt a data-driven approach to the problem of angle estimation of the targets using MIMO radars. Our motivation for such an approach is to prevent angular estimation performance from being impacted by any inaccuracies in the array shapes. Therefore, in our approach, instead of relying on a measurement model which is highly dependent on the array geometry and calibration of the RF components, motivated by the works in [24], [25] and [26] we aim to learn the measurement model directly from the training/calibration data through an artificial neural network. The main contributions of this study can be listed as

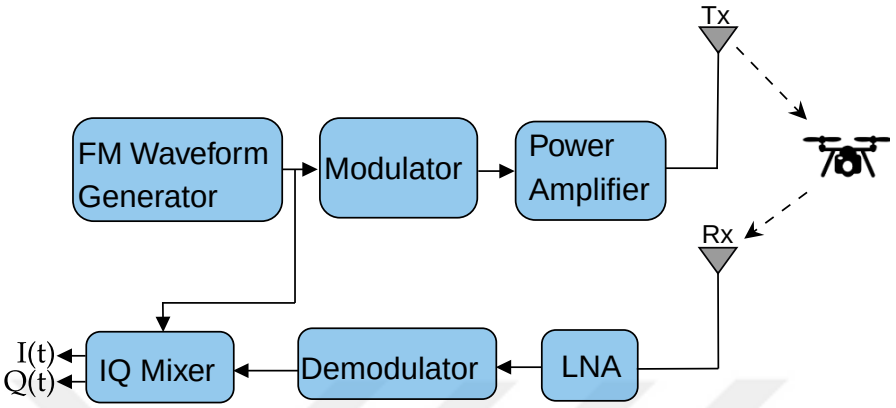
follows: 1) Explicit range expressions for the FMCW operation are derived, 2) an artificial neural network-based learning technique for the estimation of target angle using a single snapshot angle measurement is proposed and implemented 3) the performance of the proposed approach under different SNR conditions and model uncertainty is compared with the existing methods through the extensive end-to-end FMCW MIMO radar simulations performed in the physical layer.

The rest of the chapter is structured as follows: In Section 4.2, we present our system and signal model, including explicit range expressions for the FMCW operation. Section 4.3 delves into our proposed technique, covering aspects such as the generation of training data from radar simulations, details of the neural network utilized, and the training procedure. Our numerical results are presented in Section 4.4, followed by conclusions in Section 4.5.

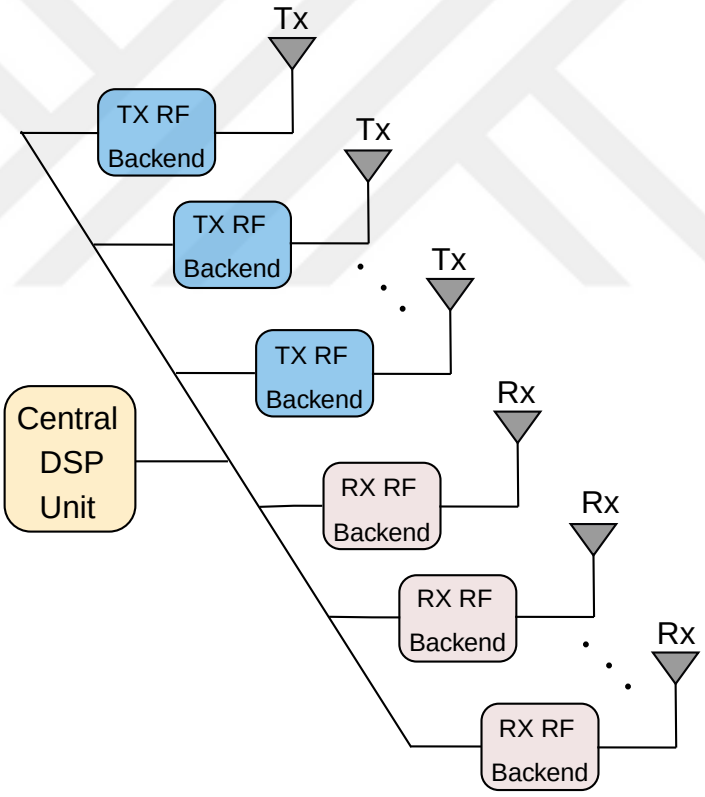
4.2 System Model and Signal Processing

We consider an FMCW MIMO radar system with a uniform linear array (ULA) antenna both at the transmitter and the receiver ends. In Figure 4.1, a simplified system model is demonstrated, where Figure 4.1a shows a single transmitter and receiver pair and their respective simplified RF backend circuitry and Figure 4.1b provides an integral system overview for the studied MIMO radar model.

In most MIMO radars, transmission occurs in a time-division (TD) manner, where transmitting antennas take turns for transmission while receiver antennas simultaneously collect the echo signals. During this operation, a total of the number of Tx antennas multiplied by the number of Rx antenna pairs are formed. Each pair can be individually regarded as a single transceiver, as depicted in Figure 4.1a. In a typical FMCW radar operation with a single Tx and Rx antenna, first a chirp signal is generated, up-converted to the RF band, then amplified and transmitted through transmitter antenna. On the receive side, reflected signals picked up by the receiver antenna is first passed through a low-noise amplifier (LNA) which only passes the frequency band of operation, down-converted to the baseband and



(A) RF backend for a single Tx-Rx pair



(B) MIMO antennas connected to the RF backends

FIGURE 4.1: Simplified model of a MIMO radar system

finally mixed with the transmitted signal to create in-phase $I(t)$ and quadrature $Q(t)$ components of the received signal, as shown in Figure 4.1a.

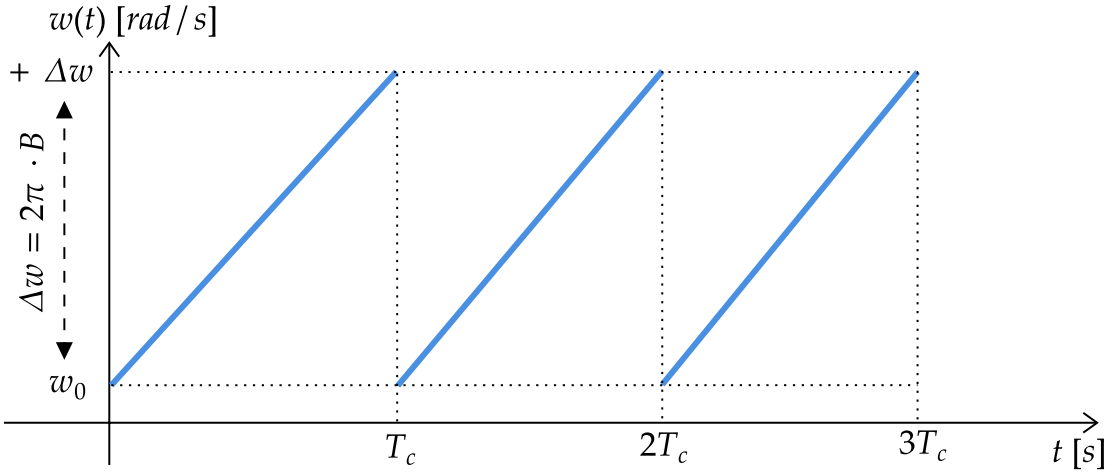
In our study, we narrow our focus to target detection using a linear FMCW MIMO radar system within a clutter-free environment. This detection task involves two primary objectives: firstly, detecting the presence of an object in the radar environment that reflects the transmitted radar signal, and secondly, determining the range and azimuth information of this object. The range information is extracted based on the principle of FMCW operation, while the azimuth angle of the target is derived from the spatial sampling of the echo signals at different positions across the array, which is the main focus of this chapter. In Section 4.2.1, we delve into how the range information is obtained through the processing of the echo signals collected with a single transmit and receive pair. Subsequently, in Section 4.2.2, our focus shifts to array signal processing, where we detail the derivation of mathematical expressions for the angle profile in the MIMO radar system.

4.2.1 Range Processing

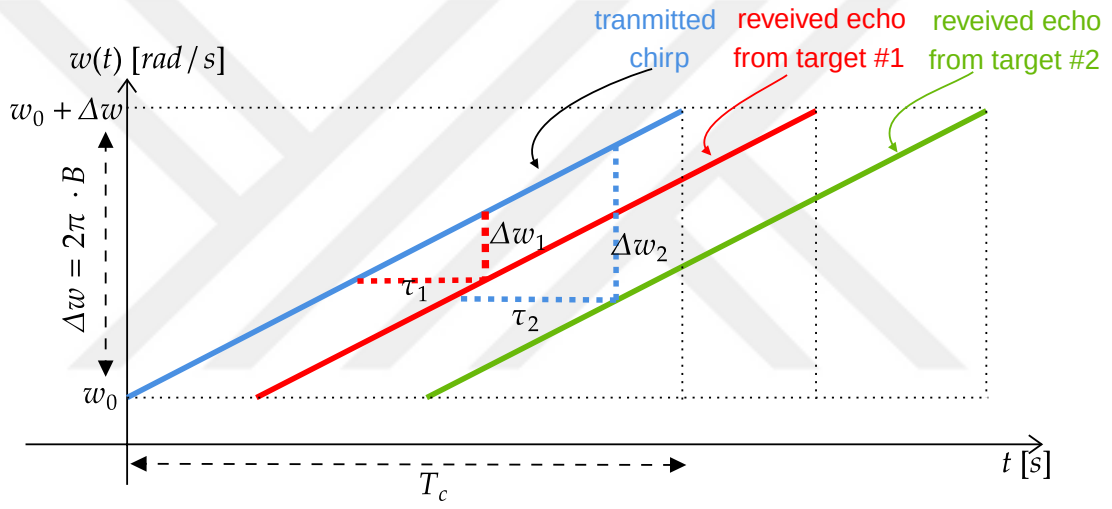
An FMCW radar transmits a sequence of chirps with the following mathematical expression:

$$s(t) = \sum_{n=0}^{N} s_p(t - nT_c), \quad \text{with} \quad s_p(t) = \Big(U(t) - U(t - T_c) \Big) \cos(\Phi(t)), \qquad t \in [0, T_c]$$

where $U(t)$ denotes the unit step function, T_c is the chirp period and N is the number of chirp pulses to be transmitted. The instantaneous angular frequency is given by $\omega(t) = \frac{d\Phi(t)}{dt}$. If $\omega(t)$ is selected to linearly increase in time with a slope of m, i.e., $\omega(t) = \omega_0 + mt$, then by integrating $\omega(t)$ with respect to t, we obtain $\Phi(t) = \omega_0 t + \frac{1}{2} m t^2$, where ω_0 is the initial angular frequency and m is the slope of the chirp, also known as the chirp rate, defined as $m = \frac{\Delta\omega}{T_c}$, with $\Delta\omega$ denoting the total angular frequency swept. This can also be expressed as the total bandwidth of the chirp signal in Hertz, $B = \frac{\Delta\omega}{2\pi}$. The instantaneous frequency of the chirp



(A) Transmission cycle with linear up-chirps



(B) Echo signals due to two targets at different ranges

FIGURE 4.2: Transmitted and received chirp signals

increases for T_c seconds, then returns to its initial value, ω_0, after sweeping a band of $\Delta\omega$. This continuous cycle is shown in Figure 4.2a.

Let us consider K arbitrary targets, each of which has a radar cross section (RCS) of σ_i and radial distance to the radar of R_i, $i \in \{1, 2, \ldots, K\}$. The echo signal reflecting from the ith reflector comes back to the radar after a two-way propagation delay of $\tau_i = \frac{2R_i}{c}$, where c denotes the speed of light. In Figure 4.2b, time-delayed versions of a single transmitted chirp signal due to two targets at different distances are shown. Due to this time delay, there is a difference in frequency between

the transmitted and received signals, which is proportional to the amount of the delay. Since the slope of the chirps is a known quantity, one can determine the time delay from the frequency shift and hence the distance of the reflector object. The received signal at the radar is therefore nothing but the superposition of the amplitude-scaled and time-delayed versions of the transmitted signal, given by

$$r(t) = \sum_{i=1}^{K} G_i \sigma_i \cos\left(\omega_0(t-\tau_i) + \frac{1}{2}m(t-\tau_i)^2 + \theta_i\right) \tag{4.1}$$

Here G_i entirely captures propagation related two-way channel effects between the radar and the ith reflector object. The received signal given in expression (4.1) is next mixed with $\cos(\omega_0 t + \frac{1}{2}mt^2)$ and $\sin(\omega_0 t + \frac{1}{2}mt^2)$ to form in-phase and quadrature components, respectively. Using the following trigonometric identities:

$$\cos(\alpha)\cos(\beta) = \frac{1}{2}\Big(\cos(\alpha+\beta) + \cos(\alpha-\beta)\Big)$$
$$\cos(\alpha)\sin(\beta) = \frac{1}{2}\Big(\sin(\alpha+\beta) - \sin(\alpha-\beta)\Big)$$

and filtering out high frequency terms, the received signal is obtained as follows:

$$I(t) = \frac{1}{2}\sum_{i=1}^{K} G_i \sigma_i \cos\left(m\tau_i t + \omega_0\tau_i - \frac{1}{2}m\tau_i^2\right)$$
$$Q(t) = \frac{1}{2}\sum_{i=1}^{K} G_i \sigma_i \sin\left(m\tau_i t + \omega_0\tau_i \frac{1}{2}m\tau_i^2\right)$$

Here $I(t)$ and $Q(t)$ represent the demodulated in-phase and quadrature components of the received radar signal, $r(t)$ given in (4.1). Using Euler's identity, complex baseband received signal can then be expressed as:

$$r(t) = I(t) + jQ(t) = \frac{1}{2}\sum_{i=1}^{K} G_i \sigma_i \exp\left\{j\Big(m\tau_i t + \omega_0\tau_i\Big)\right\} \tag{4.2}$$

where we have ignored $\frac{1}{2}m\tau_i^2$ since $4mR_i^2 \ll c^2$. Note that complex equivalent baseband expression for received signal in (4.2) states that received signal at a

single antenna is the sum of complex exponential signals whose magnitude, frequency and phase angle are given by

$$A_i = \frac{G_i \sigma_i}{2}, \qquad w_i = m\tau_i = \frac{2 \cdot R_i \cdot \Delta w}{c \cdot T_c} = \frac{4\pi \cdot R_i \cdot B}{c \cdot T_c}, \qquad \theta_i = \omega_0 \tau_i = \frac{2\omega_0 R_i}{c} \tag{4.3}$$

Writing the expression in (4.2) with the newly defined parameters in (4.3), we obtain the final form of the complex baseband equivalent of the received signal, often referred to as the *beat* signal:

$$r(t) = \sum_{i=1}^{K} A_i \exp\left\{ j\Big(\omega_i t + \theta_i\Big) \right\} \tag{4.4}$$

From (4.3) and (4.4), it is apparent that the frequency content of the received signal contains the range information of the targets within the radar's coverage. In order to perform digital signal processing, the beat signal is sampled at a sampling rate of $F_s = \frac{1}{T_s}$, with T_s being the sampling period. During each chirp cycle, a total of $N_s = T_c \cdot T_s$ samples are collected. The sampled beat signal in discrete time can be expressed by replacing t with nT_s:

$$r[n] = r(t)\Big|_{t=nT_s} = \sum_{i=1}^{K} A_i \exp\left\{ j\Big(\hat{\omega}_i n + \theta_i\Big) \right\}, \qquad 0 \le n < N_s \tag{4.5}$$

where $\hat{\omega} = \omega T_s$ denotes the normalized discrete time angular frequency. The discrete time continuous Fourier transform of this signal is

$$\begin{aligned} R(\hat{\omega}) = \mathcal{F}\Big\{ r[n] \Big\} = & \sum_{n=0}^{N_s-1} r[n] e^{-j\hat{w}n} = \sum_{n=0}^{N_s-1} \sum_{i=1}^{K} A_i \exp\left\{ j\Big(\hat{\omega}_i n + \theta_i\Big) \right\} e^{-j\hat{w}n} \\ = & \sum_{i=1}^{K} A_i e^{j\theta_i} \sum_{n=0}^{N_s-1} e^{j\hat{\omega}_i n} e^{-j\hat{w}n} = \sum_{i=1}^{K} A_i e^{j\theta_i} \underbrace{\sum_{n=0}^{N_s-1} e^{-jn(\hat{w}-\hat{\omega}_i)}}_{P_{N_s}(\hat{\omega}-\hat{\omega}_i)} \\ = & \sum_{i=1}^{K} A_i e^{\theta_i} P_{N_s}\left(\hat{\omega} - \hat{\omega}_i\right) \end{aligned} \tag{4.6}$$

where $P_{N_s}(\hat{\omega} - \hat{\omega}_i)$ is the sinc pulse whose center is shifted by $\hat{\omega}_i$ in $\hat{\omega}$

$$P_{N_s}(\hat{\omega}) = \sum_{i=0}^{N_s-1} e^{-jn\hat{\omega}} = \frac{sin(\hat{\omega}N_s/2)}{sin(\hat{\omega}/2)} \exp\{-j\hat{\omega}(N_s-1)/2\} \tag{4.7}$$

Note that $P_{N_s}(\hat{\omega})$ is the Fourier transform of the N_s-point rectangle window. Similarly, by sampling normalized angular frequency such that $\hat{\omega} = \frac{2\pi k}{N_s}$, the Fourier transform expressed in continuous frequency can be converted to discrete frequencies as follows:

$$R[k] = R(\hat{\omega})\Big|_{\hat{\omega}=\frac{2\pi k}{N_s}} = \sum_{i=1}^{K} A_i e^{\theta_i} P_{N_s}\left(\frac{2\pi k}{N_s} - \hat{\omega}_i\right), \qquad 0 \leq k < N_s \tag{4.8}$$

Here, k represents the discrete frequency index and can be associated with the actual range denoted by $r[k]$ through the following relation:

$$r[k] = \frac{c \cdot w \cdot T_c}{2 \cdot \Delta w} = \frac{c \cdot f_k \cdot T_c}{2 \cdot B} = \frac{c \cdot T_c \cdot F_s}{2 \cdot B \cdot N_s} k = \frac{c}{2B} k, \qquad 0 \leq k < N_s \tag{4.9}$$

Range and frequency response vectors $\{r[k], R[k]\}$ together provide complete information regarding the range profile of the radar scene when $|R[k]|$ is plotted against $r[k]$. Targets result in peaks at their respective range cells whose magnitude is proportional to the target RCS. It is also worth noting that the radar systematic range is determined by the full sampling rate, F_s, not $F_s/2$, since the received signal is complex and thus has a single-sided spectrum. Therefore, the radar maximum range is given by

$$R_{max} = \frac{c \cdot F_s \cdot T_c}{2 \cdot B} \tag{4.10}$$

It is also worthwhile to note that the expression (4.8) given in discrete Fourier domain is the sum of sinc pulses shifted in frequency with an amount from which any reflector object's radial distance to the radar can be determined.

4.2.2 Angular Processing

The incoming angle of an incident radio wave can be determined by using a receiver array. Therefore, MIMO radars are capable of extracting angular information of the reflector objects in their coverage without mechanically rotating the antenna. This is done by what is known as *digital beamforming* algorithms. With MIMO radars, it is possible to achieve high angular resolutions with less antennas compared to that of a single input multiple output (SIMO) radar system.

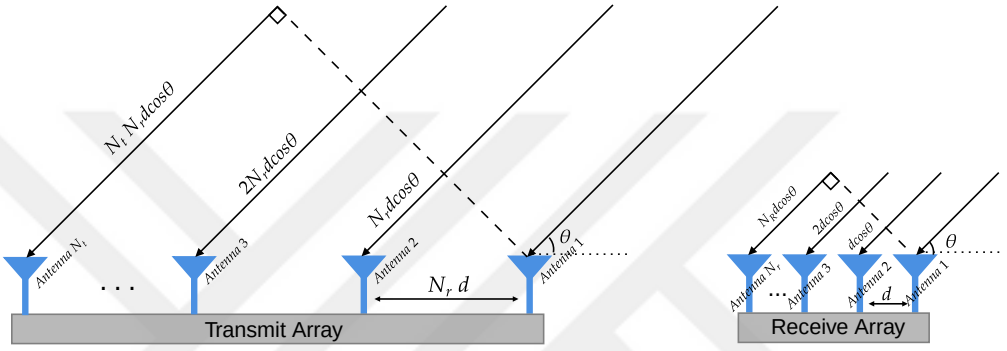


FIGURE 4.3: MIMO radar transmit and receive antenna array configuration

A MIMO radar with co-located ULA antennas both at the transmitter and receiver side is shown in Figure 4.3. In the studied MIMO radar model, transmit array is equipped with N_t antennas, while receive array is equipped with N_r antennas. Both the transmit and receive antennas are assumed to have suitable beam coverage for the space under surveillance. The separation between receive antennas is d, while transmit antennas are separated by $N_r \cdot d$. The purpose of this special placement of transmit and receive antennas is to create a virtual uniform linear array with $N_{MIMO} = N_t \cdot N_r$ antennas. In principle, one can achieve the same angular resolution with N_t transmit and N_r receive antenna elements as a SIMO radar with single transmitter and receiver array with N_{MIMO} antennas does as the two systems are equivalent in terms of angular resolution characteristics. This is essentially what makes MIMO radars attractive for the applications where high angular resolution is required with limited number of hardware. For our development of angular processing, we start with the receiver ULA only for the azimuth angle processing and then extend this to MIMO radar including transmitter ULA.

After applying the DFT in range at each receiver channel, objects located at the same distance from the radar are mapped to the same range cell. The received signal model for an arbitrary range cell k can be expressed as the sum of contributions from all equidistant reflector objects:

$$R_k[m] = \sum_{i=1}^{K} X_k[i] e^{j\omega_i m}, \qquad 1 \leq m \leq N_r \quad \text{and} \quad 0 \leq k < N_s \tag{4.11}$$

where m denotes the antenna index, K is the total number of targets at the kth range cell, $\omega_i = 2\pi d \sin(\theta_i)/\lambda$ represents the phase difference at successive receiver antennas due to the path length difference, as illustrated in Figure 4.3. Here, we assume that the objects are assumed to be all in the far field region of the radar. In other words, the distance of the targets to the radar is much larger than radar aperture. This far field assumption directly implies planar wavefront, making it convenient for the parallel ray assumption. $X_i[k]$ denotes the signal from the ith target at the kth range cell. The azimuth angle profile at the kth range cell can be obtained by performing the angle-DFT of the virtual channel measurement samples, $R_k[m] = \{R_k[1], R_k[2], \ldots, R_k[N_{\text{MIMO}}]\}$. Thus,

$$\begin{aligned} Y_k(\hat{\omega}) = \text{DFT}\Big\{R_k[m]\Big\} = & \sum_{m=0}^{N_r-1} R_k[m] e^{-j\hat{w}m} = \sum_{m=0}^{N_r-1} \sum_{i=1}^{K} X_i e^{j\hat{\omega}_i m} e^{-j\hat{w}m} \\ = & \sum_{i=1}^{K} X_i \sum_{m=0}^{N_r-1} e^{j\hat{\omega}_i n} e^{-j\hat{w}n} = \sum_{i=1}^{K} X_i \underbrace{\sum_{m=0}^{N_r-1} e^{-jn(\hat{w}-\hat{\omega}_i)}}_{P_{N_r}(\hat{\omega}-\hat{\omega}_i)} \\ = & \sum_{i=1}^{N_r} X_i P_{N_s}(\hat{\omega} - \hat{\omega}_i) \end{aligned} \tag{4.12}$$

Azimuth spectrum, as given by (4.12), is expressed in continuous normalized angular frequency. Analogous to range processing, we can discretize this spectrum by setting $\hat{\omega} = \frac{2\pi m}{N_r}$:

$$Y_k[m] = Y_k(\hat{\omega})\Big|_{\hat{\omega}=\frac{2\pi m}{N_r}} = \sum_{i=1}^{K} X_i P_{N_r}\left(\frac{2\pi m}{N_r} - \hat{\omega}_i\right), 0 \leq k < N_s \quad , \quad 0 \leq m < N_r \tag{4.13}$$

Using $\hat{\omega} = \frac{2\pi m}{N_r}$ and $\hat{\omega}_i = 2\pi d \sin(\theta_i)/\lambda$, we can construct the relationship between discrete angular frequency index, k and the true azimuth angle of the ith target such that:

$$\theta_i = \sin^{-1}\left(\hat{\omega}_i \frac{\lambda}{2\pi d}\right) = \sin^{-1}\left(\frac{\lambda}{N_r d} m\right), \qquad -\frac{N_r}{2} \leq m < \frac{N_r}{2} \tag{4.14}$$

When $d = \frac{\lambda}{2}$, the maximum field of view is attained within $-90° \leq \theta < 90°$. With expressions for the azimuth spectrum of an array featuring N_r receiver elements in equations (4.12) and (4.13), it's feasible to derive a closed-form mathematical expression for the array factor of a MIMO radar. Considering a single object at $\theta_i = 0$ at an arbitrary range cell k, normalized measurements in each receiver element at the kth range cell become $R_k[m] = \{1, 1, \ldots, 1\}$ since $\sin(0) = 0$.

$$x_r[m] = \{1, 1, \ldots, 1\} = \sum_{k=0}^{N_r - 1} \delta(m - kd) \overset{\mathbb{FT}\{\cdot\}}{\Longleftrightarrow} X_r(\hat{\omega}) = P_{N_r}(\hat{\omega}) \tag{4.15}$$

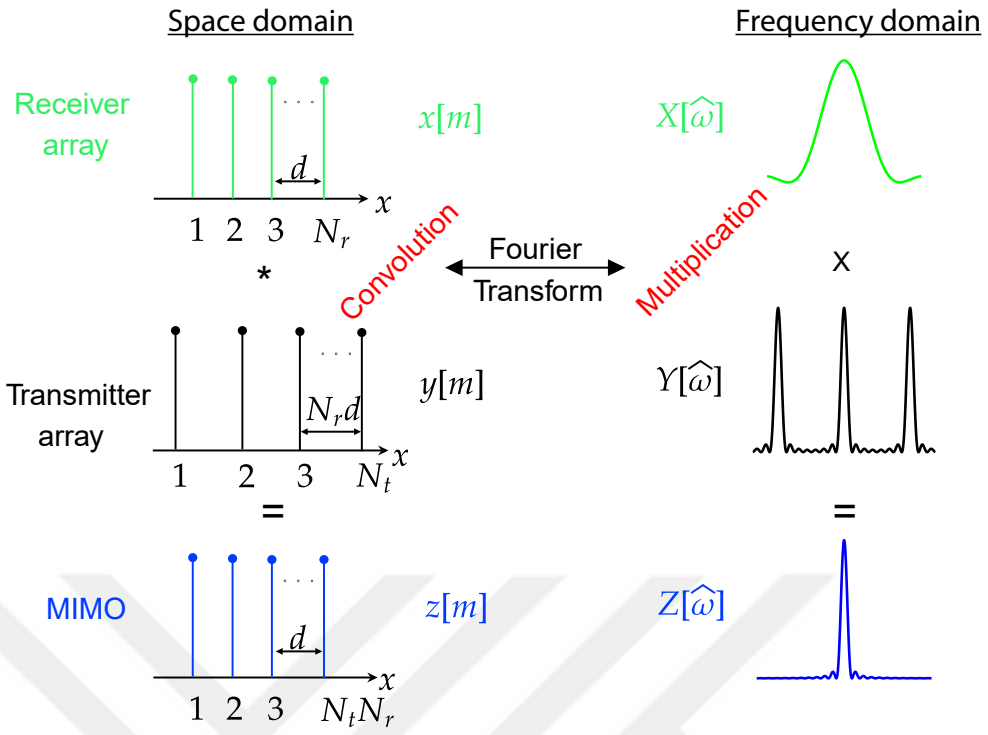
where $\mathbf{X}_r(\hat{\omega})$ is the array factor of the receiver array and $P_{N_r}(\hat{\omega})$ is the sinc function described by expression (4.7). By the same argument, we obtain the array factor of the transmitter array as follows:

$$x_t[m] = \{1, 1, \ldots, 1\} = \sum_{k=0}^{N_t - 1} \delta(m - kN_r d) \overset{\mathbb{FT}\{\cdot\}}{\Longleftrightarrow} \mathbf{X}_t(\hat{\omega}) = P_{N_t}(\hat{\omega}) \tag{4.16}$$

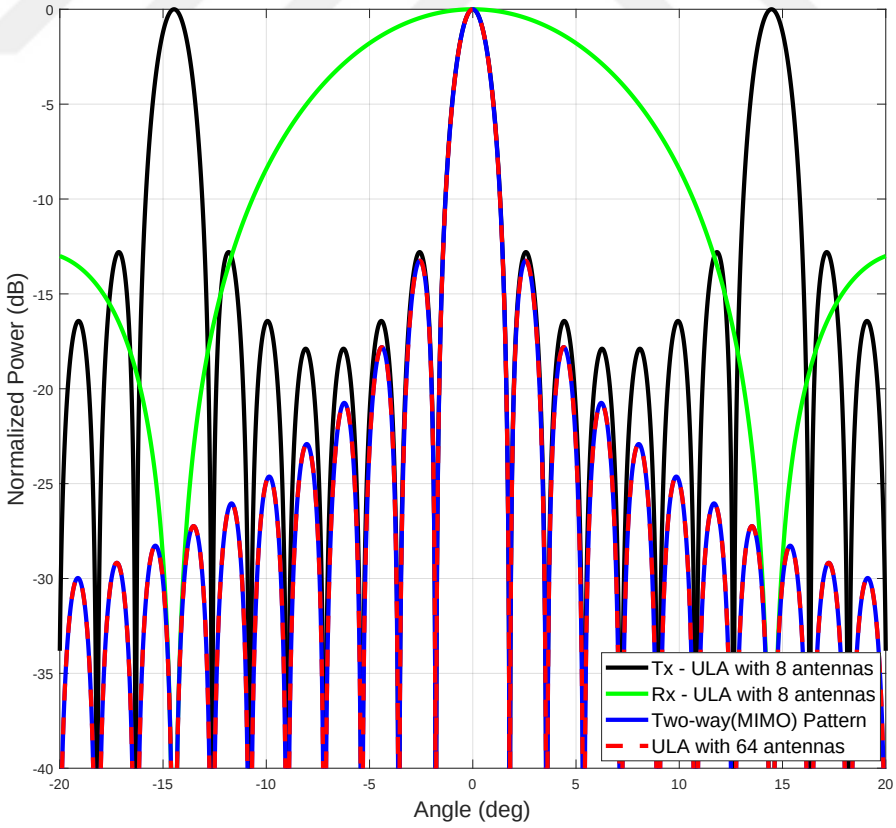
Two-way array factor of the MIMO radar is given by the product of the transmit and receive array factor:

$$\begin{aligned} X_{\text{MIMO}}(\hat{\omega}) = X_t(\hat{\omega}) X_r(\hat{\omega}) &\overset{\mathbb{FT}\{\cdot\}}{\Longleftrightarrow} x_t[m] * x_r[m] \\ x_t[m] * x_r[m] = \sum_{k=0}^{N_t - 1} \delta(m - kN_r d) * \sum_{k=0}^{N_r - 1} \delta(m - kd) &= \sum_{k=0}^{N_t N_r - 1} \delta(m - kd) \end{aligned} \tag{4.17}$$

where we have used the convolution-multiplication duality property of the Fourier transform and $*$ denotes convolution. Equation (4.17) establishes that a MIMO radar comprising N_t transmit antennas and N_r receive antennas, illustrated in Figure 4.3, is equivalent to a ULA with $N_t \times N_r$ receiver antennas in terms of angular resolution. Figure 4.4a visually depicts the mathematical equivalence



(A) Demonstration of the equivalence between the array factor of $N_t \times N_R$ MIMO radar and ULA with $N_t \times N_r$ antennas



(B) Array pattern of an 8×8 MIMO radar array at 24 GHz, $d = 0.5\lambda$

FIGURE 4.4: Array factor calculation for a MIMO radar

between these two systems. To exemplify this equivalence, we calculate the array factor of an 8×8 MIMO radar and a ULA 64 receive antennas, both operating at 24 GHz, as shown in Figure 4.4b. The array patterns demonstrate that the 8×8 MIMO radar array exhibits precisely the same array pattern as a 64-element uniform linear array does.

The model described by (4.11) can also be expressed in matrix form as $\mathbf{R} = \mathbf{AX}$, where $\mathbf{R} \in \mathbb{C}^{M \times 1}$, $\mathbf{X} \in \mathbb{C}^{N \times 1}$, and $\mathbf{A} \in \mathbb{C}^{M \times N}$. Here, the columns of $\mathbf{A}$ represent the steering vectors:

$$\mathbf{A} = \Big[\mathbf{a}(\hat{\omega}_1), \mathbf{a}(\hat{\omega}_2), \ldots, \mathbf{a}(\hat{\omega}_N)\Big]$$

with each steering vector being

$$\mathbf{a}(\hat{\omega}_i) = \Big[1, e^{j\hat{\omega}_i}, e^{j\hat{\omega}_i 2}, e^{j\hat{\omega}_i 3}, \ldots, \mathrm{e}^{j\hat{\omega}_i(M-1)}\Big]^T$$

With this, expression (4.11) can be written explicitly as follows:

$$\begin{bmatrix} R_1[k] \\ R_2[k] \\ \vdots \\ R_M[k] \end{bmatrix} = \begin{bmatrix} 1 & 1 & \ldots & 1 \\ e^{j\hat{\omega}_1} & e^{j\hat{\omega}_2} & \ldots & e^{j\hat{\omega}_N} \\ e^{j\hat{\omega}_1 2} & e^{j\hat{\omega}_2 2} & \ldots & e^{j\hat{\omega}_N 2} \\ \vdots & \vdots & \ddots & \vdots \\ e^{j\hat{\omega}_1(M-1)} & e^{j\hat{\omega}_2(M-1)} & \ldots & e^{j\hat{\omega}_N(M-1)} \end{bmatrix} \begin{bmatrix} X_1[k] \\ X_2[k] \\ \vdots \\ X_N[k] \end{bmatrix} \tag{4.18}$$

By setting $\theta_i = \sin^{-1}\left(\frac{\lambda}{Md}i\right)$ for $i \in \{1, 2, \ldots, M\}$ and uniformly dividing the entire azimuth interval into M azimuth bins, the linear system in (4.18) becomes:

$$\begin{bmatrix} R_1[k] \\ R_2[k] \\ R_3[k] \\ R_4[k] \\ \vdots \\ R_M[k] \end{bmatrix} = \underbrace{\begin{bmatrix} 1 & 1 & 1 & 1 & \ldots & 1 \\ 1 & W^1 & W^2 & W^3 & \ldots & W^{(M-1)} \\ 1 & W^2 & W^4 & W^6 & \ldots & W^{2(M-1)} \\ 1 & W^3 & W^6 & W^9 & \ldots & W^{3(M-1)} \\ \vdots & \vdots & \vdots & \vdots & \ddots & \vdots \\ 1 & W^{(M-1)} & W^{2(M-1)} & W^{3(M-1)} & \ldots & W^{(M-1)(M-1)} \end{bmatrix}}_{M \times M \text{ inverse DFT matrix}} \begin{bmatrix} X_1[k] \\ X_2[k] \\ X_3[k] \\ X_4[k] \\ \vdots \\ X_M[k] \end{bmatrix} \tag{4.19}$$

The linear model states that the azimuth profile at any range cell can be computed by taking the Fourier transform of the complex signals at that range cell over the MIMO channels. This is expressed as:

$$\mathbf{R}[k] = IDFT\Big\{\mathbf{X}[k]\Big\} \Longleftrightarrow \mathbf{X}[k] = DFT\Big\{\mathbf{R}[k]\Big\} \tag{4.20}$$

In conventional MIMO radar signal processing, two different FFTs are applied to the collected signals. The first FFT is performed over the received signal samples collected at each virtual MIMO element to form the range profile data. The second FFT is performed over the MIMO channels at each range cell to form the angle profile data. To illustrate these steps, let us consider an 8×8 MIMO radar operating in a clutter-free environment with three reflecting objects, each located at different ranges and azimuth angles. Figure 4.5 demonstrates the formation of the radar image by applying two successive FFTs to the raw radar data.

4.3 ANN Based DoA Estimation

Including Fourier Transform-based angle profile extraction, most direction of arrival estimation algorithms rely on the forward measurement model described in equation (4.18). The downside of all these model-based algorithms is that any uncertainty in the model leads to estimation inaccuracies. In the direction of arrival estimation problem, the forward model is determined by the sensing geometry

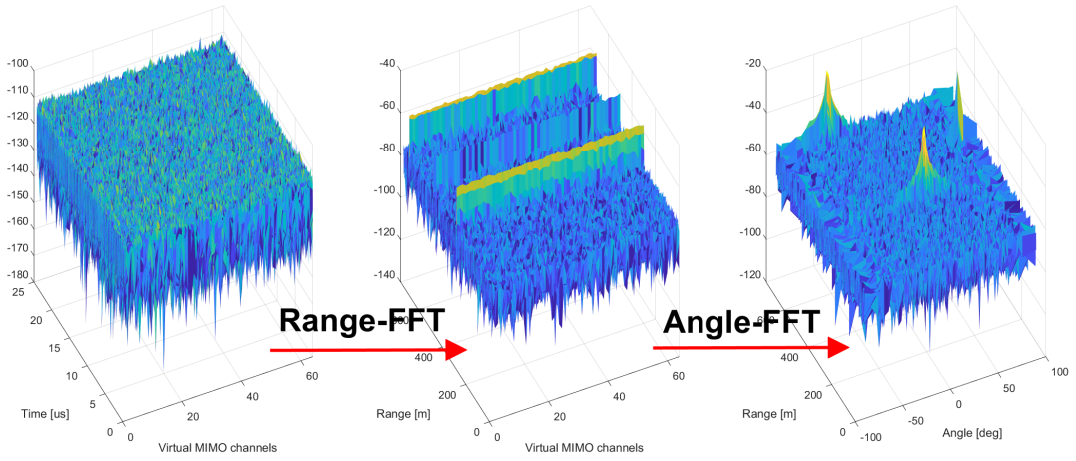
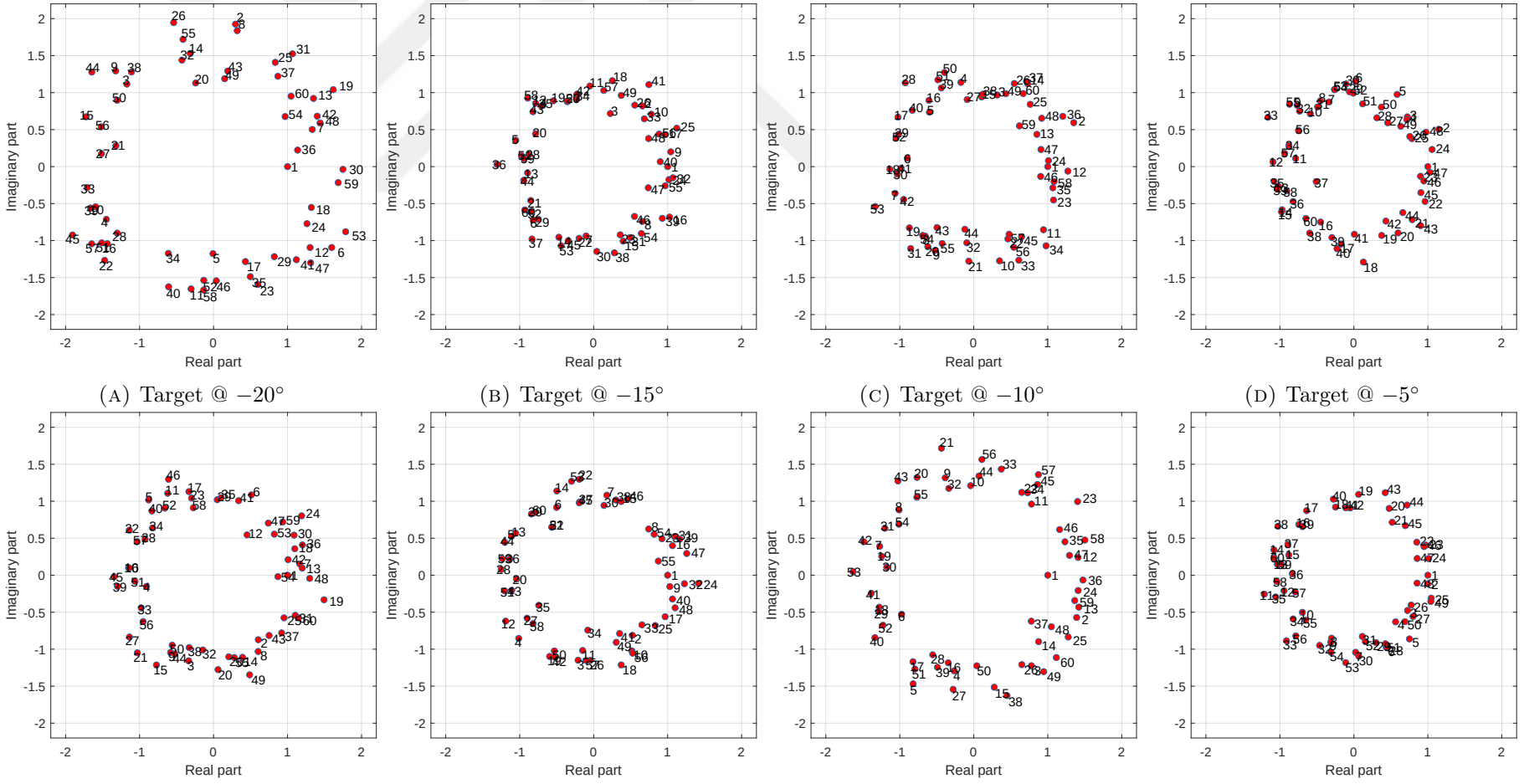


FIGURE 4.5: Left: Radar data acquired by an 8×8 MIMO radar system showing three targets. Middle: Radar data post range FFT processing, revealing the targets' range information. Right: Radar data post angle FFT processing, unveiling the targets' angular information.

of the radar. Poorly displaced antenna elements or insufficiently calibrated RF circuits lead to model inaccuracies when they are considered calibrated, and calculations are performed accordingly. Unlike traditional model-based approaches, we propose adopting a data-driven approach for the angular position estimation of objects in our detection problem. Our goal is to learn the mapping between complex radar measurements at each virtual MIMO element and the azimuth angle of the detected object. Instead of relying on a measurement model highly dependent on array geometry and RF component calibration, we employ a neural network to learn the measurement model directly from training/calibration data.

Depending on the azimuth angle of a target, the snapshot angle measurements at the respective range cell of the target show different patterns. An artificial neural network can learn the relation between these snapshot measurement patterns and the respective target angle. To better illustrate these patterns, we demonstrate 4 different snapshot angle measurements of a single target at 4 different azimuth angles from a 6×10 MIMO radar in Figure 4.6. Here, the numbers next to each measurement mark represent the corresponding MIMO index. It should also be noted that the snapshot angle measurements are normalized with respect to 1st MIMO element to make the measurements range-independent.



(A) Target @ −20° (B) Target @ −15° (C) Target @ −10° (D) Target @ −5°

(E) Target @ 20° (F) Target @ 15° (G) Target @ 10° (H) Target @ 5°

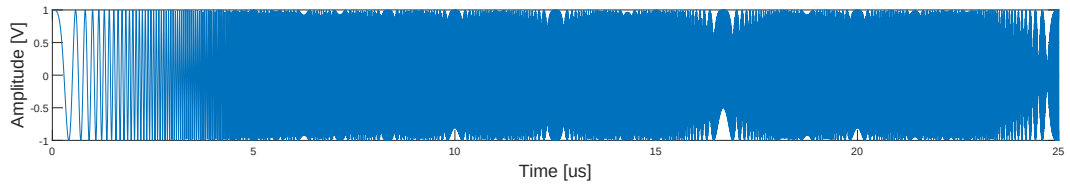
FIGURE 4.6: Normalized angle measurements of a point target with an RCS of 40 db located 400m away from the array center at each virtual MIMO element in complex IQ plane with respect to changing target azimuth angle. Numbers next to each plot represent the corresponding virtual array index. With 6 transmit and 10 receive antenna, we form a virtual array with 60 elements.

4.3.1 MIMO Simulation & Training Data Generation

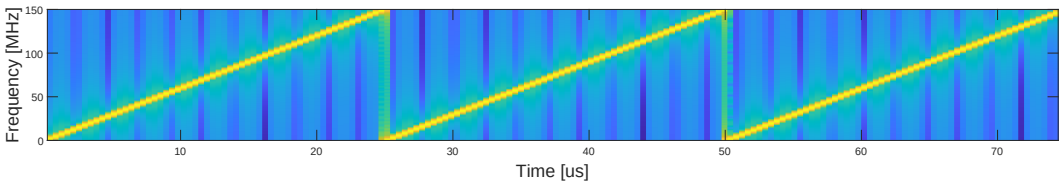
In order to generate a training dataset, we conduct end-to-end MIMO radar simulations at the physical layer using the Phased Array System Toolbox in Matlab 2021b. The simulation environment comprises three main components: the radar, the channel, and the target. In the simulations, both the radar and target objects remain stationary, meaning no Doppler effect is considered. We employed a free-space model for simulating the two-way channel. The radar setup involves a 6×10 MIMO radar, where transmissions occur sequentially, with each transmitter utilizing the channel in non-overlapping time slots. The radar parameters are summarized in Table 4.1.

Parameters	Value	Parameters	Value
Frequency	24 GHz	Peak power	200 mW
Number of Tx antennas	6	Tx gain	0 dB
Number of Rx antennas	10	Rx gain	0 dB
Number of Virtual MIMO elements	60	Noise figure	0 dB
Sweep time	25 us	Sampling rate	300 MHz
Sweep bandwidth	150 MHz	Range resolution	1 m
Chirp rate	6×10^{12}	Max. allowed range	750 m

TABLE 4.1: Radar parameters used in the MIMO radar simulations.



(A) Time plot of the single linear FMCW chirp signal transmitted from TX antennas



(B) Spectrogram plot of the first three chirps, with window length of 256 time samples and 50 % overlapping

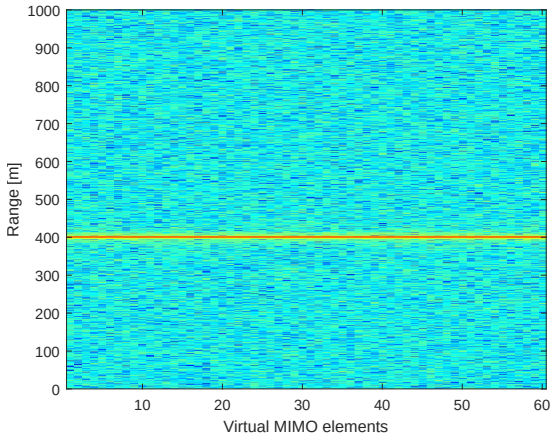
FIGURE 4.7: Linear up-chirp FMCW signal considered in our simulations

We consider linear chirp signals with a sweep bandwidth of 150 MHz and a chirp period of 25 us, as illustrated in Figure 4.7. The time and frequency plots of the linear FMCW signal used are depicted in Figures 4.7a and 4.7b, respectively. Each antenna transmits a single chirp waveform, which reflects from the target, undergoes channel effects, and is simultaneously collected by each receiver. Receiver noise is assumed to be complex white noise, with its power determined by the frequency band used and the noise figure of the receiver. After dechirping and additional post-processing steps, Fast Fourier Transform (FFT) is applied to the received signal at each MIMO element to obtain the range profile. The FFT results are stored in a data matrix, $\mathbf{D}(r, m) \in \mathbb{C}^{R \times M}$, where $r = 1, 2, \ldots, R$ denotes the range index and $m = 1, 2, \ldots, M$ represents the index for each MIMO Tx-Rx pair. Therefore, each column of the data matrix becomes the range profile seen by the corresponding Tx-Rx antenna pair. On the data matrix, next a peak detection algorithm is run along the range axis, and if a target is detected, then the complex snapshot measurements at each detection range cell are fed into a neural network to estimate the angle of the target. These steps are summarized in Algorithm 1.

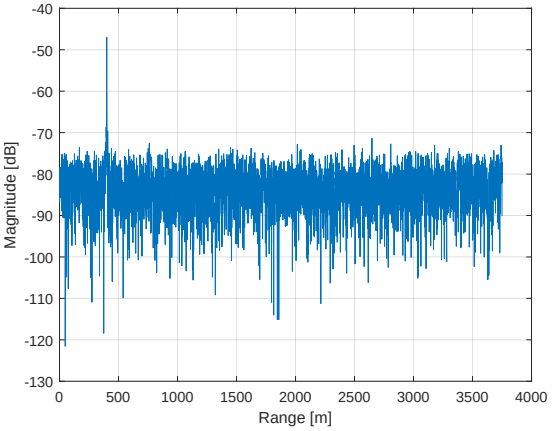
Algorithm 1: Creation of Radar Data Matrix in Simulation Environment

$i_{TX} \leftarrow 1, i_{RX} \leftarrow 1, m \leftarrow 0$; /* Initialize antenna index */
$\mathbf{D} \leftarrow \mathbf{0}(R, M)$; /* Allocate a radar data matrix */
while $i_{TX} \neq N_T$ **do**
  while $i_{RX} \neq N_R$ **do**
    $m \leftarrow m + 1$; /* Increment index for each TX-RX pair */
    $\mathbf{D}[:, m] \leftarrow FFT\{\mathbf{r}(\mathbf{t})\}$; /* Take the FFT of received signal and store the resulting vector in m^{th} column of $\mathbf{D}$ */
    $i_{RX} \leftarrow i_{RX} + 1$;
  end
  $i_{TX} \leftarrow i_{TX} + 1$;
end

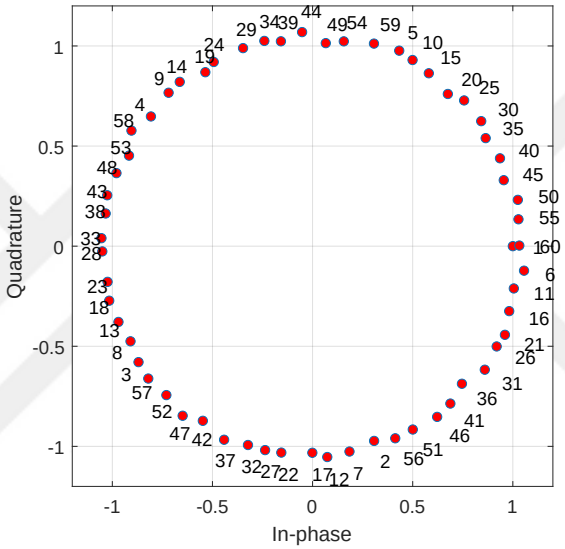
An example of radar measurements for a single target located 400 m away from the radar is shown in Figure 4.8. The radar data matrix is presented in Figure 4.8a. The range profile seen by the 1st MIMO element is displayed in Figure 4.8c, and the normalized complex angle measurements are plotted in the complex plane in Figure 4.8c. Each target, having a different azimuth angle, yields different complex measurements, which we refer to as angle measurements. Therefore, these



(A) Radar Data Matrix - Range profile/MIMO channels



(B) Range profile observed at the first element of MIMO array



(C) Normalized angle measurements at each element

FIGURE 4.8: An illustrative MIMO measurements for a single target

complex measurements form the input of our training data. On the other hand, the output is the azimuth angle of the target. Angle measurements are normalized with respect to the 1st MIMO element in order to make the measurements range-independent: $\mathbf{D}[r, m] = \mathbf{D}[r, m]/\mathbf{D}[r, 1]$. A single target is placed at 250 m away from the radar, and the azimuth angle is uniformly distributed within the range $[-20°, 20°]$.

For each random azimuth angle of the target, a different angle measurement is obtained, forming a distinct input and output data pair. For the training dataset, we run 10^4 Monte Carlo simulations, resulting in a dataset of 10^4 samples. This

dataset is divided into three different sets: a training set of 7500 samples, a test set of 1500 samples, and a validation set of 1500 samples. To test the network performance under different Signal-to-Noise Ratio (SNR) conditions, we also create different datasets considering various target Radar Cross Section (RCS) values under fixed receiver noise levels. We consider 6 different RCS levels to provide varying SNR conditions.

4.3.2 Proposed Neural Network Architecture & Training

We use a fully connected neural network with a single hidden layer in order to learn the mapping between angle measurements at each MIMO element and the azimuth angle of the target. Input layer has 120 neurons, where first 60 input neurons take the real part of the measurements and last 60 neurons takes the imaginary part of the measurements. The hidden layer consists of 20 neurons. The output layer is a single neuron. In the hidden layer, hyperbolic tangent sigmoid function is used while in output layer linear activation function is used.

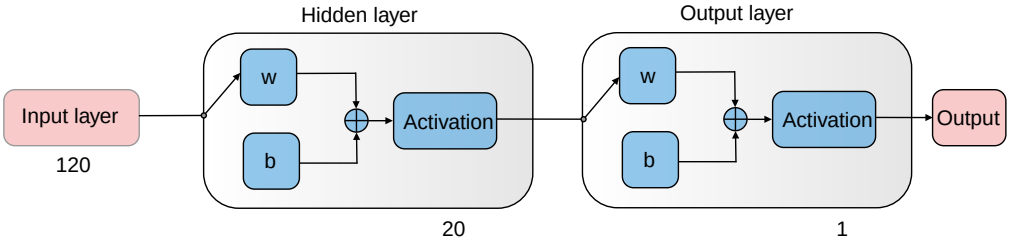
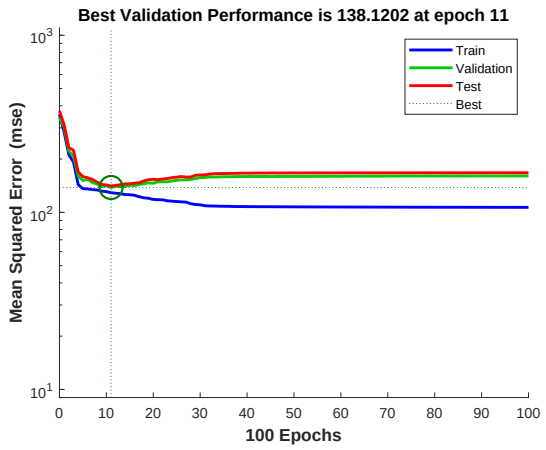
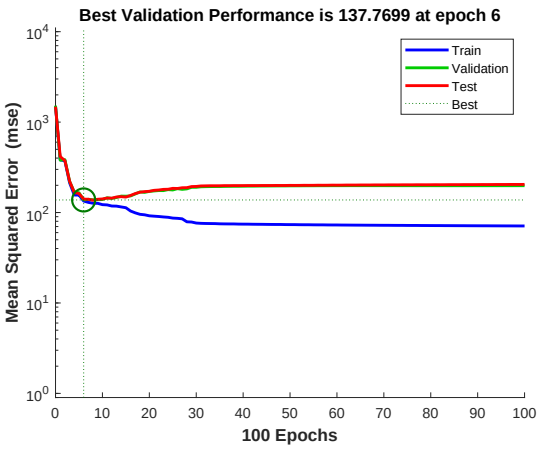


FIGURE 4.9: Artificial neural network used for the regression of the AoA. The numbers below the each layer represent the number of neurons in each layer

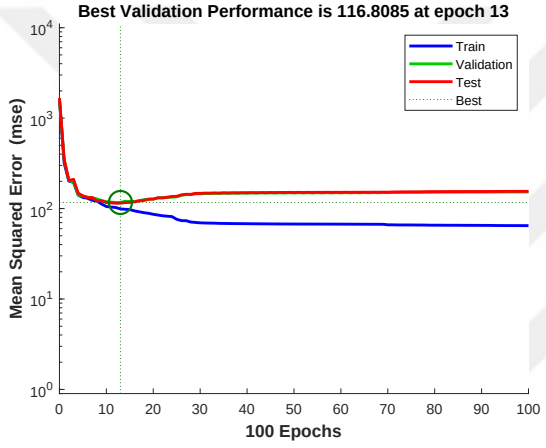
A simplified architecture of the used network is given in Figure 4.9. We train our neural network on 6 different training data generated at 6 different RCS levels. Mean-square-error(MSE) is chosen as the cost function in the optimization. The network is implemented using Deep Learning Toolbox of Matlab 2021b. For each training data set generated with different target RCS levels, a separate network is trained. The progression of cost function during the training of these networks are given in the Figure 4.10.



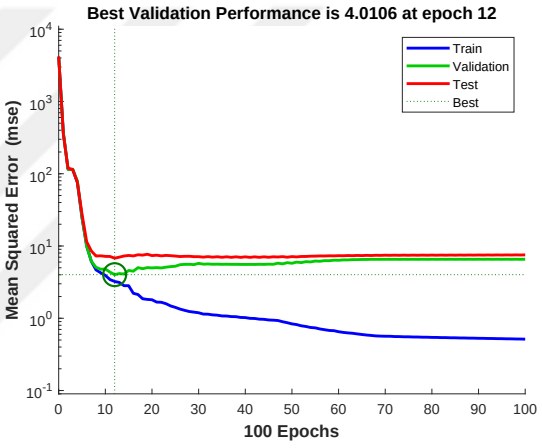
(A) Network # 1 (RCS: 15 db)



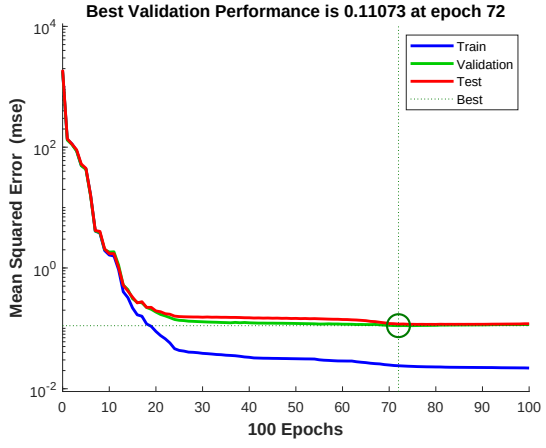
(B) Network # 2 (RCS: 20 db)



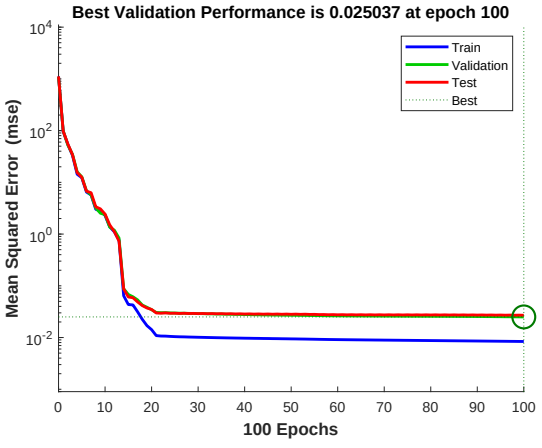
(C) Network # 3 (RCS: 25 db)



(D) Network # 4 (RCS: 30 db)



(E) Network # 5 (RCS: 35 db)



(F) Network # 6 (RCS: 40 db)

FIGURE 4.10: Mean square error plots during the progression of the training (100 epochs) of the six different networks trained at six different RCS levels. MSE performance is plotted for train, test and validation data sets with a circle mark indicating the best validation performance during the training

The steps of the overall ANN-based target angle estimation algorithm are outlined in Algorithm 2. In Step 5, complex MIMO measurements at the detected range cell are passed through an ANN, whose complexity depends on the selected neural network architecture and the number of neurons at each layer. Figure 4.11 illustrates the main computational blocks in the proposed algorithm.

Algorithm 2: Steps of the proposed DoA estimation technique

1 Perform CFAR on $\mathbf{D}$ along the range dimension to detect targets
2 Take the angle measurements at the detected range cells and store it in $\mathbf{v}$.
3 Normalize $\mathbf{v}$ with respect to the measurement at the 1st MIMO element, $\overline{\mathbf{v}} = \frac{\mathbf{v}}{|\mathbf{v}(1)|}$.
4 Concatenate real and imaginary parts of $\mathbf{v}$, $\mathbf{w} = \text{conc}(\text{Re}\{\overline{\mathbf{v}}\}, \text{Im}\{\overline{\mathbf{v}}\})$.
5 Feed $\mathbf{w}$ to pre-trained ANN to estimate target angle $\hat{\theta} = \sigma(\mathbf{w})$.
6 Return to step 4 and repeat the procedure for each detection.

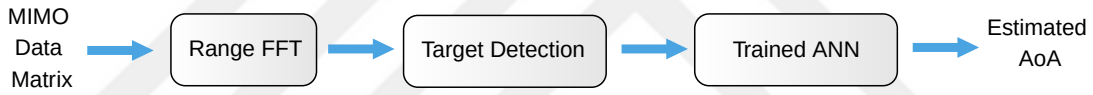


FIGURE 4.11: Data processing steps of the proposed method: 1) Range extraction through FFT along the fast-time axis 2) Target detection 3) DoA estimation with the trained neural network.

4.4 Numerical Results

Test performance is assessed in terms of MSE on the test data set which contains 1500 measurement-angle pairs. We first show the validity of our proposed solution under different SNR conditions. The scatter plots in Figure 4.12 show the correlation between the ground truth and the neural network response. Here x-coordinate of the each data point shows the target azimuth angle (ground truth) and the y-coordinate is the neural network estimation. The correlation coefficient is computed and provided at the top of each figure. The best line fit is also shown with a blue line in the plots. As SNR in the training data increases, the best line fit gets closer to the line $Y = T$, and the correlation coefficient approaches 1. It

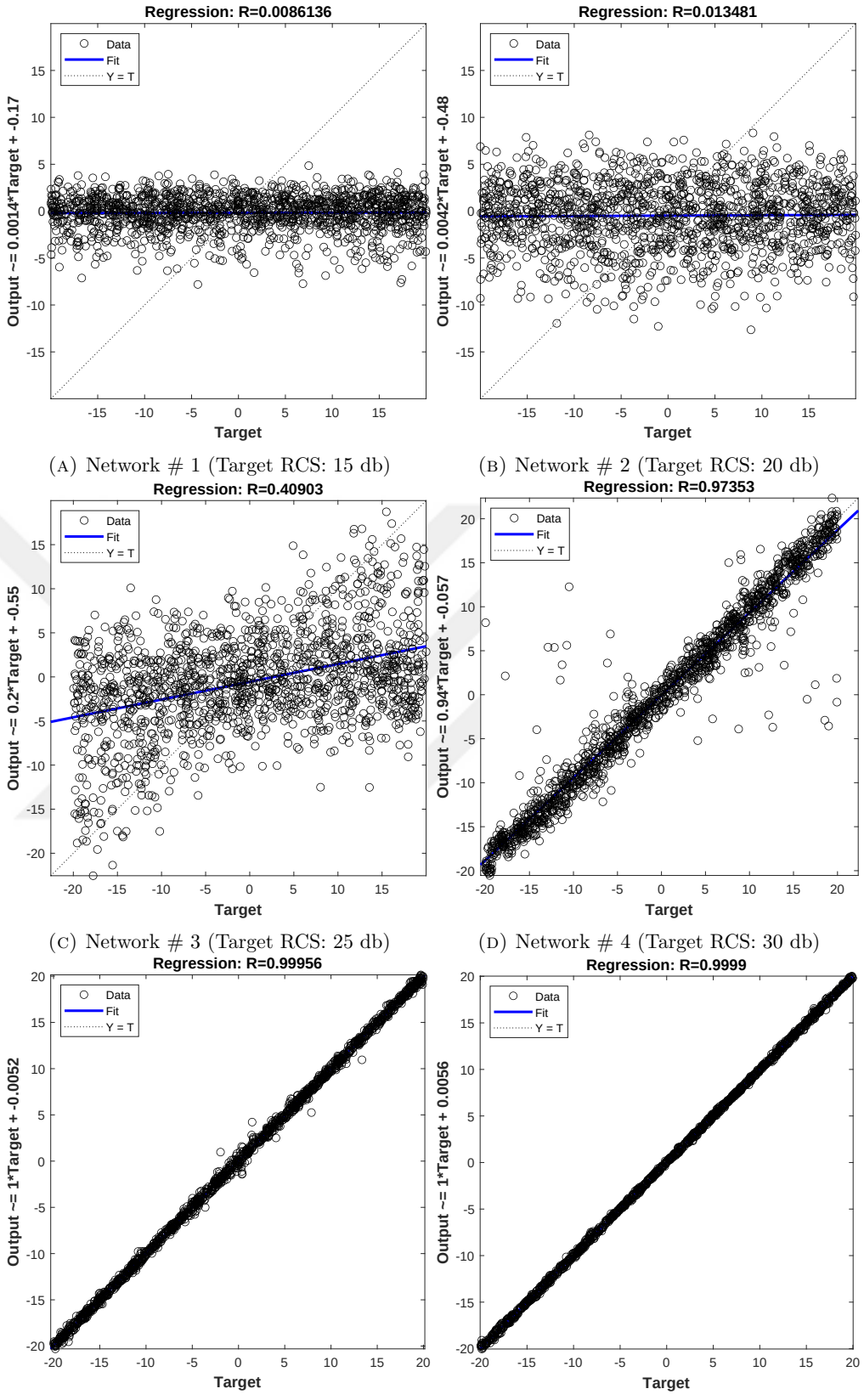
clearly shows that the proposed network is able to learn the given task and the estimation accuracy of the model improves with increasing SNR.

Similarly, the error histogram of each neural network is given for train, validation, and test data sets in Figure 4.13. Here, we define the error as the difference between the model response and the ground truth, i.e., $e = Y - T$. Zero error levels are also indicated with a vertical red line. As seen from the figures, errors exhibit a normal-like distribution around zero. It is also quite clear that as SNR increases in the training data set, the learning performance of the network improves, which leads to a smaller error standard deviation.

Having validated the model and its learning capability by checking the estimation accuracy in incremental SNR conditions, we next compare the MSE performance of the proposed technique with the other existing model-based DoA algorithms for different SNR and model uncertainty levels. The results are shown in Figure 4.14. The MSE values are the average values, calculated by averaging over 1500 test samples. Each green diamond mark in the plots represents the performance of the neural network trained for that specific scenario. MSE performances of the different methods are evaluated under different SNR conditions in Figure 4.14a. Under low SNR conditions, the proposed technique shows superior performance in terms of MSE as compared to the other benchmark methods. In Figure 4.14b, we present the effect of the model uncertainty. In order to introduce model uncertainty, we corrupt the phase of measurements at each MIMO element by adding random phases to the measurements and we use the standard deviation of the phase randomness as a metric to quantify the model uncertainty, as shown in the x-axis of the plot in Figure 4.14b. In practice, these model uncertainties could stem from perturbed antenna positions or poorly calibrated RF circuitry. Apparently, performances of all the model-based DoA methods deteriorate as the uncertainty in the underlying model increases. On the other hand, the proposed neural network based solution shows almost no dependency on the uncertainty in the model. This can be explained by the fact that the proposed method truly relies on the training data, which already contains the model uncertainties in it. In other words, since the proposed method learns the mapping from the measurements to the azimuth

angle of the targets directly from the calibration data, it remains unaffected by the model uncertainties while all the model-based methods strictly depend on how accurately the underlying measurement model is known.

All analyses conducted thus far have been based on a single SNR condition, both in training and testing phases. To assess the performance of the proposed method under diverse conditions, we introduce variations not only in the azimuth dimension but also in the range direction while creating data set. This introduces varying radar losses, thereby leading to different SNR conditions for each target. The performance results for this test case are presented in Figure 4.15. The experiments distinctly demonstrate the robustness of the target angle learning also under varying target SNR conditions.



(A) Network # 1 (Target RCS: 15 db)

(B) Network # 2 (Target RCS: 20 db)

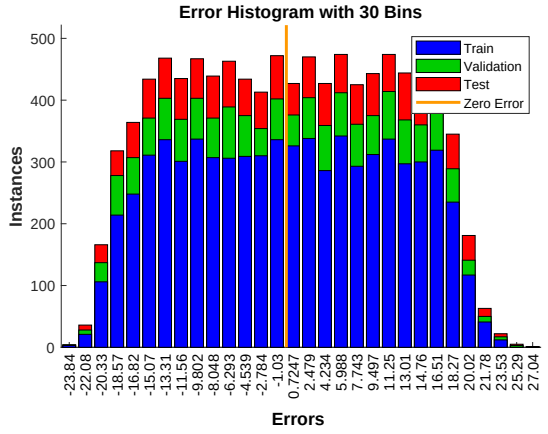
(C) Network # 3 (Target RCS: 25 db)

(D) Network # 4 (Target RCS: 30 db)

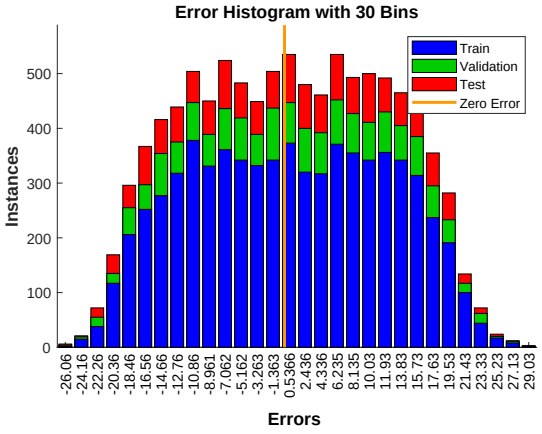
(E) Network # 5 (Target RCS: 35 db)

(F) Network # 6 (Target RCS: 40 db)

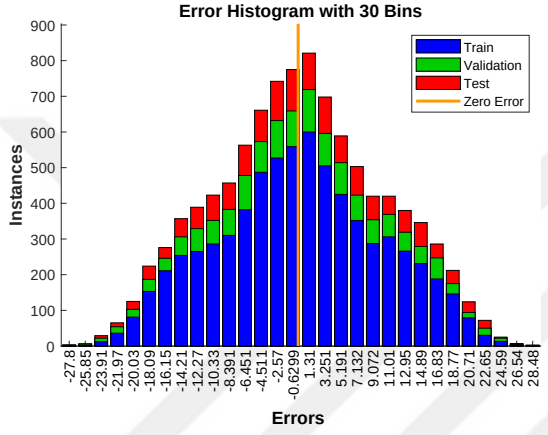
FIGURE 4.12: Regression performances of 6 different networks trained at different target RCS level. Each data points show true azimuth angle of the network prediction. Correlation coefficient for each regression is also given on the top of the figures. Equation for the best line fit is provided in the y axis of the each plot. $y = x$ line is also plotted to provide goodness of the each fit



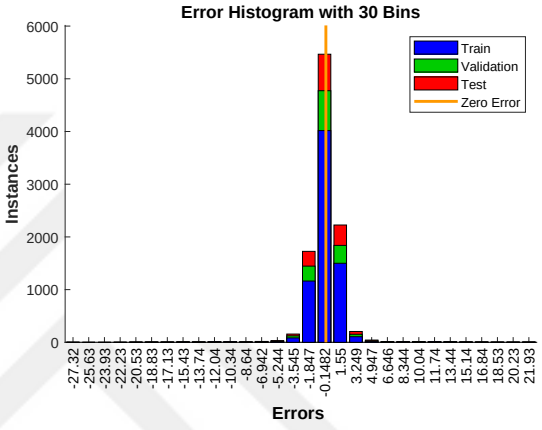
(A) Network # 1 (RCS: 15 db)



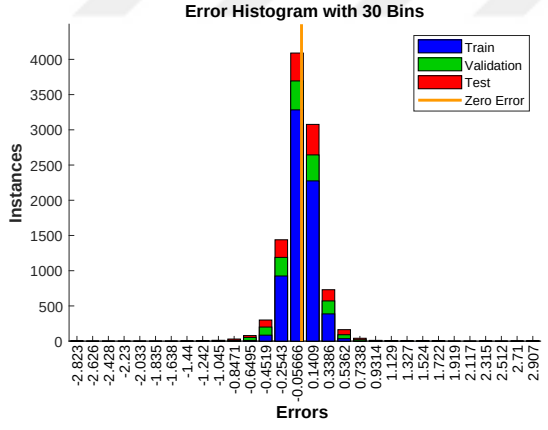
(B) Network # 2 (RCS: 20 db)



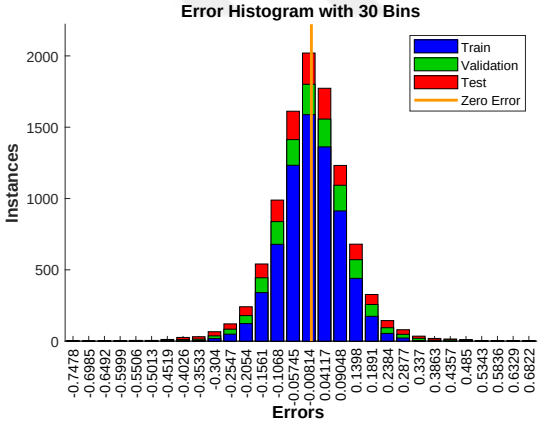
(C) Network # 3 (RCS: 25 db)



(D) Network # 4 (RCS: 30 db)

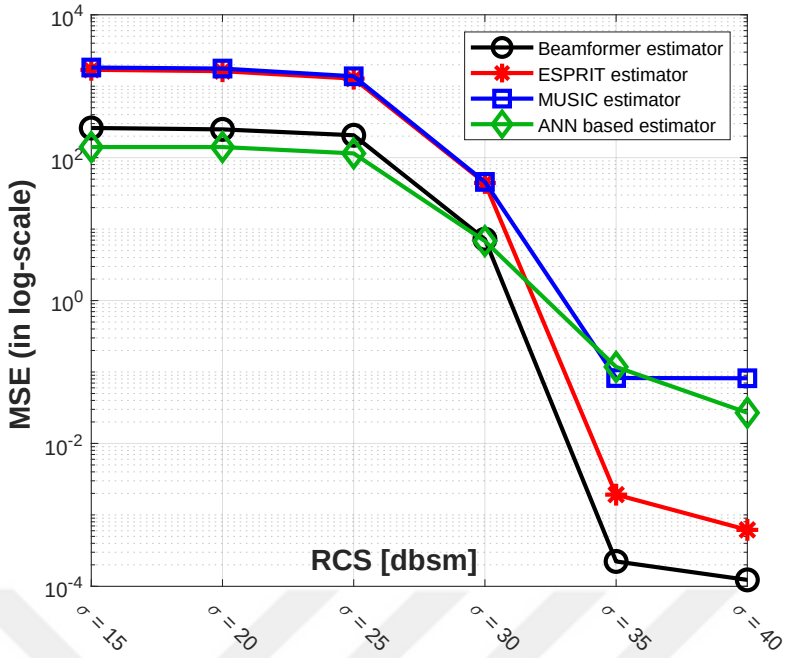


(E) Network # 5 (RCS: 35 db)

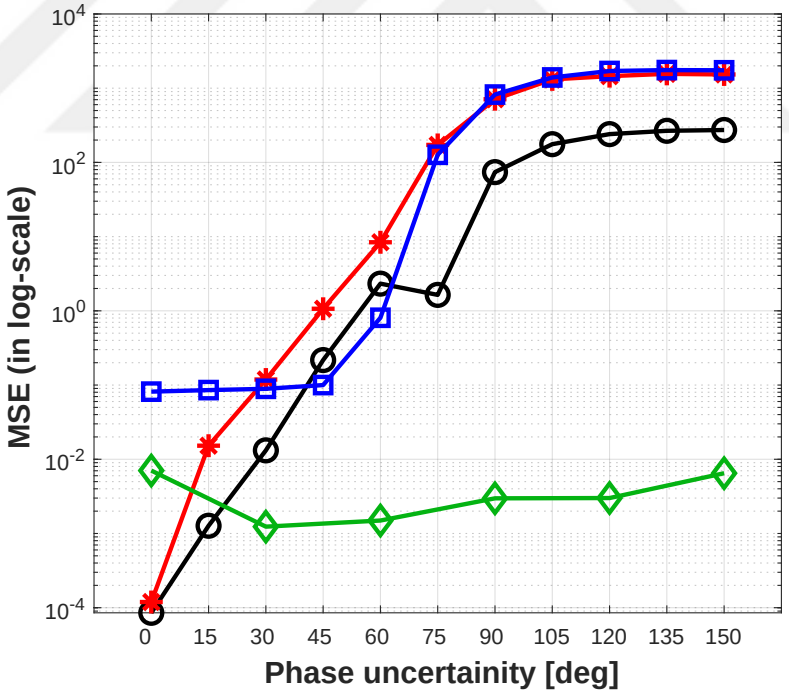


(F) Network # 6 (RCS: 40 db)

FIGURE 4.13: Histogram plots of the 6 different networks trained at 6 different target RCS. Error bars for the train, validation and test set are colored in blue, green and red, respectively. Zero error level is also indicated with vertical red line. Each histogram uses 30 bins.

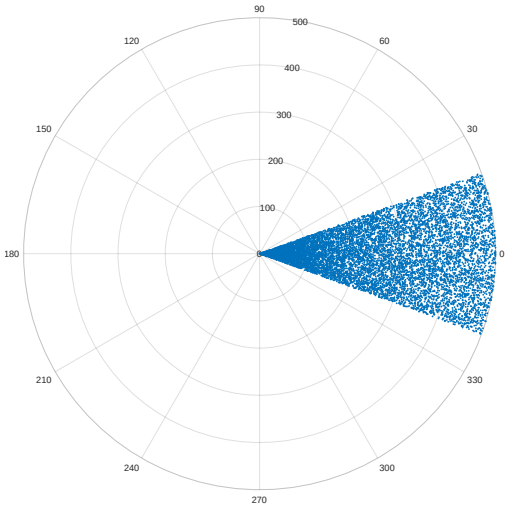


(A) MSE performance of different methods as a function of target RCS. For the each RCS level , responses are obtained from the corresponding neural network trained at that RCS level. Plots are obtained by averaging each method response to the test data (1500 samples)

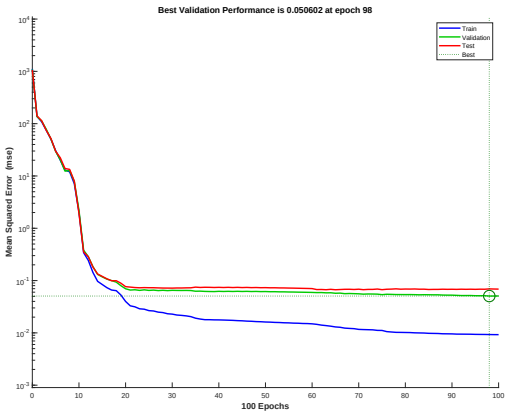


(B) MSE performance of different methods as a function of measurement model uncertainty. State of the art methods are averaged over 1000 realizations of phase angle of the TX and RX elements of the MIMO radar. Both train and test data sets are created using a target RCS of 50 dbsm.

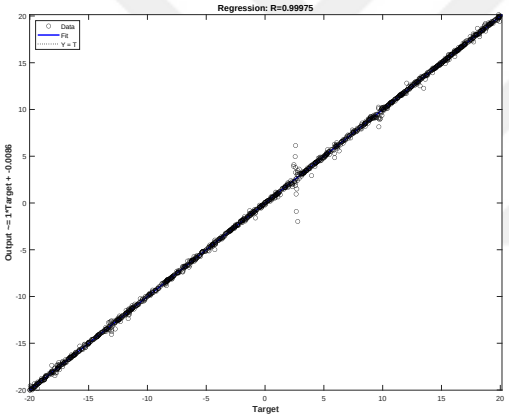
FIGURE 4.14: Performance comparison of the proposed technique with other existing DoA methods



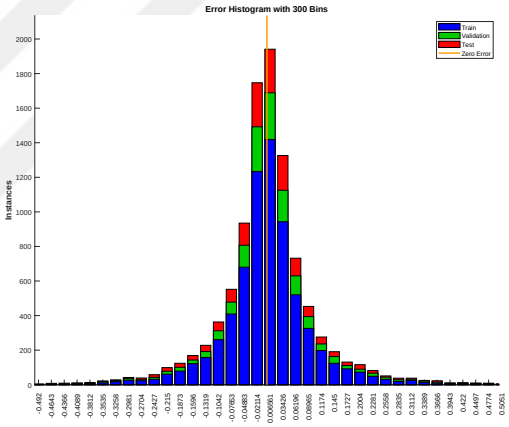
(A) Random distribution of the target positions. Range is uniformly distributed in $[0, 500m]$ and azimuth angles are uniformly distributed in $[-20°, 20°]$



(B) Loss (Mean-square-error) during the training. Training consists of 100 epochs and the best validation performance is achieved at epoch 98.



(C) Regression plot of the model



(D) Error distribution of the model

FIGURE 4.15: Simulation results for the randomly distributed target experiment

4.4.1 Computational Analysis

For applications where computation and memory budget is limited, the complexity of the employed algorithms become quite critical. Therefore, in addition to MSE performance of the proposed method, we have also evaluated the computational complexity of our DoA method in a practical manner. For this purpose, we take one of the test data set and ran all the methods on a 3.4 GHz Quad-Core Intel Core i5 processor and measured the time elapsed during the execution of each method.

The averaged elapsed times are given in Table 4.2. The proposed method was shown to consume only 5 ms more CPU time than the other methods. The neural network we use for DoA estimation of radar targets consists of total 2420($120 \times 20 + 20$) weights and 21 biases. Assuming weight and bias parameters have double precision(8 bytes), our neural network requires approximately 19 KBytes of RAM. The memory consumption of the other DoA methods can be found in [27].

Beamformer	ESPRIT	MUSIC	ANN
699.2 ms	700.33 ms	700 ms	705 ms

TABLE 4.2: The average computation times of DoA methods, calculated with 1500 runs of each method.

4.4.2 Extension to 2D DoA

In many applications, it is also desirable to have a 2D DoA estimation, i.e. both azimuth (θ) and elevation (ϕ) angles of the radar target with respect to the radar. We show how our proposed method can be extended to cover also 2D DoA estimation. It is necessary to distribute the MIMO radar antennas over a plane instead of along a line for 2D DoA estimation. Therefore, we consider a plus shape antenna array with 4 TX antenna and 4 RX antenna placed on the x and y axis. For the MIMO configuration, RX antennas are separated by $\lambda/2$ while TX antennas are separated $3\lambda/2$. This way we would achieve a virtual aperture of 16 antennas along both the x and y directions.

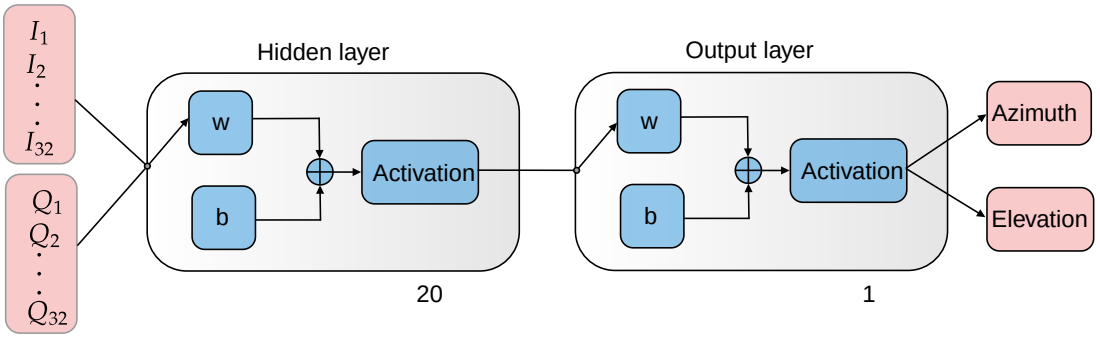
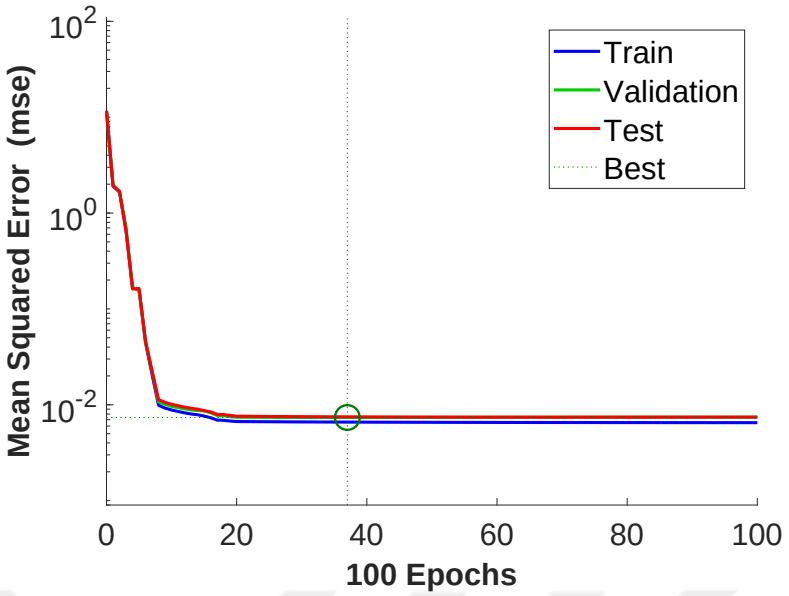
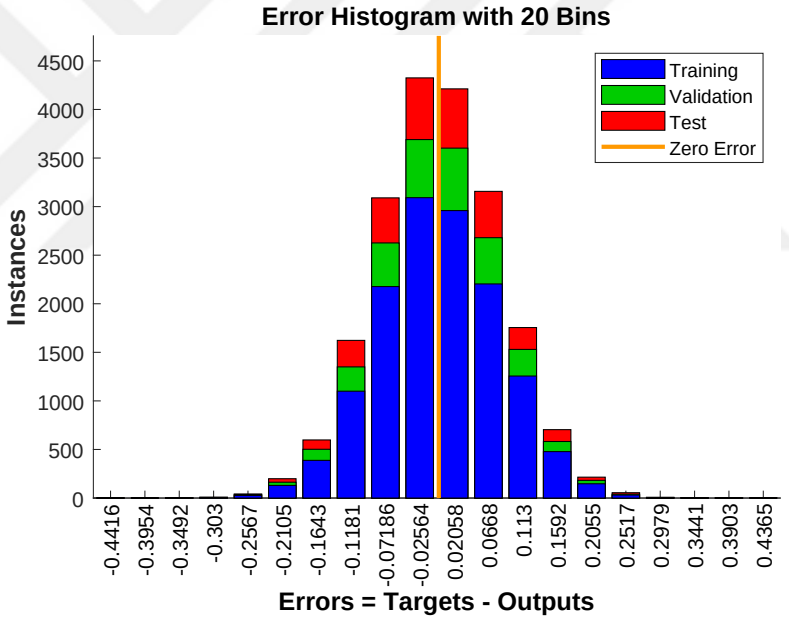


FIGURE 4.16: Neural network architecture used for 2D DoA estimation



(A) Training of 2D DoA network



(B) Error histograms

FIGURE 4.17: Training and test results of the network for 2D DoA estimation

We use the same algorithm as given in Algorithm 2 with only difference being the neural network structure, as shown by Figure 4.16. For this 2D DoA estimation network, the input layer has 32 neurons for the real part of the measurements and 32 neurons for the imaginary part, making it total of 64 neurons in the input layer. The other difference is the output layer, which has two neurons to account for the

azimuth and elevation angles of the target. Over a simulated training data set, we trained the 2D DoA network and test its performance over the test data set. Figure 4.17a shows the MSE error during training, while Figure 4.17b shows the estimation error for θ and ϕ. As it is clear from Figure 4.17, learning is achieved with a significantly small MSE and error histogram plot shows a normal distribution around zero with very low variance. With this, we verify the applicability of our proposed technique also for the 2D DoA estimation problems.

4.5 Conclusions

A neural network-based target angle estimation technique is proposed in this chapter to overcome the practical issues in MIMO radars caused by imperfect array shapes or poorly calibrated RF components. The proposed technique proceeds in two stages with range profile formation being the first stage fed to the second stage as the input for the ANN model. Our ANN model is trained on the simulated data generated by the MIMO radar simulations performed in the physical layer under different SNR conditions and model inaccuracies. The numerical results suggest that the proposed technique performs better than the other existing DoA estimation techniques in low SNR scenarios. More importantly, the proposed technique is shown to remain almost unaffected by the model perturbations/inaccuracies caused by the external factors given that network is trained over the data generated with the same simulation configuration as the test set. It is demonstrated that while the performance of all the model-based DoA estimation techniques dramatically deteriorates in the case of model uncertainties, the proposed technique is proven to be independent of the underlying model since it learns the relation between the measurements and the target angle directly from the training data. Finally, we also show the applicability of our proposed ANN based DoA method to the 2D DoA estimation with a 2D MIMO radar array.

Chapter 5

PnP-ADMM BASED RADAR RANGE PROFILE RECONSTRUCTION USING DEEP PRIORS

Range profile formation plays a pivotal role in various radar applications, including runway radar surveillance [3] and the automatic target recognition of high-resolution radar systems [28], where achieving high-quality range resolution is of great significance. This process involves the estimation of reflectivity for each radar range cell and constitutes an inherently challenging inverse problem. The primary goal is to reconstruct the range profile of a scene using radar return measurements at a specific viewing angle. These radar returns are characterized by bandwidth limitations and are often affected by measurement noise, primarily attributed to receiver electronics.

This chapter of the thesis concentrates on a radar range profile reconstruction technique that improves radar range resolution, particularly in scenarios where

reconstruction suffers from the low bandwidth and high measurement noise conditions. Leveraging the ADMM formulation discussed in the Chapter 3, we integrate deep learning techniques to enhance the reconstruction process.

5.1 Related Work

Reconstructing range profiles from noisy, band-limited radar returns presents an inherently challenging task, characterized as an ill-posed inverse problem. The ultimate goal is to reconstruct the radar reflectivity profile of a scene at a specific looking angle from the radar returns. Radar measurements typically suffer from bandwidth limitations and are susceptible to noise, primarily stemming from receiver electronics. The conventional approach to range profile formation typically involves mathematically inverting the observation model. In Frequency Modulated Continuous Wave (FMCW) radar, this is accomplished by applying a Fourier Transform to the measurements [29], while Pulse-Doppler radar relies on processing measurements through a matched-filter/pulse-compression [30]. Both methodologies hinge on specific measurement models. However, these approaches are notably constrained by available bandwidth and often fail to consider any available prior knowledge about the range profile.

To incorporate prior knowledge into the observation model's inversion, recent advances have seen the adoption of regularized inversion. In this approach, an objective cost function is minimized, typically comprising a data-fidelity term to ensure alignment of the reconstructed range profile with measurements and a regularization term to emphasize certain features in the profile. By regularizing the solution, it becomes feasible to mitigate issues introduced by band-limited and noisy radar measurements. For example, regularized deconvolution is employed in [31] to enhance the range resolution in ground-penetrating radar, and in SAR imaging, point-based and region-based features are improved through regularization, as outlined in [32].

Similar to [32], a non-quadratic optimization method for enhancing features in the reconstruction of high range-resolution (HRR) radar range profiles is introduced in [33]. Here, the challenge of forming HRR profiles from phase history data is approached as an optimization problem. The resolution and feature enhancements are achieved by introducing non-quadratic regularizing constraints into the optimization problem. This approach has been proven effective in preserving high-resolution features like the precise locations and amplitudes of the dominant scatterers within the HRR profile. The proposed method suggest that resolution improvement obtained by the non-quadratic regularization of the constraints through an optimization problem may help improve the Automatic Target Recognition (ATR) systems' detection performance.

On the other hand, sparsity-based regularization is utilized in near-field MIMO radar imaging, as seen in [34], where sparsity is taken as a measure of reconstruction. Nonetheless, conventional regularization methods often struggle to capture complex, hidden features within the data, tending to promote only predefined features based on prior assumptions about the unknown data being reconstructed, whether in its original space or in some transformed space. Moreover, more intricate regularizers do not easily lend themselves to the analytical minimization of the cost function. To circumvent these issues associated with conventional regularization, authors in [35] propose an iterative solution to this inverse problem. This iterative approach carefully formulates the experiments used to construct the discrete linearized inverse problem.

As a proximal method, the ADMM framework [12] has garnered substantial attention in the realm of computational imaging as it is possible to separate the optimization of data fidelity and priors within this framework. ADMM has found diverse applications, ranging from computational tomographic imaging [36] to Synthetic Aperture Radar (SAR) imaging applications [37].

The ADMM framework allows for the optimization of the data fidelity and prior terms to be treated as independent modules with their updates occurring in alternating steps during the ADMM iterations. Consequently, the modularity of the

ADMM framework enables the use of any regularizer in a plug-and-play fashion, as in [38] and [39]. This "plug-and-play" approach empowers the incorporation of various denoisers as a way of regularization within the ADMM framework, all while leaving the data fidelity optimization steps untouched. Various types of denoisers have been applied across a spectrum of applications, including B3MD [40], Total Variation (TV) [41], Recursive Filter (RF) [42], and Non-Local Means (NLM) [43].

PnP ADMM framework has been applied to the field of radar imaging, yielding superior image reconstruction performance. For example, [44] introduces a high-resolution inverse synthetic aperture radar (ISAR) imaging technique using a plug-and-play 2D ADMM-Net framework. Another a plug-and-play ADMM framework is employed for the sparse ISAR imaging in [45]. Additionally, [46] presents a PnP ADMM framework for SAR radar image reconstruction problem, incorporating convolutional neural networks (CNNs) as regularizers and training separate networks under diverse measurement conditions. In practice, the measurement conditions such as the signal-to-noise ratio (SNR) of radar echo signals from targets is often uncertain. Therefore, an optimal solution would perform efficiently across a broad spectrum of SNR values. Drawing inspiration from [46], we approach the radar range profile reconstruction problem using the PnP ADMM framework, our study adopts the PnP ADMM framework for radar range profile reconstruction for frequency-modulated continuous wave (FMCW) radar, addressing the issue of variable SNR conditions in practical scenarios. We demonstrate the potential of using a CNN trained on a dataset with mixed SNR levels, proposing a method that utilizes a single network for this purpose. This approach enhances therefore efficiency and practical applicability, ensuring robust performance across varying SNR conditions.

In this chapter of the dissertation, we focus on the radar range profile formation problem under two main assumptions. The first assumption pertains to complex-valued radar range profiles, where we introduce two distinct approaches: regularization performed over both magnitude and phase of the radar range profile data, as discussed in Section 5.3 and regularization performed over magnitudes only, as discussed in Section 5.4. The second assumption pertains to a real-valued radar

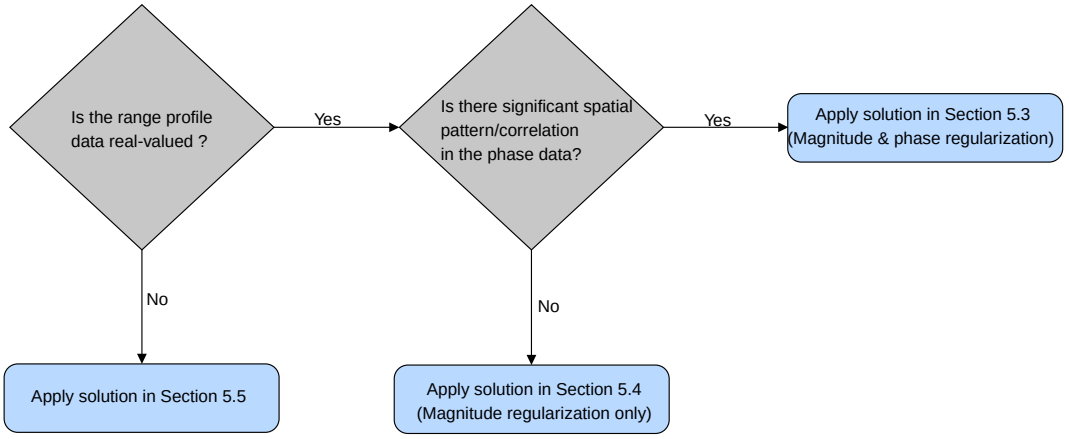


FIGURE 5.1: Decision tree for the proposed algorithms' use cases with their respective sections in the manuscript.

range profile, expounded upon in Section 5.5. Here, we assume that the phase of reflected radar signals undergoes changes solely due to propagation, with no influence from scatterers along the range profile.

It is important to note that phase regularization has found prior application in complex-valued imaging modalities, as in works such as [47–50]. Inspired by the insights from these studies, we integrate phase regularization through a deep learning model within the PnP ADMM framework initially presented in [46]. Our objective is to learn the prior distributions of the range profile data, rather than relying on predefined or fixed priorsn for both magnitude and phase angle of the radar range profiles. To decipher the complex spatial patterns embedded in the radar range profile, encompassing both magnitude and phase, we employ a variety of convolutional neural networks as denoisers. While most radar imaging applications emphasize the magnitude of the unknown field to derive the intensity image corresponding to the scene or profile, the determination of the phase of the unknown field remains critical for model data fidelity. In summary, this chapter outlines distinct solutions tailored to different scenarios, each corresponding to the respective sections within the manuscript, as illustrated in Figure 5.1.

We demonstrate the effectiveness of integrating a denoising Convolutional Neural Network (CNN) into the prior update step within the PnP ADMM framework. At the end of each section, we conduct performance assessment, encompassing both

traditional model-based inversion technique and various regularizers implemented within the PnP ADMM framework. Our findings highlight the superior performance of CNN-based reconstruction, surpassing both the conventional methods and other regularizers in terms of reconstruction error. This study is poised to make contributions to the radar literature in the following ways:

- We study the inverse problem of radar range profile formation from band-limited noisy radar measurements for real-valued and complex valued radar profile by utilizing PnP ADMM framework.
- For the complex-valued profile, we propose two solutions with magnitude regularization only in Section 5.4 and magnitude & phase regularization in Section 5.3, respectively depending on the significance of the spatial phase distribution of the radar range profile being reconstructed.
- We provide an organized formulation of the range profile reconstruction problem for a side-looking radar with both continuous and discrete Fourier-based observation/sensing models for a side-looking radar, which relates the radar range profile to radar measurements.
- In section 5.4, we directly work with the raw radar measurement data and propose a range profile reconstruction approach based on PnP ADMM directly from a given raw radar data. To the best of our knowledge, this study represents the first application of PnP ADMM on raw radar data.
- We have implemented convolutional neural networks and trained them using diverse datasets, aiming to learn the intricate spatial patterns within both the magnitude and phase components of the range profile data
- In practice, the radar measurement noise is often uncertain. Therefore, an ideal solution should be capable of operating effectively across a range of SNR levels. In Section 5.5, we address this practical concern by demonstrating the feasibility of training a convolutional neural network (CNN) on mixed SNR training data. Unlike previous approaches such as the one described

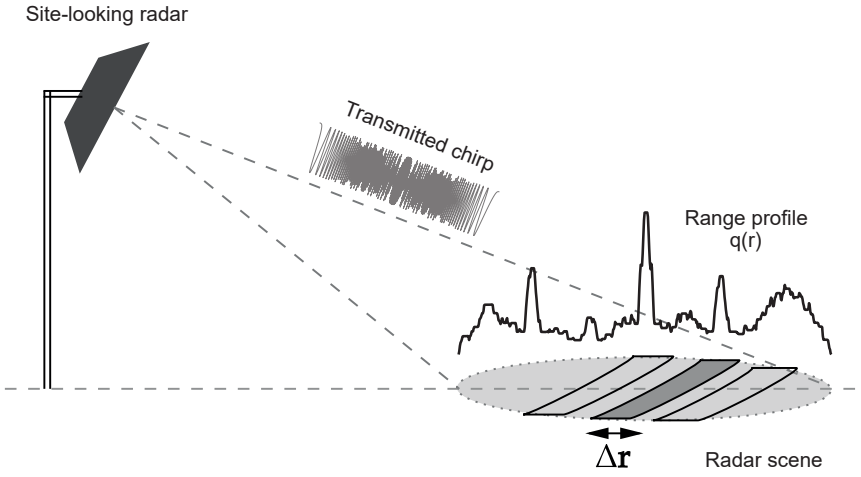


FIGURE 5.2: Simplified representation of a side-looking radar observation model

in [17], which necessitated separate networks for different SNR levels, our method utilizes a single network trained on mixed SNR data. This approach enhances efficiency and practical applicability, ensuring robust performance across varying SNR conditions.

5.2 Observation Model for Side-Looking Radars

We focus on a radar surface imaging application, where a remote area is scanned using a mono-static radar. This scanning operation is assumed to be achieved either through mechanical means by employing a highly directional antenna or electronically by using a phased-array radar. A simplified representation of the studied imaging setup is depicted in Figure 5.2. Here, a side-looking mono-static radar with a beam-steering capability illuminates a radar scene, illustrated by the grey footprint, to obtain a radar image of the surface being scanned. In both scanning modes, an angular area is scanned, where radar video signals are collected for each specific azimuth angle to form the range profile associated with its looking angle. The range profile represents the reflectivity of the radar scene along the look angle direction, as exemplified in Figure 5.2 with Δr indicating a radar range cell along the radial axis. Assuming each scatterer within a given range cell is equidistant from the radar, the collective contribution of these scatterers defines

the reflectivity of that range cell. Therefore, the range profile can be envisioned as the projection of these equidistant scatterers onto a specific distance r, effectively capturing a slice from the radar scene's reflectivity. As the radar beam scans the surface to be imaged, radar collects range profile data for each azimuth angle, then these range profiles are combined to create the radar image of the surface.

Radar video signal received by the radar receiver antenna is sampled by an analog-to-digital converter (ADC) and then these measurement samples are organized into columns of a so called radar data matrix, based on their respective angle tags, sourced from either the pedestal encoder, in the case of mechanical rotation, or the phase-shifters' encoder in the case of electronic rotation. Subsequently, a series of digital range processing operations are performed on each video signal collected from different looking angles by employing the techniques for creating range profiles, which were discussed in Chapter 2.

The data matrix, after undergoing various range processing operations, transforms into the radar scene image in polar format. If desired, this image can be converted into Cartesian format to obtain the radar image of the scene. The angular resolution of such an imaging radar system is determined by the 3-dB beam width of the radar's antenna, with higher antenna gain resulting in improved angular resolution. On the other hand, range resolution is primarily determined by the bandwidth of the transmission signal, as defined by the range resolution formula in Chapter 2. To achieve high-quality images, both range and cross-range resolutions are of paramount importance.

In this section, our focus lies on the observation model of such side-looking imaging radar within a mono-static setup. Our objective is to establish mathematical expressions for the observation/measurement model that establishes the relationship between the radar range profile and the radar measurements.

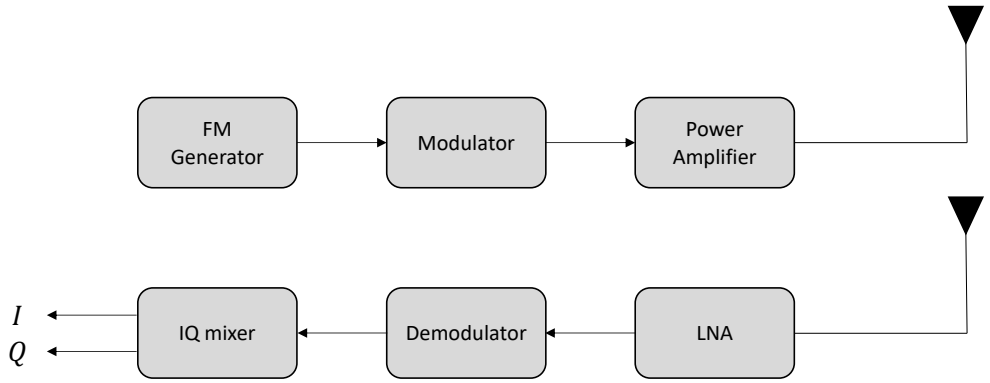


FIGURE 5.3: RF block diagram for bi-static FMCW radar in its simplest form

5.2.1 Signal Processing

A monostatic FMCW radar system incorporates both transmitter and receiver antennas in close proximity. The process begins with the creation of chirp signals in an FM generator, which are then modulated to the carrier frequency and transmitted via the transmit antenna. Echo radio waves, on the receiving end, are initially captured by the receiver antenna. These signals then pass through several components, including the LNA, demodulator, and IQ mixer, ultimately producing the baseband IQ signals. This transmission and reception flow is illustrated in a simplified manner in Figure 5.3. During the FMCW operation Tx signal leaks into the Rx chain leading to what is known as "self-interference". For an optimal radar reception this interference signal needs to be taken care of. For the optimization of Tx power in the context of wireless comminications can be found in [51–53].

A typical FMCW radar transmits a cosine waveform with the phase angle changing with time is described as follows:

$$s(t) = \begin{cases} \cos\left(\Phi(t)\right), & \text{if } 0 \leq t \leq T_c \\ 0, & \text{otherwise} \end{cases} \tag{5.1}$$

The angular frequencies of this signal is given by

$$\omega(t) = \frac{d\Phi(t)}{dt}, \tag{5.2}$$

If the $\omega(t)$ is selected as linearly increasing in time with a slope of m as follows

$$\omega(t) = \omega_0 + mt \tag{5.3}$$

then by integrating (5.3) with respect to t, we get

$$\Phi(t) = \omega_0 t + \frac{1}{2}mt^2 \tag{5.4}$$

where ω_0 is the initial angular frequency and m is the slope of the chirp or chirp rate defined as

$$m = \frac{\Delta\omega}{T_c} \tag{5.5}$$

where $\Delta\omega$ denotes the total angular frequency swept . Substituting (5.4) into (5.1), we obtain widely used up-chirp signal waveform with the following mathematical form

$$s(t) = \begin{cases} \cos\left(\omega_0 t + \frac{1}{2}mt^2\right), & \text{if } 0 \leq t \leq T_c \\ 0, & \text{otherwise} \end{cases} \tag{5.6}$$

As (5.6) indicates, instantaneous frequency of the chirp increases for T_c seconds, then returns to the its initial value, ω_0 after sweeping a band of $\Delta\omega$. This continuous cycle is shown in Figure 5.4.

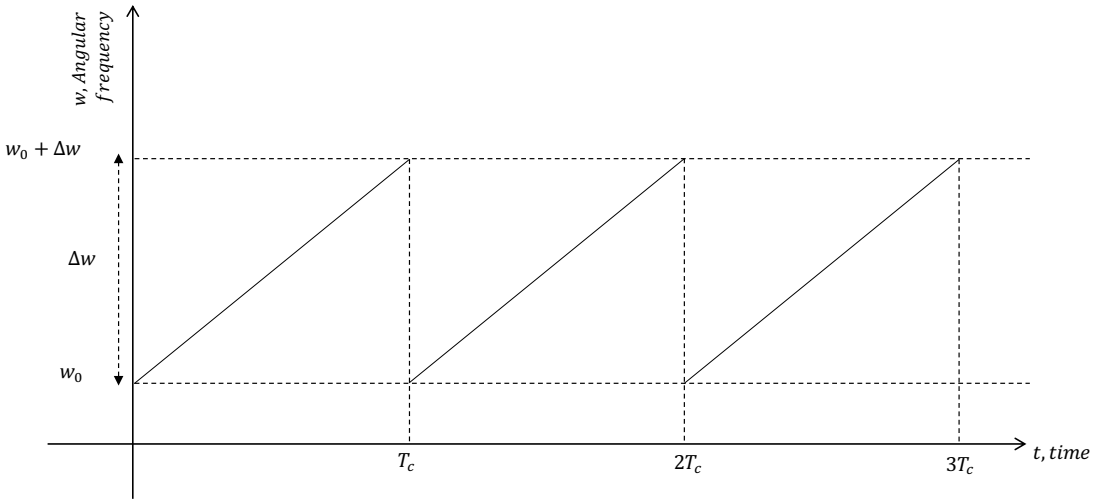


FIGURE 5.4: FMCW waveform

For the sake of mathematical development, let us consider a single chirp with a duration of T_c. The echo signal originating from a differential surface centered around x_0, y_0 at a distance of R_0 will reach the radar after a two-way propagation delay of

$$\tau_0 = \frac{2R_0}{c} \tag{5.7}$$

with c denoting the speed of light. Therefore, the received echo signal from a differential surface, denoted by Δs, is the amplitude-scaled and time-shifted version of the transmitted signal, $s(t)$ as follows:

$$r_{\Delta s}(t) = |f(x_0, y_0)| \cos\left(\omega_0(t-\tau) + \frac{1}{2}m(t-\tau)^2 + \sphericalangle f(x_0, y_0)\right) dxdy \tag{5.8}$$

Here, $f(x_0, y_0)$ represents the complex reflectivity value of this differential surface Δs, where $|f(x_0, y_0)|$ denotes its magnitude and $\sphericalangle f(x_0, y_0)$ denotes the phase angle. This definition allows us to express the reflectivity of a differential surface as:

$$f(x_0, y_0) = |f(x_0, y_0)| e^{j \sphericalangle f(x_0, y_0)} \tag{5.9}$$

If we take equidistant point scatterers on a slice from this scene as shown in Figure 5.2, then $q(r)$ would be the sum of the reflectivity contribution from each of these scatterers as a function of radial distance, r, and can be expressed as the Radon

transform of the reflectivity function $f(x, y)$ as in [54]:

$$q(r) = \int\int_{\{x,y\}\in S} f(x, y)\delta(u - x\cos\theta - y\sin\theta)dxdy \tag{5.10}$$

This is the projection of the reflectivity field onto a single point at a distance of r. Here S represents the total scene illuminated by the radar. The received signal at the receiver is then given by the convolution of the projection of the reflectivity function and the transmitted signal:

$$r(t) = \int_{R_{min}}^{R_{max}} q(r)s\Big(t - \frac{2r}{c}\Big)dr \tag{5.11}$$

where R_{min} and R_{max} denote two ends of the radar scene in the radial direction. By expanding $s(t)$ and substituting $\tau = \frac{2r}{c}$, received signal can be written as follows:

$$r(t) = \int_{R_{min}}^{R_{max}} q(r)\cos\left(\omega_0\Big(t - \frac{2r}{c}\Big) + \frac{1}{2}m\Big(t - \frac{2r}{c}\Big)^2\right)dr \tag{5.12}$$

The received signal defined in (5.12) is then mixed with $\cos(\omega_0 t + \frac{1}{2}mt^2)$ and $\sin(\omega_0 t + \frac{1}{2}mt^2)$ to obtain in-phase and quadrature components, respectively. Using the following trigonometric identities

$$\cos(\alpha)\cos(\beta) = \frac{1}{2}\Big(\cos(\alpha + \beta) + \cos(\alpha - \beta)\Big) \tag{5.13}$$

$$\cos(\alpha)\sin(\beta) = \frac{1}{2}\Big(\sin(\alpha + \beta) - \sin(\alpha - \beta)\Big) \tag{5.14}$$

we would obtain

$$\begin{aligned} I(t) = \int_{R_{min}}^{R_{max}} q_{\mathbf{u}}(r)\Bigg\{&\frac{1}{2}\cos\left(\omega_0 t - \omega_0\left(\frac{2r}{c}\right) + \frac{1}{2}mt^2 + \frac{1}{2}m\left(\frac{2r}{c}\right)^2\right. \\ &\left. - mt\left(\frac{2r}{c}\right) + \omega_0 t + \frac{1}{2}mt^2\right)\frac{1}{2}\cos\left(\omega_0 t - \omega_0\left(\frac{2r}{c}\right)\right. \\ &\left.\left. + \frac{1}{2}mt^2 + \frac{1}{2}m\left(\frac{2r}{c}\right)^2 - mt\left(\frac{2r}{c}\right) - \omega_0 t - \frac{1}{2}mt^2\right)\right\}dr \end{aligned} \tag{5.15}$$

After low-pass filtering the signal in (5.15), it simplifies to

$$I(t) = \frac{1}{2}\int_{R_{min}}^{R_{max}} q(r)\left\{ \cos\left(m\left(\frac{2r}{c}\right)t + \omega_0\left(\frac{2r}{c}\right) - \frac{1}{2}m\left(\frac{2r}{c}\right)^2\right)\right\}dr \tag{5.16}$$

By the same argument, quadrature component of $r(t)$ can be written as:

$$Q(t) = -\frac{1}{2}\int_{R_{min}}^{R_{max}} q(r)\left\{ \sin\left(m\left(\frac{2r}{c}\right)t + \omega_0\left(\frac{2r}{c}\right) - \frac{1}{2}m\left(\frac{2r}{c}\right)^2\right)\right\}dr \tag{5.17}$$

Here, $I(t)$ and $Q(t)$ represent the demodulated in-phase and quadrature component of the received radar signal $r(t)$. Letting $\overline{r}(t)$ denote the complex baseband equivalent of $r(t)$

$$\overline{r}(t) = I(t) + jQ(t) \tag{5.18}$$

Using Euler's identity, the complex signal in (5.18) can be expanded as follows:

$$\overline{r}(t) = \frac{1}{2}\int_{R_{min}}^{R_{max}} q(r)\exp\left\{ -j\left[m\left(\frac{2r}{c}\right)t + \omega_0\left(\frac{2r}{c}\right) - \frac{1}{2}m\left(\frac{2r}{c}\right)^2\right]\right\}dr \tag{5.19}$$

Here $\frac{1}{2}m\left(\frac{2r}{c}\right)^2$ can be ignored since since $4mr^2 \ll c^2$. We can also eliminate the coefficient of $\frac{1}{2}$ since it does not affect the development of our argument. With this, $\overline{r}(t)$ becomes

$$\overline{r}(t) = \int_{R_{min}}^{R_{max}} q(r)\exp\left\{ -j\left[m\left(\frac{2r}{c}\right)t + \omega_0\left(\frac{2r}{c}\right)\right]\right\}dr \tag{5.20}$$

Letting $\Omega(t) = \frac{2}{c}(\omega_0 + mt)$, then $r(t)$ boils down to the following form

$$\overline{r}(t) = \int_{R_{min}}^{R_{max}} q(r)\exp\left\{-j\Omega(t)r\right\}dr \tag{5.21}$$

Note that (5.21) is the band-limited spatial Fourier Transform of the projections, $q(r)$. Here $\Omega(t)$ represent the spatial frequency variable. Since both of the observation time (i.e., chirp time, T_c) and chirp slope (i.e. $s(t)$ is band-limited) are

finite, $\Omega(t)$ is limited to a finite band. It is also worthwhile to note that $\Omega(t)$ is also offset with an amount of ω_0 from the origin of Fourier domain. Given the radar measurements, one can obtain the projections, $q(r)$ by taking inverse spatial Fourier transform of $r(t)$ with respect to $\Omega(t)$.

(5.21) can be discretized assuming that entire range is uniformly sampled with a sampling interval of Δr into N range bins such that

$$q(r) = \sum_{k=1}^{N} q[k]\delta\Big(r - (k-1)\Delta r\Big) \tag{5.22}$$

where $q[k]$ denoting sampled value of projection at i^{th} range cell. Substituting (5.22) into (5.21), we have

$$\overline{r}(t) = \int_{R_{min}}^{R_{max}} \Big(\sum_{k=1}^{N} q[k]\delta\Big(r - (k-1)\Delta r\Big)\Big) \exp\{-j\Omega(t)r\}dr \tag{5.23}$$

which further simplifies to

$$\overline{r}(t) = \sum_{k=k_0}^{k_0+N-1} q[k] \exp\Big\{ - j\Omega^{'}(t)k \Big\} \tag{5.24}$$

with $\Omega^{'}(t) = \Omega(t)\Delta r$. Equation (5.24) implies that each scatterer will generate a sinusoidal wave, with an oscillation frequency linearly related to the scatterer's range. Here, $\hat{\Omega}$ represents the temporal frequency variable, often referred to as the "beat frequency". By performing the Fourier transform of $\overline{r}(t)$, one can derive spectral components that provide information about the range, given by the following relationship:

$$r = \frac{c\hat{\Omega}}{2m}$$

Note that received signal in (5.24) is still in continuous-time. If we sample this signal with a sampling period of $T_s = 1/f_s$, then we get a vector of discrete

measurement samples, $r[n]$:

$$r[n] = r(nTs) = \sum_{n=0}^{f_s \times T_c} \delta(t - nT_s) r(t) \tag{5.25}$$

5.2.2 Radar Measurement Model

As demonstrated in the preceding section, the relationship between the discrete samples of the baseband received signal and the radar range profile can be expressed through the Discrete Fourier Transform (DFT). Represented in matrix form, this relationship is defined as follows:

$$\mathbf{s} = \mathbf{T}\mathbf{q} \tag{5.26}$$

with $\mathbf{T} \in \mathbb{C}^{M \times N}$ denoting DFT matrix and $\mathbf{r} \in \mathbb{C}^{M \times 1}$ is radar measurements and $\mathbf{q} \in \mathbb{C}^{N \times 1}$ is the radar range profile. Assuming a complex white noise at the receiver we obtain our final measurement model as follows:

$$\mathbf{r} = \mathbf{T}\mathbf{q} + \mathbf{w} \tag{5.27}$$

where the term $\mathbf{w} \in \mathbb{C}^{M \times 1}$ accounts for measurement noise.

In the radar range profile reconstruction problem given by (5.27) illustrates a linear system, where $\mathbf{q}$ represents the input, $\mathbf{r}$ is the observed output, and $\mathbf{T}$ is the system transfer function that characterizes the mapping between $\mathbf{r}$ and $\mathbf{q}$. The linear system is defined by the dimensions M (the number of radar measurements) and N (the number of radar range cells to estimate). Subsequent sections evaluate this problem in various forms based on the nature of $\mathbf{q}$. In Section 5.3, $\mathbf{q}$ is considered complex-valued with significant spatial phase correlations that are taken into account in regularization. Section 5.4 assumes a complex-valued $\mathbf{q}$ vector with purely randomly distributed phase angles and thus avoids regularization over phase. In contrast, Section 5.5 assumes a real-valued $\mathbf{q}$ vector.

5.3 Complex-valued Range Profile Formation with Magnitude and Phase Regularization

In this section of the chapter, radar range profiles $\mathbf{q}$ are assumed to be complex-valued with significant spatial phase correlations. Under this assumption, we formulate the radar range profile reconstruction problem within the ADMM framework, where we perform regularization on both the magnitude and phase of the range profiles.

5.3.1 Problem Formulation

We begin our formulation by substituting the least-squares data fidelity term, as defined in Eq. (3.30), into the problem given in Eq. (5.27). This yields a typical regularized inversion problem formulated as follows:

$$\hat{\mathbf{q}} = \underset{\mathbf{q}}{\operatorname{argmin}} \left\{ \|\mathbf{r} - \mathbf{T}\mathbf{q}\|_2^2 + \lambda \mathcal{R}(\mathbf{q}) \right\} \tag{5.28}$$

Complex-valued range profile vector, $\mathbf{q}$ can be written in the following phasor form: $\mathbf{q} = |\mathbf{q}|\mathrm{e}^{j\measuredangle(\mathbf{q})}$, where $\measuredangle(\mathbf{q})$ denotes the phase angle of $\mathbf{q}$ in radians. We can also write $\mathbf{q} = \mathbf{\Psi}\mathbf{q}_m$, where $\mathbf{q}_m$ is the magnitude of $\mathbf{q}$ and $\mathbf{\Psi} \in \mathbb{C}^{N\times N}$ is a diagonal square matrix containing phase angles of $\mathbf{q}$ in the complex-phasor representation, i.e. $\mathbf{\Psi}_{ii} = e^{\measuredangle(\mathbf{q}_i)}$, $\forall i \in \{1, 2, ..., N\}$. We also define phase vector $\mathbf{q}_p \in \mathbb{C}^{N\times 1}$ which contains the diagonal elements of $\mathbf{\Psi}$. With this new definition, range profile vector can also be written as the Hadamard product of magnitude vector $\mathbf{q}_m$ and phase vector $\mathbf{q}_p$. That is;

$$\mathbf{q} = \mathbf{q}_m \otimes \mathbf{q}_p \tag{5.29}$$

where $\otimes$ operator denotes the element-wise multiplication. It is worthwhile to note that even though we are not interested in computing the phase of projections in our application, it is mandatory to come up with a relatively good estimate of it in an effort to align $\mathbf{r}$ and $\mathbf{T}\mathbf{q}$ with the minimum data fidelity error. Note that regularization applied in (5.28) due to the ill-posed nature of the problem is performed over the complete complex-valued projections vector, meaning that

both magnitude and phase are regularized together. Replacing $\mathbf{q}$ with $\mathbf{\Psi q}_m$ and splitting regularization function $\mathcal{R}$ into one for magnitude, $\mathcal{R}_m$ and one for phase, $\mathcal{R}_p$ (5.28) becomes a minimization problem over $\mathbf{q}_m$ and $\mathbf{q}_p$ as follows:

$$\{\hat{\mathbf{q}}_m, \hat{\mathbf{q}}_p\} = \underset{\mathbf{q}_m, \mathbf{q}_p}{\operatorname{argmin}} \left\{ \|\mathbf{r} - \mathbf{T\Psi q}_m\|_2^2 + \lambda_m \mathcal{R}_m(\mathbf{q}_m) + \lambda_p \mathcal{R}_p(\mathbf{q}_p) \right\} \tag{5.30}$$

Note that although we are only interested in the magnitudes of the range profile data, it is critical to have a good estimate of the phase of the complex range profile data for a good data alignment. Let us introduce two auxiliary variables $\mathbf{h_m} \in \mathbb{R}^{N\times 1}$ and $\mathbf{h_p} \in \mathbb{C}^{N\times 1}$ for magnitude and phase of the projections, respectively:

$$\begin{aligned} \left\{\hat{\mathbf{q}}_m, \hat{\mathbf{q}}_p, \hat{\mathbf{h}}_m, \hat{\mathbf{h}}_p\right\} = \quad & \underset{\mathbf{q}_m, \mathbf{q}_p, \mathbf{h}_m, \mathbf{h}_p}{\operatorname{argmin}} \left\{ \|\mathbf{r} - \mathbf{T\Psi q}_m\|_2^2 + \lambda_m \mathcal{R}_m(\mathbf{q}_m) + \lambda_p \mathcal{R}_p(\mathbf{q}_p) \right\} \\ \text{s.t.} \quad & \mathbf{q}_m - \mathbf{h}_m = 0 \\ & \mathbf{q}_p - \mathbf{h}_p = 0 \end{aligned} \tag{5.31}$$

The objective function in augmented Lagrangian form (5.31) is then written as:

Objective function in augmented Lagrangian form

$$\begin{aligned} \mathcal{L}\left(\mathbf{q}_m, \mathbf{q}_p, \mathbf{h}_m, \mathbf{h}_p, \mathbf{u}_m, \mathbf{u}_p\right) = \|\mathbf{r} - \mathbf{T\Psi q}_m\|_2^2 + \lambda_m \mathcal{R}_m(\mathbf{h}_m) + \lambda_p \mathcal{R}_p(\mathbf{h}_p) \\ + \frac{\rho_m}{2} \|\mathbf{q}_m - \mathbf{h}_m + \mathbf{u}_m\|_2^2 + \frac{\rho_m}{2} \|\mathbf{u}_m\|_2^2 + \frac{\rho_p}{2} \|\mathbf{q}_p - \mathbf{h}_p + \mathbf{u}_p\|_2^2 + \frac{\rho_p}{2} \|\mathbf{u}_p\|_2^2 \end{aligned} \tag{5.32}$$

5.3.2 Investigation on Phase Regularization

The motivation for incorporating phase optimization into our ADMM formulation for radar range profile reconstruction is based on the belief that certain patterns can be regularized or learned, contributing to improved reconstruction performance, similar to the magnitude prior step. In this section, our investigation aims to determine whether phase angles of range cells in close proximity exhibit any potential correlation that can be leveraged for beneficial purposes. To better illustrate our motivation, we use an example radar scene from 3D Gotcha SAR image

dataset [55]. The magnitude and phase maps of this scene are shown in Figure 5.5. The image on the left depicts the SAR magnitude, while the one on the right shows the phase map of the same scene.

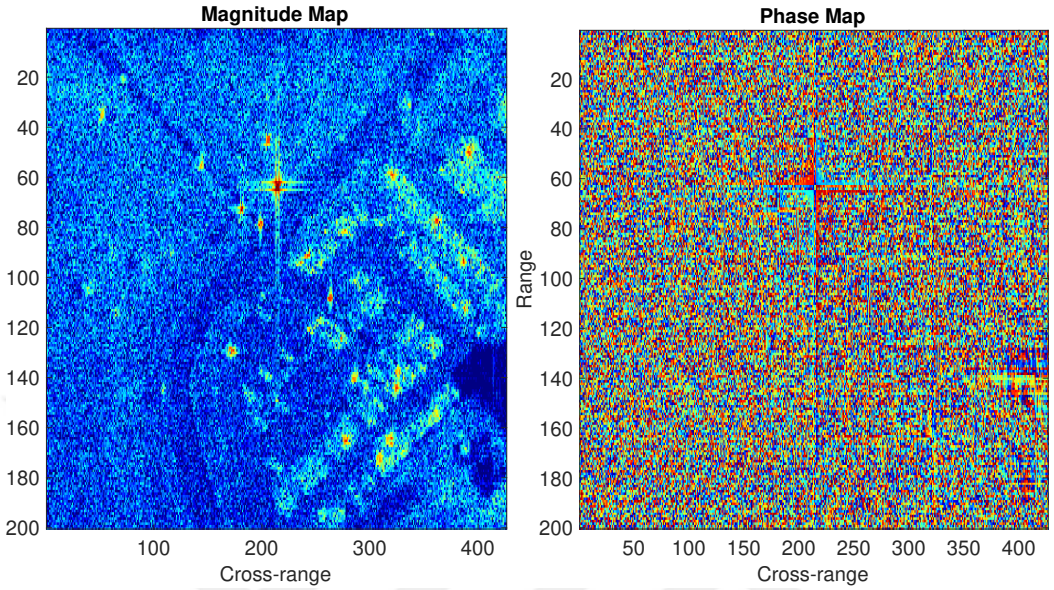
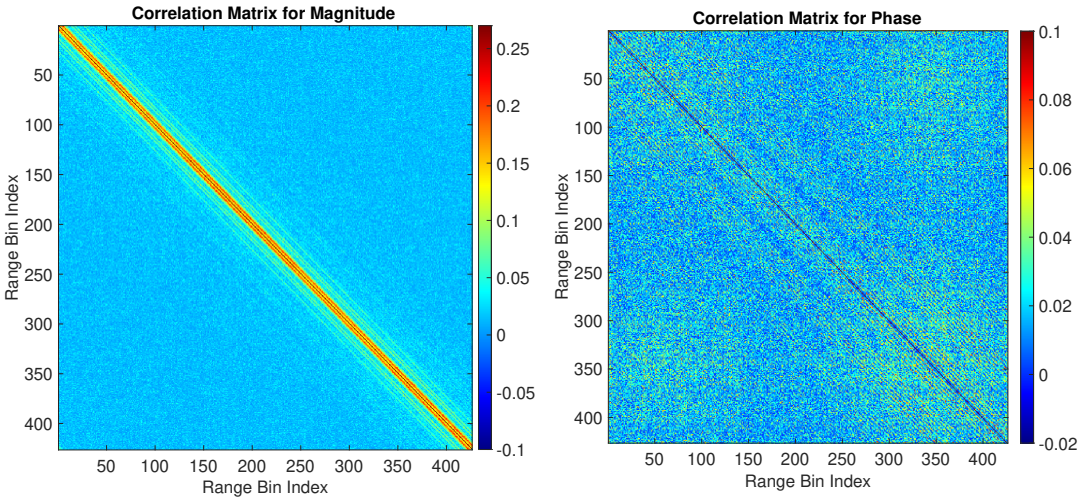
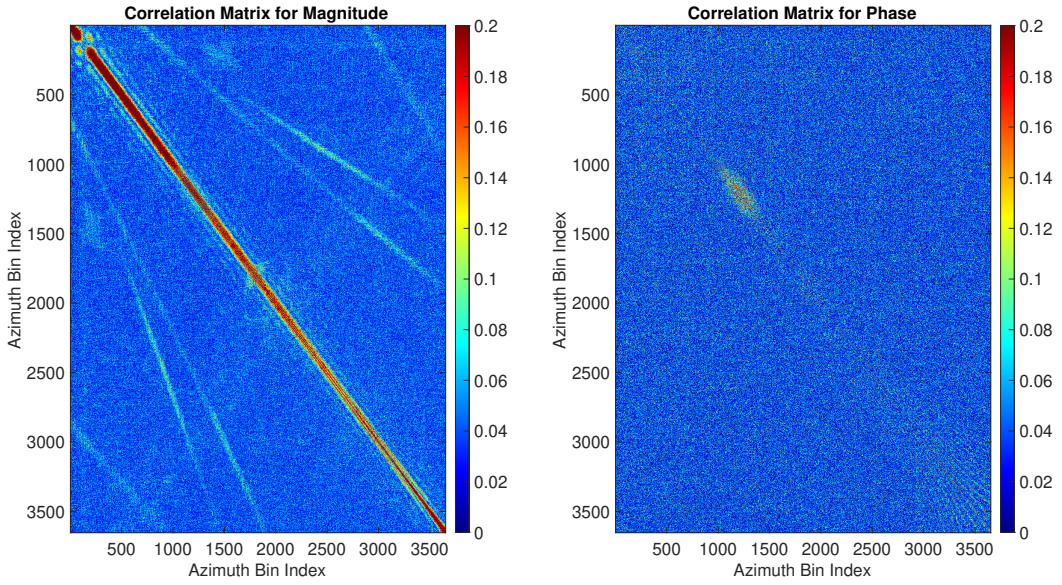


FIGURE 5.5: Magnitude & phase map of a Gotcha SAR image of a scene

As evident from the phase map of the scene depicted in Figure 5.5, phase angles do not exhibit a typical noise distribution; instead, they reveal discernible patterns, particularly around the dominant scatterers in the image. To delve deeper into this observation, we utilize a correlation matrix representation to assess the spatial correlation between the magnitude and phase of range cells, as illustrated in Figures 5.6a and 5.6b. As expected, a prominent correlation is observed between the magnitudes of range and azimuth cells in close proximity. Although the phase angle correlation is not as pronounced as that in the magnitude correlation map, some noticeable correlation persists in the phase angle of range cells in close proximity.



(A) Correlation Matrix for Range Bins



(B) Correlation Matrix for Azimuth Bins

FIGURE 5.6: Correlation matrices for the range and azimuth bins obtained from a SAR radar image

While the observed off-diagonal cross-correlation values in this SAR image example may not be particularly strong, we aim to exploit the identified phase correlation in our radar range profile formation solution, operating under the belief that there might be a spatial phase pattern in a given radar range profile. Furthermore, our proposed approach for the radar range reconstruction problem can be applied to any signal or image reconstruction scenario where the signal or image is complex-valued and exhibits significant phase patterns.

5.3.3 PnP-ADMM Based Range Profile Formation

Let us introduce another diagonal matrix, $\mathbf{Q} \in \mathbb{C}^{N \times N}$ whose diagonal elements are equal to the values of $\mathbf{q}_m$, i.e., $\mathbf{Q}_{ii} = \mathbf{q}_{m_i}$, $\forall i \in \{1, 2, ..., N\}$ and define the following auxiliary variables:

$$\tilde{\mathbf{q}}_m = \mathbf{h}_m - \mathbf{u}_m, \quad \tilde{\mathbf{h}}_m = \mathbf{q}_m + \mathbf{u}_m, \quad \tilde{\mathbf{q}}_p = \mathbf{h}_p - \mathbf{u}_p, \quad \tilde{\mathbf{h}}_p = \mathbf{q}_p + \mathbf{u}_p \tag{5.33}$$

If we impose the constraint that elements of the phase vector $\mathbf{q}_p$ all have unit magnitude, i.e.,

$$|\mathbf{q}_{p_i}| = 1, \forall i \in \{1, 2, ..., N\} \tag{5.34}$$

with this constraint, we can construct the sub-minimization problems of our ADMM formulation as follows:

ADMM subminimization steps

ADMM framework decouples model and prior optimization steps:

Model Optimization

$$\hat{\mathbf{q}}_p = \underset{\mathbf{q}_p}{\operatorname{argmin}} \left\{ \|\mathbf{r} - \mathbf{T}\boldsymbol{Q}\mathbf{q}_p\|_2^2 + \frac{\rho_p}{2} \|\mathbf{q}_p - \tilde{\mathbf{q}}_p\|_2^2 + \lambda \sum_{i=1}^{N} \left(|\mathbf{q}_{p_i}| - 1 \right)^2 \right\} \tag{5.35}$$

$$\hat{\mathbf{q}}_m = \underset{\mathbf{q}_m}{\operatorname{argmin}} \left\{ \|\mathbf{r} - \mathbf{T}\boldsymbol{\Psi}\mathbf{q}_m\|_2^2 + \frac{\rho_m}{2} \|\mathbf{q}_m - \tilde{\mathbf{q}}_m\|_2^2 \right\} \tag{5.36}$$

Prior optimization

$$\hat{\mathbf{h}}_p = \underset{\mathbf{h}_p}{\operatorname{argmin}} \left\{ \lambda_p \mathcal{R}_p(\mathbf{h}_p) + \frac{\rho_p}{2} \left\| \tilde{\mathbf{h}}_p - \mathbf{h}_p \right\|_2^2 \right\} \tag{5.37}$$

$$\hat{\mathbf{h}}_m = \underset{\mathbf{h}_m}{\operatorname{argmin}} \left\{ \lambda_m \mathcal{R}_m(\mathbf{h}_m) + \frac{\rho_m}{2} \left\| \tilde{\mathbf{h}}_m - \mathbf{h}_m \right\|_2^2 \right\} \tag{5.38}$$

Auxilary variable update

$$\hat{\mathbf{u}}_m = \mathbf{u}_m + \mathbf{q}_m - \mathbf{h}_m \tag{5.39}$$

$$\hat{\mathbf{u}}_p = \mathbf{u}_p + \mathbf{q}_p - \mathbf{h}_p \tag{5.40}$$

Equations (5.35) and (5.36) represent optimizations for the phase and magnitude of the range profile, respectively. Equations (5.37) and (5.38) denote the denoising

operation for the phase and magnitude of the range profile. Equations (5.39) and (5.40) correspond to the auxiliary updates in ADMM. We discuss how we address problems (5.35) through (5.38) in the subsequent sections.

5.3.3.1 Optimization of Data Fidelity for Magnitudes

We begin by deriving a solution for the magnitudes alignment of the data to construct ADMM framework, as expressed by

$$\hat{\mathbf{q}}_m = \underset{\mathbf{q}_m}{\operatorname{argmin}} \left\{ \|\mathbf{r} - \mathbf{T}\boldsymbol{\Psi}\mathbf{q}_m\|_2^2 + \frac{\rho_1}{2} \|\mathbf{q}_m - \tilde{\mathbf{q}}_m\|_2^2 \right\} \tag{5.41}$$

To minimize the objective function, we compute its first-order derivative with respect to $\mathbf{q}_m$, resulting in the following gradient vector $\nabla\mathbf{q}_m$:

$$\nabla\mathbf{q}_m = -2\boldsymbol{\Psi}^H\mathbf{T}^H\mathbf{r} + 2\boldsymbol{\Psi}^H\mathbf{T}^H\mathbf{T}\boldsymbol{\Psi}\mathbf{q}_m + \rho_m\left(\mathbf{I}\mathbf{q}_m - \tilde{\mathbf{q}}_m\right) \tag{5.42}$$

Arranging (5.42), we get

$$\nabla\mathbf{q}_m = \left(2\boldsymbol{\Psi}^H\mathbf{T}^H\mathbf{T}\boldsymbol{\Psi} + \rho_m\mathbf{I}\right)\mathbf{q}_m - \left(2\boldsymbol{\Psi}^H\mathbf{T}^H\mathbf{r} + \rho_m\tilde{\mathbf{q}}_m\right) \tag{5.43}$$

By equating $\nabla\mathbf{q}_m$ to zero, we get the first-order optimality condition as follows:

$$\underbrace{\left(2\boldsymbol{\Psi}^H\mathbf{T}^H\mathbf{T}\boldsymbol{\Psi} + \rho_m\mathbf{I}\right)}_{\mathbf{A}}\mathbf{q}_m = \underbrace{\left(2\boldsymbol{\Psi}^H\mathbf{T}^H\mathbf{r} + \rho_m\overline{\mathbf{q}}_m\right)}_{\mathbf{b}} \tag{5.44}$$

The linear system described by Equation (5.44), $\mathbf{A}\mathbf{q} = \mathbf{b}$, can be solved using any linear system solver. We opt for the conjugate-gradient algorithm in our numerical analyses. The parameter ρ balances the trade-off between data-fidelity error and priors of $\mathbf{q}$. It is important to note that when $\rho = 0$, the problem simplifies to a least-squares regression, and the solution is given by the Moore-Penrose pseudoinverse:

$$\hat{\mathbf{q}} = \left(\mathbf{T}^H\mathbf{T}\right)^{-1}\mathbf{T}^H\mathbf{r}$$

5.3.3.2 Optimization of Data Fidelity for Phases

The phase alignment is achieved by solving the following problem

$$\hat{\mathbf{q}}_p = \underset{\mathbf{q}_p}{\operatorname{argmin}} \left\{ \|\mathbf{r} - \mathbf{T}\boldsymbol{Q}\mathbf{q}_p\|_2^2 + \frac{\rho_p}{2} \|\mathbf{q}_p - \tilde{\mathbf{q}}_p\|_2^2 + \lambda_\theta \sum_{i=1}^{N} \left(|\mathbf{q}_{p_i}| - 1\right)^2 \right\} \tag{5.45}$$

As for magnitude optimization, we again take the first-order derivative of the objective function to obtain its gradient vector. The gradient vector for the objective function is given by

$$\nabla \mathbf{q}_p = \left(2\mathbf{Q}^H\mathbf{T}^H\mathbf{T}\mathbf{Q} + (\rho_p + 2\lambda_\theta)\,\mathbf{I}\right)\mathbf{q}_p - \left(2\mathbf{Q}^H\mathbf{T}^H\mathbf{r} + \rho_p\tilde{\mathbf{q}}_p + 2\lambda_\theta e^{j\measuredangle(\mathbf{q}_p)}\right) \tag{5.46}$$

where we have used:

$$\frac{\partial\left(\lambda\sum_{i=1}^{N}\left(|\mathbf{q}_{p_i}| - 1\right)^2\right)}{\partial \mathbf{q}_{p_i}} = \lambda_\theta\left(2\mathbf{q}_{p_i} - \frac{2\mathbf{q}_{p_i}}{|\mathbf{q}_{p_i}|}\right) = \lambda_\theta\left(2\mathbf{q}_{p_i} - 2e^{j\measuredangle(\mathbf{q}_{p_i})}\right) \tag{5.47}$$

Setting $\nabla\mathbf{q}_p = 0$, we obtain the first-order optimality conditions for phase alignment:

$$\underbrace{\left(2\mathbf{Q}^H\mathbf{T}^H\mathbf{T}\mathbf{Q} + (\rho_p + 2\lambda_\theta)\,\mathbf{I}\right)}_{\mathbf{C}}\mathbf{q}_p = \underbrace{\left(2\mathbf{Q}^H\mathbf{T}^H\mathbf{r} + \rho_p\tilde{\mathbf{q}}_p + 2\lambda_\theta e^{j\measuredangle(\mathbf{q}_p)}\right)}_{\mathbf{f}(\mathbf{q}_p)} \tag{5.48}$$

The solution to $\mathbf{C}\mathbf{q}_p = \mathbf{f}(\mathbf{q}_p)$ corresponds to the local minimizer of $\mathcal{L}_p(\mathbf{q}_p)$. This can be found using gradient-descent algorithms or fixed-point algorithms.

5.3.3.3 Prior Updates Using Convolutional Neural Networks

As discussed in the previous chapter, the solution to the prior optimization problems in (5.38) and (5.37) can be approximated by any denoiser. In [38], the authors propose the use of any off-the-shelf denoising algorithm for this problem in what they term the Plug-and-Play ADMM framework. Following a similar approach, we employ a convolutional neural network (CNN) as in [46] to address the subproblems (5.37) and (5.37). This network takes patches from one-dimensional

noisy range profile magnitude data as input and produces the cleaned version of it at the output. A simplified architecture of the implemented network is illustrated in Figure 5.7, depicting all the biases and weights. For a more detailed layer-by-layer description of the network, refer to Figure 5.8. The denoising network used for phase priors is quite similar to the one shown in Figure 5.7, with the distinction that it takes two input vectors: the real and imaginary parts of the normalized complex range profiles.

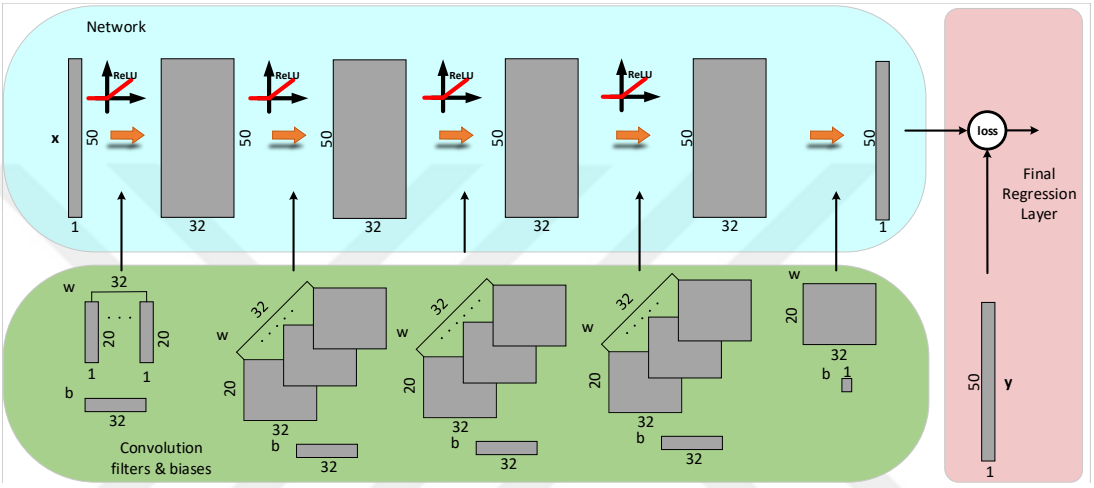
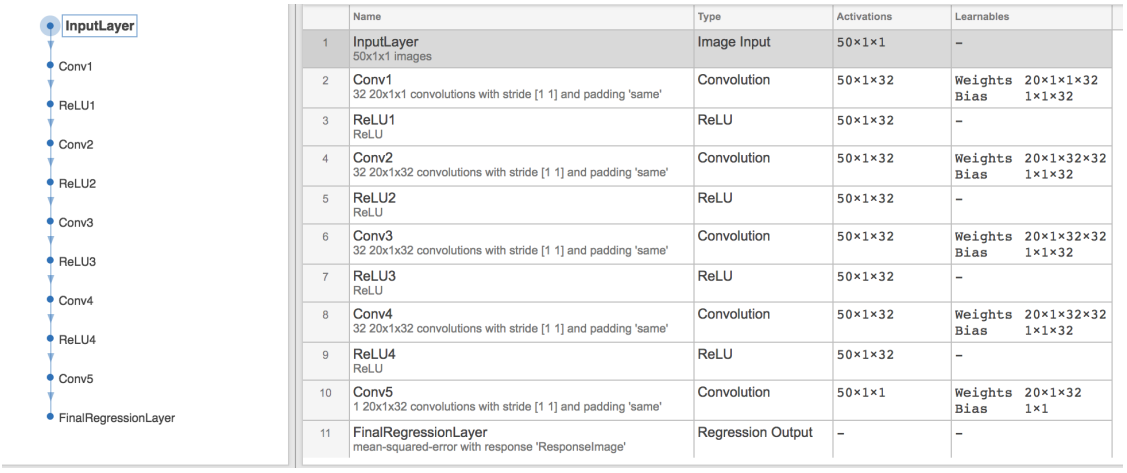


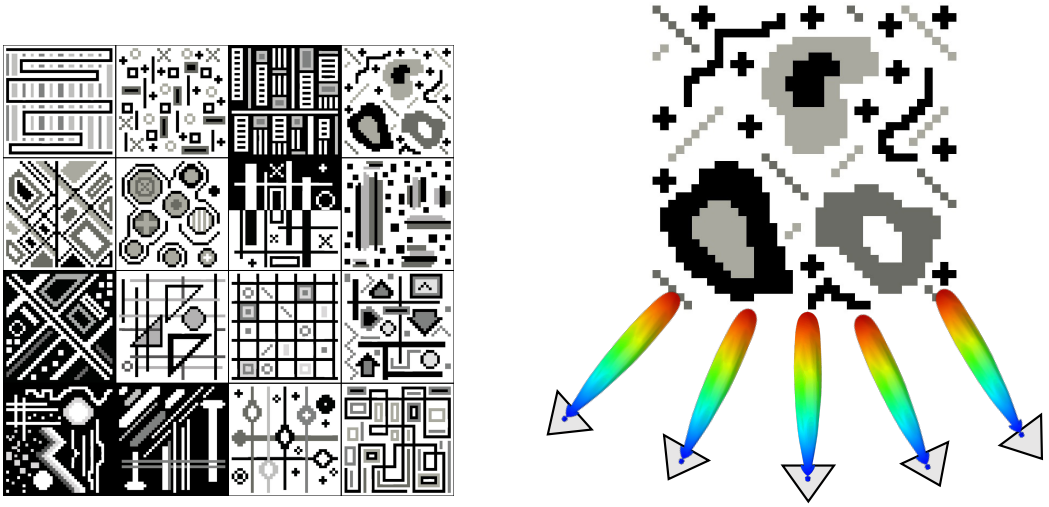
FIGURE 5.7: Network architecture



	Name	Type	Activations	Learnables
1	InputLayer 50x1x1 images	Image Input	50×1×1	–
2	Conv1 32 20x1x1 convolutions with stride [1 1] and padding 'same'	Convolution	50×1×32	Weights 20×1×1×32 Bias 1×1×32
3	ReLU1 ReLU	ReLU	50×1×32	–
4	Conv2 32 20x1x32 convolutions with stride [1 1] and padding 'same'	Convolution	50×1×32	Weights 20×1×32×32 Bias 1×1×32
5	ReLU2 ReLU	ReLU	50×1×32	–
6	Conv3 32 20x1x32 convolutions with stride [1 1] and padding 'same'	Convolution	50×1×32	Weights 20×1×32×32 Bias 1×1×32
7	ReLU3 ReLU	ReLU	50×1×32	–
8	Conv4 32 20x1x32 convolutions with stride [1 1] and padding 'same'	Convolution	50×1×32	Weights 20×1×32×32 Bias 1×1×32
9	ReLU4 ReLU	ReLU	50×1×32	–
10	Conv5 1 20x1x32 convolutions with stride [1 1] and padding 'same'	Convolution	50×1×1	Weights 20×1×32 Bias 1×1
11	FinalRegressionLayer mean-squared-error with response 'ResponseImage'	Regression Output	–	–

FIGURE 5.8: Layer by layer description of network

To create our own dataset, we utilize synthetically generated radar scenes, as depicted in Figure 5.9a. Each pixel in these radar images corresponds to the radar reflectivity of the respective scene cell. For training of the implemented networks,



(A) Synthetically generated radar scenes.

(B) Representation of monostatic radar measurements taken at different angles

FIGURE 5.9: An example set of synthetically created radar scenes and representative monostatic measurements taken around a radar scene at several observation angles.

we generate a dataset of range profiles from these synthetic radar scenes, assuming monostatic measurements captured at various viewing angles, as illustrated in Figure 5.9b. For each radar scene, we consider the radar illuminating the scene from various viewing angles. The range profiles, denoted as $q(r)$ and observed from each angle, are obtained through the Radon Transform applied to the reflectivity map of the scene, denoted as $f(x, y)$. The Radon Transform is mathematically defined as follows:

$$q(r, \theta) = \sum_{x,y} f(x, y)\delta(x \cos\theta + y \sin\theta - r) \tag{5.49}$$

This corresponds to the projection of the reflectivity field onto an arc at a distance of r to the radar when the radar observes the scene from an angle θ. The symbol S denotes the radar scene illuminated by the radar. The Radon transform effectively converts the 2D radar reflectivity map into 1D projectional data. Consequently, we perform discrete Radon transform on the radar scenes from various observation angles to acquire the range profile data. A representative collection of radar range profile data generated through the mentioned method is illustrated in Figure 5.10. It is important to note that the Radon Transform yields real-valued range profiles. To assign phase angles to the range profile vector, we randomly

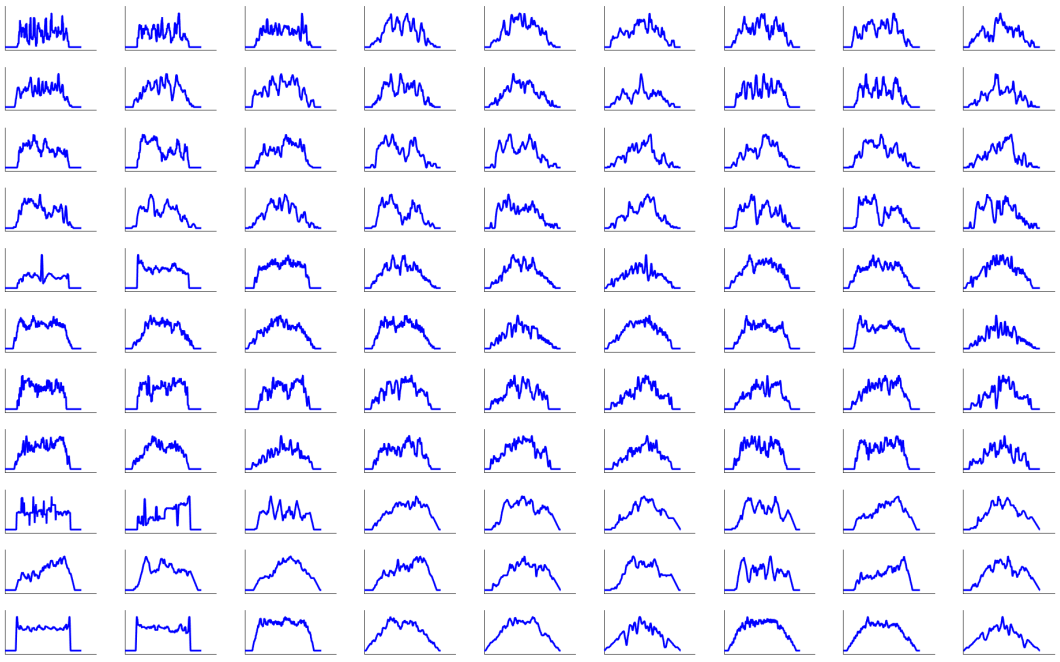


FIGURE 5.10: A representative set of radar range profiles is obtained by applying the Radon transform to synthetic radar scenes at various observation angles

generate phase values within the range $[0, 2\pi]$. In an effort to introduce some regularities, we subject this uniformly distributed random sequence of phase angles to a low-pass filter. This process results in spatial correlations in the distribution of phase angles. These range profiles are called ground truth range profiles hereinafter. Having obtained the ground truth range profiles in complex form, the next step involves simulating radar measurements by taking the Fourier Transform of the given complex-valued ground truth range profiles. In our measurement simulations, we consider an undersampled scenario, reflecting limitations in radar bandwidth. This undersampling, often due to frequency spectrum constraints or RF circuitry limitations, is introduced by selecting only 10% of the spectrum data from the Fourier transform of the range profiles. To achieve this, a rectangular mask is applied in the Fourier space of the range profile data. Two different levels of measurement noise, denoted as σ_0 and $2\sigma_0$, are considered, resulting in separate datasets for each noise level. Subsequently, the radar range profiles are reconstructed from these undersampled, noisy radar measurement datasets through inverse Fourier transform.

For training the magnitude and phase networks used in the priors optimization steps of our ADMM framework, we use ground-truth and FFT-based reconstructed range profiles as input-output pairs. Figure 5.12 illustrates two sample range profiles. The red plots represent the ground truth range profiles, while the blue plots represent the range profiles reconstructed using FFT. The first row displays the magnitude of the range profiles, the second and third rows show the normalized real and imaginary parts of the range profiles, respectively. The fourth row displays the phase angle of the range profiles in radians. CNNs for denoising phase data take the real and imaginary components of the range profile as inputs, while the CNN for denoising magnitude data takes only the magnitude of the range profiles. The ground truth range profiles serve as the pristine reference for the profiles. The implemented networks are trained to learn the mapping between the noisy and clean range profiles.

While mean square error is employed as the loss function for the magnitude network,

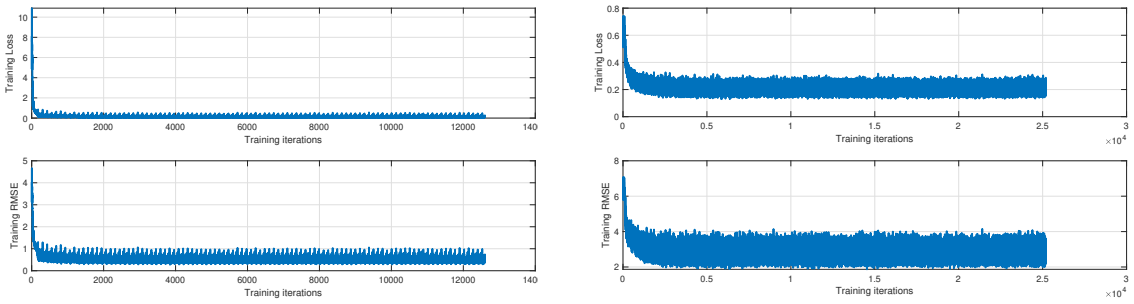
$$loss_{magnitude} = \frac{1}{N_{batch}} \sum_{i=1}^{N_{batch}} \left(\|\mathbf{x}_i - \mathbf{y}_i\|^2 \right) \tag{5.50}$$

we utilize the following regularized loss function for the phase network:

$$loss_{phase} = \frac{1}{N_{batch}} \sum_{i=1}^{N_{batch}} \left(\|\mathbf{x}_i - \mathbf{y}_i\|^2 + \lambda \|\mathbf{x}_i - \mathbf{1}\|^2 \right) \tag{5.51}$$

to enforce the $|\mathbf{q}_p| = 1$. For the training of CNNs for magnitudes and phases, we employ Stochastic Gradient Descent with Momentum (SGDM) as the optimizer. The training process is conducted in MATLAB 2020 utilizing the Deep Learning Toolbox and is executed on an NVIDIA GeForce MX250 GPU. The progression of the training loss is visualized in Figure 5.11.

The output of a trained network for two different test range profiles is visualized in Figure 5.13. As evident from the figure, the CNN effectively generates a refined version of the input range profiles reconstructed by FFT, demonstrating its denoising capability.



(A) Training of CNN for magnitudes. (B) Training of CNN for phase.

FIGURE 5.11: Training loss and RMSE during training of magnitude and phase networks with training data set with $\sigma = \sigma_0$

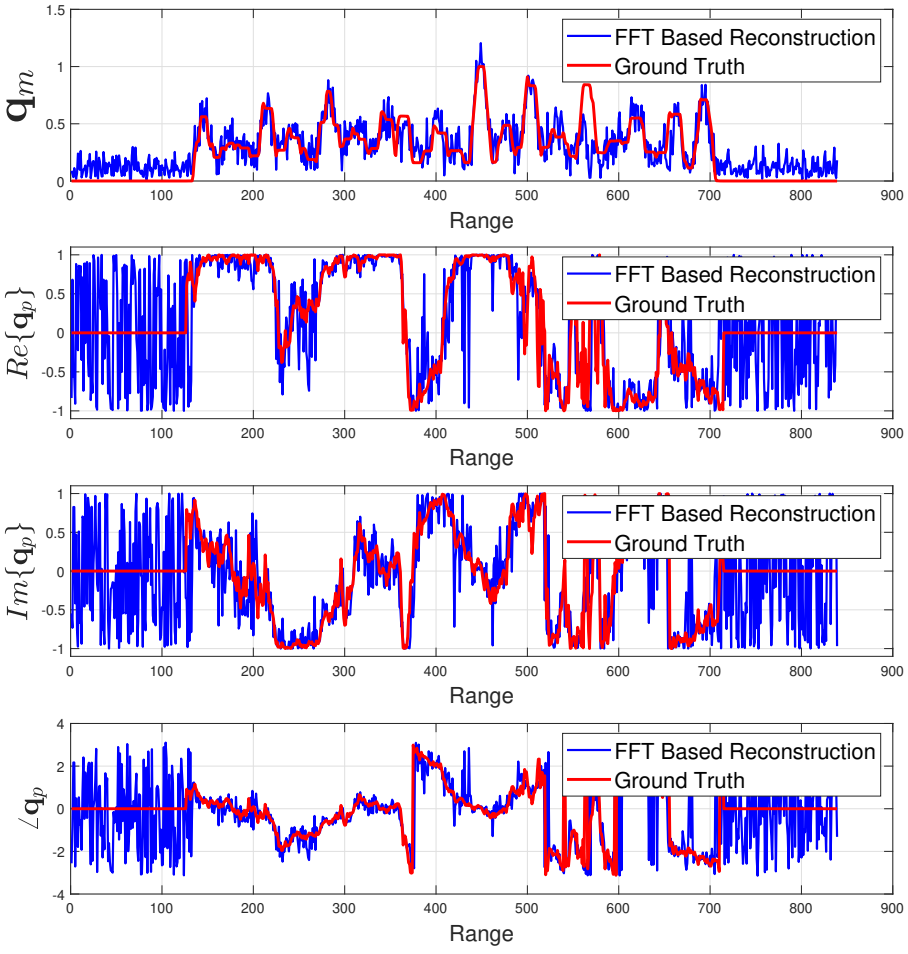
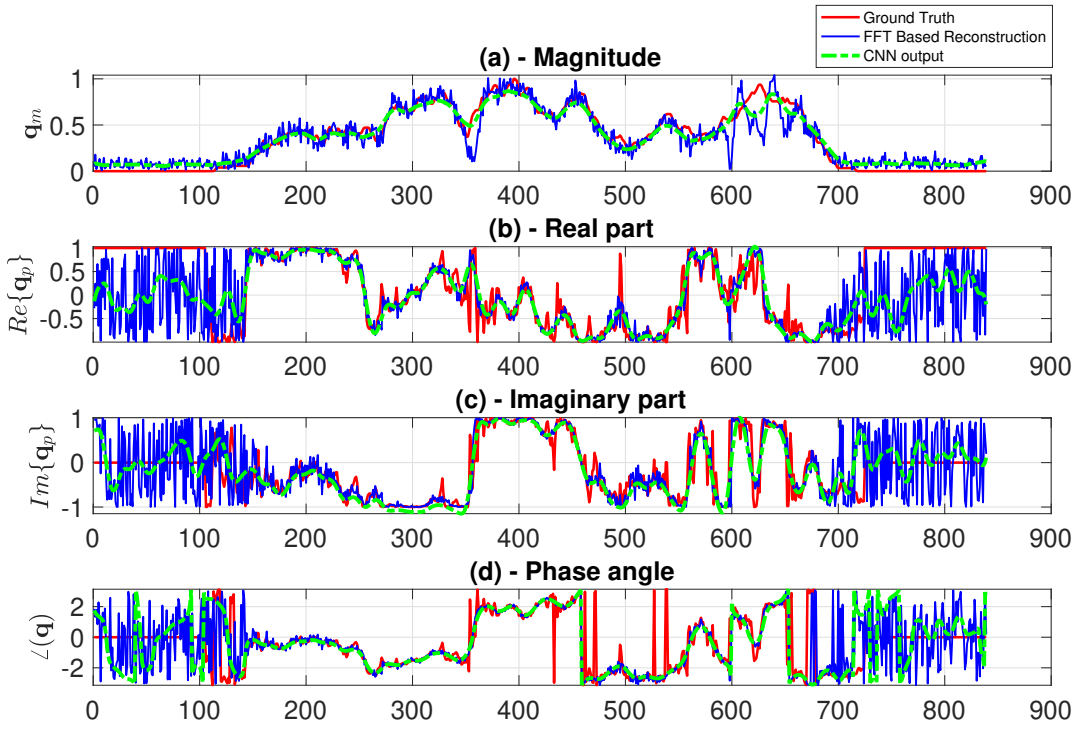
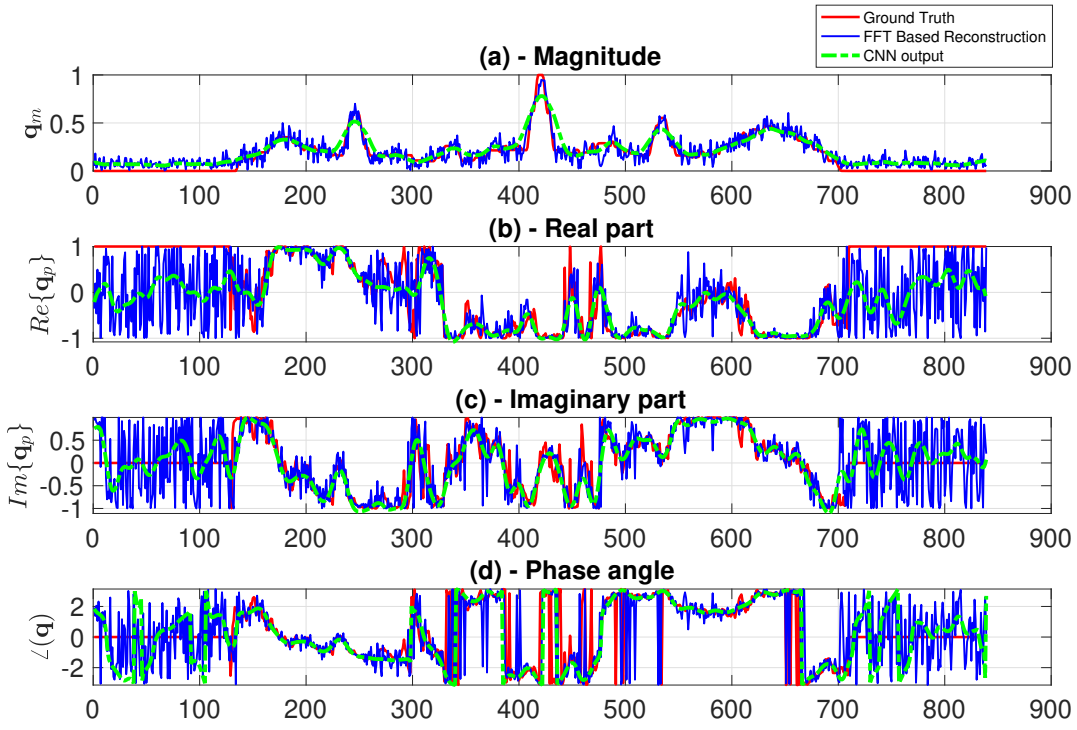


FIGURE 5.12: An arbitrary sample input-output pairs to magnitude and phase CNNs.



(A) An arbitrary test range profile from the data set



(B) An arbitrary test range profile from the data set

FIGURE 5.13: CNN response to a given noisy radar range profile reconstructed by FFT

5.3.3.4 PNP ADMM Framework with Complete Solution

Having developed all the necessary tools for our PnP ADMM framework, we put them together in a software implementation whose pseudocode is provided in Algorithm 3. The algorithm starts with an initial estimation of range profiles reconstructed by the Fast Fourier Transform (FFT) and iteratively refines this estimate. The algorithm halts either upon reaching the maximum specified number of iterations or when the change in $\mathbf{u}_m$ falls below a predefined tolerance threshold.

Algorithm 3: PnP ADMM algorithm for radar range profile formation with both magnitude and phase regularization

Data: $\mathbf{T}, \mathbf{y}, \mathcal{D}_\sigma, \rho$

Result: $\mathbf{h}_m$

$\mathbf{q}^{(0)} \leftarrow \mathbf{T}^{-1}\mathbf{r}$ - Initial estimation by the forward model inversion

$\mathbf{q}_m \leftarrow \left|\mathbf{q}^{(0)}\right|$, $\mathbf{q}_p^{(0)} \leftarrow \measuredangle\mathbf{q}$ $\boldsymbol{Q} \leftarrow diag\{\mathbf{q}_p\}$, $\boldsymbol{\Psi} \leftarrow diag\{\mathbf{q}_m\}$,

$\mathbf{h}_m \leftarrow \mathbf{q}_m$, $\mathbf{u} \leftarrow \mathbf{0}$

while *stopping criteria is not satisfied* **do**

  $\tilde{\mathbf{q}}_m \leftarrow \mathbf{h}_m - \mathbf{u}_m$

  $\tilde{\mathbf{q}}_p = \mathbf{h}_p - \mathbf{u}_p$

  while *stopping criteria is not satisfied* **do**

    $\mathbf{q}_p \leftarrow$ solution of (5.35) - Phase alignment

    $\boldsymbol{Q} \leftarrow diag\{\mathbf{q}_p\}$

    $\mathbf{q}_m \leftarrow$ solution of (5.36) - Magnitude alignment

    $\boldsymbol{\Psi} \leftarrow diag\{\mathbf{q}_m\}$

  end

  $\tilde{\mathbf{h}}_m \leftarrow \mathbf{q}_m + \mathbf{u}_m$

  $\tilde{\mathbf{h}}_p \leftarrow \mathbf{q}_p + \mathbf{u}_p$

  $\mathbf{h}_m \leftarrow \mathcal{D}_m(\tilde{\mathbf{h}}_m)$ - Approximation to (5.37) for prior update of magnitudes

  $\mathbf{h}_p \leftarrow \mathcal{D}_p(\tilde{\mathbf{h}}_p)$ - Approximation to problem (5.37) for prior update of phases

  $\hat{\mathbf{u}}_m \leftarrow \mathbf{u} + \mathbf{q}_m - \mathbf{h}_m$ - Auxilary update (5.39)

  $\hat{\mathbf{u}}_p \leftarrow \mathbf{u}_p + \mathbf{q}_p - \mathbf{h}_p$ - Auxilary update (5.40)

end

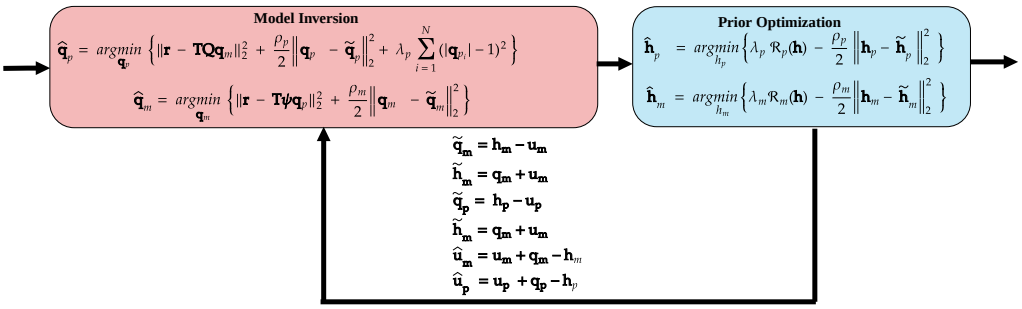
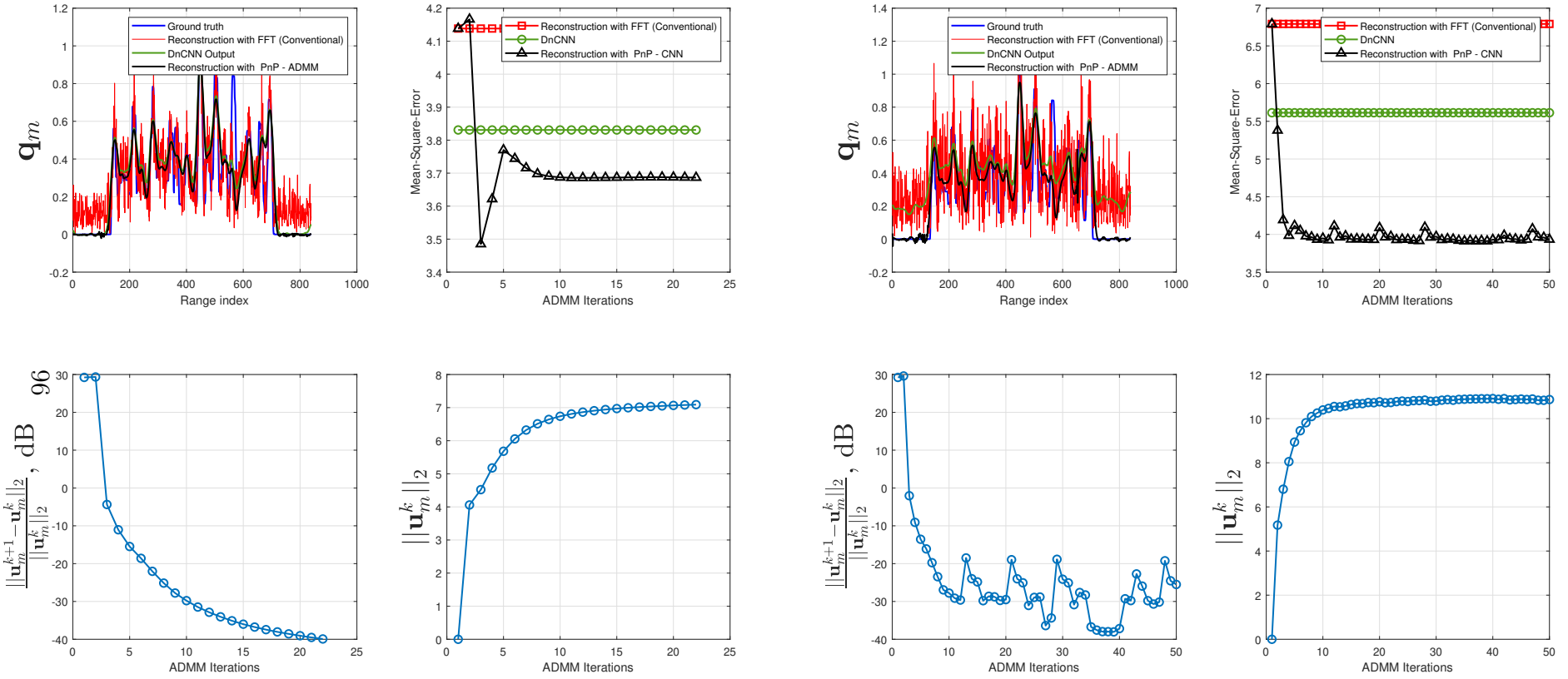


FIGURE 5.14: A block diagram representation of alternating optimization steps of PnP ADMM framework: Forward model is inverted for magnitude and phase and any appropriate denoiser can be chosen in a Plug-And-Play manner

In Figure 5.14, the alternating steps of data and priors optimization are illustrated. Throughout the ADMM iterations, the optimizations for data alignment and priors update steps alternate, gradually converging to a more accurate estimate of the range profile.

We evaluate our algorithm on example test data to demonstrate the effectiveness of the proposed approach for the radar range reconstruction problem. In Figure 5.15, the progression of the algorithm is illustrated for two different experiments with varying noise levels. The figure includes plots of the final reconstructed range profile, Mean Squared Error (MSE) over the course of ADMM iterations, and the change in the auxiliary parameter. As depicted in the figure, the auxiliary update parameter $\mathbf{u}_k$ converges, and the change in $\mathbf{u}_k$ approaches 0. We terminate the iterations when the change in $\mathbf{u}_k$ reaches the threshold or the maximum number of iterations is reached. It is important to note that convergence is not guaranteed in the proposed approach, and numerical instabilities may cause the algorithm to oscillate.

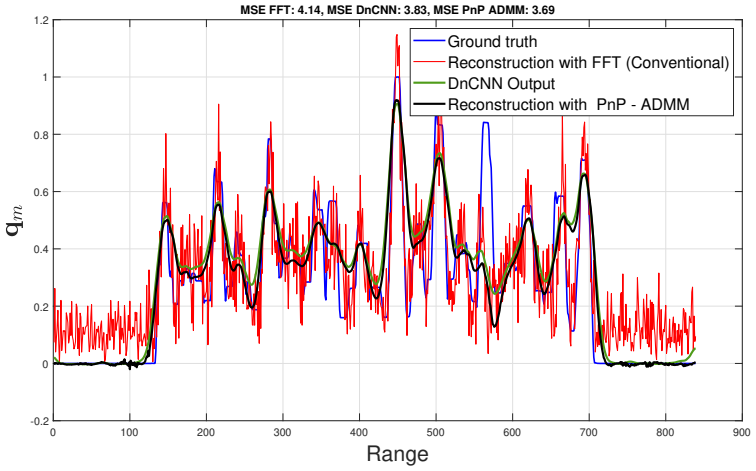
Figure 5.16 displays the reconstructed range profiles from 10% undersampled radar measurements under two different levels of measurement noise for two distinct test range profiles. Our proposed reconstruction method is compared against conventional FFT-based reconstruction and FFT-based reconstruction with CNN denoising. The top of each plot includes Mean Squared Error (MSE) values. Across all experiments, our approach demonstrates superior reconstruction performance with the lowest MSE values.



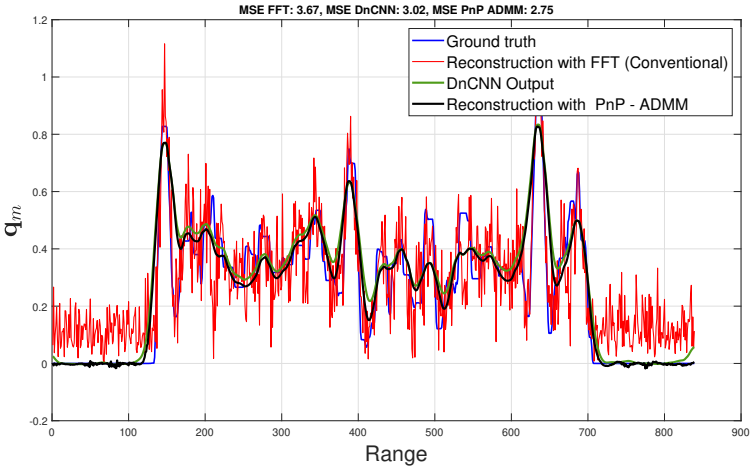
(A) Sample #1 - Data level : 10%, $\sigma = \sigma_0$

(B) Sample #2 - Data level : 10%, $\sigma = 2\sigma_0$

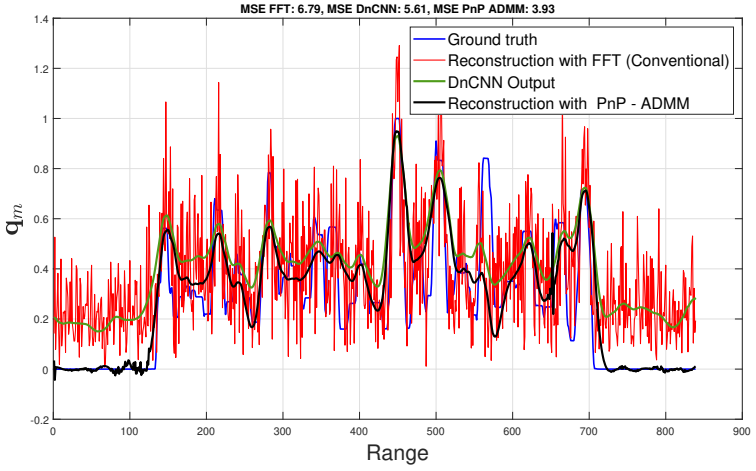
FIGURE 5.15: ADMM progression on arbitrary range profile



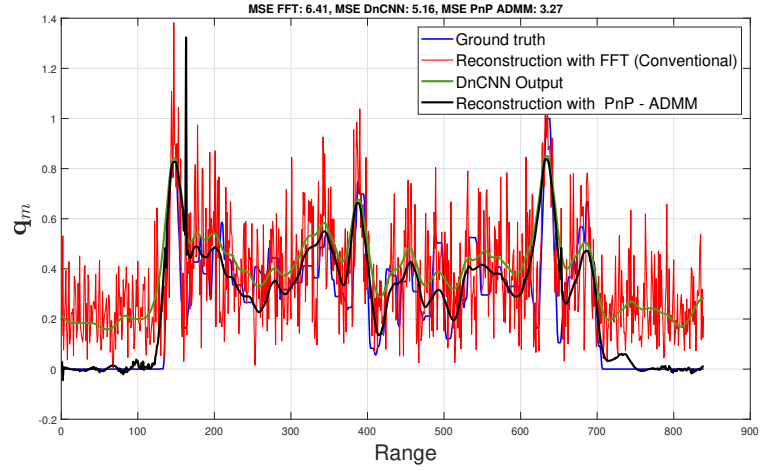
(A) Arbitrary sample #1 - Data level : 10%, $\sigma = \sigma_0$



(B) Arbitrary sample #2 - Data level : 10%, $\sigma = \sigma_0$



(C) Arbitrary sample #1 - Data level : 10%, $\sigma = 2\sigma_0$



(D) Arbitrary sample #2 - Data level : 10%, $\sigma = 2\sigma_0$

FIGURE 5.16: Performance comparison of conventional (FFT based) and proposed range profile reconstruction technique under different data availability and noise power conditions on two test profiles

5.4 Complex-valued Range Profile Formation with Magnitude Regularization Only

In this section, our focus is on the range profile reconstruction problem where significant phase patterns are not present for regularization during the inversion process. Therefore, the problem addressed here is a specific instance of the one discussed in Section 5.3. The method proposed in this section is advised for complex-valued signal reconstruction problems where phase regularities are minimal and provide limited benefits in the inversion process.

5.4.1 ADMM Formulation

We begin by considering the problem (5.28) with a slight modification: the regularization term is applied only to the magnitude vector $\mathbf{q}_m$ and regularization term for phase is removed from the objective function. With this adjustment, expression (5.28) transforms into a minimization problem over $\mathbf{q}_m$ and $\mathbf{q}_p$ with regularization only on magnitudes, expressed as follows:

$$\{\hat{\mathbf{q}}_m, \hat{\mathbf{q}}_p\} = \underset{\mathbf{q}_m, \mathbf{q}_p}{\operatorname{argmin}} \left\{ \|\mathbf{r} - \mathbf{T}\boldsymbol{\Psi}\mathbf{q}_m\|_2^2 + \lambda \mathcal{R}_m(\mathbf{q}_m) \right\} \tag{5.52}$$

Introducing a new auxiliary variable $\mathbf{h_m} \in \mathbb{R}^{N\times 1}$, we can write problem 5.52 as follows:

$$\begin{aligned} \{\mathbf{q}_m, \mathbf{q}_p, \mathbf{h}_m\} = &\underset{\mathbf{q}_m, \mathbf{q}_p, \mathbf{h}_m}{\operatorname{argmin}} \left\{ \|\mathbf{r} - \mathbf{T}\boldsymbol{\Psi}\mathbf{q}_m\|_2^2 + \lambda_m \mathcal{R}_m(\mathbf{q}_m) \right\} \\ &\text{s.t.} \quad \mathbf{q}_m - \mathbf{h}_m = 0 \end{aligned} \tag{5.53}$$

The objective function in augmented Lagrangian form is then written as follows:

$$\mathcal{L}\left(\mathbf{q}_m, \mathbf{q}_p, \mathbf{h}_m, \mathbf{u}_m\right) = \|\mathbf{r} - \mathbf{T}\boldsymbol{\Psi}\mathbf{q}_m\|_2^2 + \lambda_m \mathcal{R}_m(\mathbf{h}_m) + \frac{\rho_m}{2} \|\mathbf{q}_m - \mathbf{h}_m + \mathbf{u}_m\|_2^2 + \frac{\rho_m}{2} \|\mathbf{u}_m\|_2^2 \tag{5.54}$$

Let us introduce another diagonal matrix, $\mathbf{Q} \in \mathbb{C}^{N\times N}$ whose diagonal elements are equal to the values of $\mathbf{q}_m$, i.e., $\mathbf{Q}_{ii} = \mathbf{q}_{m_i}$, $\forall i \in \{1, 2, ..., N\}$ and define the

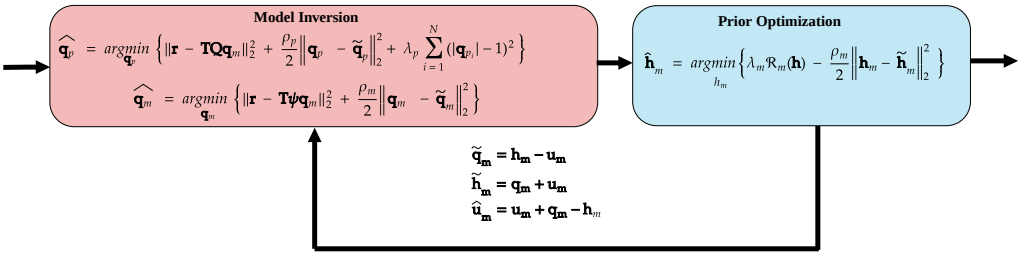


FIGURE 5.17: A block diagram representation of alternating optimization steps of ADMM

following auxiliary variables:

$$\begin{aligned} \tilde{\mathbf{q}}_m &= \mathbf{h}_m - \mathbf{u}_m \\ \tilde{\mathbf{h}}_m &= \mathbf{q}_m + \mathbf{u}_m \end{aligned} \tag{5.55}$$

with which we can construct the sub-minimization problems of our ADMM formulation as follows:

Overal ADMM subminimization problems with magnitude regularization

$$\hat{\mathbf{q}}_p = \underset{\mathbf{q}_p}{\operatorname{argmin}} \left\{ \|\mathbf{r} - \mathbf{T}\boldsymbol{Q}\mathbf{q}_p\|_2^2 + \lambda_\theta \sum_{i=1}^{N} \left(|\mathbf{q}_{p_i}| - 1\right)^2 \right\}, \tag{5.56}$$

$$\hat{\mathbf{q}}_m = \underset{\mathbf{q}_m}{\operatorname{argmin}} \left\{ \|\mathbf{r} - \mathbf{T}\boldsymbol{\Psi}\mathbf{q}_m\|_2^2 + \frac{\rho_m}{2} \|\mathbf{q}_m - \tilde{\mathbf{q}}_m\|_2^2 \right\}, \tag{5.57}$$

$$\hat{\mathbf{h}}_m = \underset{\mathbf{h}_m}{\operatorname{argmin}} \left\{ \lambda_m \mathcal{R}_m(\mathbf{h}_m) + \frac{\rho_m}{2} \left\| \tilde{\mathbf{h}}_m - \mathbf{h}_m \right\|_2^2 \right\}, \tag{5.58}$$

$$\hat{\mathbf{u}}_m = \mathbf{u}_m + \mathbf{q}_m - \mathbf{h}_m \tag{5.59}$$

Equations (5.56) and (5.57) correspond to the phase and magnitude optimizations, respectively. Eq. (5.58) represents the denoising operation for the magnitude of the range profiles, while equation (5.59) denotes the auxiliary updates in the ADMM framework. It is important to note that this problem differs from the one in Section 5.3 in the sense that the phase regularization step is absent in the ADMM formulation presented here. Additionally, the solutions to these sub-optimization problems remain the same as those discussed in Section 5.3. The alternating steps of data and prior updates are illustrated in 5.17.

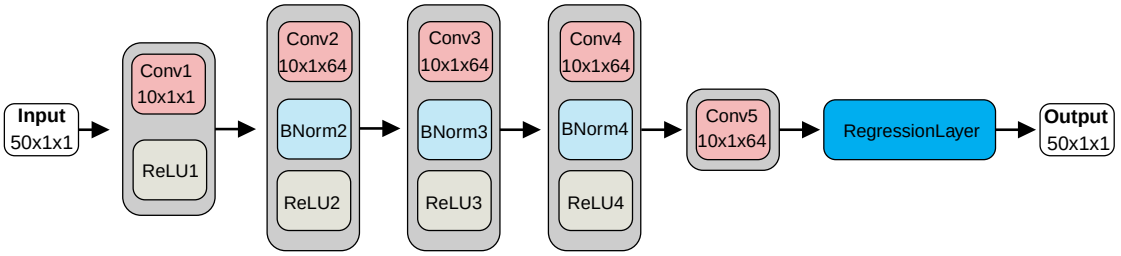


FIGURE 5.18: Implemented CNN architecture.

5.4.2 Simulation Results

In order to test the performance of ADMM based range profile reconstruction framework described in the previous section, we use Gotcha Volumetric SAR Data Set, Version 1.0 which is publicly available in [55]. The Gotcha volumetric SAR data set contains SAR phase history data from a scene consisting of numerous civilian vehicles and calibration targets. Measurements are taken in X-band radar with a bandwidth of 640 MHz from a 360° azimuth coverage at 8 different elevation angles with all possible polarization combinations. Each of this phase history data consists of 117 pulses with complex IQ samples. Since the radar measurements are collected in the Fourier space, conversion from measurements to range profile data is carried out by Fourier Transform as suggested by relation (5.21). Measurement model $\mathbf{T}$ for this setup is therefore inverse Fourier Transform matrix.

We employed a slightly modified version of Algorithm 3 by excluding the prior update for the phase from the ADMM iterations. As a denoiser for the magnitude of the range profiles, we explore three different solutions: a recursive filter denoiser from [42], a total variation denoiser from [41], and a denoising convolutional neural network, the architecture of which is depicted in Figure 5.18. For the training process, we divided the 360-phase history data into a training set of 288 samples (80%) and a test set of 72 samples (20%). The network takes range profile data reconstructed with FFT from a single pulse as input, and the output is the range profile data reconstructed with FFT with a 64-pulse noncoherent integration. Consequently, the output represents a relatively denoised version of the input data with 64 pulses. A subset of the range profile dataset used for training is illustrated in Figure 5.19.

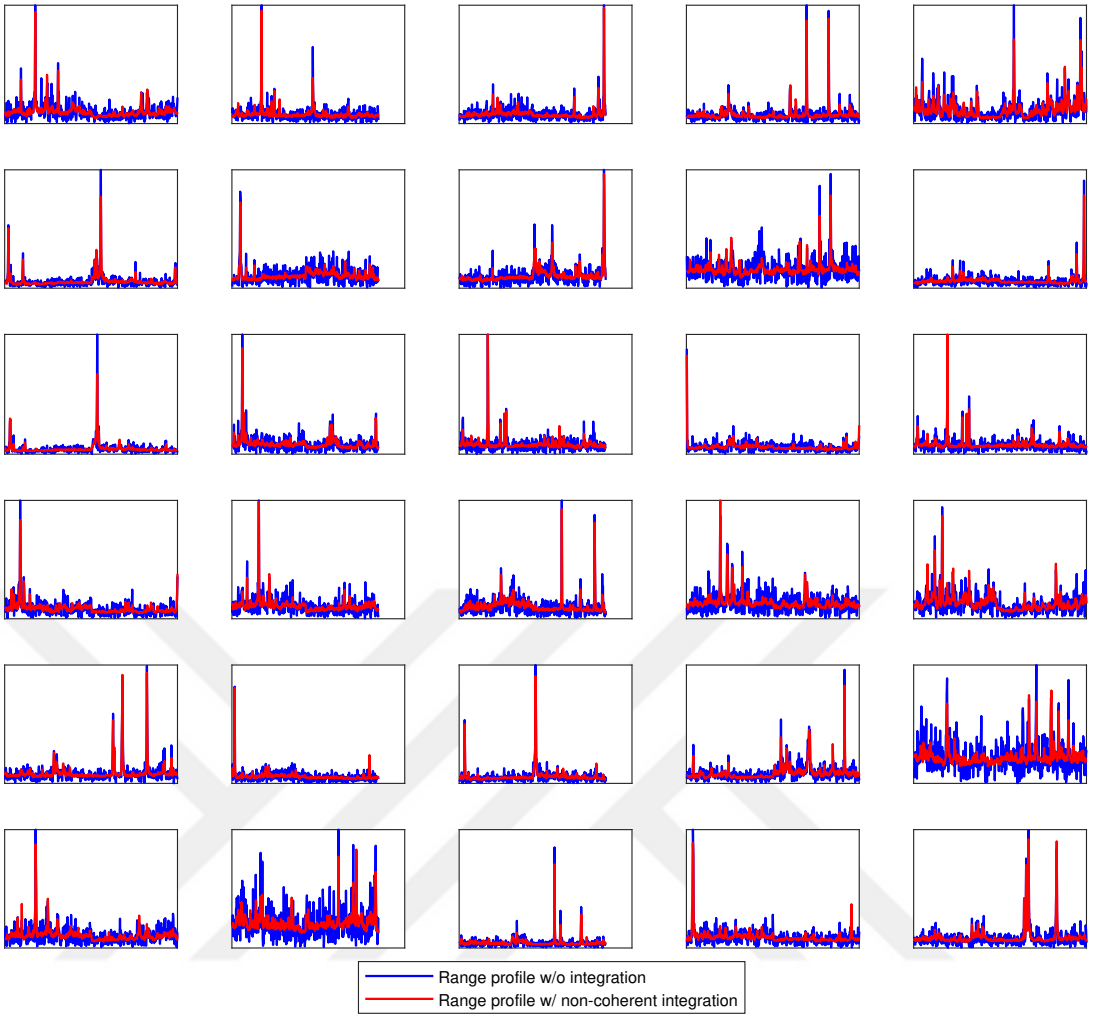


FIGURE 5.19: A sample set of input/output pairs of range profiles used during training. Range profiles in blue are obtained with a single pulse, while range profiles in red are obtained by integrating successive 64 pulses non-coherently

To enhance the training dataset, we randomly extract patches with 50 range cells. Optimization is performed using Stochastic Gradient Descent with Momentum (SGDM) as the optimizer, and the network is trained on an NVIDIA GeForce MX250 GPU. The training parameters are summarized in Table 5.1. The training process takes place in MATLAB 2020 using the Deep Learning Toolbox. The network's loss during 100 epochs of training is illustrated in Figure 5.20. ADMM iterations terminate when the change in $\mathbf{u}$ becomes smaller than the tolerance value, i.e., $\frac{\left\|\mathbf{u}^{(k+1)}-\mathbf{u}^{(k)}\right\|2^2}{\left\|\mathbf{u}^{(k)}\right\|2^2} < \epsilon$, or when the maximum number of ADMM iterations is reached.

For the performance comparison of various denoisers, we employ two key metrics:

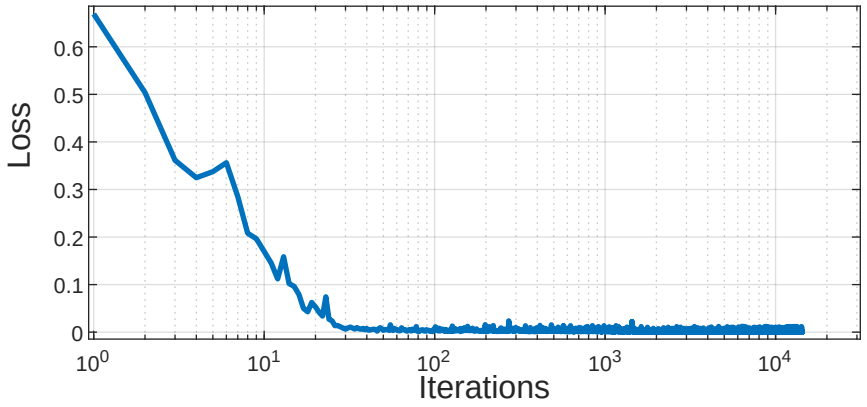


FIGURE 5.20: Loss during training of the network

mean square error (MSE) and peak signal-to-noise ratio (PSNR). The mean square error is calculated as the average of the squared differences between the test vector and the reference vector:

$$MSE = \frac{1}{N} \left\| \hat{\mathbf{q}}_m - \mathbf{q}_m^{ref} \right\|_2^2 = \frac{1}{N} \sum_{i=1}^{N} \left[\hat{\mathbf{q}}_m(i) - \mathbf{q}_m^{ref}(i) \right]^2 \tag{5.60}$$

PSNR is defined as:

$$PSNR = 10 \log_{10} \left(\frac{1}{MSE} \right) \tag{5.61}$$

In Figure 5.21, we showcase a set of range profiles reconstructed using various methods from the test dataset. The corresponding PSNR values are indicated above each plot. PnP ADMM with CNN attains the highest PSNR, whereas FFT-based reconstruction shows the lowest PSNR performance. For a thorough performance evaluation, each reconstruction method is applied individually to entire the test data set, and the average MSE and PSNR values are presented in Table 5.2. The proposed approach consistently demonstrates superior PSNR performance compared to the other methods.

Parameter	Value	Parameter	Value
Epoch	100	L2 Regularization	0.001
Initial Learning Rate	0.1	Learning Rate Drop Period	10
Momentum	0.9	Learning Rate Drop Factor	0.1

TABLE 5.1: Training parameters for CNN

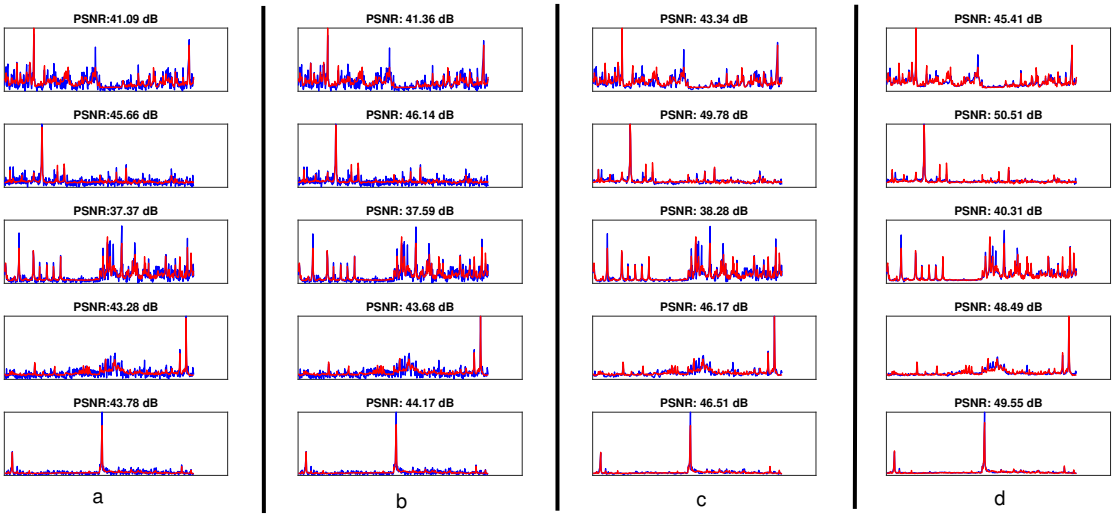


FIGURE 5.21: Performance comparison of conventional (FFT based) and ADMM based based range profile reconstructions with different PnP denoisers. Denoised range profiles with 64-pulse non-coherent integration are shown in blue and range profiles reconstructed from a single pulse with different techniques are shown in red. a) Conventional reconstruction (FFT based) b) ADMM based reconstruction with Total Variation (TV) denoiser c) ADMM based reconstruction with Recursive Filter (RF) denoiser d) ADMM based reconstruction with CNN denoiser

	FFT Based	**PnP-ADMM-TV**	**PnP-ADMM-RF**	**PnP-ADMM-CNN**
MSE (dB)	-81.67	-82.24	-84.80	**-89.23**
PSNR (dB)	42.44	42.82	45.24	**47.58**

TABLE 5.2: Performance comparison of different methods

5.5 Real-valued Range Profile Formation

In this section, we address the real-valued radar range profile reconstruction problem. Here, we make the assumption that changes in the phase of reflected radar signals are solely due to propagation, with no influence from scatterers along the range profile. We envision that this scenario is plausible when a sparse radar scene with dominant or strong scatterers is illuminated by a very narrow beam. In such cases, the range profile data can be reasonably assumed to be real-valued. Consequently, the ADMM formulation provided in Section 5.3 for complex-valued

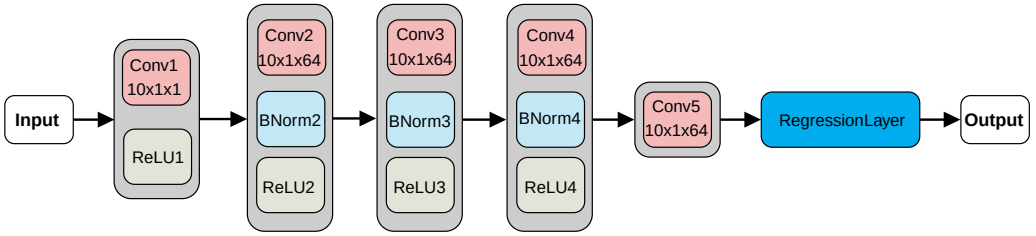


FIGURE 5.22: Convolutional neural network architecture

range profile data simplifies to the following set of alternating sub-optimization problems:

ADMM suboptimization problems

ADMM framework decouples model and prior optimization steps:

Model Optimization

$$\hat{\mathbf{q}}_{k+1} := \underset{\mathbf{q}\in\mathbb{C}^{N\times 1}}{\operatorname{argmin}} \left\{ \mathcal{D}(\mathbf{q}) + \frac{\rho}{2} \left\| \mathbf{q} - \tilde{\mathbf{q}}_k \right\|_2^2 \right\} \tag{5.62}$$

Prior optimization

$$\hat{\mathbf{h}}_{k+1} := \underset{\mathbf{h}\in\mathbb{C}^{N\times 1}}{\operatorname{argmin}} \left\{ \lambda\mathcal{R}(\mathbf{h}) + \frac{\rho}{2} \left\| \tilde{\mathbf{h}}_k - \mathbf{h} \right\|_2^2 \right\} \tag{5.63}$$

Auxilary variable update

$$\mathbf{u}_{k+1} := \mathbf{u}_k + (\mathbf{h}_{k+1} - \mathbf{q}_{k+1}) \tag{5.64}$$

Similar to the previous sections, we adopt a deep-learning-based approach, utilizing a convolutional neural network (CNN) as a denoiser to address the sub-problem (5.63). The simplified architecture of the implemented network is illustrated in Figure 5.22. The key distinction from the CNN in Figure 5.18 in the previous section is that the network takes the entire range profile data instead of a patch. Detailed information regarding the implemented CNN is provided in Figure 5.23.

To execute the ADMM steps, Algorithm 4 is implemented. The ADMM iterations terminate once the algorithm converges. Convergence is achieved if the change in the auxiliary variable $\mathbf{u}$ becomes smaller than the specified tolerance

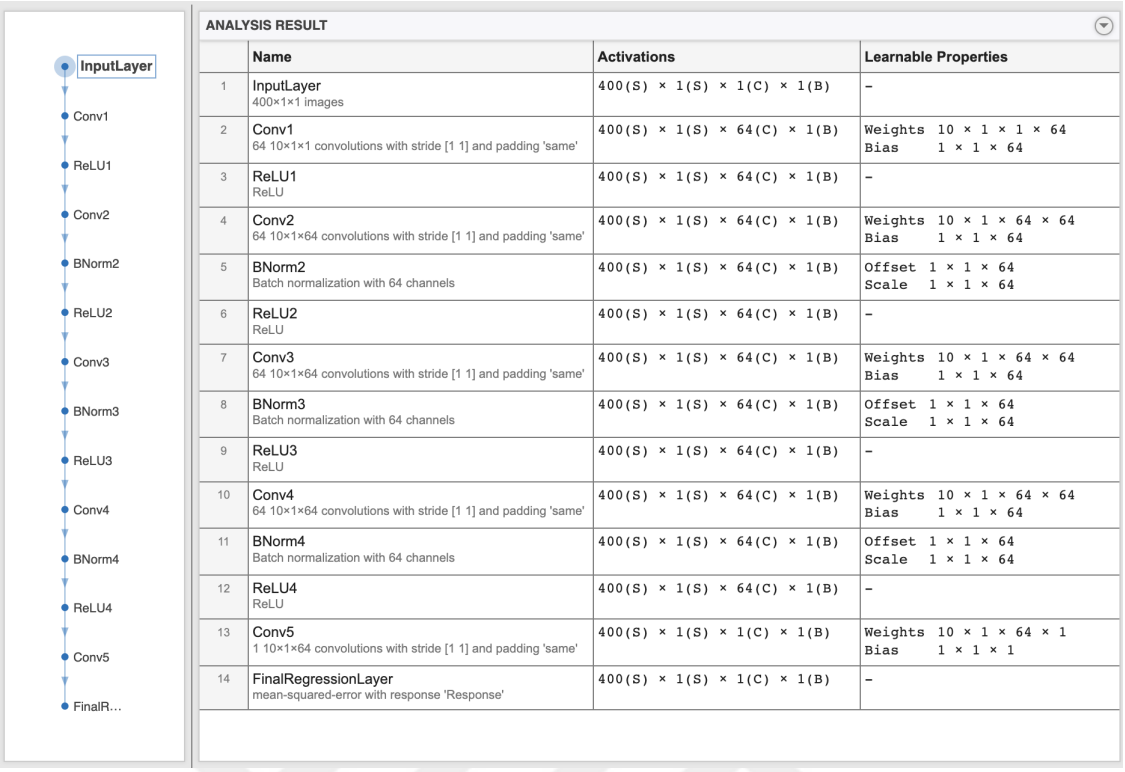


FIGURE 5.23: Network architecture with the detailed layer information. Total number of learnables is 124.8k.

value, i.e., $\left\|\mathbf{u}^{(k+1)} - \mathbf{u}^{(k)}\right\|_2^2 < \epsilon$, or if the maximum number of ADMM iterations is reached. These alternating sub-minimization steps of ADMM are illustrated in a block diagram in Figure 5.24.

Algorithm 4: PnP ADMM algorithm steps for real-valued radar range profile reconstruction

Data: $\mathbf{T}, \mathbf{y}, \mathcal{D}_\sigma, \rho$

Result: $\mathbf{h}$

$\mathbf{q} \leftarrow \mathbf{T}^{-1}\mathbf{r}$ - Initial estimation with model inversion

$\mathbf{h} \leftarrow \mathbf{q}$, $\mathbf{u} \leftarrow \mathbf{0}$

while *stopping criteria is not satisfied* **do**

  $\tilde{\mathbf{q}} \leftarrow \mathbf{h} - \mathbf{u}$

  $\mathbf{q} \leftarrow$ Solution of problem (5.62) - Model optimization

  $\tilde{\mathbf{h}} \leftarrow \mathbf{q} + \mathbf{u}$

  $\mathbf{h} \leftarrow$ Solve for problem (5.63) - Prior optimization

  $\mathbf{u} \leftarrow \mathbf{u} + \mathbf{q} - \mathbf{h}$ - Auxilary update

end

In order to test the performance of ADMM based range profile reconstruction framework described in the previous section, we use Gotcha Volumetric SAR Data

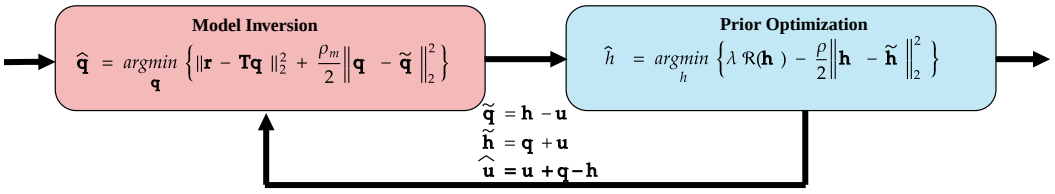


FIGURE 5.24: A block diagram representation of alternating optimization steps of ADMM.

Set, Version 1.0 which is publicly available in [55]. The dataset contains SAR phase history data from a scene consisting of numerous civilian vehicles and calibration targets. Measurements are taken in X-band radar with a bandwidth of 640 MHz from a 360° azimuth coverage at 8 different elevation angles with all possible polarization combinations. Each of this phase history data consists of 117 pulses with complex IQ samples. Since the radar measurements are collected in the Fourier space, conversion from measurements to range profile data is carried out by Fourier Transform as suggested by relation (5.21). Measurement model $\mathbf{T}$ for this setup is therefore inverse Fourier Transform matrix.

Using phase history data in GOTCHA SAR data we derive our own data set of range profiles in the following way: we first convert each and every fast-time radar data in the phase history matrix to a range profile by taking FFT. Then, we perform a non-coherent pulse integration using all the pulses available in the phase history matrix in order to get a relatively less noisy range profile data and finally pass it through a low-pass filter to further reduce the background noise in the reconstructed range profile. A sample set of range profiles obtained from the phase history data set is shown in Figure 5.25. The total number of range profile samples obtained in the described way is 11520. Note that the reconstructed range profile data is real-valued. The reason for us to make our own data set for range profile data is because we want to simulate our own measurements based on these generated range profiles considering different levels of measurement bandwidth and noise. We simulate our own measurements by using the measurement model given in (5.27). We select DFT matrix as the measurement model $\mathbf{T}$ and $\mathbf{w}$ is chosen to be complex white noise for the measurement simulations. In order to test the



FIGURE 5.25: A sample set of range profiles used in the simulations. (Horizontal axis is the range axis and vertical axis is the radar reflectivity magnitude)

performance of the proposed framework under different noise and bandwidth conditions, we consider six different bandwidth levels $(5\%, 10\%, 15\%, 20\%, 25\%, 30\%)$ and six different relative noise levels $(\sigma_0, 2\sigma_0, 3\sigma_0, 4\sigma_0, 5\sigma_0, 6\sigma_0)$. Bandwidth level is adjusted by means of a mask chosen around the middle row of the DFT matrix, which corresponds to DC frequency. For example, 5% data availability case is obtained by slicing 20 rows around the center row (rows corresponding to the low frequencies) of 400×400 DFT matrix. Hence for 5% data availability, we use a 20×400 DFT matrix as a forward measurement model. Reconstruction problem would be estimating radar range profile of 400 range cells from 20 radar measurement samples, which corresponds to solving a highly under-determined system of equations.

Data set for the implemented CNN consists of noisy and clean range profile data pairs. The noisy range profile data is obtained by adding a measurement noise

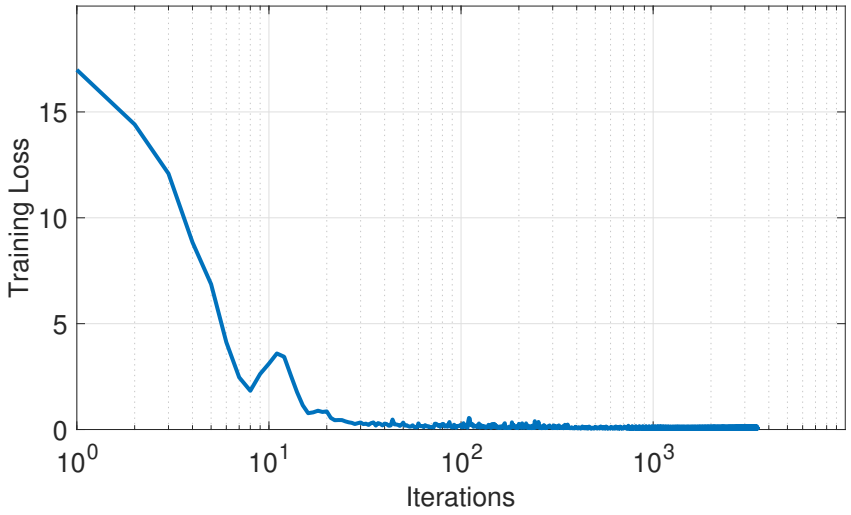


FIGURE 5.26: Loss during training of the network

with a variance randomly drawn from these 6 noise power levels. For the training of CNN, we divide the range profile data set into a training set (80 %), a test set (10 %) and a validation set (10 %). With a proper training, the network is believed to learn the mapping between the noisy and clean range profile data. We use Stochastic Gradient Descent with Momentum (SGDM) as an optimizer for the training of the network. For the training of network, the same training parameters as those listed in Table 5.1 are employed. Training is performed in MATLAB 2020 using Deep Learning Toolbox running on a NVIDIA GeForce MX250 GPU. The loss of the network during 100 epochs of training is plotted in Figure 5.26.

As a qualification metric to assess the performance of ADMM based range profile reconstruction method we have used Mean-Square-Error (MSE). We evaluate the performances of different methods on the test data set considering different measurement bandwidth and noise. We compare the proposed range profile formation method with a conventional (FFT) and l_2-norm regularized reconstruction, as well as ADMM based reconstruction with two different denoiser, namely Total-variation (TV) in [41] and Recursive-filter (RF) in [42]. We call these methods ADMM-TV, ADMM-RF and ADMM-CNN depending on the denoiser used. Among these methods, FFT-based reconstruction is the conventional and most commonly employed approach, relying solely on the Fourier measurement matrix without the use of any regularization techniques. l_2-norm regularized reconstruction on the

other hand regularizes the solution in l_2-norm sense. The other methods are implemented within the ADMM framework, differing only in the denoising technique employed to address the prior optimization step in (5.63).

In Figure 5.27, we present a representative range profile reconstructed through various methods, with corresponding Mean Squared Error (MSE) values displayed atop each subplot. Figure 5.27 showcases an illustrative range profile constructed from simulated measurements at three distinct noise levels and the full bandwidth. In contrast, Figure 5.28 depicts three different bandwidth levels without any measurement noise. In these figures, columns represent distinct reconstruction methods, each denoted at the top, while rows signify various measurement conditions, including the presence of measurement noise and bandwidth variations. The original range profile is represented in red, while the range profiles reconstructed from simulated measurements are depicted in blue.

Upon close examination of these plots, it becomes evident that conventional FFT-based reconstruction and l_2-norm regularized reconstruction suffer significantly under conditions of low bandwidth and/or high measurement noise. In contrast, the ADMM-based reconstruction methods consistently deliver superior performance. Notably, among the ADMM-based approaches, employing a CNN as a denoiser in the prior optimization step of the ADMM framework yields the most outstanding reconstruction results. ADMM-CNN method stands out for its ability to effectively capture the distinct peaks within the range profile data while substantially mitigating noise in the signal, resulting in the lowest Mean Squared Error (MSE) across all test cases. It is noteworthy that the ADMM-CNN algorithm exhibits remarkable resilience, showcasing promising reconstruction performance even in scenarios featuring limited measurement data or high levels of measurement noise.

For a comprehensive evaluation of the ADMM-CNN range profile reconstruction method and to establish a statistical overview of its MSE performance, we applied each reconstruction method over a small subset of the test dataset, comprising 100 range profile samples. We then computed the MSE values for each sample, calculated their average, and present the results in Figure 5.29, which encapsulates

the MSE performance across all 100 range profiles. Figure 5.29a shows the average MSE concerning measurement with respect to noise power, whereas Figure 5.29b shows the average MSE in relation to measurement bandwidth. Similar to the example case demonstrated in Figure 5.28 and Figure 5.27, the average MSE values further affirm that the ADMM-CNN method excels in terms of reconstruction performance when compared to the other investigated reconstruction methods under the examined measurement conditions.

5.6 Conclusions

In this study, we investigate the radar range profile reconstruction problem using the Plug-and-Play ADMM framework. We formulate the observation model specifically for side-looking FMCW radar. The problem is divided into three distinct scenarios, each addressed with a different solution:

- Complex-valued radar range profile reconstruction with both magnitude and phase regularization
- Complex-valued radar range profile reconstruction with only magnitude regularization
- Real-valued radar range profile reconstruction

We formulate the ADMM steps, where a denoising CNN acts as solver for the optimaztion of priors. We showcase the potential of utilizing a denoising CNN as a powerful tool to learn the intricate spatial patterns embedded within the range profile data and use it as a means of regularization. Through comprehensive simulations, we substantiate the effectiveness of employing deep learning networks as a regularization mechanism within the ADMM framework for radar range profile formation.

We conduct an extensive performance evaluation of the ADMM framework that employed CNN as a regularizer, drawing comparisons with alternative methods

across diverse measurement scenarios. Remarkably, among the reconstruction techniques under investigation, the ADMM approach with CNN as a regularizer emerge as the most successful one for radar range profile reconstruction problem in terms of reconstruction performance under both real and complex valued range profile scenarios.

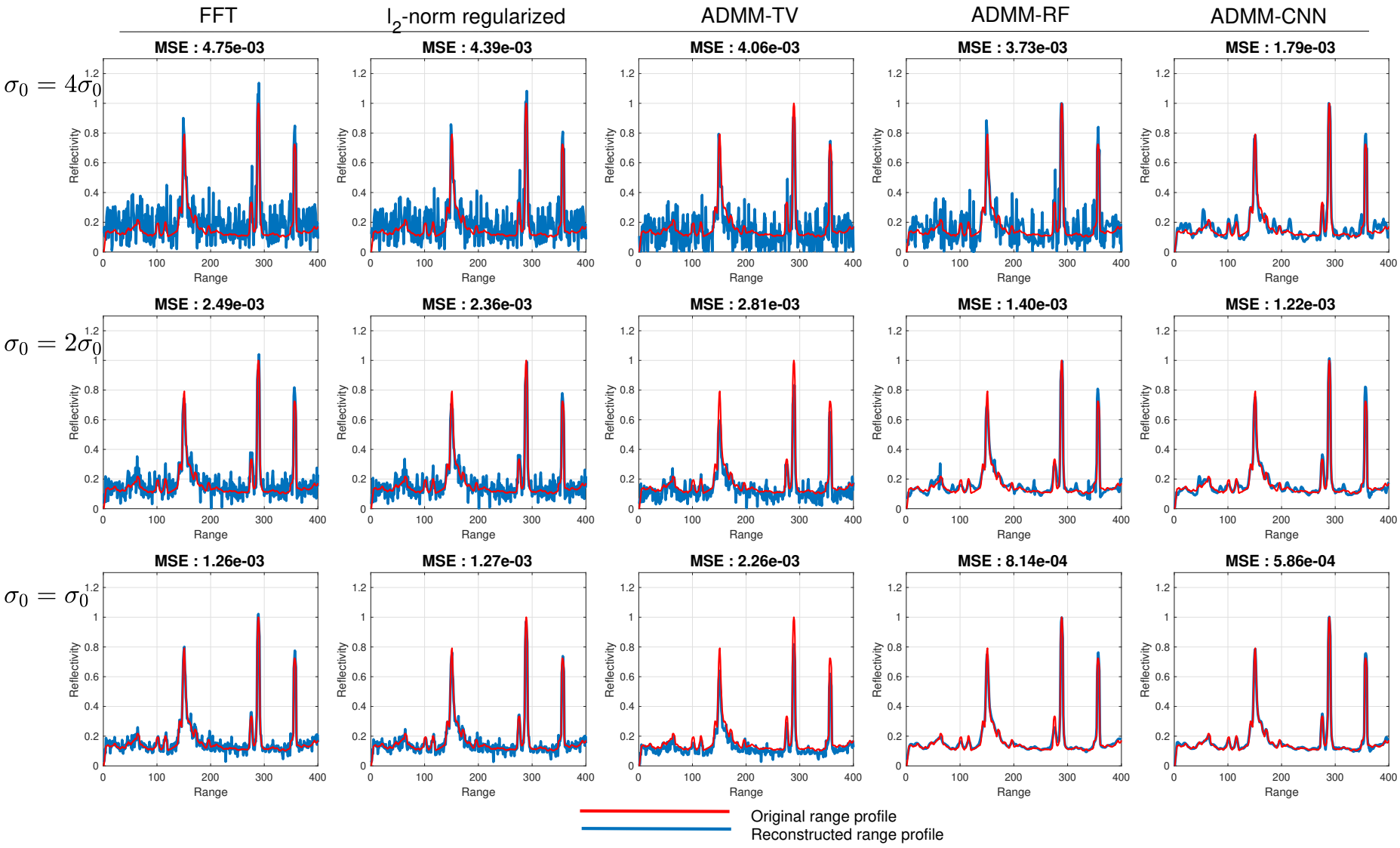


FIGURE 5.27: Comparison of various range profile reconstruction approaches on an example range profile data in terms of MSE performance under different noise - Reconstruction at three different measurement noise values (full-bandwidth)

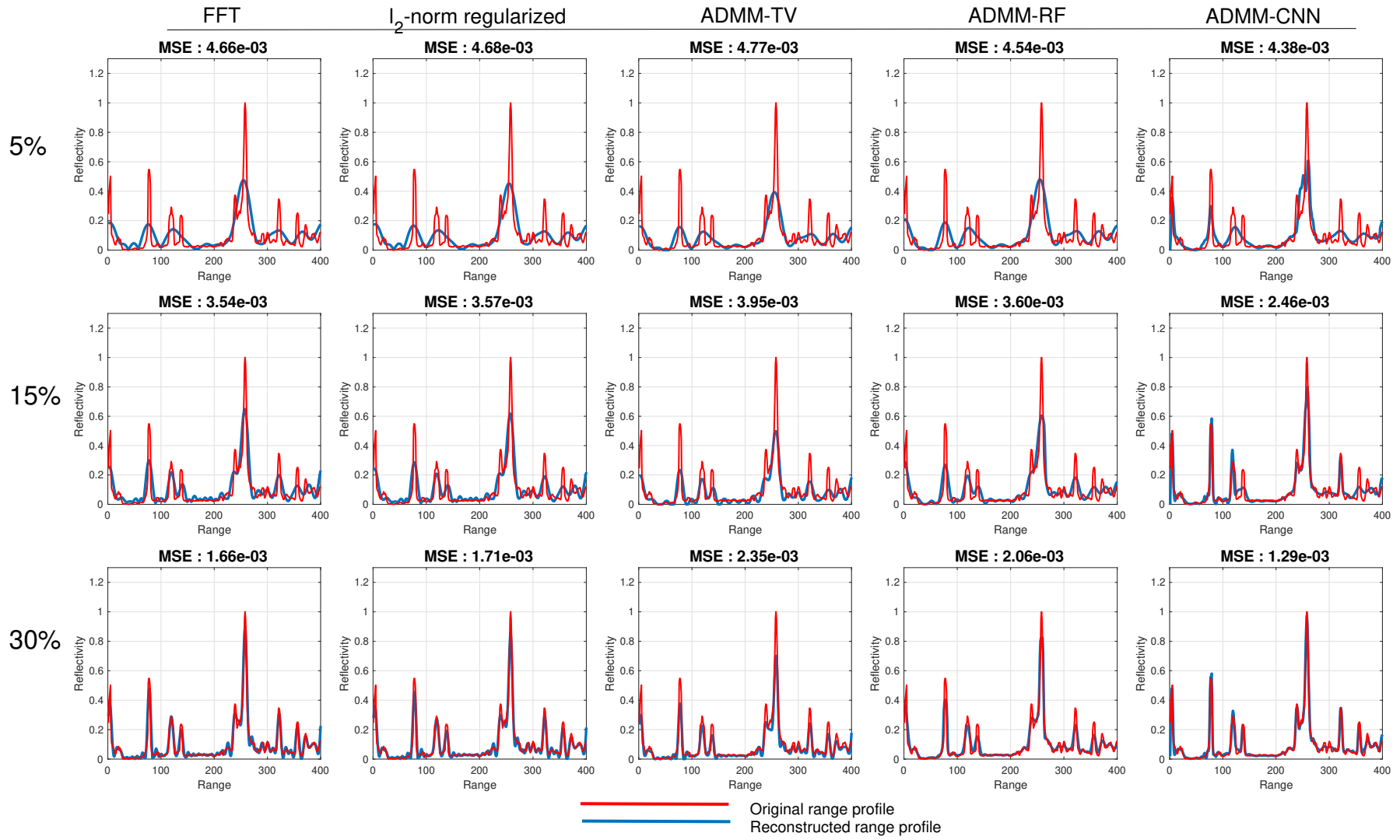
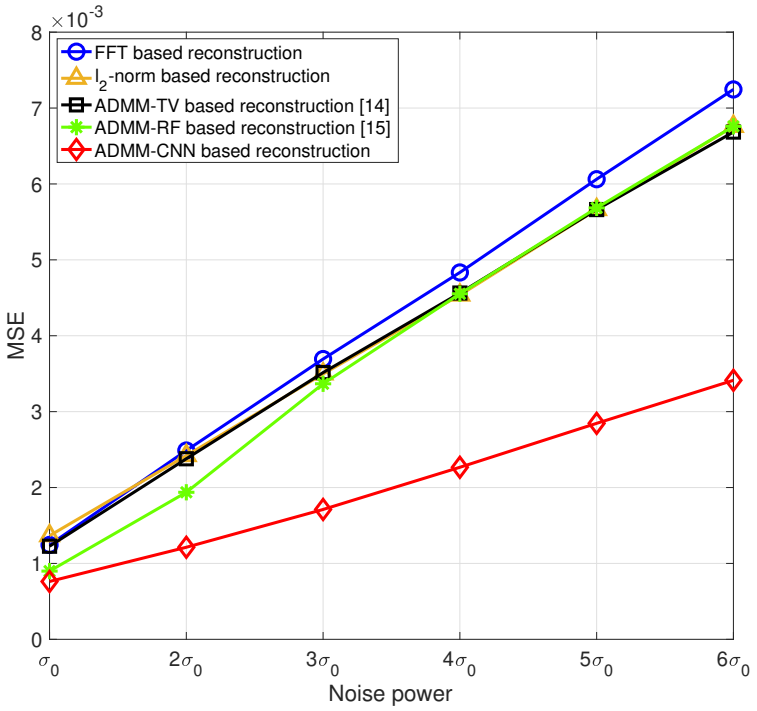
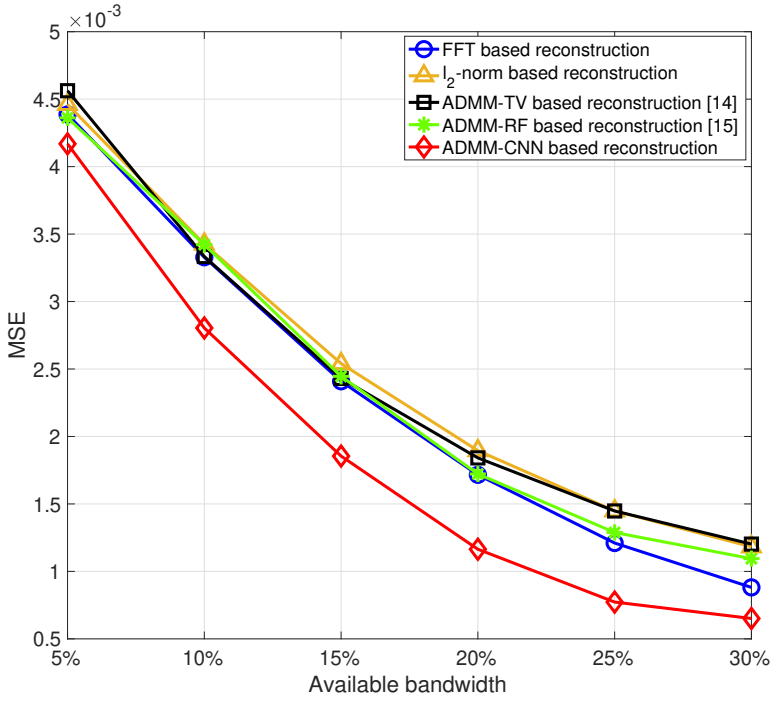


FIGURE 5.28: Comparison of various range profile reconstruction approaches on an example range profile data in terms of MSE performance under different bandwidth conditions - Reconstruction at three measurement bandwidth values (no measurement noise present)



(A) Measurement noise power vs. MSE



(B) Measurement bandwidth vs. MSE

FIGURE 5.29: MSE performance comparison of different reconstruction methods under different bandwidth availability and measurement noise conditions

Chapter 6

RADAR IMAGING WITH DEEP LEARNING

In this chapter, we present our proposed methodologies for enhancing MIMO radar imaging through the application of deep learning techniques. We begin by providing an overview of prior research in MIMO radar imaging and the utilization of deep learning in MIMO radar image reconstruction applications in Section 6.1. Subsequently, we investigate two distinct MIMO radar imaging scenarios, each employing a different deep learning-based approach. These approaches are detailed in Section 6.2 and 6.3, respectively.

6.1 Related Work

While radars are predominantly recognized for their prowess in target localization, they also possess robust imaging capabilities, operating reliably day and night regardless of weather conditions, which sets them apart from optical imaging systems [56]. Radar imaging essentially entails estimating the reflectivity distribution of a 2D or 3D space.

Radar imaging, a subset of microwave imaging, utilizes electromagnetic radiation spanning from 300 MHz to 300 GHz and has garnered considerable attention across diverse applications. Examples include concealed weapon detection systems (CWD) [57], through-wall imaging (TWI) [58], ground-penetrating radar (GPR) [31], and medical diagnosis, among others [59]. Furthermore, radar imaging systems play pivotal roles in emerging domains such as production processes [60], surface inspection [61], and airport runway security [3].

In [62], radar imaging modalities are classified into two main groups: direct imaging and indirect imaging. In direct imaging, electromagnetic radiation from the radar transmitter is focused into a desired angle using highly directive antennas or phased array radars, which employ multiple antennas with varying phases. This approach captures a thin slice of the radar scene by directing the radar beam in a specific direction. By scanning an area or volume, the complete radar image data is obtained, which is then processed to construct the final desired radar image. Scanning can be achieved through mechanical scanning, where the radar antenna is mounted on a rotating pedestal, or electronic scanning, where a phased array antenna steers the beam towards a specific direction. In indirect imaging, spatial diversity or digital beamforming is utilized. Radar returns are collected from different positions to achieve a variety of look angles. This can be accomplished using an array of antennas distributed in various locations or by moving the radar itself to obtain distinct look angles. Multiple Input Multiple Output (MIMO) radar employs the former technique, while Synthetic Aperture Radars (SAR) use the latter.

In [63], a 2D MIMO radar is employed for volumetric imaging, where a range migration algorithm is proposed to reconstruct volumetric images in the frequency-wavenumber domain. This algorithm compensates for the curvature of the wavefront in the near field using interpolation techniques, resulting in high computational efficiency achieved through multiple FFT operations. The authors extensively discuss implementation aspects, providing insights on MIMO aperture and sampling criteria. In [64], a Bayesian estimation-based design methodology is presented for 2D MIMO arrays in ultra-wideband imaging. The optimality criterion

is defined based on image reconstruction quality, and the designs obtained by the proposed algorithm are compared with various sparse array topologies.

Addressing the incorporation of scene sparsity into image restoration, [65] explores the use of a Mills cross array for near-field MIMO imaging. Total variation regularization is employed in the objective function of the optimization problem, enabling iterative calculation of the radar scene's reflectivity distribution without the need for computations involving large matrices. In [66], a 3D FMCW MIMO design is described with a focus on the design process and radar signal processing. Additionally, [67] combines MIMO imaging with SAR imaging to provide a 3D radar image using a Fourier-based image reconstruction technique with a sparsely sampled array aperture.

In addition to conventional model-based inversion approaches, deep learning-based methods have emerged as a promising alternative for solving inverse imaging problems. [11] offers a comprehensive overview of the different approaches in this field, showcasing how deep learning techniques efficiently tackle various forms of inverse imaging problems. As yet another powerful tool for addressing inverse imaging problems, compressive sensing, when integrated with deep learning methodologies, has also attracted significant interest and has been effectively utilized in addressing inverse imaging challenges, as shown by studies like [68], [69], [70], and [71].

Existing studies utilizing deep learning in radar imaging can be categorized into four main approaches:

- **Full Learning of Inversion Process without Utilizing Any Observation/Physics Model:**
  - In this approach, no physics-based models are used, and the mapping from measurement space to image space is directly learned.
- **Learning Post-processing:**
  - Here, images are formed from the measurements using conventional reconstruction techniques. Deep learning learns the mapping between

the reconstructed images and ground truth images (or images reconstructed under optimal measurement conditions, such as minimal noise and maximum bandwidth).

- **Learning Priors/Regularizers and Using Them with the Forward Model in the Inversion Process:**
  - In this approach, deep learning is used to learn priors or regularizers, which are then incorporated with the forward model in the inversion process.
- **End-to-End Learning:**
  - Measurements of the scene to be imaged are captured under both favorable (maximum bandwidth and/or minimum measurement noise) and unfavorable (less bandwidth and/or more measurement noise) conditions. Reference images of the scene are reconstructed using conventional techniques under optimal conditions. The network then learns the mapping between measurements taken under unfavorable conditions and the reference image.

6.2 Surface Imaging with Side-Looking MIMO Radar with Post-processing Learning

We investigate a surface imaging application scenario utilizing a side-looking MIMO radar, such as for surface quality inspection or crack monitoring. A simplified representation of system model illustrating the imaging setup is depicted in Figure 6.1.

Each MIMO element is assumed to provide a side-looking view of the illuminated radar scene. The scene itself has a reflectivity map denoted by $f(x, y)$, where x and y represent spatial coordinates. We assume isotropic reflectivity, meaning each antenna receives the same reflection from a scatterer regardless of the angle.

Our goal is to estimate the reflectivity map of the scene with minimal estimation error based on the collected MIMO measurements.

For instance, let us consider an array comprising 4 transmitter elements and 3 receiver elements, evenly distributed along the physical aperture. With this configuration, we effectively obtain 12 discrete measurements from unique look angles to the scene. The distinction from a classical SAR system lies in how measurements are acquired: in our scenario, discrete measurements are taken from the scene, whereas in SAR, continuous measurements are gathered as the radar platform moves along its scan trajectory. In other words, the MIMO imaging differs from SAR imaging in that SAR takes monostatic measurements in a continuous manner, while MIMO imaging setup considered here gathers multistatic measurements from various looking angles to the scene. In this example case, virtually formed aperture is equivalent to a SAR sensor taking the discrete snapshots of the radar scene while moving along the line MIMO elements placed. The number of radar snapshots is $4 \times 3 = 12$ since there are 12 virtual elements in this example.

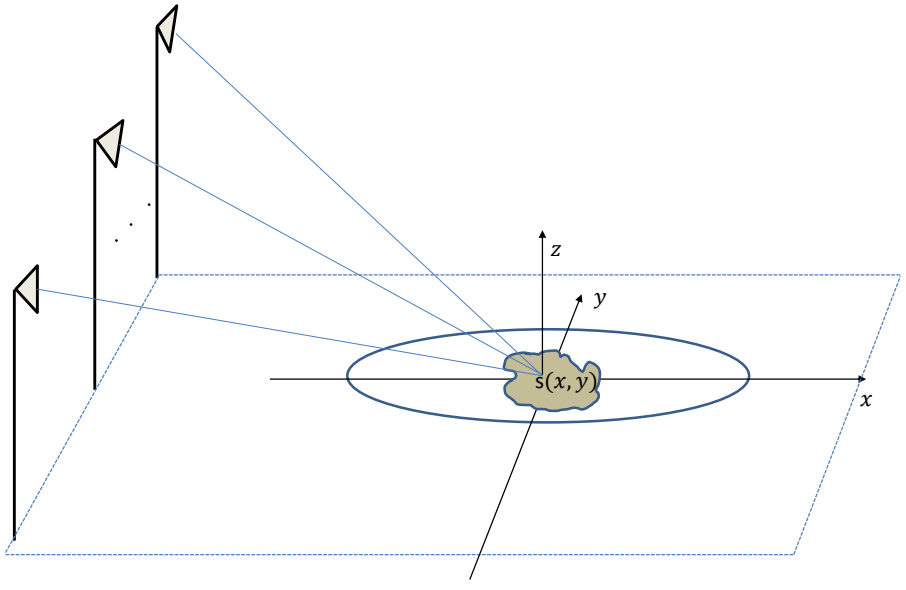


FIGURE 6.1: Simplified imaging geometry

6.2.1 Derivation of Observation/Forward Model

For the development of our measurement model for radar imagery, as illustrated in Figure 6.1, let us assume that the scene $f(x, y)$ is illuminated by a time-harmonic field originating from a transmitter positioned at $\mathbf{s}_t = (x_t, y_t, z_t)$.

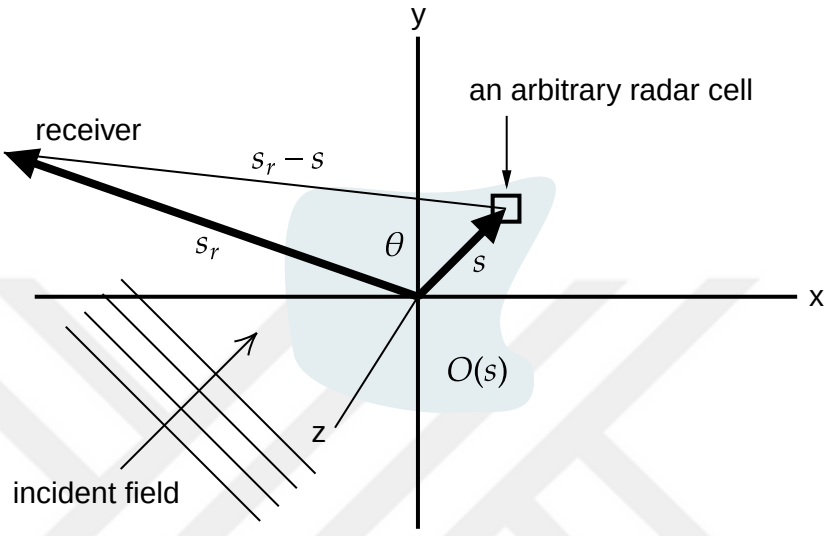


FIGURE 6.2: Projection of imagery setup onto 2D horizontal plane.

The field observed at point $\mathbf{s}$ resulting from the transmitter's emissions is described by Green's functions as follows:

$$dE_i(\mathbf{s}, \mathbf{s}_t) = E_0 \frac{1}{4\pi \|\mathbf{s} - \mathbf{s}_t\|} \exp\left\{jk \|\mathbf{s} - \mathbf{s}_t\|\right\} d\mathbf{s} \tag{6.1}$$

where E_0 is the initial amplitude value, and $k = \|\mathbf{k}\| = 2\pi/\lambda$ is the norm of the wavenumber vector with λ being the wavelength of the field. This incident field governed by (6.1) induces induction currents in the scene medium, $\mathbf{s} = s(x, y)$, so that every arbitrary point, $\mathbf{s}$, starts to act like an antenna, giving rise to the back-scattering phenomena. The amount of energy reflected back from the scene is determined by the reflection coefficient of the point scatterers in the scene. This parameter is also referred to as radar cross section (RCS) in the radar literature. Assuming that these point-like scatterers back-radiate isotropically and the back-scattering field propagates spherically in space, we can obtain the observed field

at the receiver at position $\mathbf{s}_r = (r_x, r_y, r_z)$ due to the back-radiation of point, $\mathbf{s}$ in the scene in the following phasor form:

$$dE_r(\mathbf{s}_r, \mathbf{s}) = f(\mathbf{s}) \frac{1}{4\pi \left\| \mathbf{s} - \mathbf{s}_t \right\|} \exp\left\{ jk \left\| \mathbf{s} - \mathbf{s}_t \right\| \right\} d\mathbf{s} \tag{6.2}$$

with E_0 being replaced by $f(\mathbf{s})$. Here the reflectivity value is a complex number, i.e., $f(\mathbf{s}) = |f(\mathbf{s})| e^{\angle f(\mathbf{s})}$. The complex reflectivity value means that the incident wave is scaled in magnitude and also phase-shifted. Having obtained two-way propagation models, we can express the field observed at the receiver at $\mathbf{s}_t$ due to the transmission at $\mathbf{s}_r$ after reflecting back from the point-like scatterer at $\mathbf{s}$ as equal to the product of (6.1) and (6.2):

$$dE(\mathbf{s}_t, \mathbf{s}_r, \mathbf{s}) = dE_i(\mathbf{s}, \mathbf{s}_t) dE_i(\mathbf{s}_r, \mathbf{s}) d\mathbf{s} \tag{6.3}$$

When the distance of radar to the scene is much larger than the radius of the scene, we use the far field assumption as in [72] to further simplify (6.3). For this purpose, let us start by finding an approximate expression for the distance between receiver and an arbitrary point in the scene. Assuming that $\|\mathbf{s}_r\|$ and $\mathbf{s}$ are the two legs of triangle, we can express the $\|\mathbf{s}_r - \mathbf{s}\|$ using Law of Cosines as follows [72]:

$$\begin{aligned} \|\mathbf{s}_r - \mathbf{s}\| &= \sqrt{\|\mathbf{s}_r\|^2 + \|\mathbf{s}\|^2 - 2\cos\theta \|\mathbf{s}_r\| \|\mathbf{s}\|} \\ &= \|\mathbf{s}_r\| \sqrt{1 + \frac{\|\mathbf{s}\|^2}{\|\mathbf{s}_r\|^2} - 2\frac{\|\mathbf{s}\|}{\|\mathbf{s_r}\|}\cos\theta} \end{aligned} \tag{6.4}$$

Since $\|\mathbf{s}_r\| >> \|\mathbf{s}\|$, the term $\frac{\|\mathbf{s}\|^2}{\|\mathbf{s}_r\|^2}$ is much smaller the third term inside the square root in 6.4 so that we can neglect it. Additionally, the remaining terms under the square root can be approximated using the first two terms of Taylor series expansion $\sqrt{1+x} \approx 1 + \frac{x}{2}$, which is valid for $x \ll 1$, we obtain

$$\|\mathbf{s}_r - \mathbf{s}\| \approx \|\mathbf{s}_r\| \sqrt{1 - 2\frac{\|\mathbf{s}\|}{\|\mathbf{s_r}\|}\cos\theta} \approx \|\mathbf{s}_r\| - \|\mathbf{s}\|\cos\theta \tag{6.5}$$

Furthermore, using the following inner product definition:

$$\mathbf{s}_r \cdot \mathbf{s} = \|\mathbf{s}_r\| \, \|\mathbf{s}\| \cos\theta \rightarrow \|\mathbf{s}\| \cos\theta = \frac{\mathbf{s}_r}{\|\mathbf{s}_r\|} \cdot \mathbf{s} = \mathbf{u}_r \cdot \mathbf{s} \tag{6.6}$$

where the term $\mathbf{u}_r$ represents the unit vector pointing towards the transmitter at position $\mathbf{s}_r$, defined as $\mathbf{u}_r = \frac{\mathbf{s}_r}{\|\mathbf{s}_r\|}$. The distance of any arbitrary point in scene to the receiver antenna is approximated by

$$\|\mathbf{s}_r - \mathbf{s}\| \approx \|\mathbf{s}_r\| - \mathbf{u}_r \cdot \mathbf{s} \tag{6.7}$$

Likewise, the approximate distance of any arbitrary point in scene to the transmitter antenna is given by

$$\|\mathbf{s}_t - \mathbf{s}\| \approx \|\mathbf{s}_t\| - \mathbf{u}_t \cdot \mathbf{s} \tag{6.8}$$

with $\mathbf{u}_t = \frac{\mathbf{s}_t}{\|\mathbf{s}_t\|}$ denoting the unit vector which points transmitter antenna at position $\mathbf{s}_t$. Substituting the approximated distance expressions in (6.8) & (6.7) into (6.3), we obtain

$$dE(\mathbf{s}_t, \mathbf{s}_r, \mathbf{s}) \approx f(\mathbf{s}) \frac{\exp\Big\{jk(\,\|\mathbf{s}_t\| + \|\mathbf{s}_r\|\,)\Big\}}{(4\pi)^2 \, \|\mathbf{s}_t\| \, \|\mathbf{s}_r\|} \exp\Big\{ -jk\mathbf{s} \cdot (\mathbf{u}_t + \mathbf{u}_r)\Big\} d\mathbf{s} \tag{6.9}$$

Here, the terms $\|\mathbf{s}_t - \mathbf{s}\|$ and $\|\mathbf{s}_r - \mathbf{s}\|$ in the denominator are approximated by $\|\mathbf{s}_t\|$ and $\|\mathbf{s}_r\|$, respectively. Note that Eq. (6.9) provides an expression for the field at the observation point $\mathbf{s}_r$ of a spherical wave emanating from a point-like source at $\mathbf{s}_t$ and back-reflecting from a point-like scatterer at $\mathbf{s}$ in the scene. By superposition, each scatterer's field is added at the observation point. Consequently, the total field observed at point $\mathbf{s}_r$ is given by the integral of Eq. (6.9):

$$E(\mathbf{s}_t, \mathbf{s}_r) = \frac{\exp\Big\{jk(\,\|\mathbf{s}_t\| + \|\mathbf{s}_r\|\,)\Big\}}{(4\pi)^2 \, \|\mathbf{s}_t\| \, \|\mathbf{s}_r\|} \iint_{\|\mathbf{s}\| \leq R} f(\mathbf{s}) \exp\Big\{ -jk\mathbf{s} \cdot (\mathbf{u}_t + \mathbf{u}_r)\Big\} d\mathbf{s} \tag{6.10}$$

Since $\|\mathbf{s}_t\|$ and $\|\mathbf{s}_r\|$ both are known quantities, their attenuation effect can be normalized. After this normalization, the observations can then be expressed as a

function of illumination point, $\mathbf{s}_t$, observation point, $\mathbf{s}_r$ and the wavenumber, k

$$O(\mathbf{s}_t, \mathbf{s}_r, k) = \iint_{\|\mathbf{s}\| \leq R} f(\mathbf{s}) \exp\Big\{ - jk(\mathbf{u}_t + \mathbf{u}_r) \cdot \mathbf{s} \Big\} d\mathbf{s} \tag{6.11}$$

Defining $\mathbf{k}' = k(\mathbf{u}_t + \mathbf{u}_r) = (k'_x, k'_y)$ and noting that $\mathbf{s} = (x, y)$, we get

$$O(\mathbf{s}_t, \mathbf{s}_r, k) = \iint_{\|\mathbf{s}\| \leq R} f(x, y) \exp\Big\{ - jk(k'_x x + k'_y) \Big\} dxdy \tag{6.12}$$

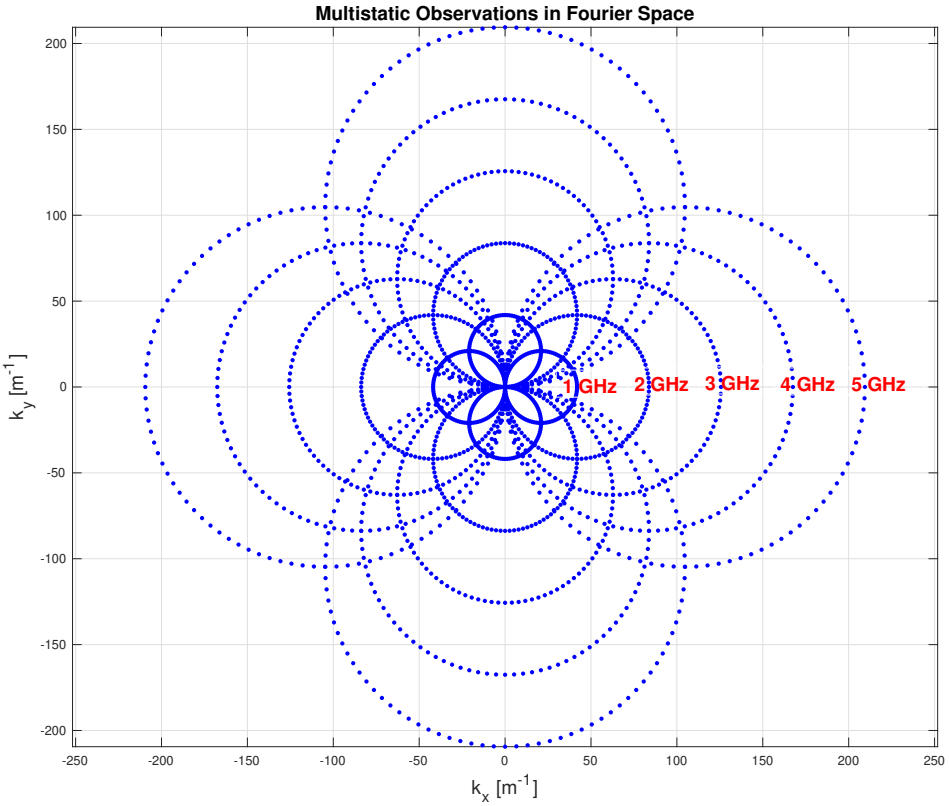
As seen from Equation (6.12), observations are the spatial two-dimensional Fourier transform of the scene reflectivity map, $\mathbf{f}$, evaluated at $\mathbf{k}' = k(\mathbf{u}_t + \mathbf{u}_r)$. That is,

$$O(\mathbf{s}_t, \mathbf{s}_r, k) = \mathcal{FT}\{f(x, y)\} = F(k'_x, k'_y)\Big|_{\substack{k'_x = k(\mathbf{u}_t + \mathbf{u}_r) \cdot \hat{\mathbf{x}} \\ k'_x = k(\mathbf{u}_t + \mathbf{u}_r) \cdot \hat{\mathbf{y}}}} \tag{6.13}$$

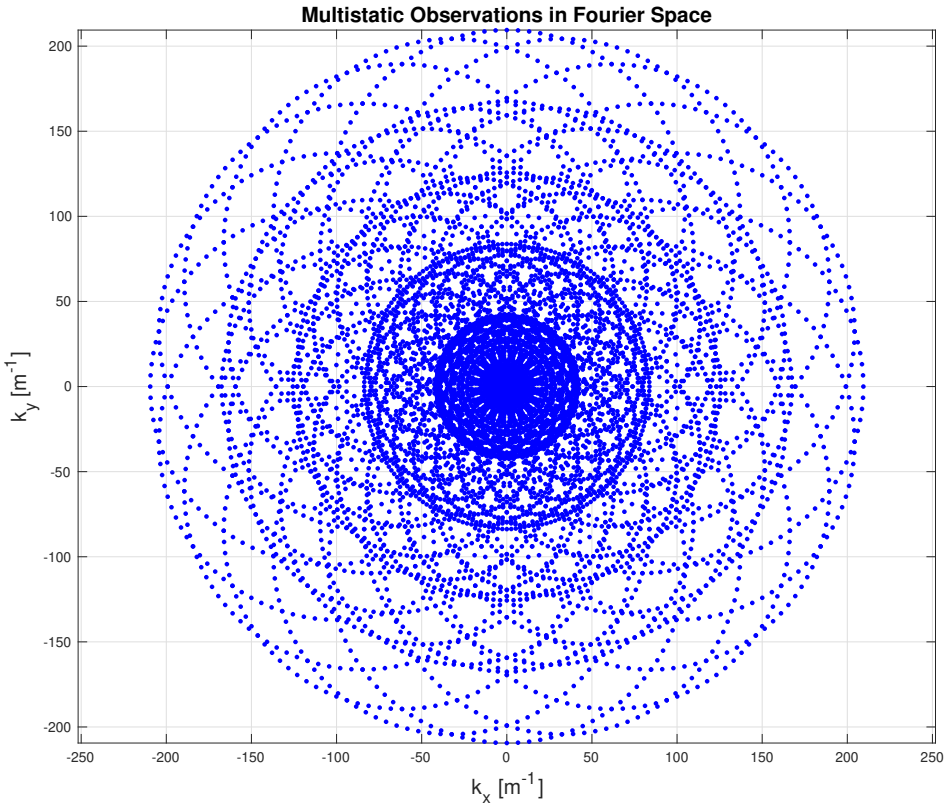
Eq. (6.13) illustrates that each TX-RX antenna pair and transmission frequency corresponds to a single measurement sample in the 2D Fourier space. The scene reflectivity map can be reconstructed by taking the inverse Fourier Transform of these measurements after some interpolation steps. Consequently, collecting more samples from the Fourier space leads to a better reconstruction of the radar reflectivity map.

6.2.2 Sampling over Fourier Space

In order to illustrate this further, we simulate a measurement setup with circular array configuration. Figure 6.3 shows the corresponding positions of measurements in the 2-dimensional spatial Fourier space. In this configuration 4 transmit antennas circularly are positioned around the scene with a azimuth separation of 90° and and 100 receive antennas are circularly placed around the scene with a azimuth separation of 3.6 Transmissions are made at 1 GHz, 2 GHz, 3 GHz, 4 GHz, 5 GHz, respectively. We increase the number of transmit antennas to 20 and observations corresponding to this case is demonstrated in In Figure 6.3b.



(A) 4 Tx antennas, 100 Rx antennas



(B) 20 Tx antennas, 100 Rx antennas

FIGURE 6.3: Fourier space observations with different antenna settings.

As clearly seen from Figure 6.3a and 6.3b, one can obtain different observations from the Fourier space by changing the configuration of the antennas and transmission frequency. Obviously, the quality of the radar image reconstructed is proportionally dependent on how many samples are collected from the Fourier space.

6.2.3 Learning Post-processing

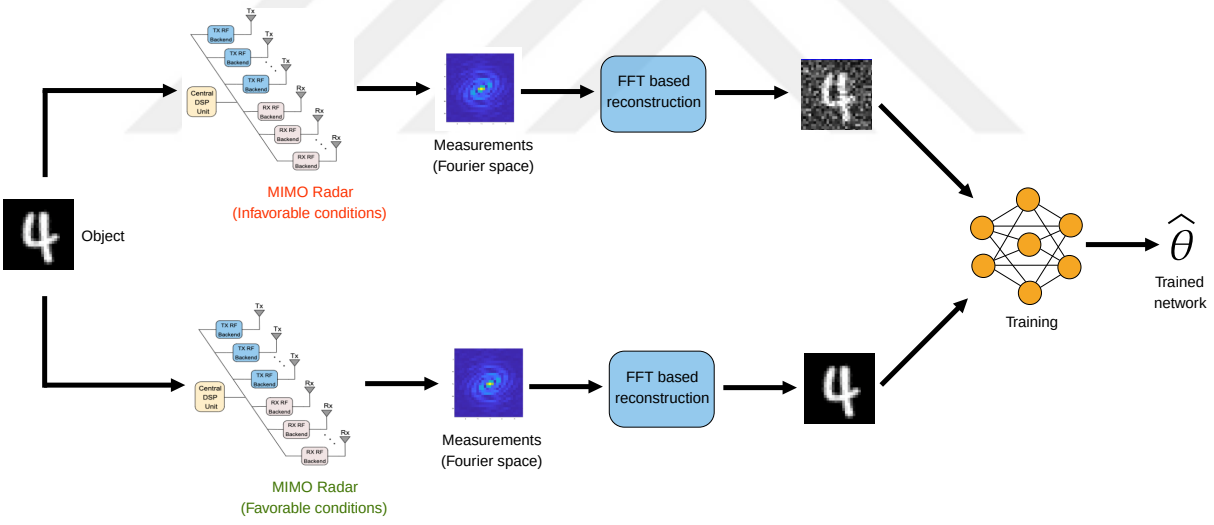
We have demonstrated in Section 6.2.1 that multi-static MIMO measurements are samples from the 2D Fourier transform of the scene's reflectivity map. Hence, we can establish the connection between radar measurements and the scene's reflectivity map through Fourier Transform. Although there are additional steps involved in practice, such as Polar-to-Cartesian conversion and interpolation, which impact this relationship, for simplicity, we can express this relationship in the following linear form:

$$\mathbf{F}(\mathbf{\Omega_x}, \mathbf{\Omega_y}) = \mathcal{FT}\{\mathbf{f}(x, y)\} + \mathbf{w} \tag{6.14}$$

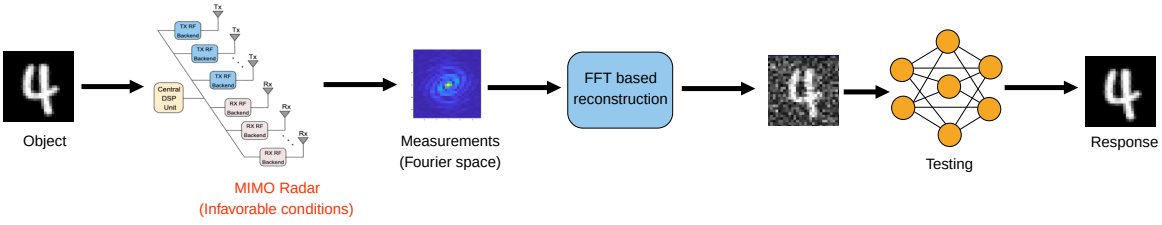
where $\mathbf{f}\{x, y\}$ is the discrete reflectivity map of the scene and $\mathbf{F}(\mathbf{\Omega_x}, \mathbf{\Omega_y})$ is the multi-static radar measurements, respectively. $\mathbf{w}$ is the additive measurement noise. It is evident from 6.14 that the inverse Fourier transform of the collected measurements can readily form the radar scene image. However, despite the apparent simplicity of reconstructing images from multi-static measurements, the practical performance of reconstruction varies depending on factors such as noise level and data/bandwidth availability.

In scenarios with high measurement noise or limited radar imaging bandwidth, the reconstruction performance suffers significantly. To address the reconstruction errors arising from limited data/bandwidth availability and/or measurement noise, we propose post-processing the reconstructed radar image of the scene, as outlined in Section 6.1, as one of the techniques to enhance the final reconstruction performance.

Figure 6.4 illustrates the steps involved during both training and testing stages of the post-processing learning-based reconstruction method. Initially, multi-static measurements of an object/scene are captured by the MIMO radar. These measurements are acquired under varying conditions, including both bad-weather conditions with low SNR and bandwidth and ideal conditions with highest possible bandwidth and SNR. The measurements are collected in spatial Fourier space. Subsequently, a traditional reconstruction method, such as Fourier transform-based reconstruction, is employed to generate images under both measurement conditions. These images reconstructed under measurement conditions are fed to a neural network tasked with learning the mapping between the two sets of radar images. Once the network is trained using this data, it undergoes testing with images from a separate test set. The training and testing procedures of the network, encompassing the described steps, are depicted in Figures 6.4a and 6.4b, respectively.



(A) Training setup to learn post-processing



(B) Radar image formation of a test scene with post-processing through a trained network

FIGURE 6.4: Training and testing stages of the proposed reconstruction method with post-processing learning

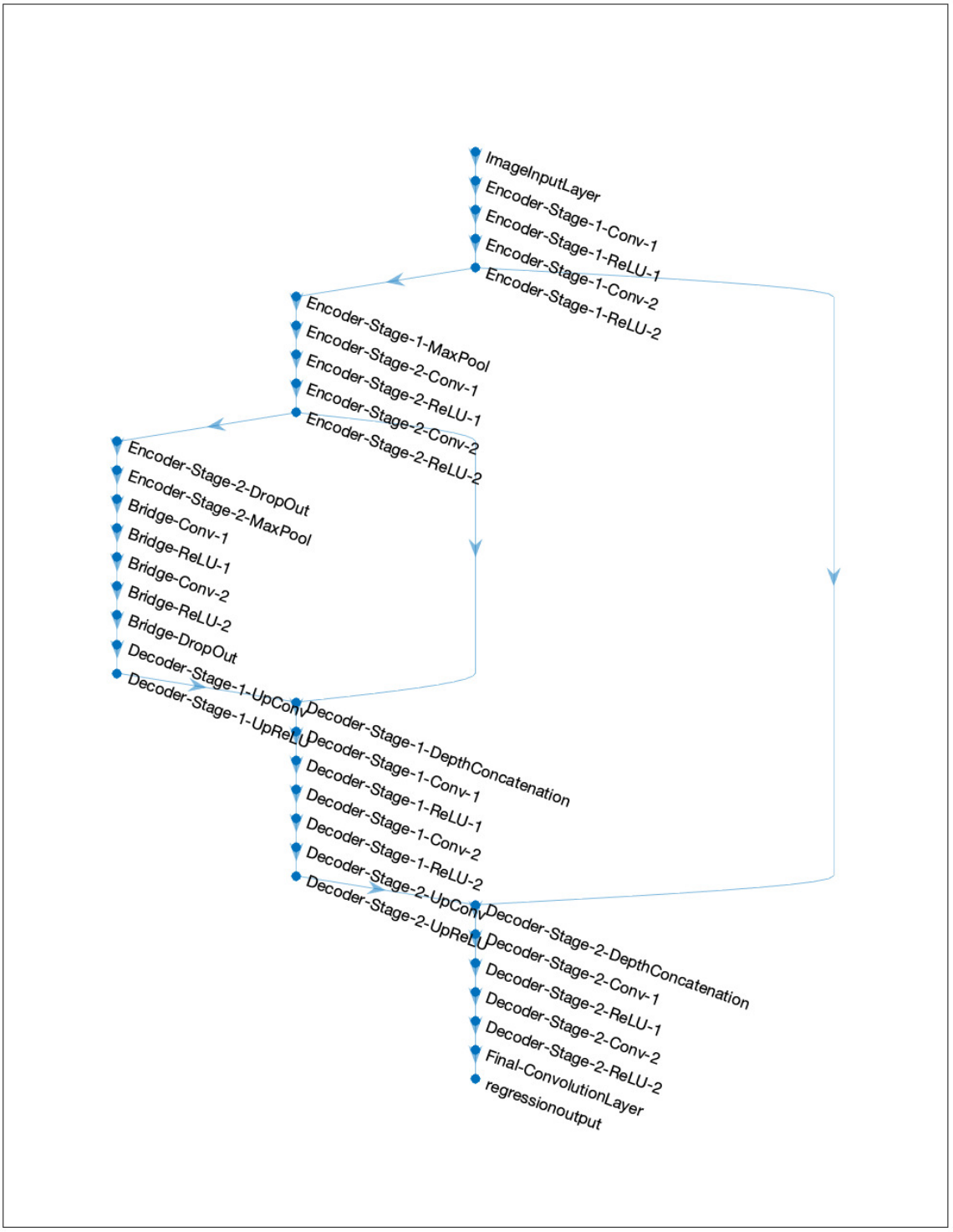


FIGURE 6.5: Architecture of the implemented U-Net with the connections

We utilize a U-Net architecture for the post-processing task. A slight modification

1.8M total learnables **33** layers

ANALYSIS RESULT

	Name	Type	Activations	Learnable Properties
1	ImageInputLayer 28×28×1 images with 'zerocenter' normalization	Image Input	28(S) × 28(S) × 1(C) × 1(B)	–
2	Encoder-Stage-1-Conv-1 64 3×3 convolutions with stride [1 1] and padding 'same'	2-D Convolution	28(S) × 28(S) × 64(C) × 1(B)	Weights 3 × 3 × 1 × 64 Bias 1 × 1 × 64
3	Encoder-Stage-1-ReLU-1 ReLU	ReLU	28(S) × 28(S) × 64(C) × 1(B)	–
4	Encoder-Stage-1-Conv-2 64 3×3 convolutions with stride [1 1] and padding 'same'	2-D Convolution	28(S) × 28(S) × 64(C) × 1(B)	Weights 3 × 3 × 64 × 64 Bias 1 × 1 × 64
5	Encoder-Stage-1-ReLU-2 ReLU	ReLU	28(S) × 28(S) × 64(C) × 1(B)	–
6	Encoder-Stage-1-MaxPool 2×2 max pooling with stride [2 2] and padding [0 0 0 0]	2-D Max Pooling	14(S) × 14(S) × 64(C) × 1(B)	–
7	Encoder-Stage-2-Conv-1 128 3×3 convolutions with stride [1 1] and padding 'same'	2-D Convolution	14(S) × 14(S) × 128(C) × 1(B)	Weights 3 × 3 × 64 × 128 Bias 1 × 1 × 128
8	Encoder-Stage-2-ReLU-1 ReLU	ReLU	14(S) × 14(S) × 128(C) × 1(B)	–
9	Encoder-Stage-2-Conv-2 128 3×3 convolutions with stride [1 1] and padding 'same'	2-D Convolution	14(S) × 14(S) × 128(C) × 1(B)	Weights 3 × 3 × 128 × 128 Bias 1 × 1 × 128
10	Encoder-Stage-2-ReLU-2 ReLU	ReLU	14(S) × 14(S) × 128(C) × 1(B)	–
11	Encoder-Stage-2-DropOut 50% dropout	Dropout	14(S) × 14(S) × 128(C) × 1(B)	–
12	Encoder-Stage-2-MaxPool 2×2 max pooling with stride [2 2] and padding [0 0 0 0]	2-D Max Pooling	7(S) × 7(S) × 128(C) × 1(B)	–
13	Bridge-Conv-1 256 3×3 convolutions with stride [1 1] and padding 'same'	2-D Convolution	7(S) × 7(S) × 256(C) × 1(B)	Weights 3 × 3 × 128 × 256 Bias 1 × 1 × 256
14	Bridge-ReLU-1 ReLU	ReLU	7(S) × 7(S) × 256(C) × 1(B)	–
15	Bridge-Conv-2 256 3×3 convolutions with stride [1 1] and padding 'same'	2-D Convolution	7(S) × 7(S) × 256(C) × 1(B)	Weights 3 × 3 × 256 × 256 Bias 1 × 1 × 256
16	Bridge-ReLU-2 ReLU	ReLU	7(S) × 7(S) × 256(C) × 1(B)	–
17	Bridge-DropOut 50% dropout	Dropout	7(S) × 7(S) × 256(C) × 1(B)	–
18	Decoder-Stage-1-UpConv 128 2×2 transposed convolutions with stride [2 2] and cropping [0 0 …	2-D Transposed Co…	14(S) × 14(S) × 128(C) × 1(B)	Weights 2 × 2 × 128 × 256 Bias 1 × 1 × 128
19	Decoder-Stage-1-UpReLU ReLU	ReLU	14(S) × 14(S) × 128(C) × 1(B)	–
20	Decoder-Stage-1-DepthConcatenation Depth concatenation of 2 inputs	Depth concatenation	14(S) × 14(S) × 256(C) × 1(B)	–
21	Decoder-Stage-1-Conv-1 128 3×3 convolutions with stride [1 1] and padding 'same'	2-D Convolution	14(S) × 14(S) × 128(C) × 1(B)	Weights 3 × 3 × 256 × 128 Bias 1 × 1 × 128
22	Decoder-Stage-1-ReLU-1 ReLU	ReLU	14(S) × 14(S) × 128(C) × 1(B)	–
23	Decoder-Stage-1-Conv-2 128 3×3 convolutions with stride [1 1] and padding 'same'	2-D Convolution	14(S) × 14(S) × 128(C) × 1(B)	Weights 3 × 3 × 128 × 128 Bias 1 × 1 × 128
24	Decoder-Stage-1-ReLU-2 ReLU	ReLU	14(S) × 14(S) × 128(C) × 1(B)	–
25	Decoder-Stage-2-UpConv 64 2×2 transposed convolutions with stride [2 2] and cropping [0 0 0 0]	2-D Transposed Co…	28(S) × 28(S) × 64(C) × 1(B)	Weights 2 × 2 × 64 × 128 Bias 1 × 1 × 64
26	Decoder-Stage-2-UpReLU ReLU	ReLU	28(S) × 28(S) × 64(C) × 1(B)	–
27	Decoder-Stage-2-DepthConcatenation Depth concatenation of 2 inputs	Depth concatenation	28(S) × 28(S) × 128(C) × 1(B)	–
28	Decoder-Stage-2-Conv-1 64 3×3 convolutions with stride [1 1] and padding 'same'	2-D Convolution	28(S) × 28(S) × 64(C) × 1(B)	Weights 3 × 3 × 128 × 64 Bias 1 × 1 × 64
29	Decoder-Stage-2-ReLU-1 ReLU	ReLU	28(S) × 28(S) × 64(C) × 1(B)	–
30	Decoder-Stage-2-Conv-2 64 3×3 convolutions with stride [1 1] and padding 'same'	2-D Convolution	28(S) × 28(S) × 64(C) × 1(B)	Weights 3 × 3 × 64 × 64 Bias 1 × 1 × 64
31	Decoder-Stage-2-ReLU-2 ReLU	ReLU	28(S) × 28(S) × 64(C) × 1(B)	–

FIGURE 6.6: Detailed layers of the implemented U-Net architecture with the layer types and respective number of parameters used

is made to the last two layers of the original U-Net architecture in [73]. The modified network is illustrated in Figure 6.5. For a more detailed view of the implemented U-Net, including the number of parameters in each layer, refer to Figure 6.6.

The U-Net network is implemented in MATLAB 2019b using the Deep Learning Toolbox. The toolbox provides a GUI application for designing deep neural networks, allowing users to construct networks via a drag-and-drop interface from a wide selection of network layers, as demonstrated in Figure 6.7.

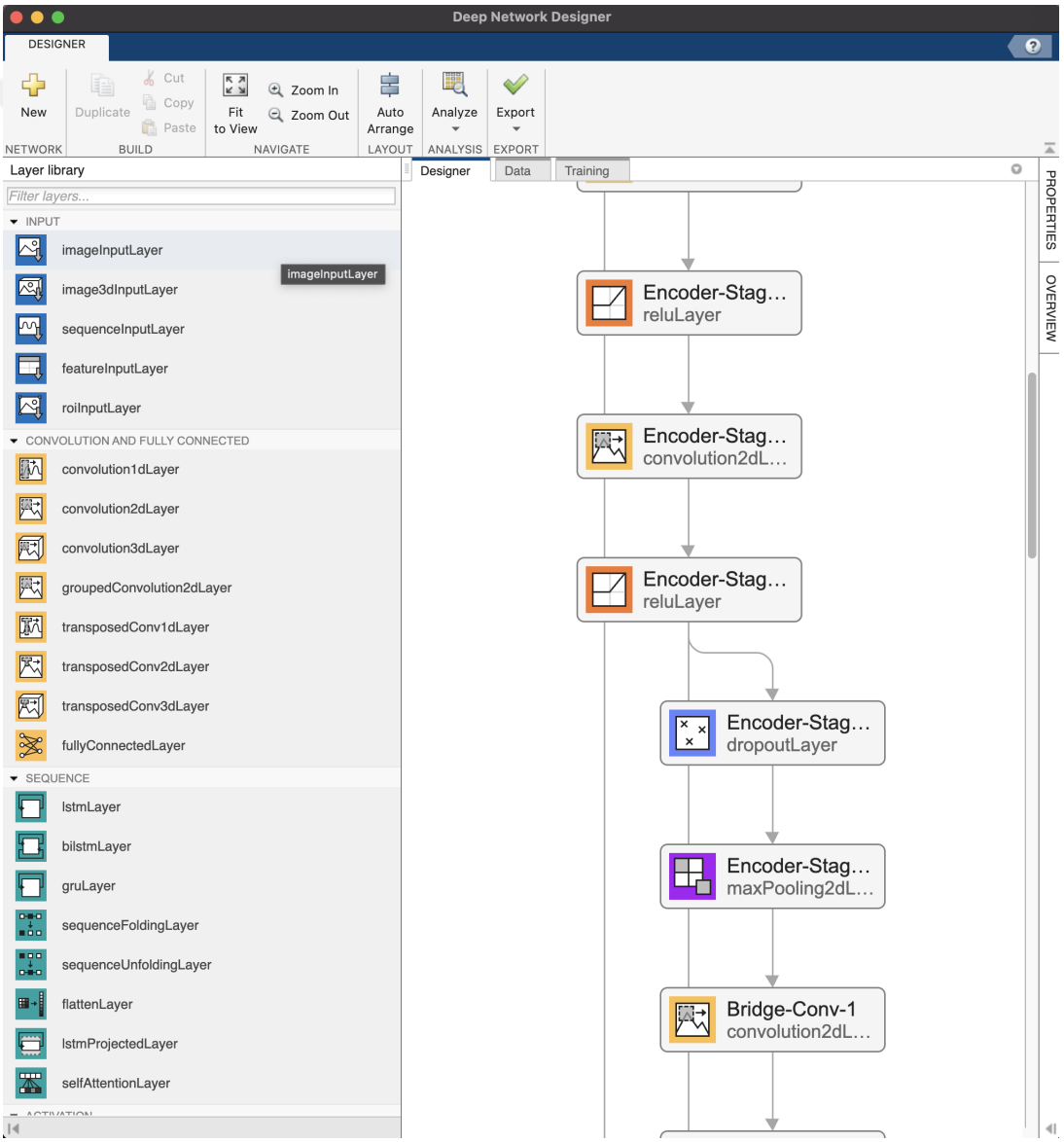


FIGURE 6.7: Deep network designer GUI of Deep Learning Toolbox in Matlab.

6.2.4 Numerical Results

We explore two distinct scenarios: 1) Reconstruction under limited data without measurement noise, and 2) Reconstruction with full data under measurement noise, denoted as "superresolution" and "denoising" respectively. In these scenarios, measurements are generated using the Fourier Transform, as described by relation (6.14).

For the denoising problem, we introduce artificial noise with varying power levels, assuming full bandwidth availability. The measurement noise follows an additive white Gaussian noise model with a probability density function of $\mathbf{w} \sim \mathcal{N}(\mathbf{0}, \sigma)$. In the superresolution problem, measurements are obtained through a high-resolution to low-resolution Fourier Transform, resulting in low-bandwidth measurements and no measurement noise is introduced. Table 6.1 provides an overview of the measurement conditions for the investigated scenarios.

Method	Bandwidth Level	Measurement Noise Level
Superresolution	Varying	0
Denoising	Full	Varying

TABLE 6.1: Measurement conditions for considered superresolution and denoising problems

To control the measurement bandwidth, we apply a low-pass filter to the discrete 2D Fourier transform of the reflectivity map of the scene, $f(x, y)$, and then convert it back to the image space as follows:

$$f(x, y) = \mathcal{F}^{-1}\left\{H(u, v) \cdot F(u, v)\right\} \tag{6.15}$$

where $F(u, v)$ denotes the Fourier Transform of the radar scene, given by

$$F(u, v) = \sum_{x=0}^{N-1} \sum_{y=0}^{M-1} f(x, y) \cdot e^{-i2\pi\left(\frac{ux}{N} + \frac{vy}{M}\right)} \tag{6.16}$$

and $H(u, v)$ is the mask that passes only low frequencies. The operator $\mathcal{F}^{-1}$ denotes the inverse 2D DFT.

We use MNIST data set [74] to train and test the performance of post-processing method under the considered scenarios. The MNIST dataset is a well-known benchmark in the fields of machine learning and computer vision. It comprises a set of 28×28 pixel grayscale images depicting handwritten digits ranging from 0 to 9, each tagged by its respective label. We consider 6 different noise levels and 5 bandwidth levels for denoising and superresolution problems and we train the network for each case individually. To vary the measurement noise level, we vary the σ and to vary the bandwidth we change the size of low-pass filter applied.

We explore six distinct noise levels and five bandwidth levels for the denoising and superresolution problems, respectively and train a network for each scenario individually. To adjust the measurement noise level, we manipulate standard deviation σ of the measurement noise, while variations in bandwidth are achieved by altering the size of the applied low-pass filter.

In the experiments, we utilize a subset of the MNIST dataset comprising 10,000 hand-written digit images. This dataset is partitioned into 70% for training, 15% for validation, and 15% for testing. Images reconstructed via FFT under specific measurement conditions serve as input, while the original images act as ground truth labels for training the U-Net model. This process is replicated for both denoising and superresolution tasks across various measurement scenarios.

For the performance evaluation of the studied method, in addition to MSE and PSNR metrics defined Chapter 5, we also use the Structural Similarity Index (SSIM). The SSIM is a metric widely used in image processing to measure the similarity between two images. It is usually represented by the following formula:

$$\mathrm{SSIM}(\mathbf{x}, \mathbf{y}) = \frac{(2\mu_x\mu_y + C_1)(2\sigma_{xy} + C_2)}{(\mu_x^2 + \mu_y^2 + C_1)(\sigma_x^2 + \sigma_y^2 + C_2)} \tag{6.17}$$

Here, μ_x and μ_y are the means of the images $\mathbf{x}$ and $\mathbf{y}$ respectively, σ_x^2 and σ_y^2 are the variances, σ_{xy} is the covariance, and C_1 and C_2 are constants to stabilize the division with weak denominators. This formula computes the similarity index

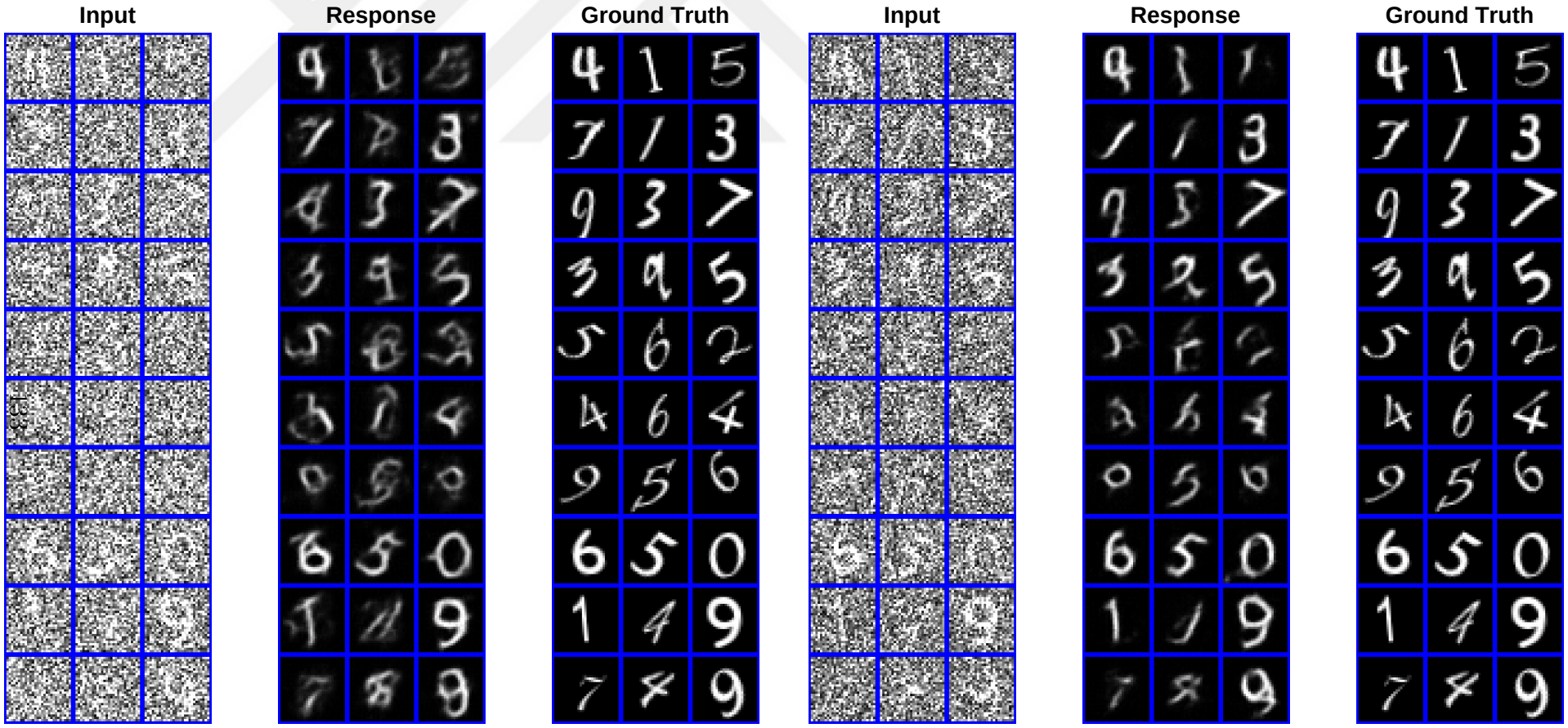
based on luminance, contrast, and structure comparisons between the two images. Higher SSIM values imply greater similarity between the images [46].

Figure 6.8 and 6.9 depict the denoising results across various measurement noise powers. The "input" images represent those reconstructed by FFT, while "response" denotes the output of the trained U-Net, and "ground truth" indicates the original MNIST images. Even in the presence of strong measurement noise, U-Net demonstrates remarkable performance in denoising the images, as observed in the demonstrated test images.

Similarly, Figures 6.10 through 6.12 showcase the superresolution task outcomes across different bandwidth levels. Analogous to the denoising results, U-Net exhibits the capability to enhance input images across various measurement bandwidths.

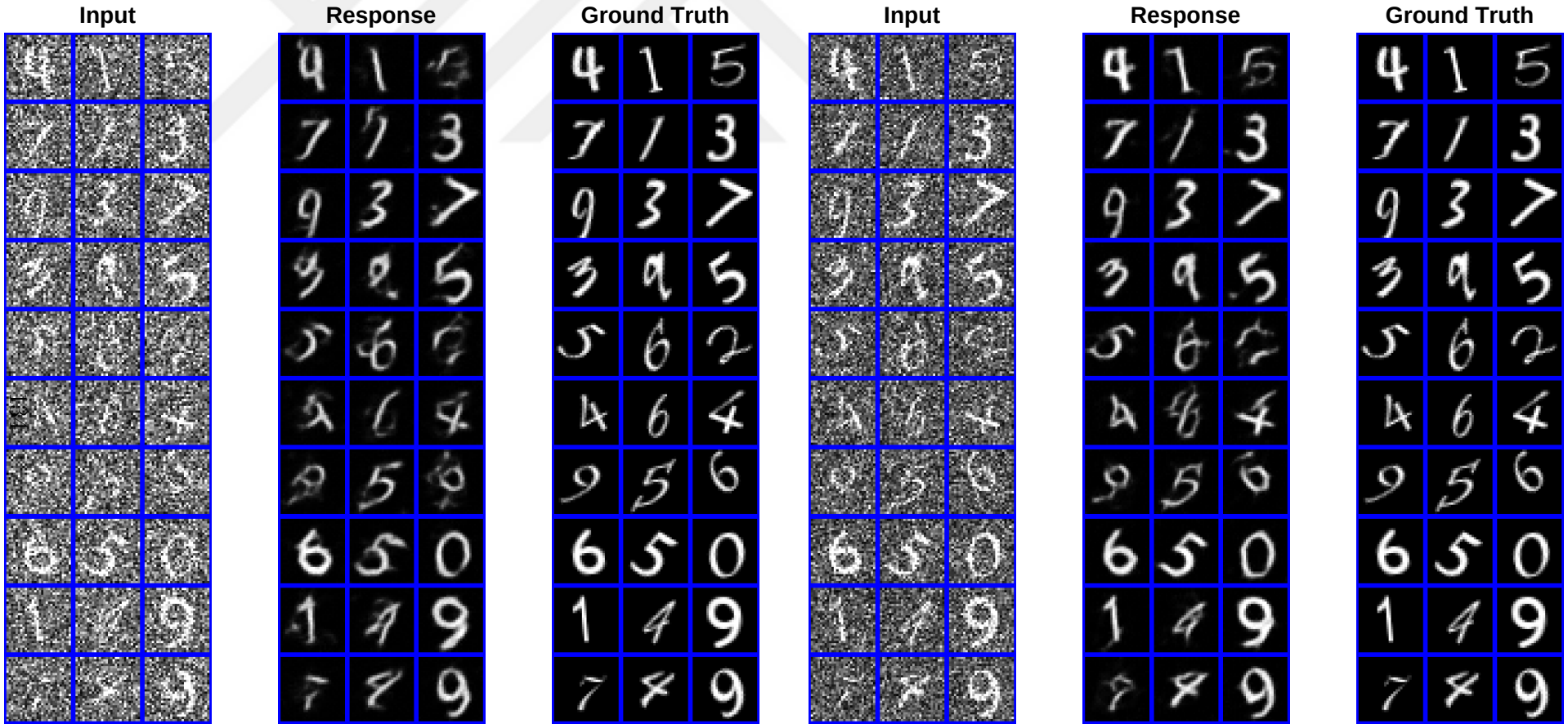
Using the images in the test data set, we simulate radar measurements through Fourier transform as a forward model, considering different measurement noise and bandwidth conditions. Subsequently, we reconstruct radar images of handwritten digit images using inverse Fourier transform. Post-processing is then performed through the trained U-Net for each respective test scenario. We calculate the MSE, PSNR, and SSIM, averaged across 1500 test images.

In Figures 6.13a and 6.13b, these averaged performance metrics are shown as a function of measurement noise power and bandwidth levels, respectively. It is evident from all the plots that incorporating U-Net in the reconstruction as a post-processing step significantly improves all performance metrics.



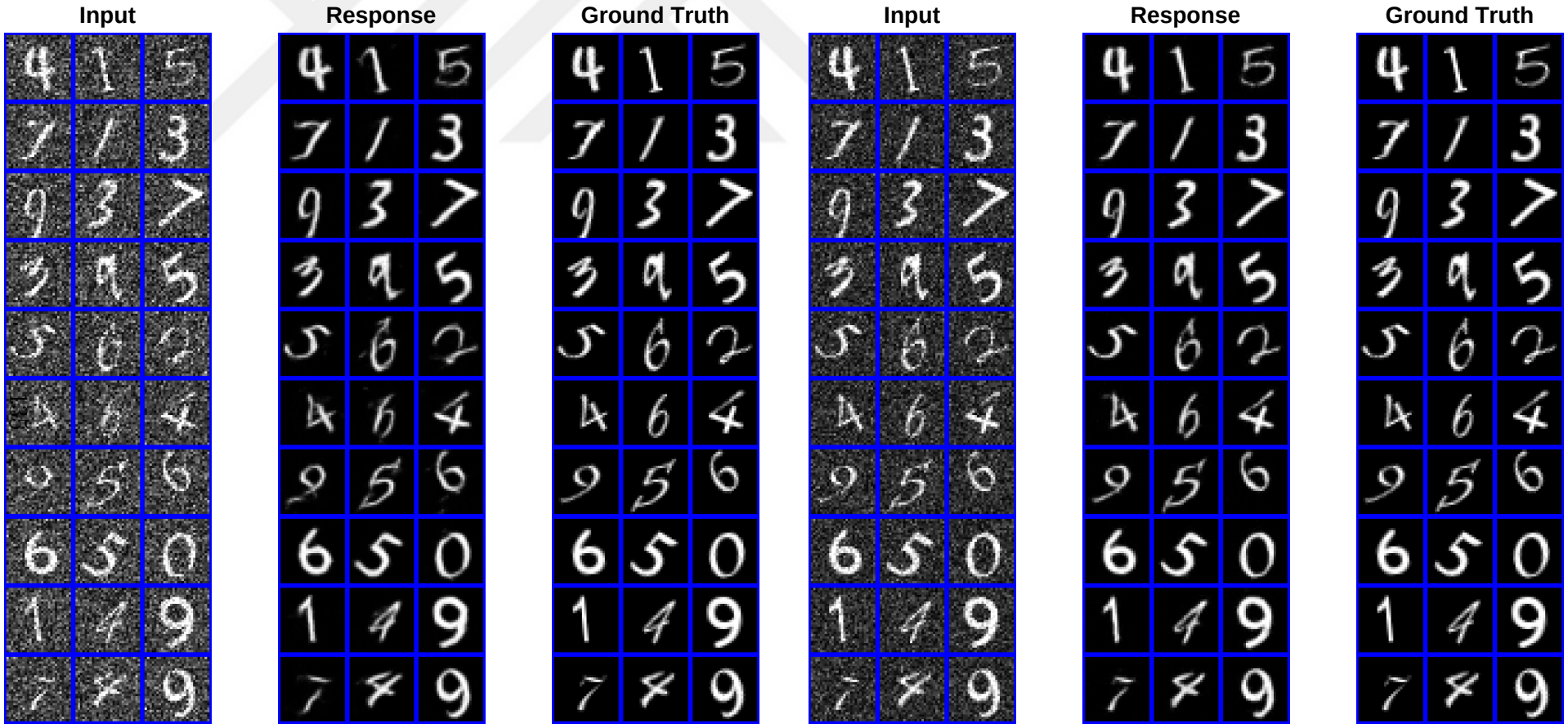
(A) $\sigma = 14$ (B) $\sigma = 12$

FIGURE 6.8: Denoising problem - Performance of conventional FFT based reconstruction and post-processing with U-Net



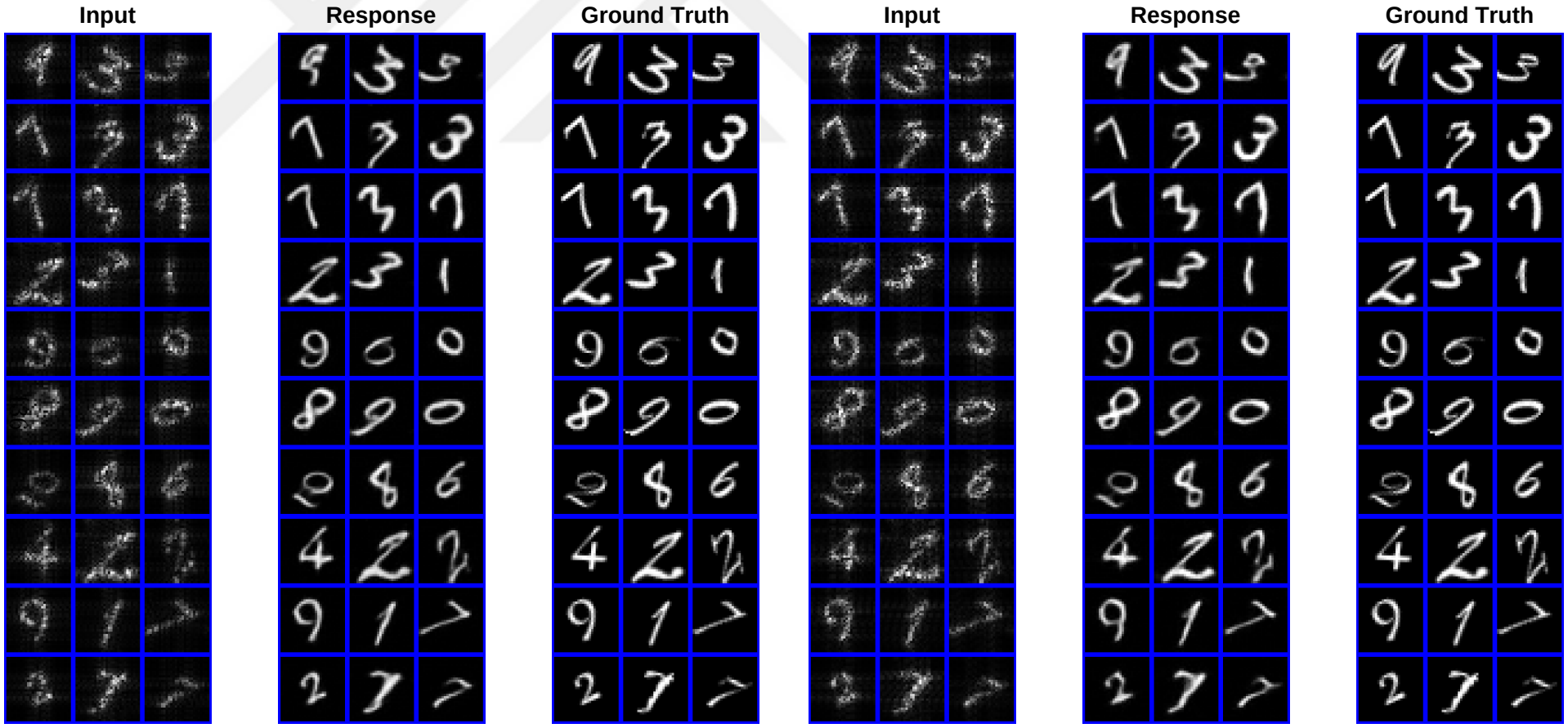
(A) $\sigma = 10$ (B) $\sigma = 8$

FIGURE 6.9: Denoising problem - Performance of conventional FFT based reconstruction and post-processing with U-Net



(A) $\sigma = 6$ (B) $\sigma = 4$

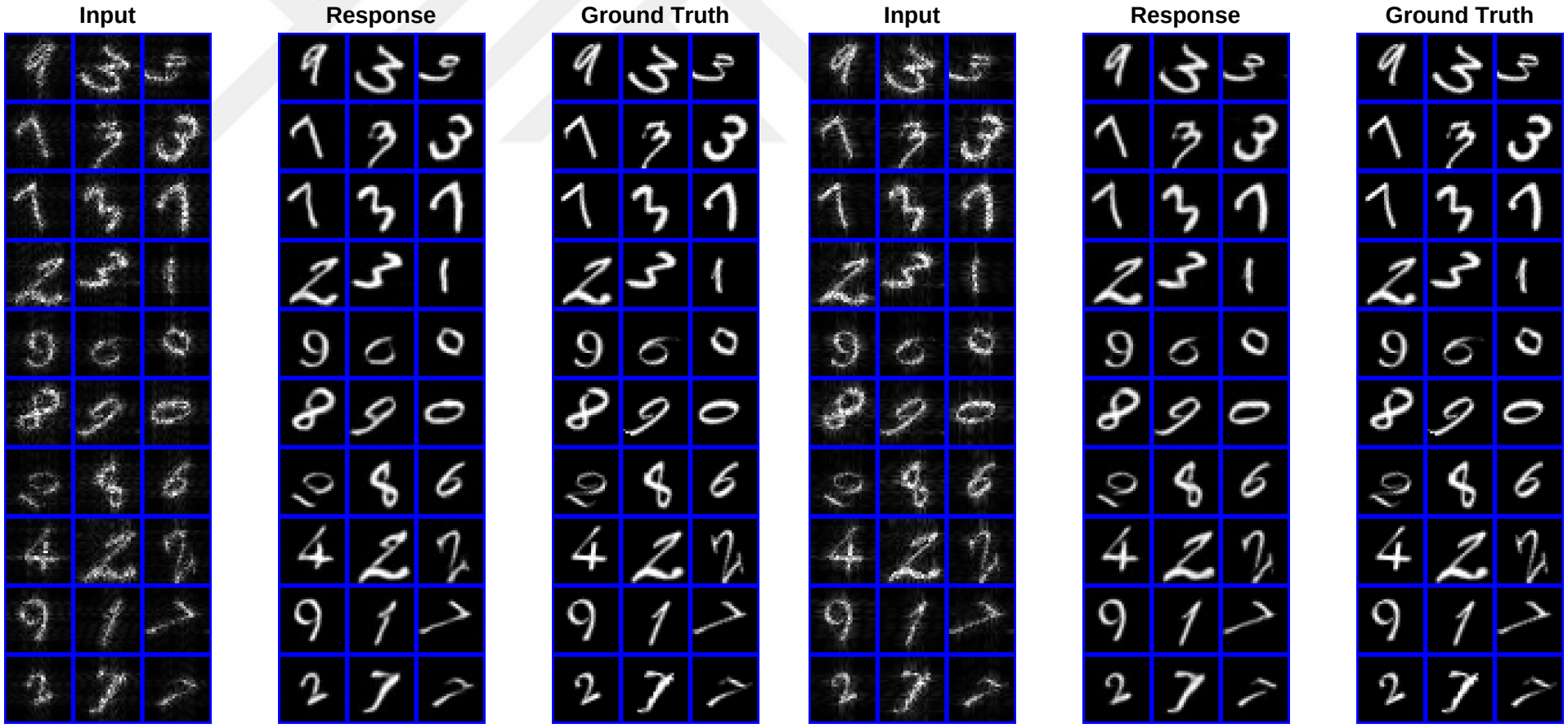
FIGURE 6.10: Superresolution problem - Performance of conventional FFT based reconstruction and post-processing with U-Net



(A) Data available, 41 %

(B) Data available, 51 %

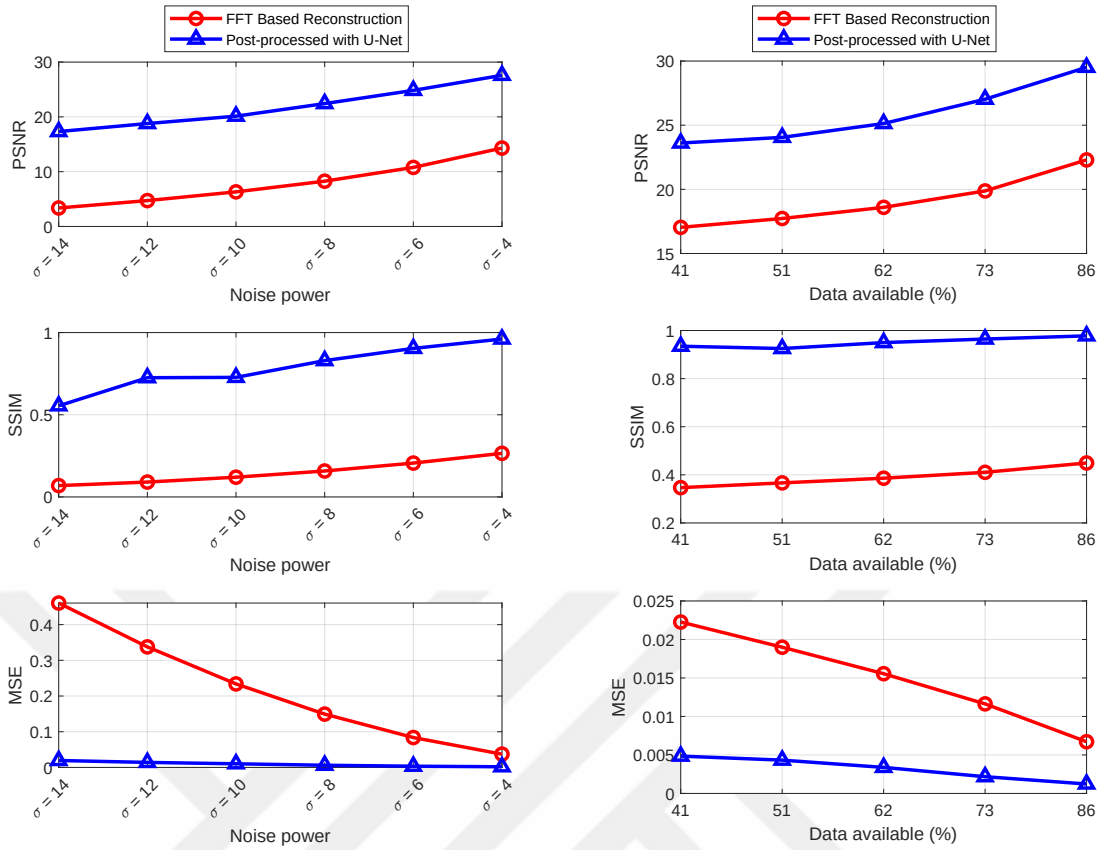
FIGURE 6.11: Superresolution problem - Performance of conventional FFT based reconstruction and post-processing with U-Net



(A) Data available 62 %

(B) Data available, 73 %

FIGURE 6.12: Superresolution problem - Performance of conventional FFT based reconstruction and post-processing with U-Net



(A) Reconstruction performances at different noise levels

(B) Reconstruction performances at different measurement data levels

FIGURE 6.13: Performance comparison of conventional (FFT based) and proposed range profile reconstruction technique under different measurement data availability and measurement noise conditions

6.3 Near-field MIMO Radar Imaging Using Plug and Play Denoisers

In this section, we explore Ultra Wide Band (UWB) near-field MIMO radar imaging, a technique initially proposed by [75]. We consider the same imaging setup as in [76]. The imaging setup involves a planar array of transmitter and receiver radar antennas positioned on an imaging platform, as illustrated in Figure 6.14. By gathering multi-static radar measurements at various spatial locations, the objective is to estimate the 3D reflectivity map of the unknown object being imaged. In this configuration, transmitters take turns transmitting signals over time, while

the receivers concurrently collect the returning signals. Within this setup, MIMO antennas are distributed on a plane at $z = 0$, whereas the center of the object lies at a distance z_0 away from the radar imaging plane.

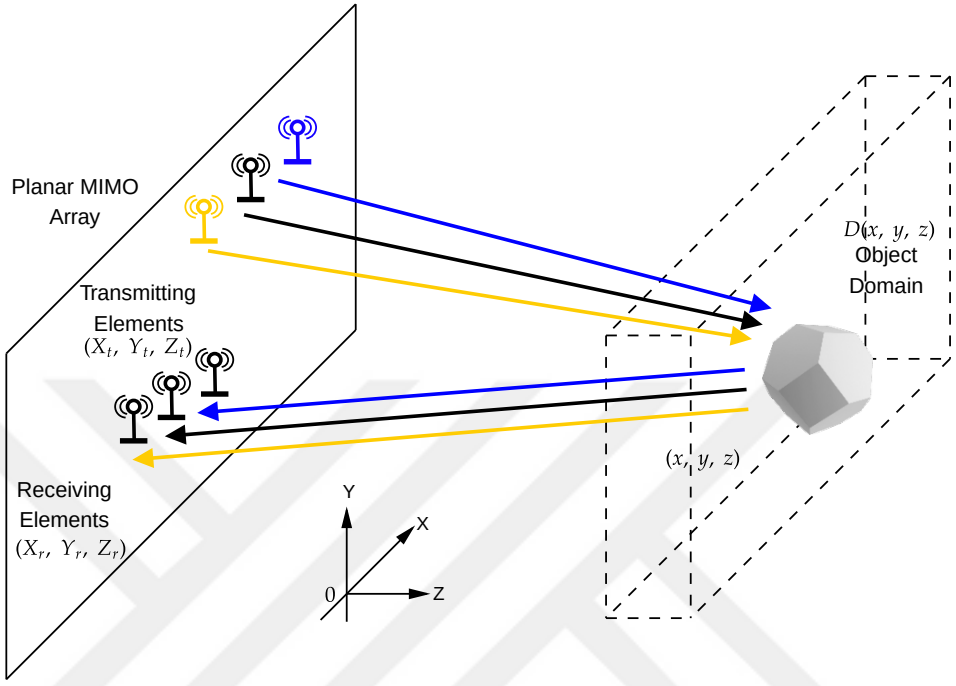


FIGURE 6.14: Representative imaging setup

The measurement/sensing model is pivotal in reconstructing the reflectivity map of the unknown object from radar returns, as it establishes a mathematical connection between the reflectivity map and the radar measurements. Once fully known, it enables the estimation of the reflectivity map under certain conditions. Therefore, we first examine the measurement model, adopting the same approach as [77]. Our configuration involves a cross-shape MIMO radar, illustrated in Figure 6.15. We adhere to the notation established in [77], where transmitting antenna positions are denoted by $p_i = (x_R, y_R, 0)$ and receiving antenna positions are represented as $p_j = (x_T, y_T, 0)$. Under Born's approximation, the scattering wave resulting from the transmission of transmitting antenna i sensed at receiver j, as a function of time, is given by:

$$r(i,j,t) = \int\int\int \frac{1}{4\pi d_{T_i} d_{R_j}} f(x,y,z) p\left(t - \left[\frac{d_{T_i}}{c} + \frac{d_{R_j}}{c}\right]\right) dx\, dy\, dz \qquad (6.18)$$

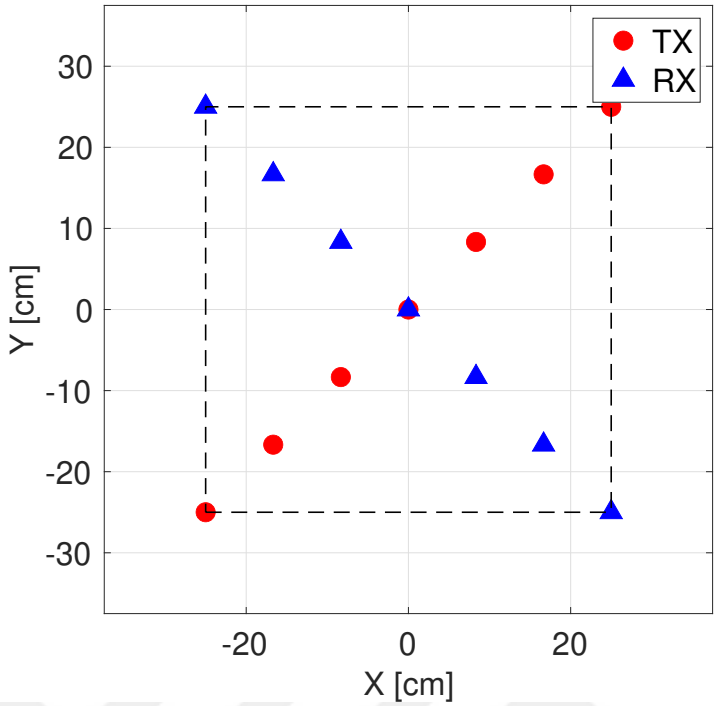


FIGURE 6.15: MIMO radar antenna configuration

Here, $f(x, y, z)$ represents the 3D reflectivity distribution function that we aim to determine. R_i and R_j denote the distances from the ith receiver and j^{th} transmitter antenna, respectively, to a specific point in the imaging space with coordinates (x, y, z). The function $p(t)$ denotes the radar pulse waveform. The distances R_i and R_j are determined by the following expressions:

$$d_{T_i} = \sqrt{(x_i - x)^2 + (y_i - y)^2 + z^2}, \quad \forall i \in \{1, 2, ..., N_T\} \tag{6.19}$$

$$d_{R_j} = \sqrt{(x_j - x)^2 + (y_j - y)^2 + z^2}, \quad \forall j \in \{1, 2, ..., N_R\} \tag{6.20}$$

where N_T and N_R are the number of transmitter and receiver antennas, respectively. By using time-shifting property, the Fourier transform of the signal described by Eq. (6.18) can be expressed as:

$$r(T_i, T_j, k) = 4\pi\ p(k) \int\int\int \frac{e^{-jkd_{T_i}}}{4\pi d_{T_i}} \frac{e^{-jkd_{R_j}}}{4\pi d_{R_j}} f(x, y, z)\ dx\ dy\ dz \tag{6.21}$$

Here, $k = \frac{2\pi}{\lambda}$ denotes the wavenumber, and $p(k)$ represents the transmitted pulses in the frequency or k-number domain. For computational purposes, expressions can be discretized by uniformly sampling the reflectivity field into voxels, yielding the following discrete relation [77]:

$$\begin{aligned} r(i,j,l) = \; & p(k_l) \sum_{v=1}^{N_v} \frac{e^{-jk_l(d_{T_i}+d_{R_j})}}{4\pi d_{T_i} d_{R_j}} q_v \\ & i \in \{1,2,...,N_T\} \\ & j \in \{1,2,...,N_R\} \\ & l \in \{1,2,...,N_L\} \\ & v \in \{1,2,...,N_v\} \end{aligned} \tag{6.22}$$

Here, i denotes the transmitter antenna index, j represents the receiver antenna index, l indicates the transmission frequency, and v is the voxel index. We assume that each voxel individually contributes to the signal received at each receiver antenna. The model given by (6.22) represents a linear system of equations and can be expressed as matrix multiplication. To represent this relation in a compact matrix form, we arrange the reflectivity values of each voxel in lexicographic order in vector $\mathbf{q}$. Similarly, measurements are stacked in vector $\mathbf{r}$ in the same manner. With these data arrangements, we define our discrete forward model in matrix form as follows:

$$\mathbf{r} = \mathbf{T}\mathbf{q} \tag{6.23}$$

In this context, $\mathbf{T} \in \mathbb{C}^{M \times N}$ represents the measurement/sensing matrix, while $\mathbf{w} \in \mathbb{C}^{N \times 1}$ denotes the measurement noise. The vector $\mathbf{r} \in \mathbb{C}^{M \times 1}$ contains the radar measurements, and $\mathbf{q} \in \mathbb{C}^{N \times 1}$ is the unknown vectorized radar scene that we aim to estimate from the noisy radar measurements. Here, $M = N_T \times N_R \times N_L$ denotes the total number of measurements, and $N = N_v$ represents the total number of voxel reflectivity values to be determined.

The model described in (6.23) represents the noise-free scenario. However, in real-life applications, radar measurements are often affected by both internal and external noise sources. Incorporating a complex white noise uncorrelated at each

receiver antenna, denoted by $\mathbf{w} \in \mathbb{C}^{M\times 1}$, our final linear measurement model is given by:

$$\mathbf{r} = \mathbf{T}\mathbf{q} + \mathbf{w} \tag{6.24}$$

In this study, we rely on the following assumptions: 1) Radar reflectivity values of each pixel in the volume under examination are assumed to be real-valued. This implies that they merely scale the incoming RF signal without altering its phase. This assumption is common in various inverse electromagnetic problems studied in the literature, as seen in references such as [78] and [79]. 2) We employ Born's approximation to model the electromagnetic scattering phenomena, following the approach outlined in [77]. 3) Each voxel in the volume acts as an independent 3D radar cell, without causing any inter-cell interference in terms of reflection and is assumed to have isotropic reflectivity.

6.3.1 Plug-and-Play Radar Image Formation

In many radar imaging scenarios, the number of measurements is often significantly lower than the number of voxels, i.e., $M << N$. In such cases, the sensing matrix becomes ill-conditioned, and traditional inversion methods may not yield satisfactory solutions. To address this issue, regularization techniques are necessary. In this section, we delve into solving this inverse imaging problem in a regularized manner, leveraging the Plug and Play ADMM framework.

Although we consider 3D reflectivity function up until this point and derive the measurement model in 3D, we work with 2-D radar images in the next section without any loss of generality. For this purpose we choose to work with 2D MNIST data set which contains 2D hand-written digits. This could be considered as a simplified problem with one dimension dropped.

After formulating the problem as shown in Equation 6.24, we can adopt the same approach as in Section 5.5 for the range profile reconstruction problem, as both reconstructed vectors are real-valued. Initially, we formulate a regularized inversion with a least squares data fidelity term, followed by setting the ADMM steps

for our radar imaging problem. For the objective function, we use a weighted sum of the least squares data fidelity term and a regularizer term, resulting in a typical regularized inversion problem formulated as follows:

$$\hat{\mathbf{q}} = \underset{\mathbf{q}}{\operatorname{argmin}} \left\{ \|\mathbf{r} - \mathbf{T}\mathbf{q}\|_2^2 + \lambda \mathcal{R}(\mathbf{q}) \right\} \tag{6.25}$$

Here, $\hat{\mathbf{q}}$ represents the estimated reflectivity vector, λ is the regularization parameter, and $\mathcal{R}(\mathbf{q})$ is the regularizer term applied to the reflectivity vector $\mathbf{q}$. This formulation balances between fitting the measured data and enforcing desired properties or constraints on the solution.

We introduce an auxiliary variable $\mathbf{h} \in \mathbb{R}^{N \times 1}$ to the problem (6.25):

$$\begin{aligned} \{\mathbf{q}, \mathbf{h}\} = & \underset{\mathbf{q},\mathbf{h}}{\operatorname{argmin}} \left\{ \|\mathbf{r} - \mathbf{T}\mathbf{q}\|_2^2 + \lambda \mathcal{R}(\mathbf{q}) \right\} \\ & \text{s.t.} \quad \mathbf{q} - \mathbf{h} = 0 \end{aligned} \tag{6.26}$$

Then the objective function in augmented Lagrangian form of (6.26) is written as:

$$\mathcal{L} = \|\mathbf{r} - \mathbf{T}\mathbf{q}\|_2^2 + \lambda \mathcal{R}(\mathbf{h}) + \frac{\rho}{2} \|\mathbf{q} - \mathbf{h} + \mathbf{u}\|_2^2 + \frac{\rho}{2} \|\mathbf{u}\|_2^2$$

Defining two more dummy vectors:

1. $\tilde{\mathbf{q}} = \mathbf{h} - \mathbf{u}$
2. $\tilde{\mathbf{h}} = \mathbf{q} + \mathbf{u}$

we construct the sub-optimization problems of the ADMM formulation as follows:

$$\hat{\mathbf{q}} = \underset{\mathbf{q}}{\operatorname{argmin}} \left\{ \|\mathbf{r} - \mathbf{T}\mathbf{q}\|_2^2 + \frac{\rho}{2} \|\mathbf{q} - \tilde{\mathbf{q}}\|_2^2 \right\}, \tag{6.27a}$$

$$\hat{\mathbf{h}} = \underset{\mathbf{h}}{\operatorname{argmin}} \left\{ \lambda \mathcal{R}(\mathbf{h}) + \frac{\rho}{2} \left\| \tilde{\mathbf{h}} - \mathbf{h} \right\|_2^2 \right\}, \tag{6.27b}$$

$$\hat{\mathbf{u}} = \mathbf{u} + \mathbf{q} - \mathbf{h} \tag{6.27c}$$

Equation (6.27a) represents the model inversion and depends solely on the forward/measurement model and measurements. Equation (6.27b) corresponds to the denoising operator applied to the radar reflectivity function and relies on the choice of the regularizer function $\mathcal{R}$ (i.e., priors). Equation (6.27c) denotes the auxiliary updates of ADMM. It's crucial to observe how the model/data and prior optimization subproblems are decoupled from each other within this framework. The adaptable modularity of ADMM facilitates the plug-and-play integration of various denoisers in a completely independent manner.The alternating steps of the ADMM framework is illustrated in Figure 6.16.

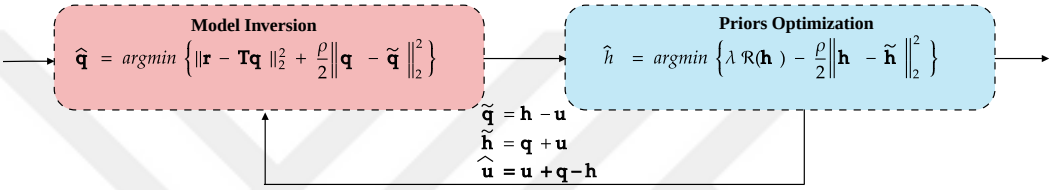


FIGURE 6.16: A block diagram representation of alternating optimization steps of ADMM: Forward model is inverted to solve the subproblem in (6.27a) and any appropriate denoiser can be chosen in a Plug-And-Play manner to solve for subproblem in (6.27b)

To find the solution of the sub-problem (6.27a) has a closed-form solution, we take the partial derivative of the objective function with respect to $\mathbf{q}$ and obtain the following gradient vector $\nabla\mathbf{q}$:

$$\nabla\mathbf{q} = -2\mathbf{T}^H\mathbf{r} + 2\mathbf{T}^H\mathbf{T}\mathbf{q} + \rho\left(\mathbf{I}\mathbf{q} - \tilde{\mathbf{q}}\right) \tag{6.28}$$

Arranging (6.28), we get

$$\nabla\mathbf{q} = \left(2\mathbf{T}^H\mathbf{T} + \rho\mathbf{I}\right)\mathbf{q} - \left(2\mathbf{T}^H\mathbf{r} + \rho\tilde{\mathbf{q}}\right)$$

By equating $\nabla\mathbf{q}_m$ to zero, we get the first-order optimality condition as follows:

$$\underbrace{\left(2\mathbf{T}^H\mathbf{T} + \rho\mathbf{I}\right)}_{\mathbf{A}}\mathbf{q} = \underbrace{\left(2\mathbf{T}^H\mathbf{r} + \rho\tilde{\mathbf{q}}\right)}_{\mathbf{b}} \tag{6.29}$$

with the following closed-form solution:

$$\hat{\mathbf{q}} = \left(2\mathbf{T}^H\mathbf{T} + \rho\mathbf{I}\right)^{-1}\left(2\mathbf{T}^H\mathbf{r} + \rho\tilde{\mathbf{q}}\right) \tag{6.30}$$

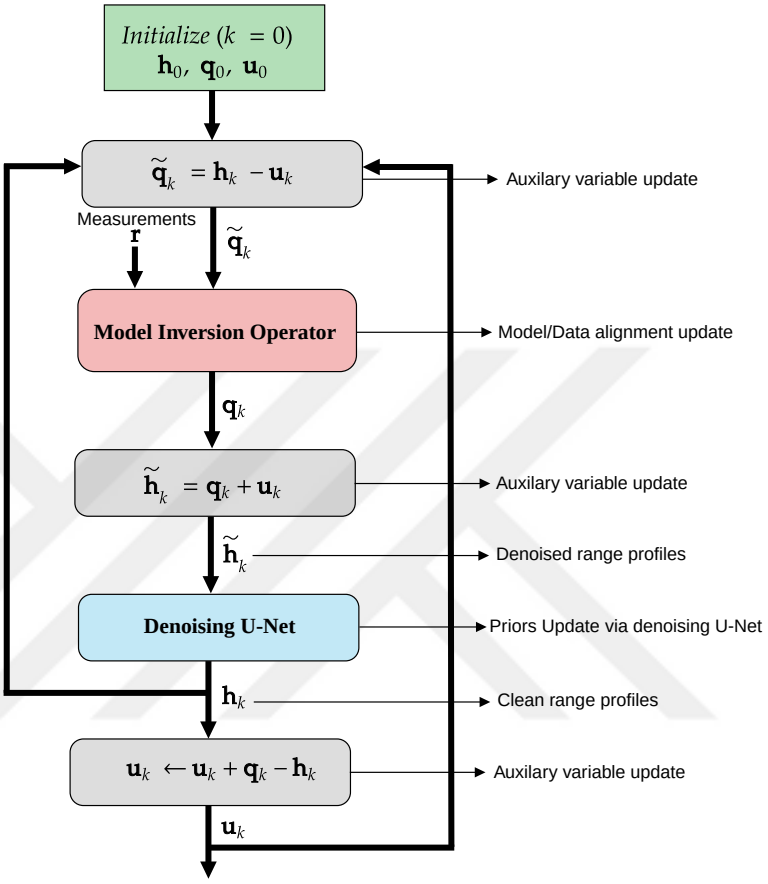


FIGURE 6.17: Flow chart describing the ADMM iterations for model/data and priors update. Model/data update is executed by computing the solution in (6.27b), and priors update is accomplished through a denoising U-Net.

To approximate the solution of sub-problem (6.27b), we employ a denoiser, the rationale for which is extensively discussed in Chapter 5. For this task, we leverage a deep learning model functioning as an estimator for sub-problem (6.27b). Given its demonstrated denoising efficacy as showcased in Chapter 5, we opt for the U-Net architecture, as depicted in Figure 6.5 of Section 6.2.

In Figure 6.17, a flow chart illustrating the ADMM updates is presented. Here, a single iteration of the ADMM framework is depicted, and this process continues until convergence. The ADMM procedure initiates with conventional FFT-based

estimation, succeeded by a model-data alignment update and priors update via a denoising U-Net. The pre-trained CNN processes noisy range profiles and generates a cleaned version for utilization in the subsequent iteration of ADMM.

6.3.2 Numerical Results

We employ a cross-shaped MIMO radar architecture comprising 7 transmit (TX) antennas and 7 receive (RX) antennas, depicted in Figure 6.15. Our aim within this imaging scenario is to infer the reflectivity characteristics of pixels lying within a plane defined by $z = z_0$ cm. The MIMO antennas are uniformly spaced over a 50 cm by 50 cm plane situated 70 cm away from the imaging center, as depicted in Figure 6.18. The operational frequency for MIMO transmissions is set to 24 GHz, and a stepped frequency MIMO approach is employed with a step frequency of 1 GHz. For image representation, we utilize the MNIST dataset, presuming a direct correlation between image intensity levels and radar reflectivity. Each MNIST image, comprising 28×28 pixels, corresponds to a radar cross-range cell, with each cell's cross-range resolution being given by:

$$\Delta x = \frac{\lambda \cdot d}{\mathrm{L}_x}$$
$$\Delta y = \frac{\lambda \cdot d}{\mathrm{L}_y}$$

The measurement matrix is generated based on the imaging setup outlined in Figure 6.18. We simulate measurements employing the imaging model given in (6.24). In our simulations, we vary the noise levels and data availability to evaluate the effectiveness of the proposed Plug-and-Play ADMM approach. Our U-Net is trained across a range of noise levels to enhance its adaptability and robustness.

We present the reconstruction performances of our proposed solution across various simulation scenarios. Additionally, we compare the performance of the Plug-and-Play ADMM with U-Net framework against other benchmark methods. Figures 6.19 through 6.22 depict the reconstruction performance of each method under different measurement data levels: 25%, 50%, 75%, and 100%, respectively for a

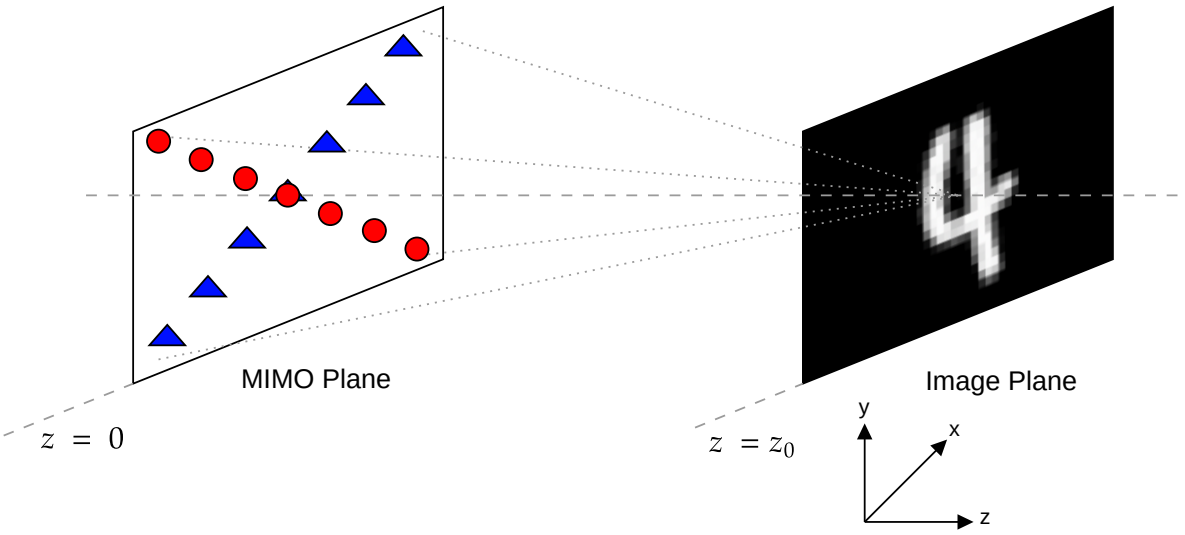


FIGURE 6.18: MIMO radar antenna configuration

test image. The number of measurements is varied by adjusting the number of step frequencies while keeping the number of antennas fixed for each investigated scenario. For instance, the 25% data measurement level is achieved when the number of stepped frequencies transmitted is set to 4, yielding $\frac{M}{N} = \frac{4\times7\times7}{28\times28} \times 100\% = 25\%$. In each figure, the columns represent the reconstruction techniques employed, while the rows depict different measurement noise conditions. We use SSIM and PSNR metrics to evaluate the reconstruction performance of each method.

In this figures, LSQR denotes the least-squares solution without any regularization, while LSQR+UNET indicates that images are first reconstructed using LSQR and then refined using UNET post-processing. PnP-ADMM-TV utilizes Total Variation as a regularizer [41], whereas PnP-ADMM-RF employs a recursive filter as a denoiser within the PnP ADMM framework [42]. Our results for this test case demonstrate the robust reconstruction performance of the proposed method for 2D radar imaging applications, even under highly ill-conditioned scenarios.

6.4 Conclusion

In this chapter, we delve into two distinct MIMO radar imaging scenarios, each adopting a unique deep learning-based reconstruction approach.

The first methodology involves directly learning the post-processing of radar images reconstructed by conventional techniques. On the other hand, the second method suggests employing the PnP-ADMM framework with a U-Net architecture as a denoiser to approximate the priors optimization step within the ADMM framework.

Integrating the U-Net architecture as a post-processing step notably enhances the reconstruction performance. Furthermore, our simulations demonstrate that incorporating U-Net as a denoiser within the ADMM framework further improves the radar image reconstruction performance.

Numerical findings indicate that PnP-ADMM with U-Net architecture achieves the highest MSE performance compared to other methodologies explored.

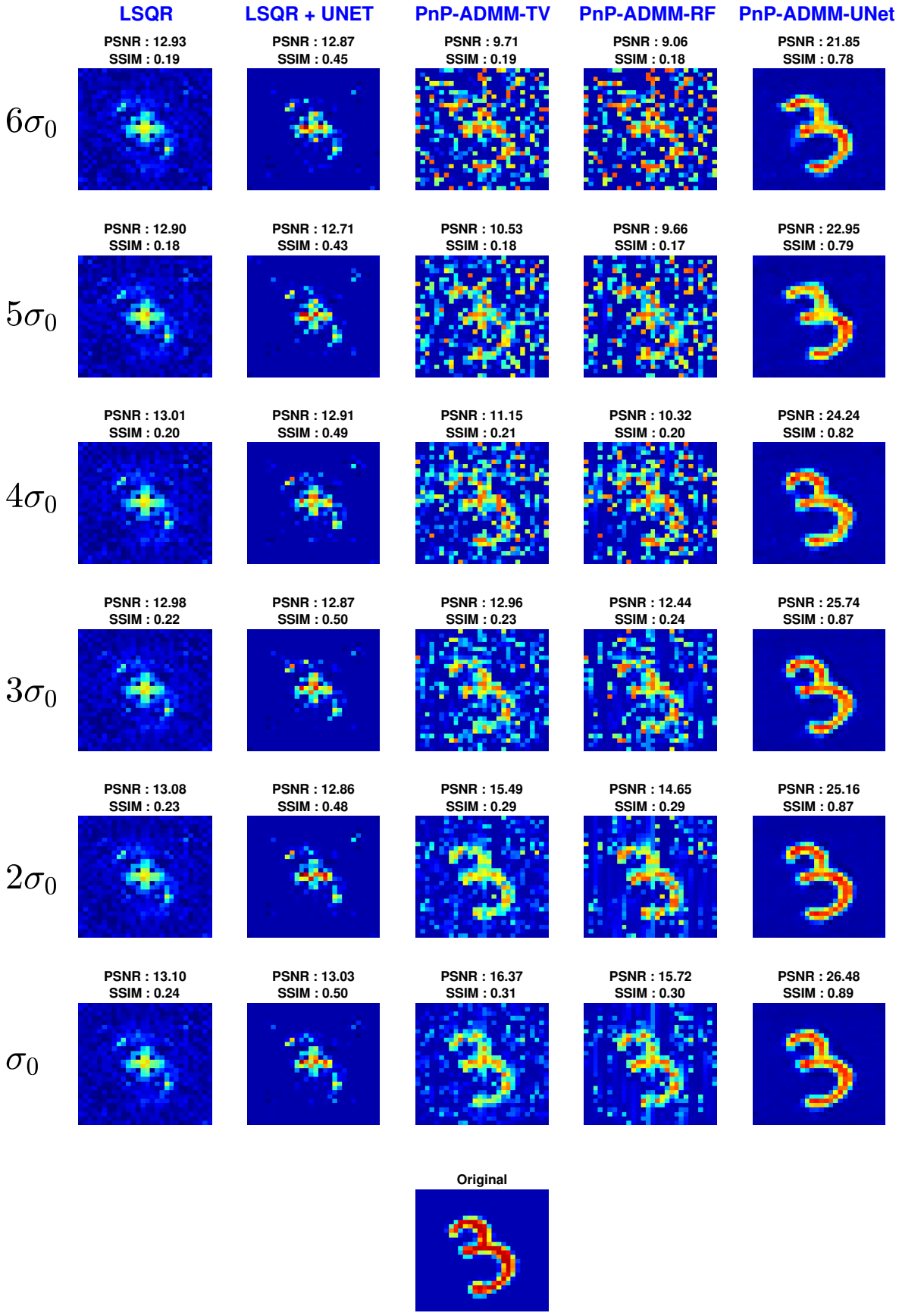


FIGURE 6.19: Measurement to unknowns ratio: 25% ($\frac{M}{N} = 25\%$)

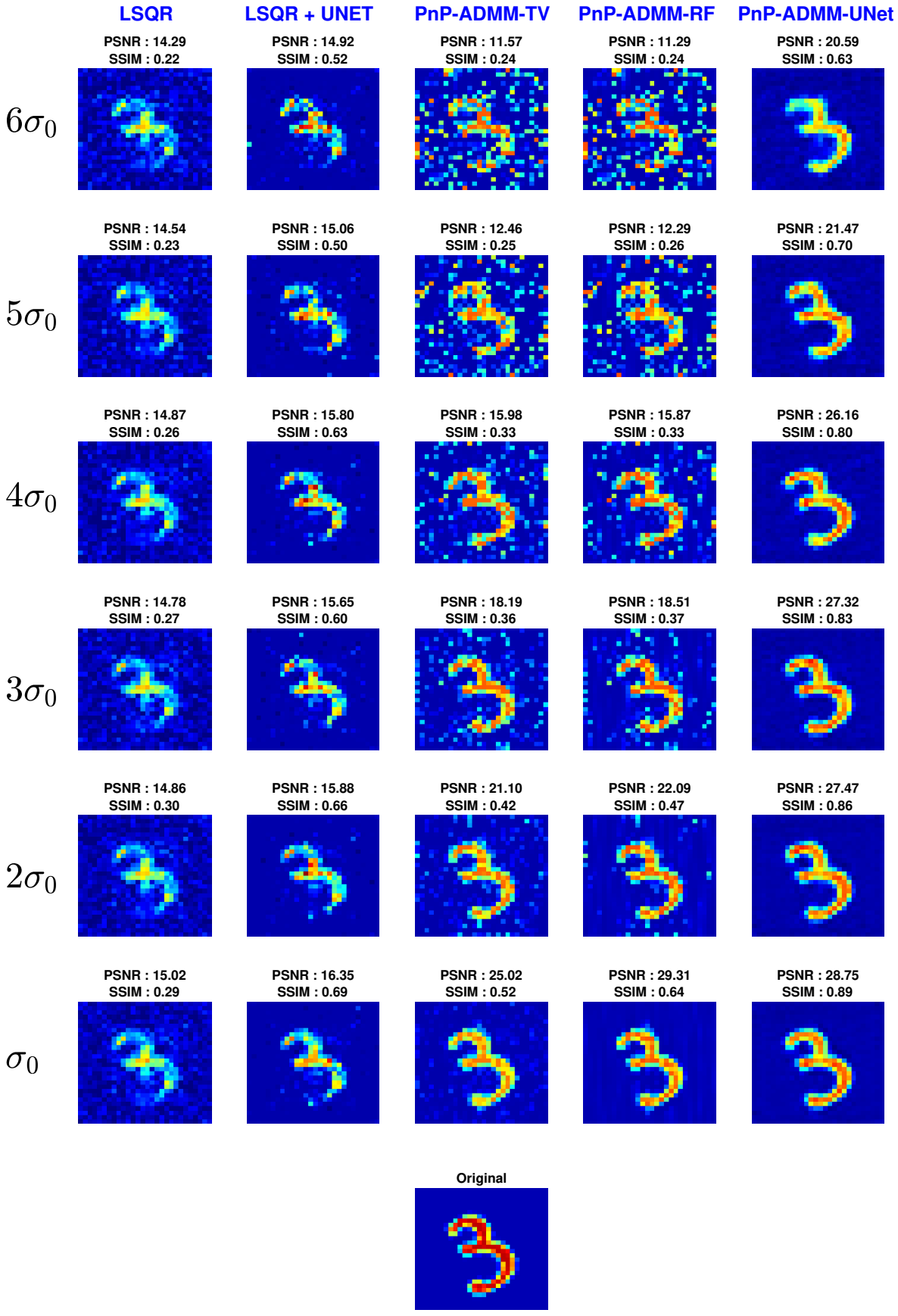


FIGURE 6.20: Measurement to unknowns ratio: 50% ($\frac{M}{N} = 50\%$)

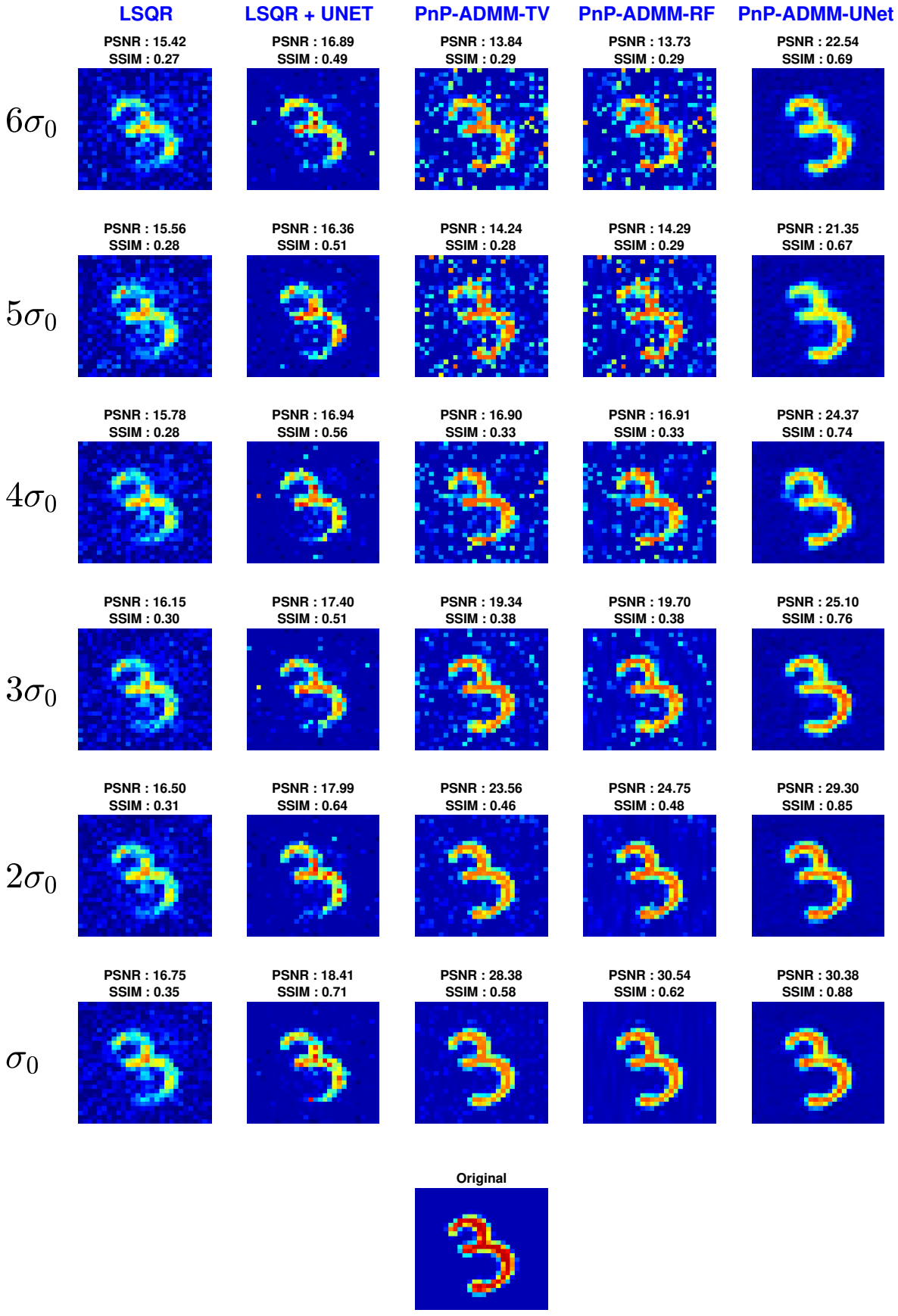


FIGURE 6.21: Measurement to unknowns ratio: 75% ($\frac{M}{N} = 75\%$)

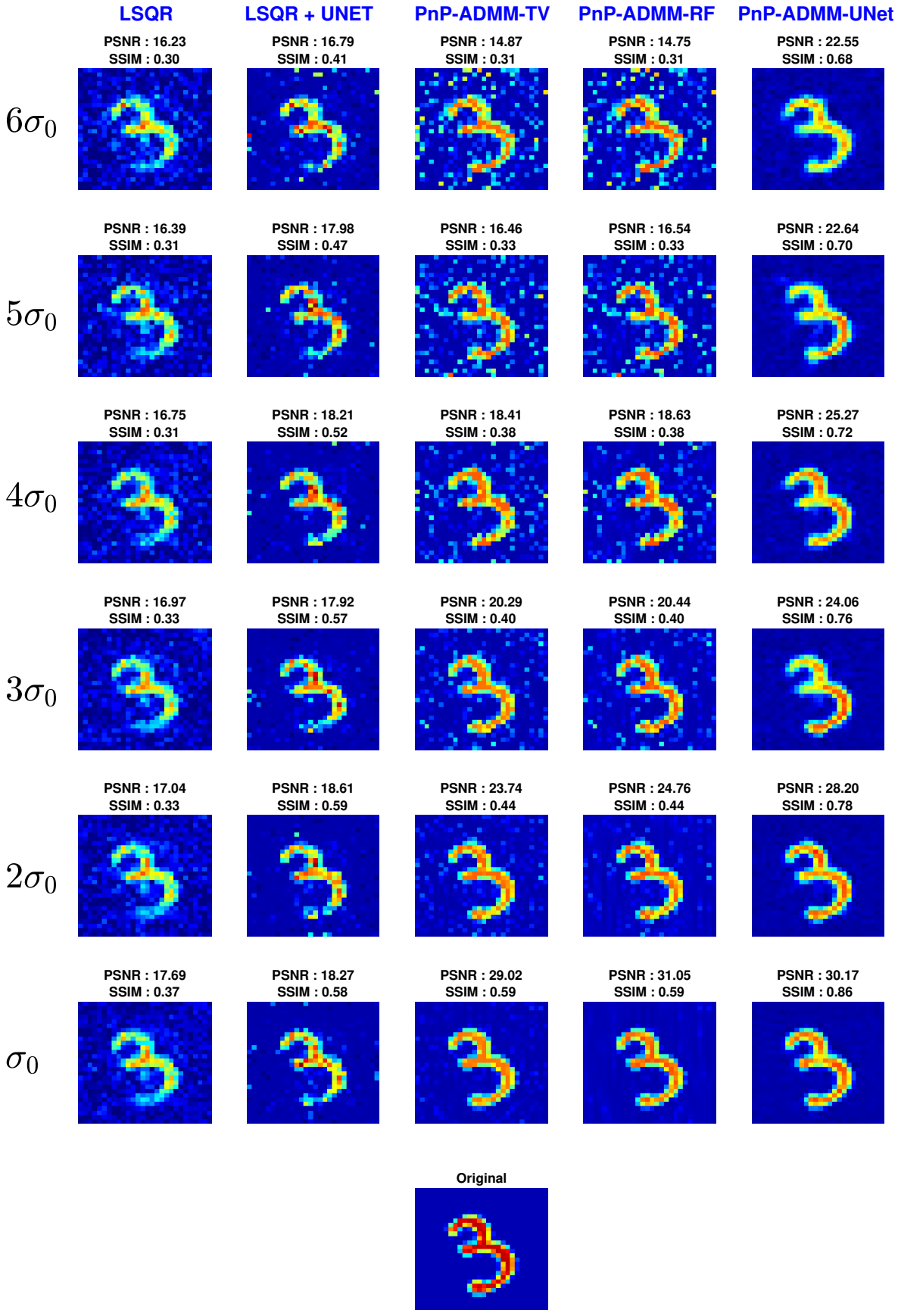
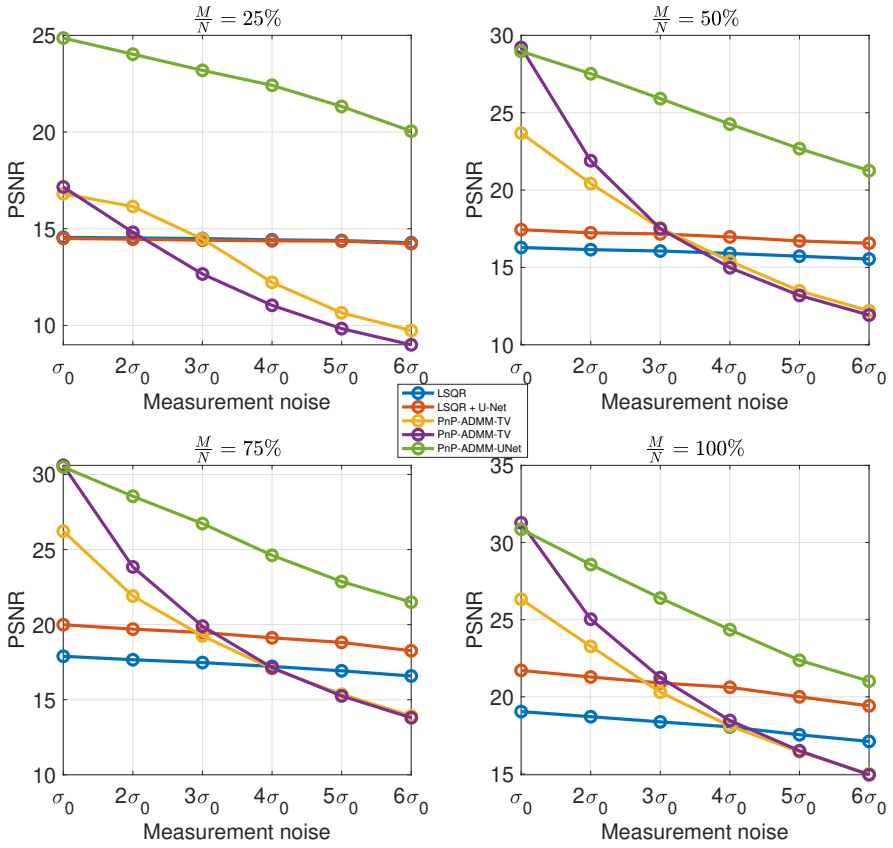
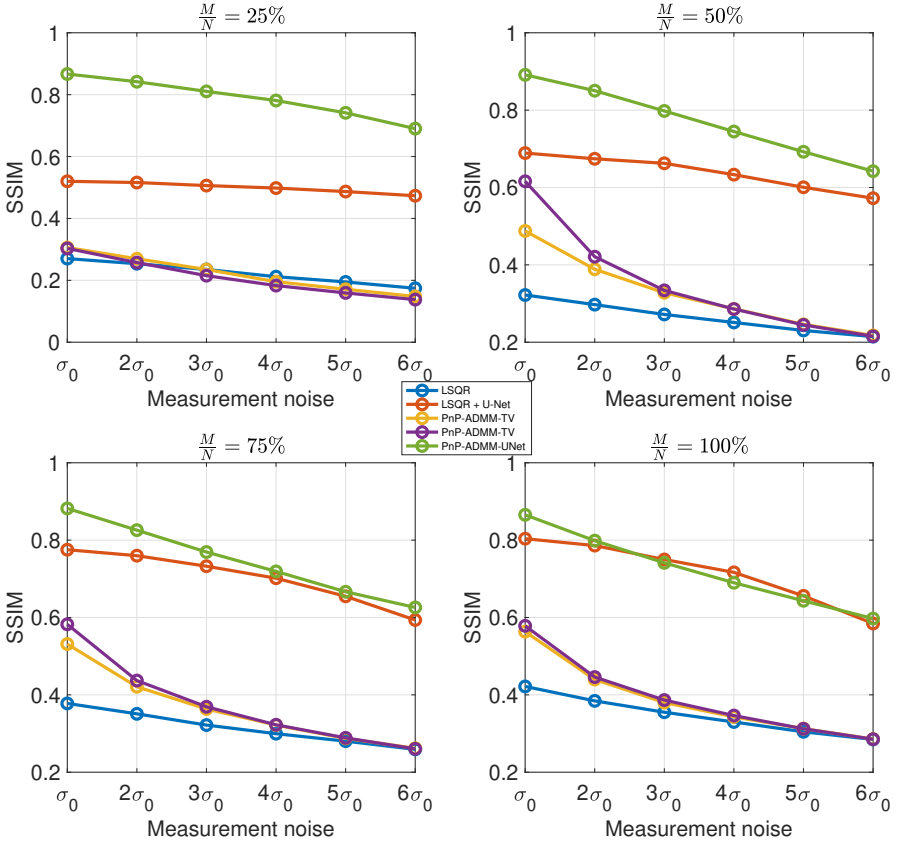


FIGURE 6.22: Measurement to unknowns ratio: 100% ($\frac{M}{N} = 100\%$)



(A) Average PSNR values



(B) Average SSIM values

FIGURE 6.23: Average PNSR and SSIM comparison of different reconstruction methods

Chapter 7

CONCLUSIONS

In this dissertation, we mainly study inverse reconstruction problems in the context of MIMO radar using deep-learning models. The first problem we study is the radar range profile reconstruction. In this problem, we focus on a side-looking FMCW MIMO radar measurement setup, where we explore the inverse problem of radar range profile reconstruction from band-limited, noisy radar measurements for real-valued and complex-valued radar range profile by utilizing PnP ADMM framework.

For the complex-valued profile assumption, we propose two solutions: one with magnitude regularization only and the other with both magnitude and phase regularization, depending on the significance of the spatial phase distribution in the radar range profile. We establish continuous and discrete Fourier-based measurement models for side-looking FMCW radar which links radar range profiles to radar measurements. Within our ADMM framework, we use deep learning networks as a regularization method to improve the inversion to tackle the issues that originates from the ill-posed nature of the inversion.

Our simulation results demonstrate the efficacy of deep learning networks as regularization methods within the ADMM framework for the radar range profile reconstruction problem. We train various networks using diverse datasets to capture

intricate spatial patterns in both magnitude and phase components of range profile data. The ADMM framework employing CNN architectures as regularizers emerges as the most successful method for radar range profile reconstruction, as indicated by our comparative analysis under different measurement scenarios.

We extend the PnP ADMM framework, initially designed for range profile reconstruction, to address MIMO radar imaging problems in two distinct imaging scenarios. Here, we employ U-Net architecture as a denoiser to learn the priors of radar images used for training. Our results highlight the superiority of the PnP ADMM framework with U-Net architecture as a denoiser in terms of reconstruction accuracy compared to other investigated methods.

Moreover, we explore the target angle estimation problem in MIMO radars. We propose an artificial neural network based approach for the estimation of the target angle using FMCW MIMO radars. The effectiveness of the proposed technique is evaluated against existing methods across various Signal-to-Noise Ratio (SNR) conditions and uncertainties in the measurement model. Simulations reveal that the model's learning capacity is significantly influenced by SNR conditions, with improvements observed in the learning process as SNR in the training data increases, as expected. Particularly under low SNR conditions, our proposed technique outperforms others in terms of Mean Square Error (MSE). Furthermore, we demonstrate that our solution remains robust in the face of model uncertainties, relying entirely on calibration data. In contrast, the performance of model-based angle estimation techniques deteriorates notably as uncertainty in the underlying model escalates.

Bibliography

[1] K. Akçapınar, N. Ö. Önhon, and Ö. Gürbüz. An artificial neural network based target angle estimation technique for FMCW MIMO radars. *Progress In Electromagnetics Research C*, 134:119–130, 2023.

[2] K. Akçapınar, N. Ö. Önhon, Ö. Gürbüz, and M. Çetin. Plug-and-play ADMM based radar range profile reconstruction using deep priors. *Progress In Electromagnetics Research*, Under Review.

[3] K. Akçapınar and S. Baykut. CM-CFAR parameter learning based square-law detector for foreign object debris radar. In *2018 48th European Microwave Conference (EuMC)*, pages 1441–1444, 2018.

[4] E. Brookner. Phased arrays around the world - progress and future trends. In *IEEE International Symposium on Phased Array Systems and Technology, 2003.*, pages 1–8, Oct 2003.

[5] J. Colin. Phased array radars in france: present and future. In *Proceedings of International Symposium on Phased Array Systems and Technology*, pages 458–462, Oct 1996.

[6] D. W. Bliss and K. W. Forsythe. Multiple-input multiple-output (MIMO radar and imaging: degrees of freedom and resolution. In *The Thrity-Seventh Asilomar Conference on Signals, Systems Computers, 2003*, volume 1, pages 54–59 Vol.1, Nov 2003.

[7] D. J. Rabideau and P. Parker. Ubiquitous MIMO multifunction digital array radar. In *The Thrity-Seventh Asilomar Conference on Signals, Systems Computers, 2003*, volume 1, pages 1057–1064 Vol.1, Nov 2003.

[8] E. Fishler, A. Haimovich, R. Blum, D. Chizhik, L. Cimini, and R. Valenzuela. MIMO radar: an idea whose time has come. In *Proceedings of the 2004 IEEE Radar Conference (IEEE Cat. No.04CH37509)*, pages 71–78, April 2004.

[9] A. M. Haimovich, R. S. Blum, and L. J. Cimini. MIMO radar with widely separated antennas. *IEEE Signal Processing Magazine*, 25(1):116–129, 2008.

[10] E. Fishler, A. Haimovich, R. S. Blum, L. J. Cimini, D. Chizhik, and R. A. Valenzuela. Spatial diversity in radars—models and detection performance. *IEEE Transactions on Signal Processing*, 54(3):823–838, March 2006.

[11] A. Lucas, M. Iliadis, R. Molina, and A. K. Katsaggelos. Using deep neural networks for inverse problems in imaging: Beyond analytical methods. *IEEE Signal Processing Magazine*, 35(1):20–36, Jan 2018.

[12] S. Boyd, N. Parikh, E. Chu, B. Peleato, and J. Eckstein. Distributed optimization and statistical learning via the alternating direction method of multipliers. *Foundations and Trends¬Æ in Machine Learning*, 3(1):1–122, 2011.

[13] S. Wang and R. Herschel. Fast 3D-CFAR for drone detection with MIMO radars. In *2021 18th European Radar Conference (EuRAD)*, pages 209–212, 2022.

[14] D. Zankl, S. Schuster, R. Feger, and A. Stelzer. What a blast!: A massive MIMO radar system for monitoring the surface in steel industry blast furnaces. *IEEE Microwave Magazine*, 18(6):52–69, 2017.

[15] J. Li and P. Stoica. MIMO radar with colocated antennas. *IEEE Signal Processing Magazine*, 24(5):106–114, 2007.

[16] A. Hassanien, M. G. Amin, Y. D. Zhang, and F. Ahmad. High-resolution single-snapshot DOA estimation in MIMO radar with colocated antennas. In *2015 IEEE Radar Conference (RadarCon)*, pages 1134–1138, 2015.

[17] R. Roy and T. Kailath. Esprit-estimation of signal parameters via rotational invariance techniques. *IEEE Transactions on Acoustics, Speech, and Signal Processing*, 37(7):984–995, 1989.

[18] R. Schmidt. Multiple emitter location and signal parameter estimation. *IEEE Transactions on Antennas and Propagation*, 34(3):276–280, 1986.

[19] O. A. Oumar, M. F. Siyau, and T. P. Sattar. Comparison between music and esprit direction of arrival estimation algorithms for wireless communication systems. In *The First International Conference on Future Generation Communication Technologies*, pages 99–103, 2012.

[20] Y. Yu, A. P. Petropulu, and H. V. Poor. MIMO radar using compressive sampling. *IEEE Journal of Selected Topics in Signal Processing*, 4(1):146–163, 2010.

[21] Z. Ni, B. Huang, and M. Cao. Angular positions estimation of spatially extended targets for MIMO radar using complex spatiotemporal sparse Bayesian learning. *IEEE Access*, 7:94473–94480, 2019.

[22] Z. Liu, C. Zhang, and P. S. Yu. Direction-of-arrival estimation based on deep neural networks with robustness to array imperfections. *IEEE Transactions on Antennas and Propagation*, 66(12):7315–7327, 2018.

[23] H. Huang, J. Yang, H. Huang, Y. Song, and G. Gui. Deep learning for super-resolution channel estimation and DoA estimation based massive MIMO system. *IEEE Transactions on Vehicular Technology*, 67(9):8549–8560, 2018.

[24] O. Bialer, N. Garnett, and T. Tirer. Performance advantages of deep neural networks for angle of arrival estimation. In *ICASSP 2019 - 2019 IEEE International Conference on Acoustics, Speech and Signal Processing (ICASSP)*, pages 3907–3911, 2019.

[25] W. Zhu, M. Zhang, P. Li, and C. Wu. Two-dimensional DOA estimation via deep ensemble learning. *IEEE Access*, 8:124544–124552, 2020.

[26] Y. Ma, Y. Zeng, and S. Sun. A deep learning based super resolution DoA estimator with single snapshot MIMO radar data. *IEEE Transactions on Vehicular Technology*, 71(4):4142–4155, 2022.

[27] M.A.G Al-Sadoon, N.T. Ali, Y. Dama, A. Zuid, S.M.R. Jones, R.A. Abd-Alhameed, and J.M. Noras. A new low complexity angle of arrival algorithm for 1D and 2D direction estimation in MIMO smart antenna systems. *Sensors (Basel)*, 9:15;17(11):2631, 2017.

[28] S.P. Jacobs and J.A. O'Sullivan. Automatic target recognition using sequences of high resolution radar range-profiles. *IEEE Transactions on Aerospace and Electronic Systems*, 36(2):364–381, 2000.

[29] A. Ganis, E. M. Navarro, B. Schoenlinner, U. Prechtel, A. Meusling, C. Heller, T. Spreng, J. Mietzner, C. Krimmer, B. Haeberle, S. Lutz, M. Loghi, A. Belenguer, H. Esteban, and V. Ziegler. A portable 3-D imaging FMCW MIMO radar demonstrator with a 24×24 antenna array for medium-range applications. *IEEE Transactions on Geoscience and Remote Sensing*, 56(1):298–312, 2018.

[30] C.J. Leuschen and R.G. Plumb. A matched-filter-based reverse-time migration algorithm for ground-penetrating radar data. *IEEE Transactions on Geoscience and Remote Sensing*, 39(5):929–936, 2001.

[31] S. Zhao and I. L. Al-Qadi. Development of regularization methods on simulated ground-penetrating radar signals to predict thin asphalt overlay thickness. *Signal Processing*, 132:261–271, 2017.

[32] M. Cetin and W.C. Karl. Feature-enhanced synthetic aperture radar image formation based on nonquadratic regularization. *IEEE Transactions on Image Processing*, 10(4):623–631, 2001.

[33] M. Çetin, W. C. Karl, and D. A. Castañón. Formation of HRR profiles by nonquadratic optimization for improved feature extraction. In *SPIE Defense + Commercial Sensing*, 2002.

[34] E. A. Miran, F. S. Oktem, and S. Koc. Sparse reconstruction for near-field MIMO radar imaging using fast multipole method. *IEEE Access*, 9:151578–151589, 2021.

[35] I. Jeffrey, Vladimir I., J. LoVetri, and C. Gilmore. An adaptive basis function solution to the 1D and 2D inverse scattering problems using the DBIM and the BIM. *The Applied Computational Electromagnetics Society Journal (ACES)*, 22(1):60–70, Jun. 2022.

[36] J. He, Y. Yang, Y. Wang, D. Zeng, Z. Bian, H. Zhang, J. Sun, Z. Xu, and J. Ma. Optimizing a parameterized plug-and-play ADMM for iterative low-dose CT reconstruction. *IEEE Transactions on Medical Imaging*, 38(2):371–382, 2019.

[37] H. E. Güven, A. Güngör, and M. Çetin. An augmented lagrangian method for complex-valued compressed SAR imaging. *IEEE Transactions on Computational Imaging*, 2(3):235–250, 2016.

[38] S. Sreehari, S. V. Venkatakrishnan, B. Wohlberg, G. T. Buzzard, L. F. Drummy, J. P. Simmons, and C. A. Bouman. Plug-and-play priors for bright field electron tomography and sparse interpolation. *IEEE Transactions on Computational Imaging*, 2(4):408–423, 2016.

[39] S. H. Chan, X. Wang, and O. A. Elgendy. Plug-and-play admm for image restoration: Fixed-point convergence and applications. *IEEE Transactions on Computational Imaging*, 3(1):84–98, 2017.

[40] K. Dabov, A. Foi, V. Katkovnik, and K. Egiazarian. Image denoising by sparse 3-D transform-domain collaborative filtering. *IEEE Transactions on Image Processing*, 16(8):2080–2095, 2007.

[41] S. H. Chan, R. Khoshabeh, K. B. Gibson, P. E. Gill, and T. Q. Nguyen. An augmented lagrangian method for total variation video restoration. *IEEE Transactions on Image Processing*, 20(11):3097–3111, 2011.

[42] E. S. L. Gastal and M. M. Oliveira. Domain transform for edge-aware image and video processing. *ACM Trans. Graph.*, 30(4), jul 2011.

[43] A. Buades, B. Coll, and J.-M. Morel. A non-local algorithm for image denoising. In *2005 IEEE Computer Society Conference on Computer Vision and Pattern Recognition (CVPR'05)*, volume 2, pages 60–65 vol. 2, 2005.

[44] X. Li, X. Bai, Y. Zhang, and F. Zhou. High-resolution ISAR imaging based on plug-and-play 2D ADMM-Net. *Remote Sensing*, 14(4), 2022.

[45] X. Gao, C. Xiao, and C. Zhang. Plug-and-play ADMM for sparse ISAR imaging. In *2021 CIE International Conference on Radar (Radar)*, pages 6–10, 2021.

[46] M. B. Alver, A. Saleem, and M. Çetin. Plug-and-play synthetic aperture radar image formation using deep priors. *IEEE Transactions on Computational Imaging*, 2020.

[47] Y. Liu and J. P. Haldar. Palmnut: An enhanced proximal alternating linearized minimization algorithm with application to separate regularization of magnitude and phase. *IEEE Transactions on Computational Imaging*, pages 1–1, 2021.

[48] F. Ong, J. Y. Cheng, and M. Lustig. General phase regularized reconstruction using phase cycling. *Magnetic Resonance in Medicine*, 80(1):112–125, 2018.

[49] F. Zhao, D. C. Noll, J.-F. Nielsen, and J. A. Fessler. Separate magnitude and phase regularization via compressed sensing. *IEEE Transactions on Medical Imaging*, 31(9):1713–1723, 2012.

[50] J.A. Fessler and D.C. Noll. Iterative image reconstruction in mri with separate magnitude and phase regularization. In *2004 2nd IEEE International Symposium on Biomedical Imaging: Nano to Macro (IEEE Cat No. 04EX821)*, pages 209–212 Vol. 1, 2004.

[51] K. Akçapınar and Ö. Gürbüz. Full duplex-ing over two hops under full interference. In *2018 Wireless Advanced (WiAd)*, pages 1–5, 2018.

[52] K. Akçapınar, Ö. Gürbüz, and T. Ünlüyurt. Power allocation and routing for full-duplex multi hop wireless networks under full interference. *Ad Hoc Networks*, 82:91–99, 2019.

[53] K. Akçapınar, Ö. Gürbüz, and T. Ünlüyurt. Optimal power control for full duplex wireless networks with full interference. In *First International Balkan Conference on Communications and Networking (BalkanCom 2017), Tirana, Albenia*, 2017.

[54] M. Çetin. *Feature-Enhanced Synthetic Aperture Radar Imaging*. PhD thesis, Boston University, 2001.

[55] Gotcha volumetric SAR data set,version 1.0. `https://www.sdms.afrl.af.mil/mai`. [Online; accessed 19-May-2022].

[56] Y. Zhang, F. Zhang, and S. Pan. Ultra-high resolution radar imaging based on microwave photonics. In *2018 19th International Radar Symposium (IRS)*, pages 1–6, June 2018.

[57] K. Mizuno, Y. Wagatsuma, H. Warashina, K. Sawayad, H. Sato, S. Miyanaga, and Y. Yamanaka. Millimeter-wave imaging technologies and their applications. In *2007 IEEE International Vacuum Electronics Conference*, pages 1–2, May 2007.

[58] C. Zhang, Y. Kuga, and A. Ishimaru. Hard-wall radar imaging: Localization of objects shadowed by metallic walls with MIMO radar. *IEEE Transactions on Antennas and Propagation*, 66(8):4240–4251, Aug 2018.

[59] X. Zhuge. Short-range ultra-wideband imaging with multiple-input multiple-output arrays. *Ph.D Dissertation*.

[60] D. Zankl, S. Schuster, R. Feger, and A. Stelzer. What a blast!: A massive MIMO radar system for monitoring the surface in steel industry blast furnaces. *IEEE Microwave Magazine*, 18(6):52–69, Sep. 2017.

[61] J. R. Gallion and R. Zoughi. Millimeter-wave imaging of surface-breaking cracks in steel with severe surface corrosion. *IEEE Transactions on Instrumentation and Measurement*, 66(10):2789–2791, Oct 2017.

[62] A. Jouade. Millimeter-wave radar imaging systems: focusing antennas, passive compressive devicefor MIMO configurations and high resolution signal processing. *Ph.D Dissertation*, 2015.

[63] X. Zhuge and A. G. Yarovoy. Three-dimensional near-field MIMO array imaging using range migration techniques. *IEEE Transactions on Image Processing*, 21(6):3026–3033, June 2012.

[64] M. B. Kocamis and F. S. Oktem. Optimal design of sparse MIMO arrays for near-field ultrawideband imaging. In *2017 25th European Signal Processing Conference (EUSIPCO)*, pages 1952–1956, Aug 2017.

[65] F. S. Oktem. Sparsity-based three-dimensional image reconstruction for near-field MIMO radar imaging. *Turkish Journal Elec. Eng. & Comp. Sci.*

[66] E. Miralles, T. Multerer, A. Ganis, B. Schoenlinner, U. Prechtel, A. Meusling, J. Mietzner, C. Weckerle, H. Esteban, M. Vossiek, M. Loghik, and V. Ziegler. Multifunctional and compact 3D FMCW MIMO radar system with rectangular array for medium-range applications. *IEEE Aerospace and Electronic Systems Magazine*, 33(4):46–54, April 2018.

[67] M. E. Yanik and M. Torlak. Near-field MIMO-SAR millimeter-wave imaging with sparsely sampled aperture data. *IEEE Access*, 7:31801–31819, 2019.

[68] A. Mousavi, A. B. Patel, and R. G. Baraniuk. A deep learning approach to structured signal recovery. In *2015 53rd Annual Allerton Conference on*

Communication, Control, and Computing (Allerton), pages 1336–1343, Sep. 2015.

[69] A. Mousavi and R. G. Baraniuk. Learning to invert: Signal recovery via deep convolutional networks. In *2017 IEEE International Conference on Acoustics, Speech and Signal Processing (ICASSP)*, pages 2272–2276, March 2017.

[70] T. N. Canh and B. Jeon. Multi-scale deep compressive sensing network. In *2018 IEEE Visual Communications and Image Processing (VCIP)*, pages 1–4, Dec 2018.

[71] K. Kulkarni, S. Lohit, P. Turaga, R. Kerviche, and A. Ashok. Reconnet: Non-iterative reconstruction of images from compressively sensed measurements. In *2016 IEEE Conference on Computer Vision and Pattern Recognition (CVPR)*, pages 449–458, June 2016.

[72] R. W. Deming. Tutorial on Fourier space coverage for scattering experiments, with application to SAR. In Edmund G. Zelnio and Frederick D. Garber, editors, *Algorithms for Synthetic Aperture Radar Imagery XVII*, volume 7699, pages 28 – 39. International Society for Optics and Photonics, SPIE, 2010.

[73] O. Ronneberger, P. Fischer, and T. Brox. U-net: Convolutional networks for biomedical image segmentation, 2015.

[74] L. Deng. The mnist database of handwritten digit images for machine learning research. *IEEE Signal Processing Magazine*, 29(6):141–142, 2012.

[75] X. Zhuge and A. G. Yarovoy. A sparse aperture mimo-sar-based UWB imaging system for concealed weapon detection. *IEEE Transactions on Geoscience and Remote Sensing*, 49(1):509–518, 2011.

[76] Q. Guo, J. Wang, T. Chang, and H.-L. Cui. Dimension-factorized range migration algorithm for regularly distributed array imaging. *Sensors*, 17(11), 2017.

[77] E. A. Miran, F. S. Oktem, and S. Koc. Sparse reconstruction for near-field MIMO radar imaging using fast multipole method. *IEEE Access*, 9:151578–151589, 2021.

[78] H. M. Yao, W. E. I. Sha, and L. Jiang. Two-step enhanced deep learning approach for electromagnetic inverse scattering problems. *IEEE Antennas and Wireless Propagation Letters*, 18(11):2254–2258, 2019.

[79] L. Li, Long G. Wang, and F. L. Teixeira. Performance analysis and dynamic evolution of deep convolutional neural network for electromagnetic inverse scattering. *IEEE Antennas and Wireless Propagation Letters*, 18(11):2259–2263, 2019.